INFORMATION TO USERS

This manuscript has been reproduced from the microfilm master. UMI films the text directly from the original or copy submitted. Thus, some thesis and dissertation copies are in typewriter face, while others may be from any type of computer printer.

The quality of this reproduction is dependent upon the quality of the copy submitted. Broken or indistinct print, colored or poor quality illustrations and photographs, print bleedthrough, substandard margins, and improper alignment can adversely affect reproduction.

In the unlikely event that the author did not send UMI a complete manuscript and there are missing pages, these will be noted. Also, if unauthorized copyright material had to be removed, a note will indicate the deletion.

Oversize materials (e.g., maps, drawings, charts) are reproduced by sectioning the original, beginning at the upper left-hand corner and continuing from left to right in equal sections with small overlaps.

Photographs included in the original manuscript have been reproduced xerographically in this copy. Higher quality 6" x 9" black and white photographic prints are available for any photographs or illustrations appearing in this copy for an additional charge. Contact UMI directly to order.

Bell & Howell Information and Learning
300 North Zeeb Road, Ann Arbor, MI 48106-1346 USA

UMI®
800-521-0600

CLASSICALLY BONDED CHALCOGENIDE ANIONS OF TIN, THALLIUM, AND LEAD IN BASIC MEDIA

By

Ayaaz M. Pirani, B. Sc.

A Thesis

Submitted to the School of Graduate Studies

in Partial Fulfillment of the Requirements

for the Degree

Doctor of Philosophy

McMaster University

CLASSICALLY BONDED CHALCOGENIDE ANIONS OF TIN, THALLIUM, AND LEAD IN BASIC MEDIA

Dedicated to the Memory of my Beloved Father,

Mehdi H. A. Pirani (1932–1994)

and

To my Wonderful Mother, Dilshad M. Pirani

DOCTOR OF PHILOSOPHY (1997) McMASTER UNIVERSITY

(Chemistry) Hamilton, Ontario

TITLE: Classically Bonded Chalcogenide Anions of Tin, Thallium, and Lead in Basic Media

AUTHOR: Ayaaz M. Pirani, B. Sc. (McMaster University)

SUPERVISOR: Professor Gary J. Schrobilgen

NUMBER OF PAGES: xxv, 299

ABSTRACT

This Thesis describes the preparation of classically-bonded chalcogenide anions of tin, thallium, and lead in basic media and their structural characterization in solution by multi-nuclear magnetic resonance (multi-NMR) spectroscopy and in the solid-state by single-crystal X-ray crystallography and vibrational (Raman) spectroscopy.

The $Sn_2Ch_6^{4-}$ and $Sn_2Ch_7^{4-}$ (Ch = Se, Te) anions have been characterized in solution for the first time by multi-NMR spectroscopy. The magnitudes of the relativistically corrected reduced coupling constants $^1K(Sn–Ch_t)_{RC}$, $^1K(Sn–Ch_{mb})_{RC}$, and $^1K(Sn–Ch_{db})_{RC}$ were shown to be consistent with a significant degree of *s*-character in the bonding. The $Sn–Ch_{mb}$ and $Sn–Ch_t$ bond distances observed in the X-ray crystal structures of the $Sn_2Ch_6^{4-}$ anions were shown to correlate with the $^1K(Sn–Ch_t)_{RC}$ values, indicating that the solid-state molecular structures of the anions are retained in solution. The Raman spectra of the $Sn_2Ch_6^{4-}$ anions are also reported along with their respective factor-group analyses. The novel $HOSnTe_3^{3-}$ anion, the hydroxide derivative of $SnTe_3^{2-}$, has been structurally characterized by X-ray crystallography and represents the first example of a simple mixed hydroxy-chalcogenide anion of tin.

The novel $Sn_4Ch_{10}^{4-}$ (Ch = Se, Te) have been characterized for the first time in solution by ^{77}Se, ^{119}Sn, and ^{125}Te NMR spectroscopy and in the solid-state by X-ray crystallography and Raman spectroscopy. The solid-state and solution anion geometry is of the adamantanoid type where the Sn^{IV} atoms occupy the bridgehead position and the Ch

atoms occupy the bridging and terminal sites. The Raman spectra of the $Sn_4Ch_{10}^{4-}$ anions have been assigned and compared with those of related adamantanoid systems and $SnSe_4^{4-}$. The X-ray crystal structure of the novel adamantanoid $Sn_4Se_9^{4-}$ anion is also reported and represents the first example of a P_4O_9-type post-transition element anion containing tin and a chalcogen.

The solution and X-ray crystal structure of the $Tl_2Te_2^{2-}$ anion and the vibrational spectra of the $Tl_2Ch_2^{2-}$ (Ch = Se, Te) anions have been determined. Density functional theory calculations at the local and nonlocal levels confirm that the butterfly geometries observed in the solid state are true minima in the gas phase but are highly deformable. This finding is supported by the variation of the ^{205}Tl–^{203}Tl spin–spin coupling constants in the $Tl_2Ch_2^{2-}$ (Se and/or Te) anions with solvent and temperature and by the observed and calculated low vibrational frequencies of the anion inversion modes. Theory indicates that the Tl–Ch bonds are essentially pure *p* in character and a significant concentration of *s*-electron density along the Tl···Tl axes and is supported by the small magnitudes of $^1K(Tl–Ch)_{RC}$ and the large magnitudes of $K(Tl–Tl)_{RC}$ observed for the $Tl_2Ch_2^{2-}$ (Ch = Se and/or Te) anions in solution.

The series of Group 14 metal trigonal bipyramidal $M_2Ch_3^{2-}$ (M = Sn and/or Pb; Ch = S, Se, and/or Te) anions has been extended to the mixed-metal $TlMTe_3^{3-}$ (M = Sn, Pb) anions which were characterized in solution by ^{119}Sn, ^{125}Te, ^{207}Pb, and ^{205}Tl NMR spectroscopy. The $TlPbTe_3^{3-}$ anion was also characterized by X-ray crystallography in the compound $(2,2,2\text{-crypt-}K^+)_3TlPbTe_3^{3-}\cdot 2en$. The small magnitudes of $^1K(M–Ch)_{RC}$ observed for $M_2Ch_3^{2-}$ and $TlMTe_3^{3-}$ are consistent with predominantly *p*-bonded cages and is supported

by local and nonlocal density functional theory calculations which indicate that the experimental structures are true minima. Although theory indicates weak M···M interactions of high *s* orbital character on M, the large $K(M–M)_{RC}$ and $K(Tl–M)_{RC}$ couplings appear to arise predominantly from multiple coupling pathways and can be rationalized in terms of the small M–Ch–M bond angles observed in the X-ray crystal structures.

The novel $Tl_2Se_x^{n-}$, $Tl_3Se_y^{m-}$, and $Tl_3Se_z^{p-}$ anions have been obtained by extraction of the alloys NaTlSe and $NaTl_{0.5}Se$ in en and liquid NH_3 in the presence or absence of 2,2,2-crypt and characterized by variable-temperature ^{77}Se, ^{203}Tl, and ^{205}Tl NMR spectroscopy. Although the detailed solution structures of the anions have not yet been determined, they were shown by an analysis of the Tl–Tl spin–spin coupling patterns and the ^{203}Tl and ^{205}Tl subspectra arising from natural abundance isotopomer distributions to be di- and trinuclear with respect to thallium. The X-ray crystal structures of the novel $Tl_4Se_8^{4-}$ and $[TlSe_{4/2}^{-}]_\infty^1$ anions are also reported and represent rare examples of thallium selenide polyanions.

ACKNOWLEDGEMENTS

I wish to thank Prof. G. J. Schrobilgen for his invaluable guidance and support throughout this work. I am grateful to Dr. H. P. A. Mercier for her friendship, support, and encouragement.

The interest and support offered by members of my supervisory committee, Drs. J. Laposa and J. Barbier, is gratefully acknowledged.

Michael Palme is gratefully acknowledged for making the glassware used during this work and for his friendship.

Special thanks to Dr. H. Borrmann (Max-Planck-Institut für Festkörperforshung (MPI), Stuttgart, Germany) for collecting the diffraction data on most compounds reported in this Thesis and for his hospitality during my visit to Stuttgart. Prof. A. Simon, MPI Stuttgart, is acknowledged for making the imaging plate diffractometer system available.

Dr. D. A. Dixon (William R. Wiley Environmental Molecular Sciences Laboratory, Richland, Washington) is acknowledged for performing the density functional theory calculations reported in this work. Dr. J. Hellmann (Bruker Spectrospin, Milton, Ontario) is gratefully acknowledged for obtaining the Raman spectra of the $Tl_2Ch_2^{2-}$ (Ch = Se, Te) anions.

Many thanks to Dr. J. Britten for his assistance with the operation of the X-ray equipment at McMaster and to Dr. D. W. Hughes and Mr. B. Sayer for their assistance with the NMR spectrometers.

I am grateful to the many people who have offered their friendship and support during my tenure at McMaster. In particular, I wish to thank Janette Campbell for her friendship and support throughout the years.

Navaz Gangji and his family are gratefully acknowledged for their continuous generosity, emotional support, and encouragement.

An extra special thanks to my father and mother for their unconditional love and support. I am deeply grateful to my brother, Raheem, for taking on the role of my father for the last three years and for his continuous guidance.

I especially thank my fiancée, Shaineez Kurji, for her emotional support, encouragement, and love without which this Thesis would not have been completed.

LIST OF ABBREVIATIONS AND SYMBOLS

General

s	second(s)
min	minute(s)
h	hour(s)
d	day(s)
o.d.	outside diameter
i.d.	inside diameter
en	ethylenediamine
THF	tetrahydrofuran
2,2,2-crypt	1,10-diaza-4,7,13,16,21,24-hexaoxabicyclo[8.8.8]hexacosane
18-crown-6	1,4,7,10,13,16-hexaoxacyclooctadecane

Nuclear Magnetic Resonance (NMR) Spectroscopy

CSA	chemical shielding anisotropy
ppm	parts per million
δ	chemical shift in ppm from a reference compound
$\Delta\delta$	chemical shift difference in ppm
J	scalar coupling constant in Hz
K	reduced coupling constant in $T^2 J^{-1}$
K_{RC}	relativistically corrected reduced coupling constant in $T^2 J^{-1}$

γ	gyromagnetic ratio of a nucleus in rad s^{-1} T^{-1}
I	nuclear spin quantum number
$\Delta\nu_{½}$	line width at half height

Vibrational Spectroscopy

ν	vibrational mode

X-ray Crystallography

σ	estimated standard deviation
F_o	observed structure factor
F_c	calculated structure factor
R_1	conventional agreement index

$$R_1 = \Sigma \big| \, |F_o| - |F_c| \, \big| \; / \; \Sigma |F_o|$$

w	overall weight parameter

$$w = 1/[\sigma^2(F_o^2) + (w_1P)^2 + (w_2P)]$$

where $P = (F_o^2 + 2F_c^2) / 3$ and w_1 and w_2 are the individual weight parameters and are given in subsequent Chapters for each compound.

wR_2	weighted agreement index

$$wR_2 = [\Sigma[w(F_o^2 - F_c^2)^2] / \Sigma[w(F_o^2)^2]]^{1/2}$$

S	Goodness of Fit

$$S = [\Sigma[w(F_o^2 - F_c^2)^2] / (n - p)]^{1/2}$$

where is n is the number of reflections and p is the total number of parameters refined.

TABLE OF CONTENTS

LIST OF TABLES

LIST OF FIGURES

CHAPTER 1

INTRODUCTION

Historical Note

Polyanions of the post-transition elements were discovered by Joannis[1,2] who reported in 1891 that lead, antimony, and bismuth dissolved in alkali-metal-liquid-ammonia mixtures to produce intensely-coloured solutions. Kraus and Franklin[3,4] subsequently demonstrated the electrolytic behaviour of the green solution obtained by dissolving lead in a sodium-liquid-ammonia mixture and attributed this behaviour to the presence of the Na^+ cations and Pb_2^- anions and also noted the electrolytic properties of a similar red sodium-tin solution. Smyth,[5] Peck,[6] Kraus,[7,8] and Bergstrom[9,10] subsequently determined the stoichiometries of the polyanions more accurately by electrolytic and/or solubility measurements and identified the Pb_9^{4-} and Sb_7^{3-} anions and also identified the Se_n^{2-} (n = 1–5) and Te_4^{2-} anions which were obtained by dissolving Se and Te in alkali-metal-liquid-ammonia solutions. In the 1930's, Zintl and coworkers[11-14] systematically investigated the compositions of the highly coloured solutions by potentiometric titrations of the solutions with liquid ammonia solutions of main-group halides and confirmed the presence of the Pb_9^{4-}, Sb_7^{3-}, Se_n^{2-}, and Te_4^{2-} anions and also identified a variety of other polyanions including Pn_n^{3-} (Pn = As, Sb, or Bi; n = 3, 5, or 7), Sn_9^{4-}, Pb_7^{4-}, and Te_n^{2-} (n = 2, 3).

A more direct approach to the synthesis of main-group element polyanion solutions

was developed by Zintl, Harder, and Dullenkopf[11,13-14] and involved the extraction of binary alloys such as $NaSn_x$ and $NaPb_x$ (x = 2.25–2.27) in liquid ammonia, resulting in the formation of Sn_9^{4-} and Pb_9^{4-}. This approach, however, was limited by the low solubilities of certain alloy phases such as NaGe; by the long alloy extraction times which ranged from several months to an entire year and often resulted in ammonolysis; and by the unavoidable exposure to atmospheric oxygen and moisture which led to the decomposition of the solutions. The experimental difficulties associated with alloy extractions led Zintl and coworkers to use the more classical synthetic approach involving the dissolution of main-group elements in alkali-metal-liquid-ammonia solutions in their studies of post-transition element polyanions. In recent years, however, the advent of inert-atmosphere techniques and the discovery of macrocyclic cryptands and crowns has renewed interests in alloy-extraction techniques, resulting in the synthesis and structural characterization of a large number of polyanions of the post-transition elements (*vide infra*).

Zintl and Harder[13] also attempted to isolate salts of the main-group polyanions for X-ray crystallographic studies by solvent evaporation from the binary alloy extracts. This technique, however, resulted in the formation of ammonia solvates which, upon further removal of the solvent, produced intermetallic phases. For example, decomposition of the $[Na(NH_3)_n^-]_3Sb_7^{3-}$ complex (eq. (1.1)) yielded a metallic phase which was identified as the

$$[Na(NH_3)_n^-]_3Sb_7^{3-} \rightarrow 3NaSb + 4Sb + nNH_3 \qquad (1.1)$$

starting alloy. Although the instabilities of the solvated polyanion salts prevented their

structural characterization by X-ray crystallography, Zintl and coworkers pioneered X-ray crystallographic studies of the intermetallic phases and obtained, for the first time, the structures of the polyanions in these phases. As a result of Zintl's extensive solution and crystallographic studies of post-transition element polyanions, the polyanions and the intermetallic A_xM_y (A = alkali or alkali-earth metal; M = post-transition element) phases from which they can be obtained have been termed by Laves[15] as "Zintl anions" and "Zintl phases", respectively.

Modern Developments

It was not until 1970 that Kummer and Diehl[16] successfully isolated the first stable salt of a Zintl polyanion. The X-ray crystal structure of the compound $Na_4(en_7)Sn_9$, which was obtained upon addition of diethyleneglycol monoethyl ether or tetrahydrofuran (THF) to an ethylenediamine (en) solution of a sodium-tin alloy, was shown to consist of a highly disordered and distorted Sn_9^{4-} polyanion. Corbett and Edwards[17] subsequently reported that stable salts containing discrete Zintl anions can be obtained from en or liquid NH_3 extracts of intermetallic phases by complexing the alkali-metal counterions with the macrobicyclic ligand, 2,2,2-crypt (1,10-diaza-4,7,13,16,21,24-hexaoxabicyclo[8.8.8]hexacosane; Figure 1.1), which contains a three-dimensional intramolecular cavity capable of accommodating alkali-metal cations, including Na^+ and K^+, resulting in the formation of highly stable 2,2,2-crypt-A^+ (A = Na, K) inclusion complexes.[18–22] These inclusion complexes prevent the formation of intermetallic phases when solvent is removed from the alloy extracts and give

a

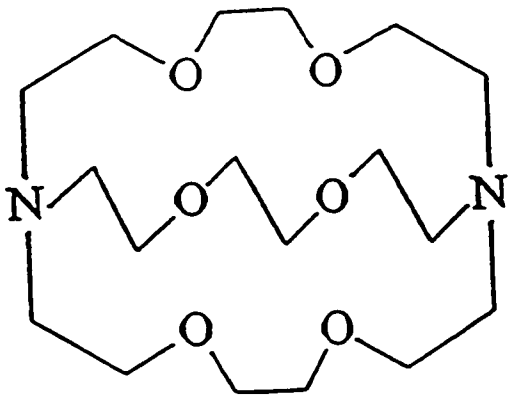

b

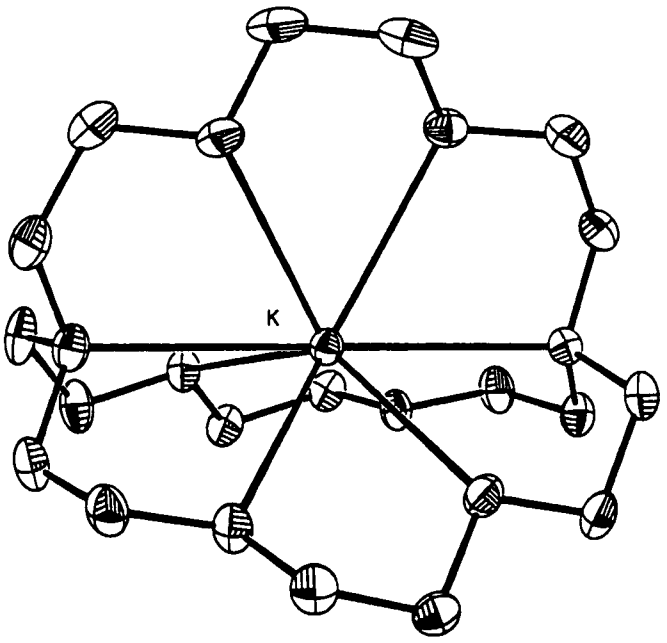

Figure 1.1. Structures of (a) 2,2,2-crypt[18] and (b) the inclusion complex 2,2,2-crypt-K^- in $(2,2,2\text{-crypt-}K^-)_2Cr_2(CO)_{10}^{2-}$.[23] Hydrogen atoms have been omitted for clarity.

rise to stable salts of polyanions having the general formula (2,2,2-crypt-A^+)$_n$$M^{n-}$, where M is a polyanion of charge $n-$. This approach has permitted the isolation and structural characterization of a large number of homo- and heteronuclear polyatomic Zintl anions including M_5^{2-} (M = Ge,[24] Sn,[25] Pb[25]), M_9^{4-} (M = Ge,[26] Sn,[27,28] Pb[29]), $TlSn_8^{3-}$,[30] $TlSn_9^{3-}$,[30] $As_{11}Te^{3-}$,[31] and $As_7Se_4^-$.[32] The use of 2,2,2-crypt also dramatically increases the solubilities of intermetallic phases in basic, non-aqueous solvents thereby decreasing alloy extraction times. For example, the alloy KTlSe when extracted in en or in liquid NH_3 in the presence of 2,2,2-crypt immediately gives rise to an intense red solution but only produces a pale red solution in the absence of 2,2,2-crypt.[33] Moreover, the dependence of the nature of the polyanions in solution on the amount of 2,2,2-crypt used has also been noted. Crystals of K^+(2,2,2-crypt-K^+)$_3$$Pb_9^{4-}$ were isolated from en solutions of $KPb_{2.05}$ when K^+ was in excess with respect to 2,2,2-crypt, whereas (2,2,2-crypt-K^+)$_3$$Pb_9^{3-}$ was isolated when 2,2,2-crypt was used in excess.[29]

Classification of Zintl Anions

Zintl anions are generally classified as "cluster" (electron-deficient) or "classical" (electron-precise) according to the type of bonding involved.[34,35] Cluster polyanions can be obtained from binary intermetallic A_xM_y phases and are electron deficient in the sense that each atom in the cluster possesses more valence orbitals than valence electrons and are therefore structurally and electronically related to boranes and carboranes. The structures of cluster anions can be deduced from simple electron-counting rules established in the 1970's

by Wade[36,37] which relate the number of skeletal electrons to cluster geometries and have been discussed in detail elsewhere.[38] Examples of cluster polyanions include M_5^{2-} (M = Ge, Sn, Pb), M_9^{4-} (M = Ge, Sn, Pb), $TlSn_8^{3-}$ and $TlSn_9^{3-}$. The incorporation of a chalcogen, Ch (Ch = S, Se, or Te), into the binary A_xM_y phases facilitates the synthesis of classical anions which represent the newest class of Zintl polyanions. The anions are termed classical because the bonding between the M atoms and the Ch ligands is electron precise and can be described in terms of "2-centre-2-electron" bonding. Electron precise Zintl anions possess a larger structural variety (Figures 1.2–1.4) and are commonly classified as chains (e.g., Se_9^{2-},[39] Te_4^{2-},[40–43] Te_6^{2-}[43]), rings (e.g., $Tl_2Te_2^{2-}$,[44] $As_2Te_6^{2-}$,[45] $Ge_2Se_8^{4-}$[46]), and cages (e.g., Sb_7^{3-},[47] $As_{11}Te^{3-}$,[31] $Ge_4Se_{10}^{4-}$[46]).

In the 1970's, Krebs and coworkers[48–54] prepared and characterized a large number of classically-bonded thio- and selenoanions of a variety of main-group elements. The anions were prepared by nucleophilic degradation of the metal sulfides or selenides with aqueous alkaline sulfide or selenide solutions. Anion mixtures were formed in most of the resulting solutions and their relative concentrations were found to be highly sensitive to pH. For example, Krebs and coworkers noted during their investigations of thiogermanates that the smaller GeS_4^{4-} was prepared exclusively in strongly basic aqueous solutions whereas the larger $Ge_2S_6^{4-}$, $Ge_2S_7^{4-}$, and $Ge_4S_{10}^{4-}$ polyanions were found to coexist with GeS_4^{4-} when the solutions were acidified. Krebs and coworkers suggested that an increase in the acidity of the aqueous medium leads to stronger solvation of the S^{2-} anion and to its subsequent protonation to form HS^- (eq. (1.2)) and proposed a series of pH-dependent condensation

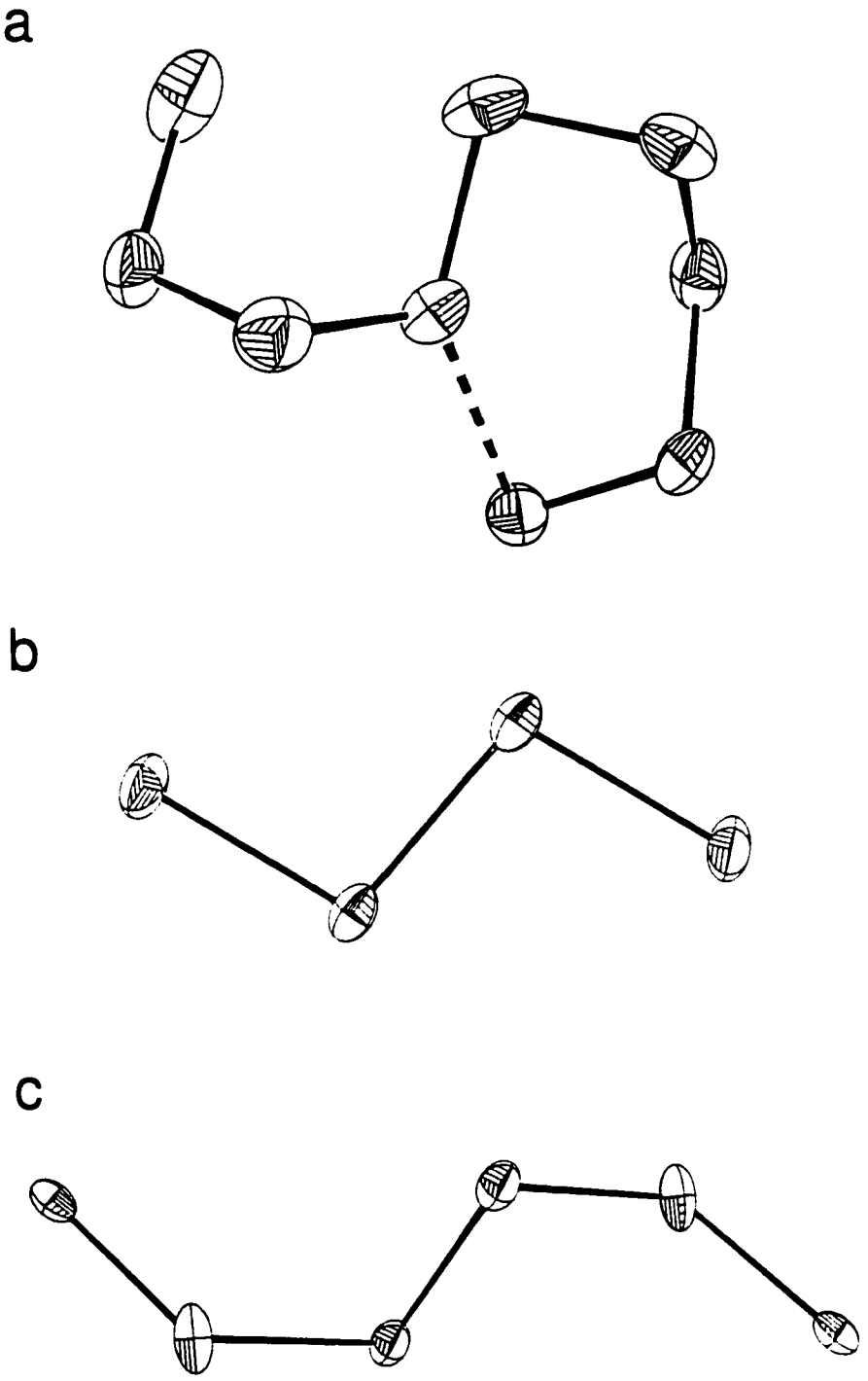

Figure 1.2. Some examples of electron precise chain anions; (a) Se_9^{2-},[39] (b) Te_4^{2-},[40–43] and (c) Te_6^{2-}.[43]

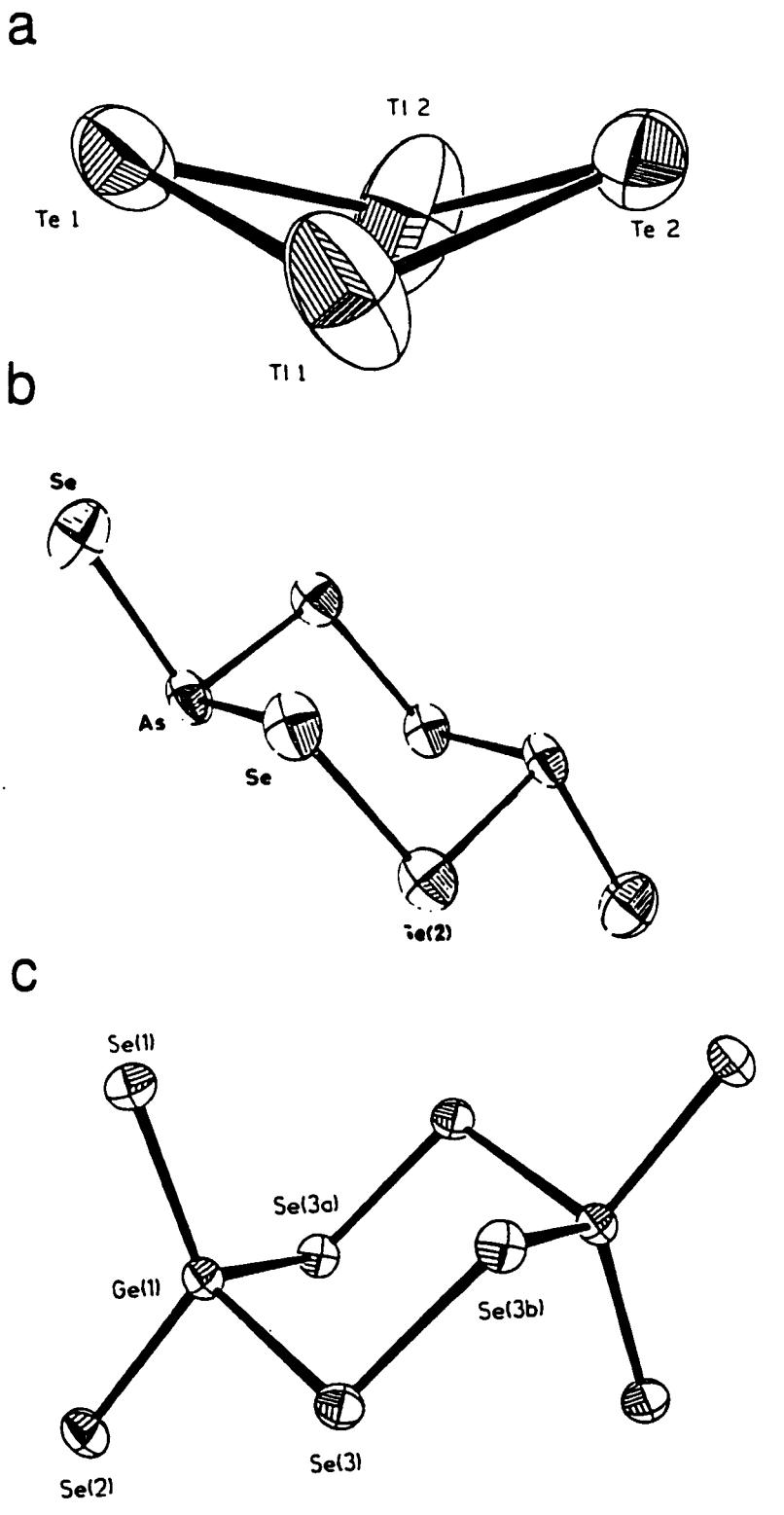

Figure 1.3. Some examples of electron precise ring anions; (a) $Tl_2Te_2^{2-}$,[44] (b) $As_2Se_6^{2-}$,[45] and (c) $Ge_2Se_8^{4-}$.[46]

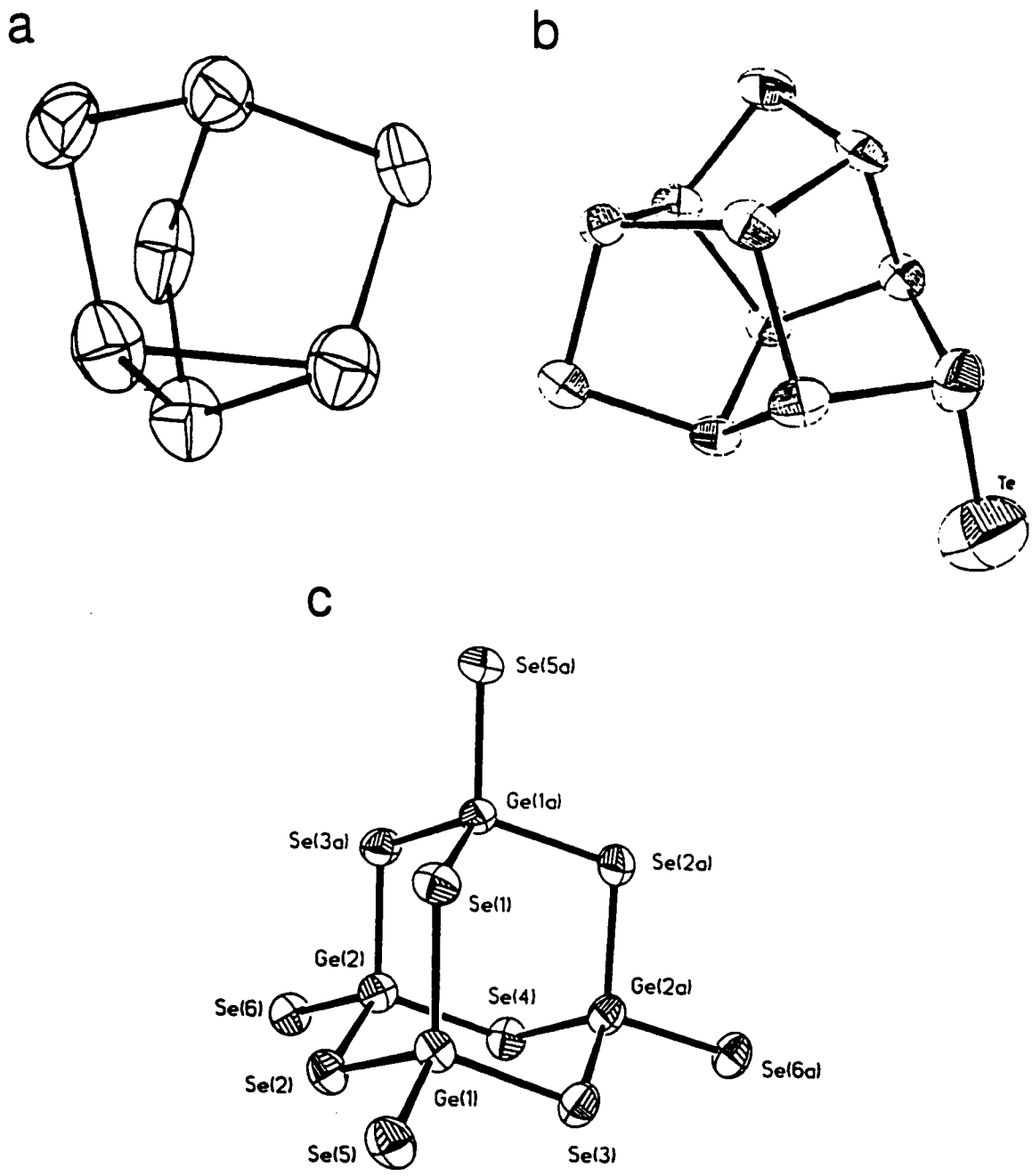

Figure 1.4. Some examples of electron precise cage anions; (a) Sb_7^{3-},[47] (b) $As_{11}Te^{3-}$,[31] and (c) $Ge_4Se_{10}^{4-}$.[46]

$$S^{2-} + H_3O^+ \rightleftharpoons HS^- + H_2O \quad (1.2)$$

reactions (eq. (1.3)–(1.6)) to account for their observations.

$$GeS_4^{4-} + H_2O \rightleftharpoons HSGeS_3^{3-} + OH^- \quad (1.3)$$

$$HSGeS_3^{3-} + GeS_4^{4-} \rightleftharpoons Ge_2S_7^{6-} + HS^- \quad (1.4)$$

$$Ge_2S_7^{6-} + H_2O \rightleftharpoons HSGe_2S_6^{5-} + OH^- \quad (1.5)$$

$$HSGe_2S_6^{5-} \rightleftharpoons Ge_2S_6^{4-} + HS^- \quad (1.6)$$

Condensation reactions have also been proposed by Kanatzidis and Chou[55] to account for the complex equilibrium among the AsS_3^{3-}, $As_2S_5^{4-}$, $As_3S_6^{3-}$, and $As_3S_7^{5-}$ anions in en solutions. Condensation processes play an important role in heavy main-group polyanion chemistry, facilitating the syntheses of large oligomeric polyanions from simple monomeric species and provide a complementary description of classical polyanions.

In subsequent years, Schrobilgen and coworkers[56] conducted extensive nuclear magnetic resonance (NMR) spectroscopic studies on solutions obtained by extracting ternary $A_xM_yCh_z$-type phases in en or liquid NH_3 and in the presence of excess amounts of 2,2,2-crypt with respect to A^+ and characterized the classical $HgSe_mTe_{2-m}^{2-}$, $CdSe_mTe_{2-m}^{2-}$, $Tl_2Se_mTe_{2-m}^{2-}$, $SnTe_nTe_{4-n}^{4-}$, $SnSe_pTe_{3-p}^{2-}$, and $TlSe_pTe_{3-p}^{3-}$ (m = 1–2; n = 1–4; p = 1–3) polyanions. The NMR-active nuclides ^{203}Tl, ^{205}Tl, ^{199}Hg, ^{125}Te, ^{117}Sn, ^{119}Sn, ^{113}Cd, and ^{77}Se served as structural probes (*vide infra*). Whereas the X-ray crystal structures of the linear ($D_{\infty h}$) $HgTe_2^{2-}$,[57] the tetrahedral (T_d) $SnCh_4^{4-}$ (Ch = Se[58] or Te[59]), and the butterfly-shaped

(C_{2v}) $Tl_2Te_2^{2-}$ [44] anions were reported prior to Schrobilgen's work, the $SnSe_pTe_{3-p}^{2-}$ and $TlSe_pTe_{3-p}^{3-}$ anions were structurally characterized for the first time and were proposed to possess trigonal-planar (D_{3h}) geometries making them isostructural with CO_3^{2-}.[56] The proposed structures of the tin compounds were confirmed by ^{119}Sn Mössbauer studies which indicated only the presence of Sn(IV) environments. Interestingly, the X-ray crystal structures of the $SnSe_pTe_{3-p}^{2-}$ and $TlSe_pTe_{3-p}^{3-}$ anions have never been reported; however, the $SnCh_3^{2-}$ (Ch = Se or Te) anions dimerize in the solid state to form the $Sn_2Ch_6^{4-}$ anions.[60–68]

In their study of classically-bonded tin-chalcogenide anions, Schrobilgen and coworkers[56] noted that the anions formed in solution were influenced by the alloy compositions. For example, only the trigonal-planar $SnTe_3^{2-}$ anion was detected by ^{119}Sn and ^{125}Te NMR spectroscopy in en extracts of $KSnTe_2$ containing a molar excess of 2,2,2-crypt with respect to K^+, whereas the tetrahedral $SnTe_4^{4-}$ anion was obtained in analogous en extracts of NaSnTe.

Nuclear Magnetic Resonance Spectroscopy

Nuclear magnetic resonance (NMR) spectroscopy is well-suited for the structural characterization of Zintl anions since all post-transition elements possess at least one naturally-occurring NMR-active (spin quantum number, I, ≥ ½) nuclide. Surprisingly, the majority of the Zintl polyanions reported to date have been structurally characterized primarily by X-ray crystallography and, to a lesser extent, by solid-state vibrational spectroscopy. Corbett has noted that a large number of $(2,2,2\text{-crypt-A}^+)_nM^{n-}$ salts possess low

solubilities in basic media and are therefore the most easily crystallized species.[35] The polyanions thus characterized may therefore not be representative of the species present in solution. This is exemplified by the $Tl_2Te_2^{2-}$ anion[44] which was obtained exclusively as the 2,2,2-crypt-K^+ salt from an en solution of KTlTe but was found by Schrobilgen and coworkers[56] to be a minor component in liquid NH_3 solutions of KTlTe where the major species was deduced by NMR spectroscopy to be $TlTe_3^{3-}$.

Nuclear magnetic resonance spectroscopy as a structural technique is limited when rapid intra- and/or intermolecular exchange (fluxionality) occurs in solution. In many cases, fluxionality renders all unique chemical environments of a polyanion equivalent on the NMR time scale and prevents observation of nuclear spin–spin couplings. For example, the ^{207}Pb NMR spectrum of Pb_9^{4-} is an exchange-averaged single line and is attributed to rapid intramolecular interconversion between the *nido*-monocapped square antiprismatic (C_{4v}) geometry observed for the anion in the solid state and the *closo*-tricapped trigonal prismatic (D_{3h}) structure *via* a C_{2v} transition state.[29] The magnetic inequivalence of coupled nuclides, however, may permit observation of exchange-averaged nuclear spin–spin couplings in fluxional molecules. The ^{119}Sn NMR spectrum of the fluxional Sn_9^{4-} anion is a five-line spectrum resulting from an exchange-averaged ^{119}Sn–^{117}Sn coupling and arises because tin possesses two NMR-active spin-½ nuclides, ^{119}Sn and ^{117}Sn.[69,70] Strong ion-pairing effects between polyanions and alkali-metal counter cations have also been noted to promote chemical exchange and result in severe line broadening of the NMR resonances. Only a single, broad peak was observed in the ^{125}Te NMR spectrum of Te_3^{2-} in en solution, whereas

the anticipated two resonances corresponding to the central and terminal environments of the anion were observed under similar experimental conditions when 2,2,2-crypt was added to the solution.[71] The 2,2,2-crypt ligand serves to minimize ion-pairing effects by sequestering the alkali-metal cations present in solution (*vide supra*).

The three most important structural parameters that can be obtained from an NMR spectrum are the chemical shift, δ, which may be used to deduce oxidation states of atoms in polyanions and the effects of electronegative substitutents on the electron densities of the atoms of interest; the scalar coupling constant, J, which can be used to assess the nature of the bonding between coupled nuclides; and the relative peak heights or peak area ratios, which provide information about the relative number of atoms in different chemical environments. Since the nuclides studied during the course of this work are spin-½ nuclides of the heavier post-transition elements and possess medium (20–90%) to low (< 20%) natural abundances, the ensuing discussion will be restricted to such nuclides. The reader is referred elsewhere for discussions of the lighter main-group[72] and quadrupolar (I > ½) nuclides.[73] Table 1.1 lists the NMR parameters of the nuclides investigated in the course of this study.

Chemical Shifts. The radiofrequency radiation used in NMR spectroscopy to observe the energy separation between nuclear spin states in the presence of an external magnetic field also induces local magnetic currents in the vicinity of the nucleus and gives rise to nuclear shielding. The relationship between the applied magnetic field, B_o, and the induced or local field, B_{eff}, is expressed by eq. (1.7) where σ is the shielding constant. When $\sigma < 0$,

Table 1.1. NMR Parameters of the Spin-½ Nuclides Investigated in the Course of This Study.[a,b]

nucleus	N.A. (%)	R^c	γ ($\times 10^7$)	Ξ (MHz)	Reference Standard
^{77}Se	7.58	3.02	5.1214	19.071523	liq. $(CH_3)_2Se$
^{117}Sn	7.61	19.9	–9.589	35.632295	liq. $(CH_3)_4Sn$
^{119}Sn	8.58	25.7	–10.0318	37.290655	liq. $(CH_3)_4Sn$
^{123}Te	0.87	0.906	–7.0576	26.169773	liq. $(CH_3)_2Te$
^{125}Te	6.99	12.8	–8.5087	31.549802	liq. $(CH_3)_2Te$
^{203}Tl	29.50	328	15.5394	57.072641	0.1 M aq. $TlNO_3$
^{205}Tl	70.50	807	15.6922	57.633833	0.1 M aq. $TlNO_3$
^{207}Pb	22.6	11.9	5.6264	20.920597	liq. $(CH_3)_4Pb$

[a] Obtained from ref. (74). [b] N.A. is the natural abundance; R^c is the receptivity relative to that of ^{13}C; γ is the gyromagnetic ratio measured in $rad \cdot s^{-1} \cdot T^{-1}$; and Ξ is the resonance frequency of the standard substance in a magnetic field in which the protons of $(CH_3)_4Si$ resonate at exactly 100 MHz.

$$B_{eff} = (1 - \sigma)B_o \qquad (1.7)$$

the induced field at the nucleus exceeds the applied field and the nucleus is "deshielded". Nuclear shielding arises when $\sigma > 0$.

Nuclear shielding is usually discussed in terms of the formalism first introduced by Ramsey[75] which expresses nuclear shielding as a sum of diamagnetic (D) and paramagnetic (P) contributions (eq. (1.8)). Diamagnetic shielding arises from the free rotation of electrons

$$\sigma = \sigma^D + \sigma^P \qquad (1.8)$$

induced by the applied magnetic field, and paramagnetic shielding results from the hindrance to this rotation caused by other electrons and nuclei in a molecule. The above definition of nuclear shielding has been expanded by Pople[76] to include local (L), nonlocal (NL), and interatomic (I) contributions to the diamagnetic and paramagnetic shieldings and is provided in eq. (1.9). The local contributions to the shielding arises from electronic currents localized

$$\sigma = (\sigma^D + \sigma^P)_L + (\sigma^D + \sigma^P)_{NL} + (\sigma^D + \sigma^P)_I \qquad (1.9)$$

on the atom containing the nucleus of interest and are the primary cause of shielding variations for a nucleus in different chemical environments. The nonlocal contributions result from remote currents on neighbouring atoms, and the interatomic currents are not localized on any atom in a molecule.

The chemical shielding of heavy-element nuclides is generally believed to be dominated by the local paramagnetic term, σ^P_L,[77] and is expressed, in the average excitation

energy approximation, by eq. (1.10); μ_o is the permeability constant; h is Planck's constant;

$$\sigma_L^P = -\frac{\mu_o e^2 h^2}{6\pi m^2 \Delta E} \langle r^{-3} \rangle_{np} P_u \qquad (1.10)$$

m is the electron mass; ΔE is the average excitation energy; P_u is the asymmetric distribution of the valence *np*-electrons about the nucleus; and $\langle r^{-3} \rangle_{np}$ is the inverse cube of the mean expectation distance, r, of the valence *np*-electrons from the nucleus. The minus sign in the equation indicates than an increase in the paramagnetic term causes deshielding of the nucleus under investigation (*vide supra*) and a corresponding high-frequency shift of the NMR resonance. According to quantum mechanics, the radial term $\langle r^{-3} \rangle_{np}$ is expressed by eq. (1.11)[78] where Z is the atomic number and a_o is the Bohr radius (0.529 Å) and indicates that

$$\langle r^{-3} \rangle_{np} = \frac{Z^3}{a_o^3 n^6} \qquad (1.11)$$

$\langle r^{-3} \rangle_{np}$ increases as Z increases. The direct dependence of σ^P_L on $\langle r^{-3} \rangle_{np}$ (eq. (1.10)) means that larger dynamic chemical shift ranges are anticipated for the heavier main-group elements as illustrated in Figure 1.5.[78]

Solution NMR spectroscopic studies of the series of $TlCh_3^{3-}$, $SnCh_3^{2-}$, and $SnCh_4^{4-}$ (Ch = Se and/or Te) anions indicated that the chemical shifts of the central metal atoms were progressively shifted to higher frequencies upon substitution of the Te atom with the more electronegtive Se atom.[56] Since this substitution resulted in a deshielding of the metal nuclei,

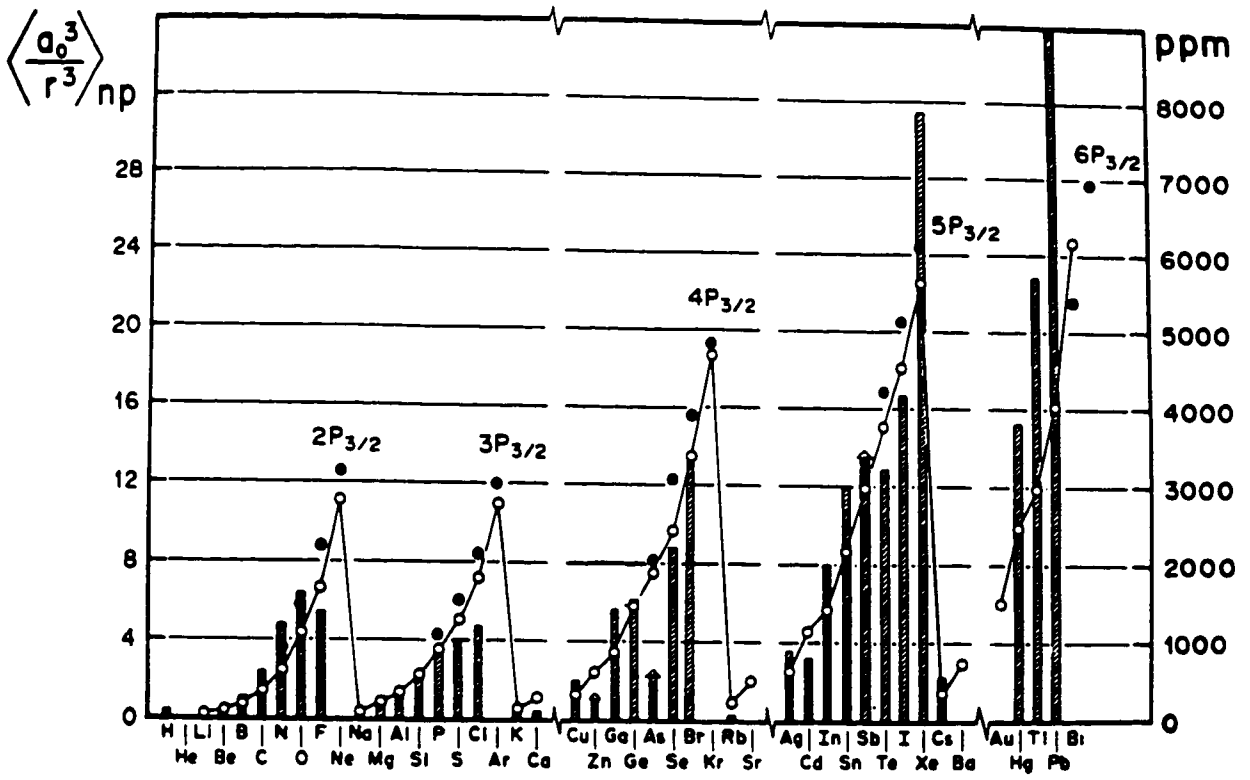

Figure 1.5. Chemical shift ranges for nuclei of the post-transition elements.[78] The $\langle r^{-3} \rangle_{np}$ values are shown as dimensionless ratios $\langle a_0^3/r^{-3} \rangle_{np}$, where a_0 is the Bohr radius (0.529 Å).

the observed trends can, in principle, be rationalized by the diamagnetic contribution, σ^D, to the nuclear shielding. However, the observed chemical shift ranges (> 300 ppm per Se atom) were too large to be attributed to σ^D and confirm that σ^P is the dominant contributor to the shielding of heavy-element nuclides.

Scalar (J) and Reduced (K and K_{RC}) Coupling Constants. The interaction between nuclear spin-states of coupled nuclei in the presence of a magnetic field gives rise to nuclear spin–spin coupling. The direct (dipole–dipole) coupling between nuclei is averaged to zero in solution by molecular tumbling, but the indirect (scalar) coupling, which is transmitted by the valence electrons, is a non-zero quantity and is observed in NMR spectroscopy.[79] Since nuclear spin–spin coupling is mediated by valence electrons, the relative magnitudes of the coupling constants provide information about the electronic environments in molecules and can be used to infer the type of bonding between atoms (*vide infra*).

Three coupling mechanisms predominate the scalar coupling: spin–orbit, spin–dipolar (the "non-contact" terms), and Fermi (the "contact" term).[79] Non-contact contributions arise from interactions of valence *p*, *d*, ... electrons and are therefore important for π-bonded systems; the contact term involves interactions of the valence *s*-electrons and dominates the coupling mechanism in σ-bonded systems. Since multiple bonding is less important in molecules comprised of heavy elements, the Fermi-contact term predominates the coupling mechanism in such molecules.

The Fermi contact mechanism is usually discussed in terms of the formalism developed by Pople and Santry[80] and is given by eq. (1.12); γ_A and γ_B are the gyromagnetic

$$J(A-B) = 16\frac{\pi^2}{9h}\left(\frac{g\beta h}{2\pi}\right)^2 \gamma_A\gamma_B \, |\psi_{ns,A}(0)|^2 \, |\psi_{ns,B}(0)|^2 \, \Pi_{AB} \qquad (1.12)$$

ratios of the coupled nuclei; $|\psi_{ns,A}(0)|^2$ and $|\psi_{ns,B}(0)|^2$ are the valence *s*-electron densities at the coupled nuclei; Π_{AB} is the mutual polarizability of the *ns*-orbitals on A and B; and the remaining symbols have their usual meanings and/or values. According to this formalism, the scalar coupling constant between two coupled nuclei, J(A–B), is dependent on the nuclear (γ) and electronic ($|\psi(0)|^2$) properties of the coupled nuclei. In order to make structural comparisons from couplings in a series of structurally-related species having different spin-coupled nuclei, it is necessary to remove the nuclear dependence on J which gives the nuclear independent, or reduced, coupling constant K(A–B) as defined by eq. (1.13).[80] The reduced

$$K(A-B) = \frac{4\pi^2}{h\gamma_A\gamma_B} J(A-B) \qquad (1.13)$$

coupling constant is directly proportional to the *s*-character of the A–B bond and therefore provides a better representation of the electronic environments between coupled nuclei. However, Pyykkö and Wiesenfeld[81] have demonstrated that relativistic effects on the *s*-electron densities of heavy atoms, particularly for those near the Au maximum for relativistic effects (Hg, Tl, Pb), are significant and dominate the magnitudes of Fermi-contact-mediated couplings. Corrections for relativistic effects can be applied by multiplying the reduced coupling constant, K(A–B), with the ratios of the calculated relativistic, $|\psi(0)|^2_{rel}$, and non-

relativistic, $|\psi(0)|^2_{nonrel}$, *s*-electron density terms, giving rise to the relativistically corrected reduced coupling constant, $K(A–B)_{RC}$ (eq. (1.14)).[56,82] The ratios of the relativistic and non-

$$K(A–B)_{RC} = \frac{|\psi_{ns,A}(0)|^2_{nonrel}}{|\psi_{ns,A}(0)|^2_{rel}} \frac{|\psi_{ns,B}(0)|^2_{nonrel}}{|\psi_{ns,B}(0)|^2_{rel}} K(A–B) \qquad (1.14)$$

relativistic *s*-electron densities are the ratios of the corresponding hyperfine integrals and have been tabulated by Pyykkö and Wiesenfeld.[81]

The importance of relativistic effects on the *s*-electron densities of heavy main-group atoms is illustrated by the K(Tl–Ch) couplings of the formally sp^2-hybridized trigonal planar $TlCh_3^{3-}$ (Ch = Se or Te) anions, which have magnitudes twice as large as the K(Sn–Ch) values observed for the sp^2-hybridized trigonal planar $SnCh_3^{2-}$ anions.[56] The magnitudes of $K(Tl–Ch)_{RC}$ and $K(Sn–Ch)_{RC}$ are, however, similar and reflect the dominance of the $|\psi(0)|^2$ term for Tl.

Spin–Spin Coupling Patterns at Low Natural Abundances. The observed coupling pattern for a single spin-½ nucleus A of 100% natural abundance coupled to *n* chemically and magnetically equivalent spin-½ nuclei B also of 100% natural abundance is a $(2n + 1)$-line multiplet. The relative intensities of the multiplet component are derived from the coefficients of the *a* and *b* terms in the binomial expansion of $(a + b)^n$.[79] Observation of the NMR spectrum of nucleus A therefore provides a count of the B nuclei, and observation the NMR spectrum of nucleus B will produce a $(2m + 1)$-line multiplet for *m* chemically and

magnetically equivalent A nuclei and will provide a count of the number of A nuclides coupled to B.

As the majority of naturally occurring spin-½ nuclei possess medium (20–90%) to low (< 20%) natural abundances (see Table 1.1), a series of isotopomeric species, or "isotopomers", results in the NMR spectrum of A (eq. (1.15)) where B collectively denotes

$$AB_n,\ AB_{n-1}{}^{*}B,\ AB_{n-2}{}^{*}B_2,\ ...,\ A{}^{*}B_n\ (n > 1) \tag{1.15}$$

the NMR inactive (spinless) isotopes of element B and *B, the spin-½ isotope.[79] Each isotopomer gives rise to a multiplet in the NMR spectrum of A and is termed a "subspectrum". The AB_n isotopomer produces a singlet subspectrum; $AB_{n-1}{}^{*}B$ produces a doublet; $AB_{n-2}{}^{*}B_2$ produces a triplet; ... and $A{}^{*}B_n$ produces an $(n + 1)$-line multiplet. The relative contribution of each subspectrum to the observed NMR spectrum of nucleus A is a function of the isotopomer probability and the abundance of *B, and the observed NMR spectrum of A is a superposition of appropriately weighted subspectra arising from all possible isotopomers. An example is illustrated in Appendix A.

When nucleus B has a low (< 20%) natural abundance, the weaker triplet, quartet, ..., $(n + 1)$-line satellite subspectra are frequently not visible. However, the number of B nuclei coupled to A (and *vice versa*) can be deduced from the intensity of one component of the satellite doublet subspectrum relative to that of the singlet subspectrum and is expressed by eq. (1.16) where I_S is the intensity of the satellite peak in the NMR spectrum of A; I_C is the

$$\frac{I_S}{I_C} = nZ\,\frac{\frac{1}{2}(1+(n-1)(n-2)Z^2)}{1+n(n-1)Z^2} \quad where \quad Z=\frac{p_\beta}{2p_y} \tag{1.16}$$

intensity of the cental singlet; n is the number of B nuclei; p_β is the natural abundance of the $^{\bullet}$B isotopes of element B; and p_y is the abundance of the spinless isotopes of element B. A detailed analysis of spin–spin coupling patterns for low-abundance spin-½ nuclides has been discussed by Björgvinsson.[83]

Purpose and Scope of the Present Study

The overall purpose of the present work was to investigate the chemical processes leading to the formation of classical main-group metal chalcogenide anions in basic, non-aqueous media and to extend the understanding of their structures and bonding by preparing new tin, thallium, and lead polychalcogenide anions. Structural characterization of the polyanions would be achieved in solution by multi-NMR spectroscopy of the spin-½ nuclides listed in Table 1.1 and in the solid state by single-crystal X-ray crystallography and Raman spectroscopy.

CHAPTER 2

EXPERIMENTAL SECTION

Standard Techniques

All compounds used and prepared during the course of this work were air and moisture sensitive. Consequently, all manipulations were carried out under rigorously anhydrous and oxygen-free conditions on a general-purpose grease-free glass vacuum line (Figure 2.1) equipped with Pyrex/Teflon stopcocks (J. Young Scientific Glassware), in a nitrogen-atmosphere dry box (two-station Vacuum Atmospheres Model DLX, with moisture and oxygen levels < 0.1 ppm; for general solid and crystal handling), or glovebag (for solution and crystal handling) which had been purged with dry nitrogen gas or argon gas for at least 12 h prior to use.

Vacuum line pressures (routinely 10^{-4}–10^{-5} Torr) were maintained by using a two-stage direct-drive rotary-oil vacuum pump (Edwards E2M8). Pressures inside the glass manifold were monitored with a mercury manometer. All volatile materials handled on the vacuum line were trapped in a liquid nitrogen trap (–196 °C) which was positioned immediately before the vacuum pump in order to prevent the passage of the volatile materials into the pump. The vacuum line, when not in use, was maintained under dynamic vacuum with the mercury manometer closed off from the glass manifold.

Materials transported into the dry box were evacuated in the attached port three times,

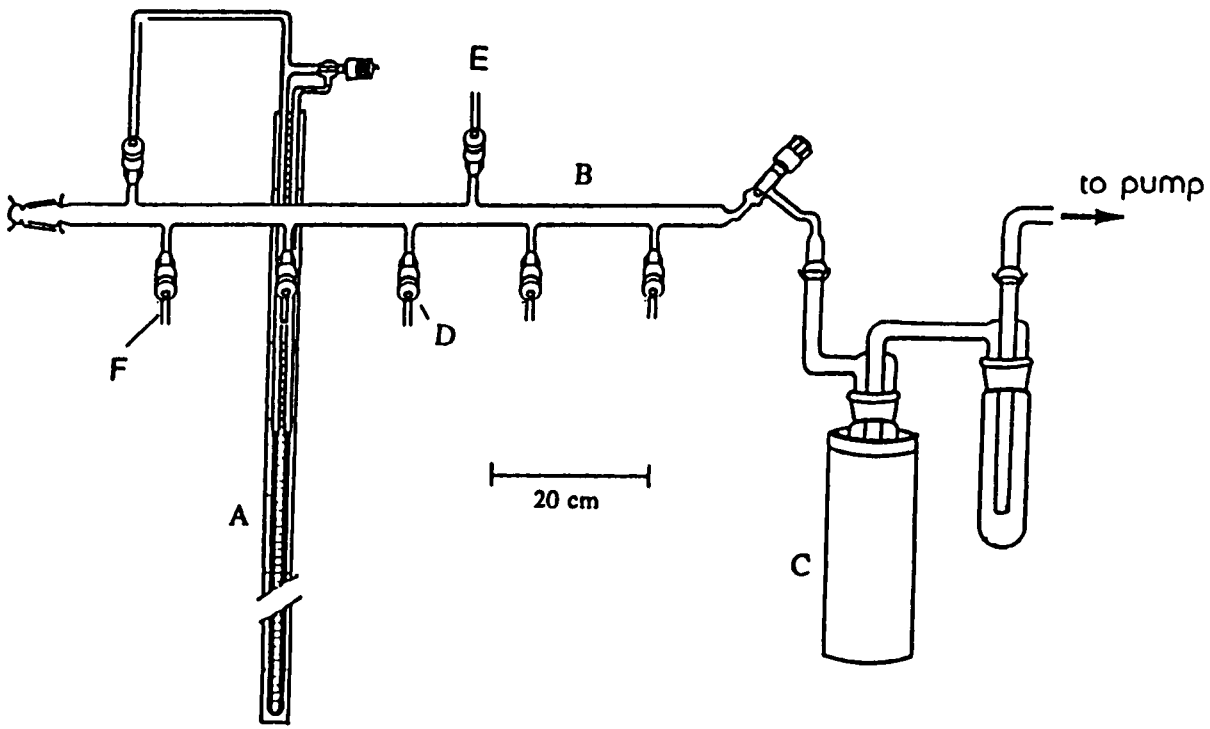

Figure 2.1. A general-purpose glass vacuum line; (A) mercury manometer (B) vacuum manifold, (C) liquid nitrogen trap, (D) greaseless 10-mm J. Young glass/Teflon stopcocks, (E) dry N_2, (F) ¼" o.d. glass tube-ends.

with each evacuation cycle lasting at least 20 min. All weighings were carried out inside the dry box on a Mettler AE 163 electronic balance equipped with a printer external to the dry box. In order to dissipate the electrostatic charges resulting from the anhydrous environment of the dry box, finely-divided powdered materials were handled and weighed out in the vicinity of an α-source consisting of a silver strip doped with $^{241}Am_2O_3$ (Amersham) having an activity of 2.4 mCi.

All synthetic preparations and extractions were performed in vessels constructed from Pyrex or quartz glass. The vessels were equipped with 4-mm grease-free Teflon/glass valves (J. Young Scientific) to which were attached ¼" o.d. glass-tube ends. All vessels were thoroughly dried under dynamic vacuum for a minimum of 12 h before use. The vessels were connected to the vacuum line through the ¼" o.d. tube-ends by means of ¼" Teflon Swagelok unions with Teflon compression fittings (¼" back and front ferrules) or ¼" stainless steel Cajon Ultra-Torr unions equipped with ¼" buna rubber O-rings.

Preparation and Purification of Starting Materials

Solvents. All solvents were thoroughly dried, transferred by vacuum distillation, and stored in round-bottom flasks (250 mL, Schott) equipped with 6-mm glass/Teflon stopcocks. Ethylenediamine (Fisher Scientific Co., 99%) and ethylamine (Aldrich, 99%) were initially dried over CaH_2 (BDH Chemicals, 99.5%) for several weeks and then vacuum-distilled onto, and stored over, fresh CaH_2 for at least an additional week prior to use. Tetrahydrofuran (Aldrich, 99.9%) was dried in an analogous manner over freshly-cut sodium pieces (BDH

Chemicals, 99.8%). Anhydrous ammonia (Matheson, 99.99%) was condensed from a gas cylinder at –78 °C into a previously vacuum-dried tube containing freshly-cut sodium metal and was further dried at –78 °C for at least 1 week prior to use. Any hydrogen gas that had formed in the solvent flasks was periodically removed under dynamic vacuum.

Alkali Metals. The oxide layers on large pieces of sodium metal (BDH Chemicals, 99.8%) and potassium metal (BDH Chemicals, > 99%), stored under paraffin oil, were cut off, and the paraffin oil was removed by washing the freshly-cut metal pieces with petroleum ether (Fisher Scientific Co., boiling range 60–80 °C). The metal pieces were then rapidly loaded into a dry tube, and the residual ether was removed under dynamic vacuum before the clean metal pieces were transferred into the dry box. Before the alkali-metal pieces were used, the thin oxide layers on the surfaces were trimmed away with a scalpel. In order to prevent the metal pieces from adhering to the sides of the reaction vessels, the metal pieces were formed into small wires by rolling them with clean gloves inside the dry box.

Main-Group Metals. Tin granules (Baker Analyzed Reagent, 99.9%), lead shot (BDH Chemicals, 99.9%), thallium rod (Alfa Inorganics, 99.9%), selenium shot (Alfa Inorganics, 99.9%), and tellurium powder (Alfa Inorganics, 99.9%) were used as received and dried in the evacuated port of the dry box for a minimum of 60 min, followed by exposure to the atmosphere of the dry box for at least two days prior to use. Inside the dry box, the oxide layer on the thallium metal rod was cut off, and the clean metal was cut into small pieces and stored in a glass vial.

Complexing Ligands. The ligand 2,2,2-crypt (1,10-diaza-4,7,13,16,21,24-

hexaoxabicyclo[8.8.8]hexacosane; Merck, 99%) was used as received and dried in the evacuated port of the dry box for a minimum of 60 min, followed by exposure to the atmosphere of the dry box for at least two days prior to use. The ligand 18-crown-6 (1,4,7,10,13,16-hexaoxacyclooctadecane, Aldrich) was recrystallized twice from freshly-distilled acetonitrile (Fisher Scientific Co.) and then distilled under vacuum (< 0.1 torr) at 115 °C. The ligand was then transferred and stored inside the dry box.

Miscellaneous Materials. Dry nitrogen gas was obtained by boiling off liquid nitrogen (Canadian Liquid Air) and passed through a Lectrodryer to give moisture levels less than 0.1 ppm. Argon gas (Matheson, oxygen levels < 1 ppm) was used directly from the gas cylinder.

Calcium hydride (Strem Chemicals, 99.5%) was used as received and ground inside a glove bag which had been previously flushed for 12 h with dry nitrogen gas and then filled with dry gas. Perfluorodecaline (Strem Chemicals) was used as received.

Preparation of Intermetallic Phases

The intermetallic phases (hereafter referred to as "alloys") prepared during the course of this work are listed in Table 2.1 along with the quantities of metals used for their preparations and their final compositions. The alloys KTlTe, Tl_2Te, and $Tl_2Pb_2Te_3$ were prepared by Devereux,[84] Björgvinsson,[83] and Czyborra,[85] respectively. Potassium monotelluride, K_2Te, was prepared by Schrobilgen and Czyborra according to reference (71).

All alloys were prepared by fusion of the appropriate elements in the required molar

Table 2.1. Quantities of Elements Used to Prepare Alloys and Final Alloy Compositions.

	g (mmol) of element used				
alloy	alkali metal	K_2Te	thallium metal	group 14 metal [a]	chalcogen
$KSn_{0.63}Se_{1.93}$	0.9591 (24.531)			2.7575 – 0.8151 = 1.9424 (16.365)	3.7318 (47.261)
$KSn_{0.90}Se_{1.93}$	0.5114 (13.080)			1.5183 – 0.1174 = 1.4009 (11.803)	1.9976 (25.299)
$KSn_{0.63}Te_{1.70}$	1.0614 (27.147)			2.9595 – 0.9246 = 2.0349 (17.145)	5.8893 (46.154)
$K_4Sn_4Te_{10}$		2.903 (1.411)		0.3344 (2.817)	0.7215 (5.654)
$NaSn_{0.43}Te$	0.1607 (6.990)			0.8196 – 0.4671 = 0.3525 (2.969)	0.9050 (7.092)
$NaSn_{0.42}Se$	0.1916 (8.334)			1.0144 – 0.5968 = 0.4176 (3.519)	0.6828 (8.647)
NaTlSe	0.2470 (10.744)		2.1059 (10.304)		0.8164 (10.339)
$NaTl_{0.5}Se$	0.3146 (13.684)		1.3392 (6.553)		10.415 (13.190)
NaTlTe	0.2202 (9.578)		1.9069 (9.331)		1.2423 (9.736)
$Tl_2Sn_2Te_3$			1.0790 (5.280)	0.6353 (5.353)	1.0676 (8.376)

[a] The final alloy stoichiometries were corrected accordingly when lumps of tin metal were isolated.

ratios in medium-wall Pyrex or quartz glass fusion vessels (Figure 2.2). The vessels were either left under 1 atm of dry nitrogen gas or partially evacuated in order to prevent sublimation of the alkali metals onto the walls of the vessels during fusion. In order to prevent strong exothermic reactions, alloy fusions were carried out in two steps. Initially, a binary alloy consisting of the alkali metal and the main-group metal was prepared by carefully heating the fusion vessel over a Meeker flame until the metals had reacted. The resulting molten binary alloy was allowed to solidify and the vessel was returned to the dry box. In the second step, the chalcogen was added to the fusion vessel which was again gently heated until the sample began to incandesce and then more strongly heated until a free-flowing homogeneous molten product was observed. When the vessel had cooled to room temperature, it was returned to the dry box, scored above the alloy level, and broken open. The recovered grey, brittle alloy was thoroughly ground into a fine powder by using a mortar and pestle and stored in a glass vial.

As fusion of the alloy $K_4Sn_4Te_{10}$ required large quantities of the chalcogen and could therefore result in a potentially strongly exothermic reaction, the fusion was carried out in a quartz vessel and in two steps: initially, K_2Te was reacted with the required amount of tin metal, and the resulting ternary K/Sn/Te alloy was reacted with tellurium powder. Excessive heating of the molten alloy was avoided since fusion of the alloy onto the walls of the quartz vessel could cause the vessel to crack upon cooling, thereby exposing the alloy to moisture and oxygen. The resulting alloy was grey, brittle, and homogeneous.

When sodium or potassium were fused with tin and a chalcogen, malleable lumps,

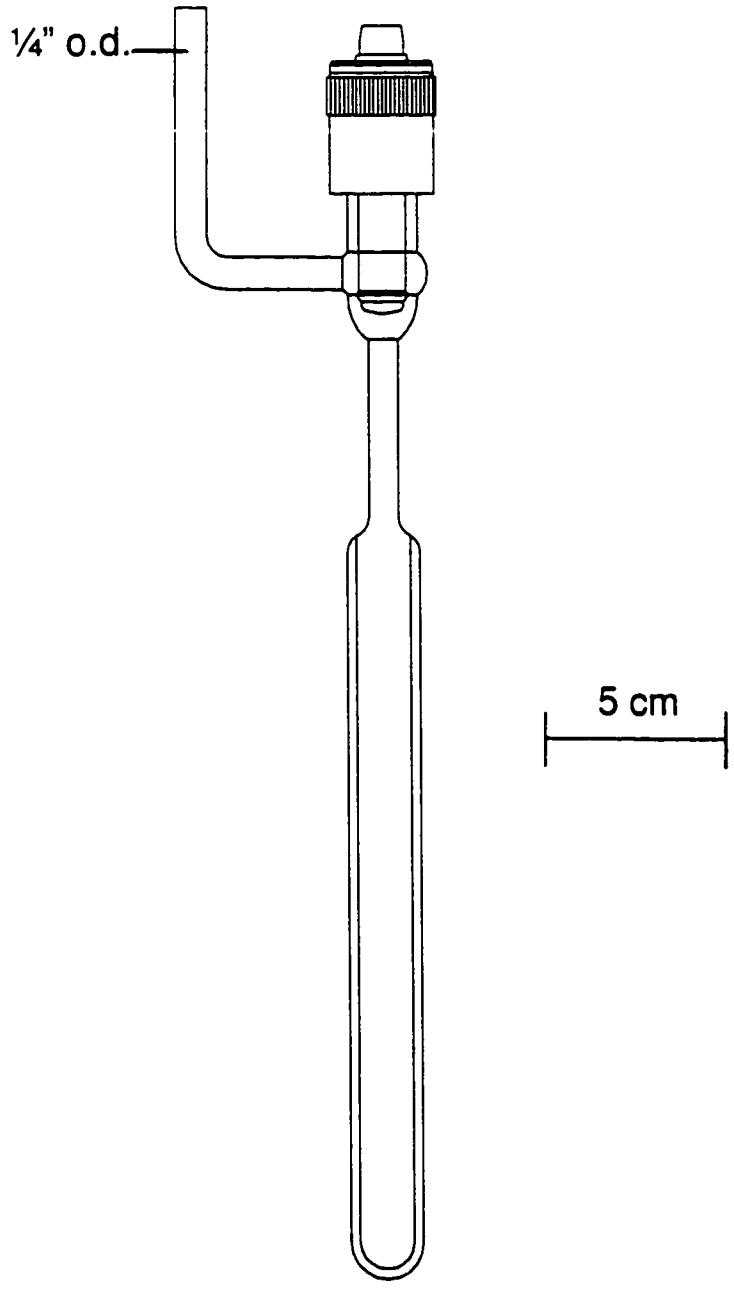

Figure 2.2. Thick-wall Pyrex vessel equipped with 6-mm J. Young glass/Teflon stopcock and used for alloy fusions

assumed to be tin, were recovered. The lumps were isolated, removed from the dry box, washed with water and acetone, air-dried, and weighed. The alloy compositions were then adjusted for the amounts of recovered tin metal (Table 2.1).

Alloy Extractions and Preparation of Zintl Anion Solutions for NMR Spectroscopy

Extractions in Ethylenediamine. Extraction vessels employed for the preparation of main-group polyanions in en either for NMR spectroscopy or for crystal growing are depicted in Figures 2.3 and 2.4, respectively. Thin-wall 10-mm o.d. Pyrex-glass NMR tubes (Wilmad Glass Co.) were used.

All alloys were extracted at room temperature and under 1 atm of dry nitrogen gas usually in the presence of a molar excess or deficit of the complexing ligands 2,2,2-crypt and/or 18-crown-6 with respect to the alkali-metal composition of the alloy. When used, the required amounts of the complexing agents were loaded into either the NMR tube or the crystal-growing chamber of the extraction vessel (labelled A in Figures 2.3 and 2.4). The powdered alloys were always loaded into arm B of the vessel. The alloys were initially separated from the complexing ligands in order to prevent possible alloy oxidation, particularly of K_2Te, by the 2,2,2-crypt.[83] After evacuation, en (*ca.* 10 mL for NMR samples and *ca.* 5 mL for crystal growing samples) was condensed under vacuum and at –196 °C onto the alloys by means of a glass Y-piece (Figure 2.5). The extraction vessels were then back-filled with 1 atm of dry nitrogen, closed, and allowed to gradually warm to room temperature.

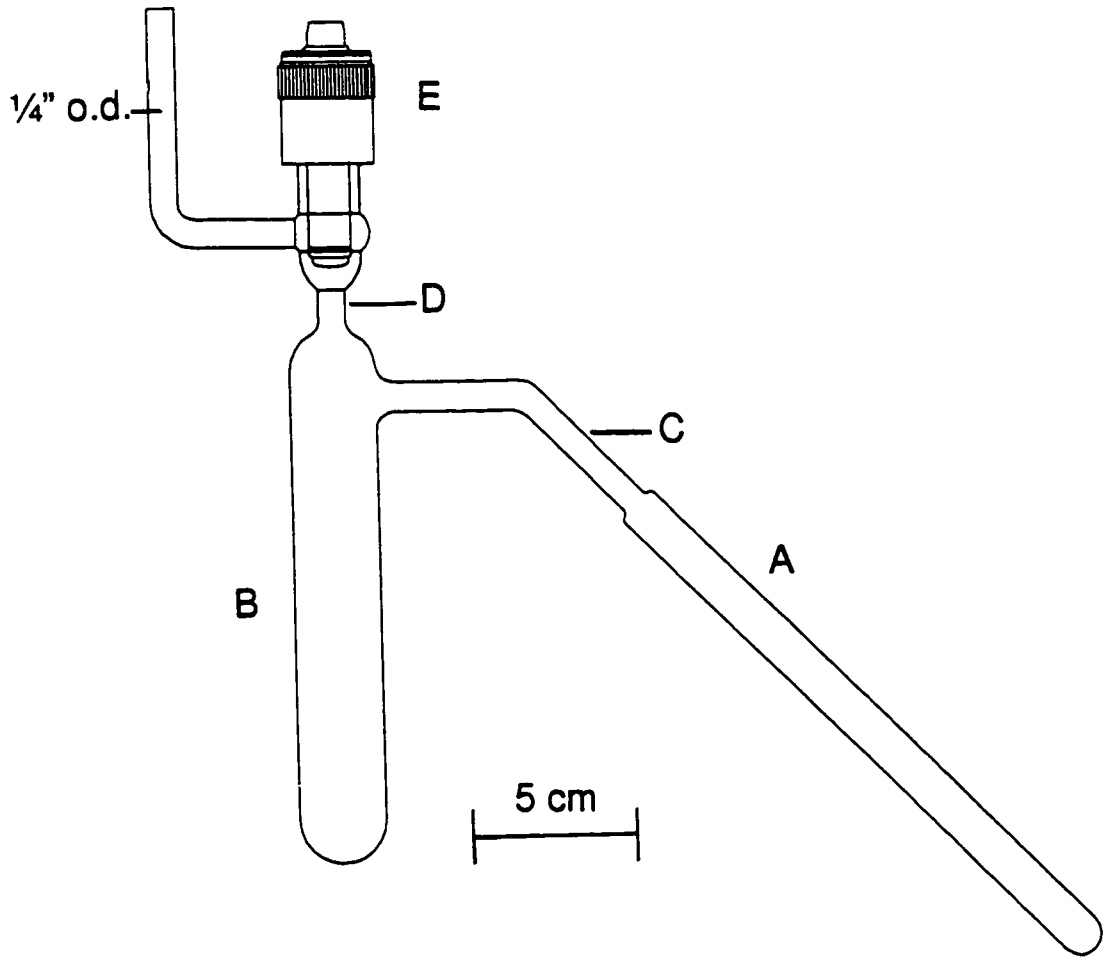

Figure 2.3. Pyrex vessel used for alloy extractions and NMR sample preparations; (A) 10-mm o.d. NMR tube, (B) reaction ampoule, (C,D) flame-sealing points, and (E) greaseless 4-mm J. Young glass/Teflon stopcock.

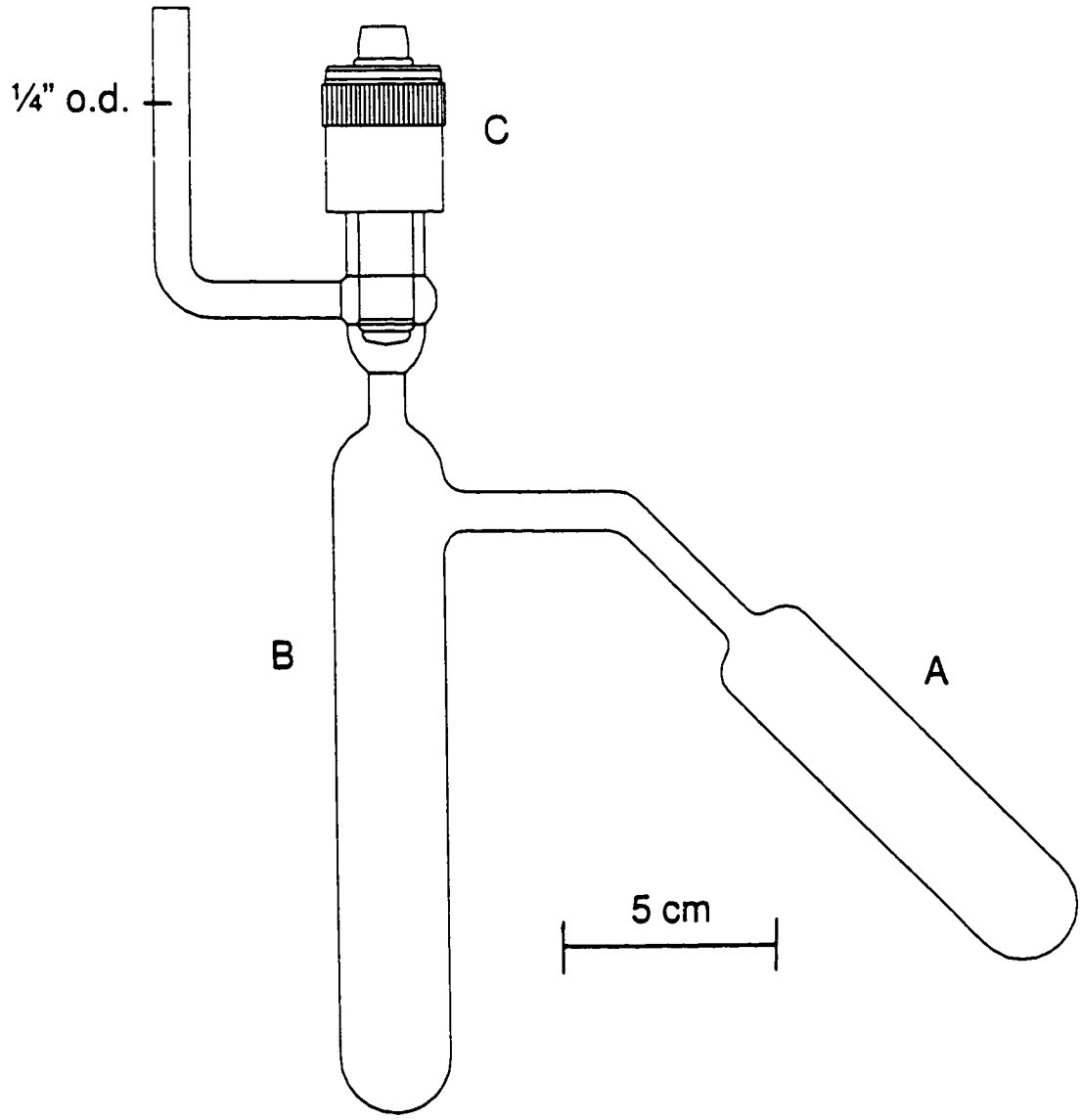

Figure 2.4. Pyrex vessel used for alloy extractions and crystal growing; (A) crystal-growing chamber, (B) reaction ampoule, (C) greaseless 4-mm J. Young glass/Teflon stopcock.

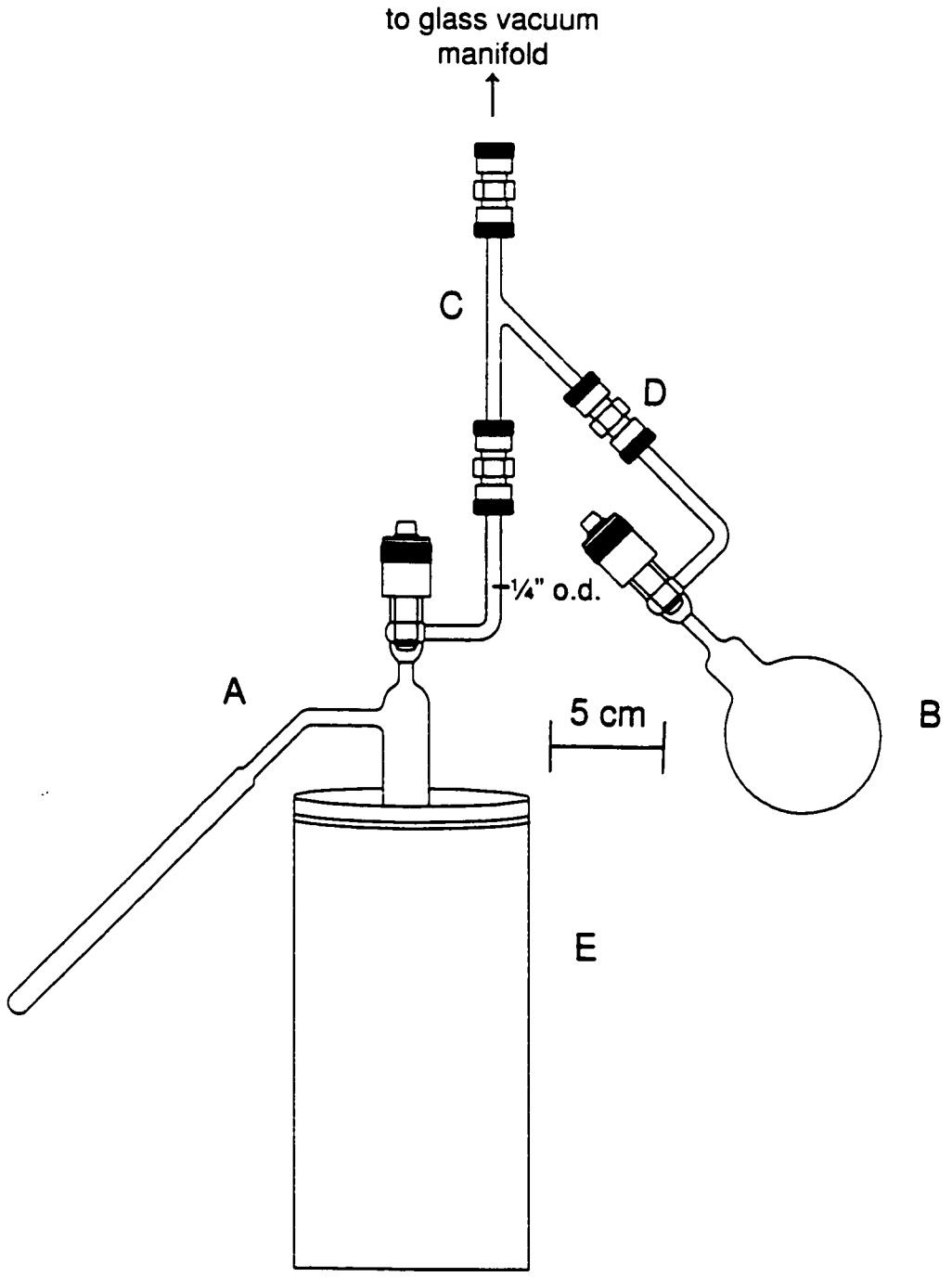

Figure 2.5. Apparatus used for static vacuum distillation of solvents into reaction vessels; (A) reaction vessel in a dewar vessel (E) filled with liquid N_2 for en distillations or with a dry ice-acetone bath for liquid NH_3 distillations; (B) solvent storage flask; (C) ¼" o.d. glass Y-piece, (D) ¼" Teflon Swagelok or stainless steel Cajon Ultra-Torr Union.

Alloy extraction commenced as soon as the mixtures warmed to room temperature and was indicated by the colours of the solutions. The complexing ligands were introduced into the en solutions after *ca.* 1–3 weeks following the initial addition of en onto the alloys and resulted in an immediate colour change and/or intensification. The samples were generally extracted for a further 1–4 weeks following addition of the complexing ligands and were periodically manually agitated during the extraction process.

Extractions in Liquid Ammonia. The procedure for extracting alloys in liquid ammonia was similar to that described for alloy extractions in en. However, a medium-walled glass extraction vessel equipped with a medium-wall 10-mm o.d. standard-glass NMR tube similar to the one illustrated in Figure 2.3 was employed, and liquid ammonia was condensed under static vacuum at –78 °C (dry ice-acetone mixture). During vacuum distillation, liquid ammonia pressures inside the vacuum manifold were monitored by using the attached mercury manometer and were not allowed to exceed 0.5 atm. Once the appropriate amount of liquid ammonia had been condensed, the solution was frozen with liquid nitrogen and the vessel flame-sealed below the stopcock at point D (Figure 2.3). The vessel was then left in a dewar containing liquid nitrogen and allowed to gradually warm to room temperature inside a well-shielded fumehood.

Preparation of Sn/Ch (Ch = Se, Te) Solutions. The $Sn_2Se_6^{4-}$, $Sn_2Se_7^{4-}$, and $Sn_4Se_{10}^{4-}$ anions were prepared by extracting the powdered $KSn_{0.67}Se_{1.93}$ alloy in en and in liquid ammonia and in the presence of a 40 mole% deficit of 2,2,2-crypt with respect to K^+. The following quantities of reagents were used for the en (liquid ammonia) solutions:

$KSn_{0.67}Se_{1.93}$, 0.1710 (0.1696) g, 0.631 (0.626) mmol; 2,2,2-crypt, 0.0990 (0.1000) g, 0.263 (0.266) mmol.

The ^{119}Sn and ^{125}Te NMR spectra of the liquid NH_3 extract of the alloy $KSn_{0.63}Te_{1.70}$ containing a K^- : 2,2,2-crypt stoichiometry of 1.00 : 0.44 could not be recorded at –70 °C because the sample gave rise to large amounts of crystalline material at this temperature. At temperatures above –70 °C, severe broadening of the NMR resonances occurred and prevented accurate satellite assignments and I_S/I_C determinations. Solutions of the $Sn_2Te_6^{4-}$ and $Sn_2Te_7^{4-}$ anions were therefore prepared by extracting $KSn_{0.63}Te_{1.70}$ (0.3892 g, 1.176 mmol) in liquid ammonia in the absence of 2,2,2-crypt. No conclusive evidence was found by ^{119}Sn and ^{125}Te NMR spectroscopy for the $Sn_4Te_{10}^{4-}$ anion in the resulting red solution (see Chapters 3 and 4).

By analogy with $Ge_4Te_{10}^{4-}$,[86] an attempt was made to prepare solutions of $Sn_4Te_{10}^{4-}$ by extracting the powdered alloy $K_4Sn_4Te_{10}$ (0.3765 g, 0.197 mmol) in liquid ammonia in the absence of 2,2,2-crypt. Only the $SnTe_3^{2-}$, $Sn_2Te_6^{4-}$, and $Sn_2Te_7^{4-}$ anions were definitively characterized by ^{119}Sn and ^{125}Te NMR spectroscopy (–70 °C) in the resulting red solution, but some evidence was obtained for $Sn_4Te_{10}^{4-}$ (Chapter 4). Interestingly, crystals of (18-crown-6-K^-)$_4Sn_4Te_{10}^{4-}$·5en were isolated upon addition of THF to an analogous en extract of $K_4Sn_4Te_{10}$ containing a molar excess of 18-crown-6 with respect to K^- (see **X-ray Crystallography**). An attempt was therefore made to prepare a solution of $Sn_4Te_{10}^{4-}$ by dissolving crystals of (18-crown-6-K^-)$_4Sn_4Te_{10}^{4-}$·5en (0.0806 g, 0.033 mmol) in liquid ammonia. However, the resulting red solution was shown by ^{119}Sn NMR spectroscopy to

contain only $SnTe_3^{2-}$.

A cherry-red solution containing the $SnTe_4^{4-}$ and $SnTe_3^{2-}$ anions was prepared by extracting $NaSn_{0.43}Te$ (0.2674 g, 1.318 mmol) in liquid ammonia in the absence of 2,2,2-crypt (*vide supra*).

Preparation of $Tl_2Te_2^{2-}$ Solutions. The reddish-brown anion solutions were prepared by extracting the alloys MTlTe (M = Na, K) in en (Na) or in liquid NH_3 (K) in the presence of molar excesses of 2,2,2-crypt. The following quantities of reagents were used for the en (NH_3) extractions: MTlTe, 0.1027 (0.1094) g, 0.289 (0.295) mmol; 2,2,2-crypt, 0.1143 (0.1193) g, 0.304 (0.317) mmol.

Preparation of Tl/Se Solutions. All attempts to record the –70 °C ^{203}Tl, ^{205}Tl, and ^{77}Se NMR spectra of the $TlSe_3^{3-}$, $Tl_2Se_x^{m-}$, $Tl_3Se_y^{n-}$, and $Tl_3Se_z^{p-}$ anions prepared by extracting NaTlSe or $NaTl_{0.5}Se$ in liquid NH_3 and in the presence of molar excesses or deficits (10–90 mole%) of 2,2,2-crypt or 18-crown-6 failed because the samples gave rise to large amounts of colourless crystalline material at temperatures below –20 °C. Solutions of the $TlSe_3^{3-}$, $Tl_2Se_x^{m-}$, $Tl_3Se_y^{n-}$, and $Tl_3Se_z^{p-}$ were therefore prepared by extracting NaTlSe (0.5514 g, 1.800 mmol) or $NaTl_{0.5}Se$ (0.3594 g, 1.757 mmol) in liquid NH_3 in the absence of complexing agents, giving rise to orange-red (NaTlSe) and deep red ($NaTl_{0.5}Se$) solutions. The increased intensity of the latter solution indicates that the anions were prepared in greater concentrations from $NaTl_{0.5}Se$ and was confirmed by ^{203}Tl, ^{205}Tl, and ^{77}Se NMR spectroscopy which provided sharper and better-resolved spectra for the deep red solution.

Preparation of $TlMTe_3^{3-}$ (M = Sn, Pb) Solutions. The $TlMTe_3^{3-}$ (M = Sn, Pb) anions

were prepared by reacting the alloys $Tl_2M_2Te_3$ (M = Sn, 0.1797 g, 0.172 mmol; M = Pb, 0.0836 g, 0.069 mmol) and K_2Te (Sn, 0.0522 g, 0.254 mmol; Pb, 0.0219 g, 0.106 mmol) in en (Sn) or in a 1 : 1 v/v mixture of en/ethylamine (Pb) and in the presence of a molar excess of 2,2,2-crypt (0.1958 g, 0.520 mmol (Sn); 0.2037 g, 0.541 mmol (Pb)) with respect to K^+. The resulting deep red (Sn) and brownish-red (Pb) solutions were isolated for NMR spectroscopy as described below.

Nuclear Magnetic Resonance Spectroscopy

Sample Preparation. When no further change in the colour of a solution was observed, the extraction was considered complete. At this point, the solution was carefully decanted from reaction ampoule B (Figure 2.3), which contained any residual alloy, into NMR tube A ensuring that none of the unreacted alloy was carried over. The sample in the NMR tube was then concentrated by static distillation of the solvent which was accomplished by cooling ampoule B in an ice-water bath and by maintaining the NMR tube at room temperature. Once the solution in the NMR tube was sufficiently concentrated (*ca.* 4–5 cm of solution in the NMR tube), the NMR tube and the reaction ampoule were simultaneously cooled either to –196 °C for liquid ammonia solutions or to 0 °C for en solutions, and the NMR sample was isolated by flame sealing at point C (Figure 2.3).

Any solid material which deposited in the NMR tube as a result of solution concentration or improper decantation was collected in the ¼"-o.d. NMR tube-end by centrifugation. The NMR tube was then carefully reinverted, leaving the solid material

lodged in the ¼" tube-end and a clear solution in the receiver coil region of the NMR tube.

Instrumentation. The ^{119}Sn, ^{77}Se, and ^{125}Te NMR spectra were recorded either on a Bruker AC-300 (7.0463 T) or on a Bruker AM-500 (11.744 T) MHz pulse spectrometer by using 10-mm probes broad-banded over the frequency ranges 13.968–121.497 and 23.276–202.460 MHz, respectively. Lead-207 NMR sepctra were recorded on the Bruker AM-500 MHz instrument. The observed spectrometer frequencies for ^{119}Sn, ^{77}Se, and ^{125}Te at 7.0463 (11.744) T were 111.922 (186.504), 57.240 (95.383), and 94.692 (157.794) MHz, respectively, and that for ^{207}Pb was 104.631 MHz at 11.744 T. The ^{203}Tl and ^{205}Tl nuclei resonate at 171.218 (285.363) MHz and at 172.902 (288.169) MHz, respectively, at field strengths of 7.0463 (11.744) T, which are outside the dynamic ranges of the AC-300 and AM-500 broad-banded probes. Consequently, all ^{203}Tl and ^{205}Tl NMR spectra were recorded on the Bruker AC-200 (4.698 T) pulse spectrometer by inserting the 10-mm Bruker AC-300 broad-banded probe into the AC-200 cryomagnet. The observed spectrometer frequencies for ^{203}Tl and ^{205}Tl at 4.698 T were 114.319 at 115.444 MHz, respectively.

Spectra were obtained unlocked (field drift < 0.1 Hz h^{-1}). The spectrometers were initially shimmed on the lock signal of deuterated acetone (d_6-acetone), and final shim parameters were optimized by shimming unlocked on the ^{119}Sn free-induction decay of neat $(CH_3)_4Sn$.

Free-induction decays were typically accumulated in 16 or 32 K computer memories. Spectral width settings of 25–100 kHz were employed, yielding data-point resolutions of 3.05–6.10 Hz/data point and acquisition times of 0.328–0.655 s, respectively. A relaxation

delay of 1.0 s was applied when recording ^{77}Se NMR spectra. Typically, 40,000–200,000 transients were accumulated depending on the concentrations and sensitivities of the nuclides under study. Pulse width settings corresponding to a bulk magnetization tip angle, θ, of ~90° were 12.5 (15.0), 11.5 (15.0), and 5.0 (10.0) μs for ^{119}Sn, ^{77}Se, and ^{125}Te at 7.0463 (11.744) T, respectively, and that for ^{207}Pb at 11.744 T was 25 μs. Pulse-width settings employed for ^{203}Tl and ^{205}Tl at 4.698 T were 10.0 and 20.0 μs, respectively.

Variable-temperature spectra were recorded by using the variable-temperature controllers of the spectrometers. The temperatures were checked by placing a copper constantan thermocouple into the sample region of the probe. The samples were allowed to equilibrate for at least 5 min, while spinning, before spectral accumulations were begun.

Line-broadening parameters used in the exponential multiplication of the free-induction decays were 10–50 Hz for the ^{77}Se, ^{125}Te, and ^{119}Sn NMR spectra and 50–100 Hz for the ^{203}Tl, ^{205}Tl, and ^{207}Pb NMR spectra. In order to enhance the resolution of some satellite peaks observed in the ^{203}Tl and ^{205}Tl NMR spectra and to determine the corresponding J-coupling values, the free-induction decays were transformed by using Gaussian line fits rather than the conventional Lorentzian line fits. For the Gaussian line fits, Gaussian broadening factors between 0.1–0.5 and the negative of the line broadening values used for Lorentzian line fits were employed. Zero-filling to 64 or 128 K of memory was also employed for resolution enhancement of ^{119}Sn, ^{203}Tl, and ^{205}Tl NMR spectra.

Referencing. The respective nuclei were referenced to samples of 0.1 M aqueous $TlNO_3$ and neat $(CH_3)_4Sn$, $(CH_3)_4Pb$, $(CH_3)_2Se$, and $(CH_3)_2Te$. The reference samples were

contained in medium-wall 10-mm o.d. standard-glass NMR tubes which had been degassed and flame-sealed under dynamic vacuum at room temparature. The chemical shift convention used was that a positive (negative) shift signified a chemical shift to higher (lower) frequency relative to that of the reference standard.

Spectral Simulations. All spectral simulations were carried out by using the program *DSYMPC*.[87] Subspectra were weighted by using the normalized total line intensities provided in subsequent Chapters and summed by using the line spectrum addition subroutine in *DSYMPC*.

Crystal Growing

$(K^+)_2$(18-crown-6-K^+)$_2Sn_2Se_6^{4-}$·4en. The powdered $KSn_{0.67}Se_{1.93}$ alloy (0.1040 g, 0.384 mmol) was transferred into arm A of a Pyrex glass crystal-growing vessel (Figure 2.3) and extracted in en and in the presence of a molar deficit of 18-crown-6 (0.0930 g, 0.352 mmol) with respect to K^+. After two weeks, the resulting deep-yellow solution was carefully decanted off the unreacted alloy residue into arm B of the reaction vessel, ensuring that none of the unreacted alloy was carried over. An excess of THF with respect to the en volume (en : THF = 1 : 2 v/v) was then condensed under static vacuum at 0 °C into the first arm of the vessel. The reactor was allowed to stand under static vacuum for 1–2 weeks over which period the THF slowly vapour phase diffused into the en solution, resulting in the formation of yellow platelets.

$(K^+)_2$(2,2,2-crypt-K^+)$_2Sn_2Te_6^{4-}$. Large deep red plate-like crystals suitable for a

diffraction study were obtained as described above by the vapour phase diffusion of THF (1 : 2 v/v) over 2–3 weeks into the deep red solution obtained by extraction of the alloy $KSn_{0.63}Te_{1.70}$ (0.1494 g, 0.452 mmol) in en and in the presence of a 40 mole% deficit of 2,2,2-crypt (0.0684 g, 0.182 mmol) with respect to K^+. The deep red plates were also obtained in an analogous manner from an en extract of $KSn_{0.63}Te_{1.70}$ (0.1015g, 0.307 mmol) containing a 60 mole% deficit of 2,2,2-crypt (0.0687 g, 0.182 mmol) with respect to K^+, but failed to diffract. However, Raman spectra were recorded on powdered crystals obtained from both experiments and indicated that both crystalline samples contained the $Sn_2Te_6^{4-}$ anion.

By analogy with that for $(K^+)_2(18\text{-crown-6-}K^+)_2Sn_2Se_6^{4-}\cdot 4en$, an attempt was also made to obtain crystals of the title compound from an en solution of the alloy $KSn_{0.63}Te_{1.70}$ (0.1107 g, 0.335 mmol) containing a molar deficit of 18-crown-6 (0.0814 g, 0.308 mmol) with respect to K^+, but failed to yield crystals after 5–6 weeks.

K^+(2,2,2-crypt-K^+)$_2HOSnTe_3^{3-}$ and K^+(2,2,2-crypt-K^+)$_2HOSnTe_3^{3-}\cdot$en. The reaction of the alloy $Tl_2Sn_2Te_3$ (0.1797 g, 0.175 mmol) with K_2Te (0.0522 g, 0.253 mmol) in en and in the presence of a molar excess of 2,2,2-crypt (0.1958 g, 0.520 mmol) with respect to K^+ gave rise to a deep red solution which was shown by ^{119}Sn and ^{125}Te NMR spectroscopy to contain mainly the $TlSnTe_3^{3-}$ anion and a new "Sn(IV)/Te" species (Chapters 3 and 7). As there was no evidence of spontaneous crystallization in the NMR sample after several weeks, the solution was transferred into arm B of a crystal-growing vessel (Figure 2.3) inside a glove bag which had been previously flushed for 12 h with dry nitrogen gas and then filled with the nitrogen gas. An excess of THF (1 : 2 v/v) was then vacuum distilled at 0 °C into arm A of

the vessel (Figure 2.3). The vapour phase diffusion of the THF into the en solution over a period of 24 h led to the formation of deep red prisms of $K^-(2,2,2\text{-crypt-}K^+)_2HOSnTe_3^{3-}\cdot en$, whereas a complete intermixing of the solvents over a further 4 d led to the formation of orange rectangular plates of $K^-(2,2,2\text{-crypt-}K^+)_2HOSnTe_3^{3-}$.

(18-crown-6-K$^+$)$_4$Sn$_4$Se$_{10}^{4-}$·5en, (18-crown-6-K$^+$)$_4$Sn$_4$Te$_{10}^{4-}$·3en·2THF, and (2,2,2-crypt-K$^+$)$_4$Sn$_4$Se$_9^{4-}$·en·THF. The vapour phase diffusion of THF (1 : 2 v/v) over 1–2 weeks into the yellow-orange coloured en solution obtained by extraction of the alloy $KSn_{0.90}Se_{1.97}$ (0.1178 g, 0.395 mmol) in the presence of a molar excess of 18-crown-6 (0.1101 g, 0.416 mmol) with respect to K^- led to the formation of two crystal morphologies. Yellow platelets exhibiting crystal habits (monoclinic unit-cell dimensions at 24 °C (Ag Kα radiation): a = 15.572(8) Å, b = 8.434(7) Å, c = 23.252(14) Å, β = 108.54(4)°, V = 2895.14(3.37) Å^3) identical to those of $(K^-)_2(18\text{-crown-6-}K^+)_2Sn_2Se_6^{4-}\cdot 4en$ were obtained and were not further studied. Orange parallelepiped-shaped crystals were also obtained and were shown by an X-ray crystal structure determination to be $(18\text{-crown-6-}K^+)_4Sn_4Se_{10}^{4-}\cdot 5en$. Crystals of $(2,2,2\text{-crypt-}K^+)_4Sn_4Se_9^{4-}\cdot en\cdot THF$ were similarly obtained over 2–3 weeks from an en extract of $KSn_{0.90}Se_{1.97}$ (0.0698 g, 0.234 mmol) containing a small molar excess of 2,2,2-crypt (0.0994 g, 0.264 mmol) with respect to K^-

Crystals of $(18\text{-crown-6-}K^+)_4Sn_4Te_{10}^{4-}\cdot 3en\cdot 2THF$ were obtained by the vapour phase diffusion of THF (1 : 2 v/v) over 3–4 weeks into the deep red en extract of $K_4Sn_4Te_{10}$ (0.3000 g, 0.157 mmol) containing a molar deficit of 18-crown-6 (0.0437 g, 0.165 mmol) with respect to K^-. Interestingly, crystals of the compound $(2,2,2\text{-crypt-}K^+)_2(Te_4^{2-})_{0.5}(Te_6^{2-})_{0.5}$ were

obtained under similar experimental conditions when 2,2,2-crypt was used instead of 18-crown-6 ($K_4Sn_4Te_{10}$, 0.1027 g, 0.054 mmol; 2,2,2-crypt, 0.0400 g, 0.106 mmol). The X-ray crystal structure of (2,2,2-crypt-K^+)$_2$(Te_4^{2-})$_{0.5}$(Te_6^{2-})$_{0.5}$ is discussed in ref. (43).

(2,2,2-crypt-K$^+$)$_2$Tl$_2$Te$_2^{2-}$. Attempts to prepare suitable single crystals of the title compound by the vapour phase diffusion of THF over 5–6 weeks into the dark brownish red en solution of the alloy NaTlTe containing a 20 mole% excess of 2,2,2-crypt with respect to Na^+ resulted in the formation of microcrystalline material. Interestingly, the dark red solution resulting from the reaction of K_2Te (0.0886 g, 0.430 mmol) and Tl_2Te (0.1124 g, 0.209 mmol) in an en/ethylamine mixture (1 : 1 v/v) and in the presence of a 63 mole% deficit of 2,2,2-crypt (0.2032 g, 0.540 mmol) had been shown by ^{205}Tl NMR spectroscopy to contain the $Tl_2Te_2^{2-}$ anion as the major species in solution along with small amounts of the known $TlTe_3^{3-}$ anion and the novel $TlTe_2^-$ anion. The NMR parameters reported for the $Tl_2Te_2^{2-}$ anion in the en/ethylamine solution ($\delta(^{205}Tl)$ = 8153 ppm; $^1J(^{205}Tl–^{125}Te)$ = 4200 Hz; $J(^{205}Tl–^{203}Tl)$ = 6328 Hz)[85] are similar to those recorded for the anion in en solutions of NaTlTe/excess 2,2,2-crypt ($\delta(^{205}Tl)$ = 8175 ppm; $^1J(^{205}Tl–^{125}Te)$ = 4004 Hz; $J(^{205}Tl–^{203}Tl)$ = 6337 Hz; Chapter 5), but are at significant variance with those reported for the anion in a saturated liquid ammonia extract of KTlTe containing a molar excess of 2,2,2-crypt ($\delta(^{205}Tl)$ = 8128 ppm; $^1J(^{205}Tl–^{125}Te)$ < 200 Hz; $J(^{205}Tl–^{203}Tl)$ = 8006 Hz).[56] The large disparity in the coupling constant suggested a modification in the bonding or in the geometry of the anion (Chapter 5). It was therefore of interest to obtain suitable single crystals containing the $Tl_2Te_2^{2-}$ anion from the dark-red en/ethylamine NMR sample.

Since there was no evidence of spontaneous crystallization in the NMR sample after several months, deep red hexagonal plates of the title compound were obtained by the vapour phase diffusion of THF (1 : 1.5 v/v) into the dark-red solution over 3–4 weeks in a manner similar to that used for the preparation of suitable single crystals of the compounds $K^+(2,2,2\text{-crypt-}K^+)_2HOSnTe_3^{3-}$ and $K^+(2,2,2\text{-crypt-}K^+)_2HOSnTe_3^{3-}\cdot en$.

(2,2,2-crypt-K$^+$)$_3$TlPbTe$_3^{3-}$·2en. The alloy $Tl_2Pb_2Te_3$ (0.0836 g, 0.069 mmol) was reacted with K_2Te (0.0219 g, 0.106 mmol) in en giving rise to a violet solution which became deep red upon addition of a molar excess of 2,2,2-crypt (0.2037 g, 0.541 mmol) with respect to K^+. The deep red solution was shown by ^{205}Tl, ^{207}Pb, and ^{125}Te NMR spectroscopy to contain mainly the novel $TlPbTe_3^{3-}$ anion (90%) along with a small amount of the known $Pb_2Te_3^{2-}$ anion (10%). Since there was no spontaneous crystallization in the NMR sample after several months, large deep red diamond-shaped crystals of the title compound were obtained by the vapour phase diffusion of THF (1 : 1.5 v/v) into the dark red solution over 5–6 weeks in a manner similar to that used for the preparation of suitable single crystals of the compounds $K^+(2,2,2\text{-crypt-}K^+)_2HOSnTe_3^{3-}$ and $K^+(2,2,2\text{-crypt-}K^+)_2HOSnTe_3^{3-}\cdot en$.

(2,2,2-crypt-Na$^+$)$_4$Tl$_4$Se$_8^{4-}$·0.5en and (2,2,2-crypt-Na$^+$)$_x$(18-crown-6-Na$^+$)$_y$[TlSe$_{4/2}^-$]$_n$·zTHF. Attempts to prepare suitable single crystals of the title compounds by the vapour phase diffusion of THF into en extracts of the alloys NaTlSe or $NaTl_{0.5}Se$ containing molar excesses or deficits (20, 40, 50, and 60 mole%) of 2,2,2-crypt with respect to Na^+ failed to yield crystals after 8–12 months. Crystals of the title compounds were therefore prepared as follows: The alloy $NaTl_{0.5}Se$ (0.0540 g, 0.264 mmol) was loaded in arm B of a Pyrex crystal-

growing vessel (Figure 2.4) and extracted in en and in the presence of an equimolar mixture of 18-crown-6 (0.0388 g, 0.147 mmol) and 2,2,2-crypt (0.0524 g, 0.139 mmol) with respect to Na^+. After four weeks, the resulting deep orange-red solution was carefully decanted off the unreacted alloy residue into arm A of the Pyrex vessel, ensuring that none of the unreacted alloy was carried over. An excess of THF (1 : 3 v/v) was then condensed under static vacuum and at 0 °C into arm A of the vessel. The vessel was then allowed to stand under static vacuum for eight months over which period the THF slowly vapour phased diffused into, and gradually intermixed with, the en solution, leading to the formation of orange plates of $(2,2,2\text{-crypt-}Na^+)_x(18\text{-crown-6-}Na^+)_y[TlSe_{4/2}^-]_\infty^1 \cdot z$THF and orange cubes of $(2,2,2\text{-crypt-}Na^+)_4Tl_4Se_8^{4-} \cdot 0.5$en.

Crystals of the title compounds were also prepared as described above from an en solution of the alloy NaTlSe (0.0996 g, 0.325 mmol) containing 18-crown-6 (0.0629 g, 0.238 mmol) and 2,2,2-crypt (0.0425 g, 0.113 mmol) in a 2 : 1 molar ratio. Rhombohedral orange crystals of unknown composition were also isolated from this solution but failed to diffract.

Crystal Isolation and Mounting

The first step in crystal isolation involved the careful decantation of the mother liquor from arm A of the Pyrex crystal-growing vessel (Figure 2.4) into extraction arm B, ensuring that none of the crystalline material was carried over. The mother liquor was subsequently pipetted out of the vessels inside a glove bag which had previously been flushed for 24 h and then filled with dry nitrogen gas. The crystals were then dried under dynamic vacuum for *ca.*

2–3 min and transferred inside the dry box. The Pyrex vessels were scored and broken open, and suitable single crystals were selected from the bulk sample under a stereo-zoom microscope (Carl-Zeiss-Jena Instruments Ltd.), cut if necessary with a scalpel, and transferred into 0.1–0.5 mm i.d. Lindemann glass capillaries by using a stainless steel or iridium stylus. The capillaries were initially sealed with dry Kel-F grease, brought out of the dry box, and immediately flame-sealed by using a natural gas/oxygen microtorch. The capillaries were glued to brass pins with epoxy cement and mounted on the goniometer head of the diffractometer.

Crystals of (2,2,2-crypt-Na^+)$_4Tl_4Se_8^{4-}$·0.5en and (2,2,2-crypt-Na^+)$_x$(18-crown-6-Na^+)$_y[TlSe_{4/2}^-]_\infty^1$·zTHF were completely degraded upon exposure to dynamic vacuum, indicating removal of solvent from the crystal lattices. Furthermore, an initial inspection of the crystals under a stereo-zoom microscope revealed that their dimensions were smaller than 0.1 mm, which is the dimension of the smallest commercially-available capillary (*vide supra*). Crystals of these compounds were therefore wet-mounted on the diffractometer by employing a slight modification of the conventional open-mount technique used for non air- and moisture-sensitive crystalline materials and is described below. The modified technique was developed by, and was carried out with the assistance of, Dr. Horst Borrmann at the Max-Planck-Institut für Festkörperforschung, Heisenbergstraße 1, Stuttgart, Germany. The crystals were manipulated inside a glove bag, located near the imaging plate of the diffractometer, which had been previously flushed for 3 d with dry argon gas and then filled with argon gas.

A bulk crystalline sample was recovered from the Pyrex vessel inside the glove bag and was deposited in a Petri dish filled to a depth of *ca.* 10 mm with perfluorodecaline. The Petri dish was then removed from the glove bag and was placed under a stereo-zoom microscope located less than 60 cm away from the imaging plate of the diffractometer. Suitable single crystals were selected from the perfluorodecaline by using glass fibers which were heavily coated at one end with Apiezon H grease (Apiezon Products, Manchester, England) and which had already been attached at the other end to the goniometer head of the diffractometer. Once the crystals were attached to the glass fibers, they were immediately mounted on the diffractometer that had been cooled with a liquid-nitrogen stream to −100 °C.

The above technique offers two advantages over the one generally used to dry-mount air- and moisture-sensitive crystals (*vide supra*): (1) The range of densities of (2,2,2-crypt-K^+)$_n$$M^{m-}$-type salts where M is heavy main-group polyanion can be deduced to a good approximation in the inert perfluorodecaline solvent which has density, ρ, of 1.92 g cm^{-1}, and different crystal morphologies in a bulk sample can also be separated on the basis of their different densities. For example, orange plates of (2,2,2-crypt-Na^+)$_x$(18-crown-6-Na^+)$_y$-$[TlSe_{4/2}^-]_\infty^1$ ·*z*THF float in the perfluorodecaline indicating that ρ < 1.92 g cm^{-1} whereas orange cubes of (2,2,2-crypt-Na^+)$_4Tl_4Se_8^{4-}$ ·0.5en are denser than the solvent. This information can be used to infer the approximate compositions of highly disordered compounds like (2,2,2-crypt-Na^+)$_x$(18-crown-6-Na^+)$_y$$[TlSe_{4/2}^-]_\infty^1$ ·*z*THF and is discussed under **X-ray Crystallography** and in Chapter 7. (2) Solvated crystals can be manipulated without

the possibility of introducing partial occupation of the solvent interstitial sites in the crystal lattices and/or disorder which can arise from partial degradation of the crystals under dynamic vacuum. For example, the X-ray crystal structure of (2,2,2-crypt-K^+)$_3Tl_5Se_5^{3-}$ contains large channels running parallel to the *a*-axis and has been attributed to significant solvent loss which occurred when the crystals were briefly dried under dynamic vacuum.[33] Interestingly, no recognizable solvent molecules could be located in the channels, implying that the above problem is compounded by severe disorder.

Collection and Reduction of X-Ray Data

The parameters employed for the collection of the diffraction data are summarized in Tables 2.2–2.4. A summary of the crystal data and refinement results can be found in subsequent Chapters.

The diffraction data for the compounds (K^+)$_2$(2,2,2-crypt-K^+)$_2Sn_2Te_6^{4-}$, K^+(2,2,2-crypt-K^+)$_2HOSnTe_3^{3-}$, K^+(2,2,2-crypt-K^+)$_2HOSnTe_3^{3-}$·en, and (2,2,2-crypt-K^+)$_2TlPbTe_3^{3-}$·en were collected at the X-ray Diffraction Facility, McMaster University on a Syntex P3 diffractometer by using silver radiation monochromatized with a graphite crystal (λ = 0.56086 Å) (Table 2.2). Unit-cell dimensions were determined from a least-squares refinement of the setting angles (χ, ϕ, and 2θ) obtained from accurately centred reflections chosen from a variety of points in reciprocal space (Table 2.2). Integrated diffraction intensities were collected with scan rates varying from 1.5–14.6° min^{-1}, so that weaker reflections were examined more slowly to minimize counting errors. During data collection,

Table 2.2. Parameters Used to Collect Diffraction Intensities for $(K')_2(2,2,2\text{-crypt-}K')_2Sn_2Te_6^{4-}$ (**1**), $K'(2,2,2\text{-crypt-}K')_2HOSnTe_3^{3-}$ (**2**), $K'(2,2,2\text{-crypt-}K')_2HOSnTe_3^{3-}\cdot en$ (**3**), and $(2,2,2\text{-crypt-}K')_2TlPbTe_3^{3-}\cdot 2en$ (**4**) on the Syntex P3 Diffractometer (λ = 0.56086 Å).

	(**1**)	(**2**)	(**3**)	(**4**)
scan type	ω	2θ	2θ	ω
T (°C)	24	−105	24	24
h	0 → 11	0 → 14	0 → 18	0 → 16
k	−11 → 11	−15 → 15	−14 → 16	0 → 28
l	−18 → 17	−22 → 21	−16 → 17	−22 → 18
θ_{max} (deg)	17.55	20.00	20.00	17.55
no. refl. for cell param. (2θ limits, deg)	35 (15.01–23.06)	43 (9.76–27.30)	36 (7.24–27.73)	24 (15.10–23.50)
no. measured refl.	4826	10639	8619	5674
no. independent refl.	4555	10109	8256	5434
no. observed refl. ($I > 2\sigma I$)	2286	5984	4619	2272
μ (mm^{-1})	1.721	1.269	1.106	2.815
absorption corr.	none applied	DIFABS	DIFABS	DIFABS

Table 2.3. Parameters Used to Collect Diffraction Intensities for $(K^+)_2(18\text{-crown-6-}K^+)_2Sn_2Se_6^{4-}\cdot 4en$ (**1**), $(18\text{-crown-6-}K^+)_4Sn_4Se_{10}^{4-}\cdot 5en$ (**2**), $(18\text{-crown-6-}K^+)_4Sn_4Te_{10}^{4-}\cdot 3en\cdot 2THF$ (**3**), and $(2,2,2\text{-crypt-}K^+)_2Sn_4Se_9^{4-}\cdot en\cdot THF$ (**4**) on the Stoe Imaging Plate Diffractometer System (λ = 0.71073 Å).[a]

	(**1**)	(**2**)	(**3**)	(**4**)
scan type	oscillation	oscillation	oscillation	oscillation
T (°C)	–123	–123	–123	–183
crystal-to-detector distance (mm)	48 (125)	55 (125)	65 (120)	80 (110)
ϕ range (deg)	0–150 (0–200)	160–286 (150–300)	0–140 (0–150)	0–150 (0–200)
oscillation angle, ϕ (deg)	0.3 (1.0)	0.3 (1.0)	0.3 (1.0)	0.4 (1.0)
no. exposures / time per exposure (min.)	500 / 4 (200 / 2)	420 / 4 (150 / 2)	467 / 4 (150 / 2)	375 / 3 (200 / 2)
h	–22 ‣ 21	–21 ‣ 29	–25 ‣ 25	–30 ‣ 30
k	–11 ‣ 11	–25 ‣ 25	–22 ‣ 22	–21 ‣ 20
l	–32 ‣ 33	–32 ‣ 24	–23 ‣ 28	–29 ‣ 34

Table 2.3. Continued.

	(1)	(2)	(3)	(4)
θ_{max} (deg)	29.00	28.00	24.11	26.99
no. refl. for cell param.	1775	1634	266	664
no. measured refl.	27121	42373	59396	93450
no. independent refl.	7794	15270	16747	24509
no. observed refl. ($I > 2\sigma I$)	6824	10398	15061	18024
μ (mm^{-1})	4.900	4.815	3.795	3.980
absorption corr.	redundant refl.	none applied	redundant refl.	redundant refl.

[a] The data were collected in two stages. Values in parentheses refer to the parameters used during the second stage of the data collection.

Table 2.4. Parameters Used to Collect Diffraction Intensities for (2,2,2-crypt-K$^+$)$_2$Tl$_2$Te$_2^{2-}$ (**1**), (2,2,2-crypt-K$^+$)$_4$Tl$_4$Se$_8^{4-}$·0.5en (**2**), and (2,2,2-crypt-Na$^+$)$_x$(18-crown-6-Na$^+$)$_y$[TlSe$_{4/2}^{1-}$]$_\infty$·zTHF (**3**) on the Stoe Imaging Plate Diffractometer System (λ = 0.71073 Å).[a]

	(**1**)	(**2**)	(**3**)
scan type	oscillation	oscillation	oscillation
T (°C)	−123	−123	−123
crystal-to-detector distance (mm)	50 (125)	80 (125)	80 (125)
ϕ range (deg)	80–280 (0–240)	0–150 (0–115)	0–200 (0–200)
oscillation angle, ϕ (deg)	0.5 (1.2)	0.5 (1.0)	0.5 (1.2)
no. exposures / time per exposure (min.)	400 / 5 (200 / 1.5)	300 / 6 (150 / 3)	400 / 3 (167 / 2)
h	−15 ‣ 15	−16 ‣ 16	−16 ‣ 16
k	−15 ‣ 15	−19 ‣ 18	−15 ‣ 16
l	−16 ‣ 16	−24 ‣ 24	−30 ‣ 30

Table 2.4. Continued.

	(1)	(2)	(3)
θ_{max} (deg)	29.00	24.12	24.09
no. refl. for cell param.	1339	608	1074
no. measured refl.	16178	30330	43412
no. independent refl.	6155	8226	8460
no. observed refl. ($I > 2\sigma I$)	5343	5748	6764
μ (mm^{-1})	7.740	9.051	8.770
absorption corr.	none applied	none applied	none applied

[a] The data were collected in two stages. Values in parentheses refer to the parameters used during the second stage of the data collection.

the intensities of three standard reflections were monitored every 97 reflections to check for crystal stability and alignment. No crystal decay was observed. The data sets were corrected for Lorentz and polarization effects and for absorption.

The diffraction data for the remaining compounds were collected by Dr. Horst Borrmann on a Stoe imaging plate diffractometer system equipped with a 1-circle goniometer and a graphite monochromator. Molybdenum radiation (λ = 0.71073 Å) was used. Diffraction intensities were collected at two crystal-to-detector distances (Tables 2.3 and 2.4). The data sets obtained at the two crystal-to-detector distances were merged, and the final data set contained 90–95% of the calculated number of observed reflections. An empirical absorption correction based on redundant reflections was applied.

Solution and Refinement of the Structures

A summary of the refinement results for each compound can be found in subsequent Chapters. All structures were solved and refined as described under the ***General Remarks*** section below. Specific details regarding the refinement of some disordered structures are discussed under subsequent sections.

General Remarks. All calculations were performed on a Silicon Graphics, Inc., Model 4600PC workstation by using the Siemens *SHELXTL-Plus* software package for structure determination, refinement, and molecular graphics.[88] The *XPREP* program was used to confirm the unit-cell dimensions and the crystal lattices. A first solution was usually obtained without absorption corrections by using conventional direct or Patterson (used for

$K^+(2,2,2\text{-crypt-}K^+)_2HOSnTe_3^{3-}\cdot en$) methods which located the general and/or special positions of the main-group and alkali-metal atoms. The full-matrix least-squares refinement of the positions and isotropic thermal parameters of the assigned atoms located the general and/or special positions of the C, N, and O atoms of the 2,2,2-crypt-M^+ and/or 18-crown-6-M^+ (M = Na, K) cations. Any disorder in the cations was modeled at this point in the refinement (see ***Specific Details***). Ethylenediamine or THF solvent molecules were assigned after the atoms of the anions and cations were refined with anisotropic thermal parameters and any disorder was satisfactorily modeled. Crystallographically well-behaved solvent molecules were refined with anisotropic thermal parameters, whereas disordered solvent molecules were refined at 0.5 occupancy and isotropically and by constraining the C–C, C–N, and C–O bond lengths and the non-adjacent C–N and C–O distances to values observed in ordered solvent molecules. Hydrogen-atom positions were usually calculated (d(C–H) = 0.96 Å, d(O–H) = 0.82 Å, d(N–H) = 0.96 Å), and U(H) was fixed to $-1.2 \times U$(C), U(O), or U(N). The hydrogen atom positions for $(K^+)_2(18\text{-crown-6-}K^+)_2Sn_2Se_6^{4-}\cdot 4en$ were located from the difference map and were refined isotropically.

The final structure solutions were obtained by using data that had been corrected for absorption. During the final stages of the refinement, all reflections with $F^2 < -2\sigma(F^2)$ were suppressed and weighting factors recommended by the refinement program were introduced. The maximum electron densities in the final difference maps were located around the anions.

Specific Details. ***$(K^+)_2(2,2,2\text{-crypt-}K^+)_2Sn_2Te_6^{4-}$.*** The positionally-disordered 2,2,2-crypt-K^+ cation was modeled by using the positions of a 2,2,2-crypt-K^+ cation from

$(enH^-)_2(2,2,2\text{-crypt-}K^+)_2Sn_2Se_6^{4-}$ [60] having the same chirality and refined by using a rigid-body refinement (*FRAG* in *SHELXTL-Plus*). The final structure solution was obtained without absorption corrections and by introducing anisotropic thermal parameters only for the tin, tellurium, and potassium atoms.

$K^+(2,2,2\text{-crypt-}K^+)_2HOSnTe_3^{3-}$. The volume of the unit cell, 2641(1) $Å^3$, suggested the presence of four 2,2,2-crypt-K^+ cations.[89] The en solution from which the crystals were obtained had been shown by ^{205}Tl, ^{119}Sn, and ^{125}Te NMR spectroscopy to contain the known $Tl_2Te_2^{2-}$, $SnTe_3^{2-}$, and HTe^- anions as minor species in solution along with larger amounts of the $TlSnTe_3^{3-}$ anion and an uncharacterized species containing "Sn(IV)/Te_3" units (Chapter 3). The initial model used for the refinement of the structure therefore involved four 2,2,2-crypt-K^+ cations and two $SnTe_3^{2-}$ anions.

Conventional direct methods located the general positions of one tin and three tellurium atoms and the general positions of all the non-hydrogen atoms of the two 2,2,2-crypt-K^+ cations. The Sn and Te atoms comprised a trigonal-pyramidal $SnTe_3$ group, in contrast with the trigonal planar geometry of the $SnTe_3^{2-}$ anion established from solution multi-NMR spectroscopic[56] and Mössbauer studies.[90] The full-matrix least-squares refinement of the positions and the isotropic thermal parameters of all the atoms confirmed the presence of an $SnTe_3$ unit having $\sim C_{3v}$ point symmetry. An examination of the difference map revealed the positions of two additional peaks corresponding to 9.29 and 21.92 electrons. The weaker peak was located 2.16 Å from the tin atoms and was perpendicular to the plane containing the three tellurium atoms. The stronger peak was independently located

and was assigned to an uncryptated-K^+ cation, implying that the anion should possess a 3– charge. By analogy with the structure of the $HOGeS_3^{3-}$ anion,[91] the weaker peak was assigned to an O atom of an OH^- group, giving rise to the $HOSnTe_3^{3-}$anion. The successive full-matrix least-squares refinement of the positions and isotropic thermal parameters of all the atoms confirmed the structure of the title compound.

K^+(2,2,2-crypt-K^+)$_2$HOSnTe$_3^{3-}$·en. The volume of the unit cell, 3131(2) Å^3, suggested the presence of five 2,2,2-crypt-K^+ cations.[89] However, since crystals of the title compound were obtained from the same en sample as were those of K^+(2,2,2-crypt-K^+)$_2$$HOSnTe_3^{3-}$, the model used for the refinement of the structure involved four 2,2,2-crypt-K^+ cations, two K^+ cations, and two $HOSnTe_3^{3-}$ anions. The composition of the title compound was confirmed by successive Fourier syntheses.

(2,2,2-crypt-K^+)$_4$Sn$_4$Se$_9^{4-}$·en·THF. Conventional direct methods located the general positions of the Sn, Se, K, C, N, and O atoms, and successive Fourier syntheses confirmed the presence of the novel adamantanoid $Sn_4Se_9^{4-}$ anion (~ C_{3v} point symmetry). Interestingly, the anisotropic thermal parameters of the capping $SnSe_3$-unit were significantly larger than those of the basal Sn_3Se_6-ring suggesting disorder and was confirmed by the presence of large peaks (17.777–10.988 e·Å^{-3}) in the difference map which were located around the $SnSe_3$ cap. Attempts are currently being made to model this disorder.

(18-crown-6-K^+)$_4$Sn$_4$Te$_{10}^{4-}$·3en·2THF. The C and O atoms of the positionally-disordered 18-crown-K^+ cations were refined with common C and O thermal parameters for each cation.

(2,2,2-crypt-K$^+$)$_2$Tl$_2$Te$_2^{2-}$. Conventional direct structural methods located the general positions of four peaks defining a $Tl_2Te_2^{2-}$ anion positionally disordered about a centre of symmetry. The two highest peaks were assigned to a thallium atom with 0.5 occupancy per site and with a common thermal parameter, and the remaining two peaks were similarly assigned to a tellurium atom. It is important to note that no solvent molecules were located in the structure of the title compound (see Chapter 5). The residual electron density (5.076 e·Å^{-3}) was located around the thallium atoms.

(2,2,2-crypt-K$^+$)$_2$TlPbTe$_3^{3-}$·2en. Conventional direct methods located the special positions of one potassium atom (1 *y* ¼) and one tellurium atom (½ *y* –¼) and the general positions of one potassium atom, one tellurium atom, and one apical (Tl/Pb) atom of the trigonal bipyramidal $TlPbTe_3^{3-}$ anion. The location of the apical atoms of the $TlPbTe_3^{3-}$ anion on one general position implied a 50:50 positional disorder and indicated that the apical atoms were equivalent by symmetry. The apical-atom position was therefore refined as 0.5 Tl and 0.5 Pb.

(2,2,2-crypt-Na$^+$)$_x$(18-crown-6-Na$^+$)$_y$[TlSe$_{4/2}^-$]$_\infty$·zTHF. The initial images indicated a non-commensurate structure. The dimensions of the two non-commensurate crystal sub-lattices were determined from reflections obtained at the two crystal-to-detector distances (monoclinic unit cell dimensions *a* = 14.246(4) [14.246(4)] Å, *b* = 14.360(3) [14.360(3)] Å, *c* = 26.673(8) [32.248(5)] Å, β = 99.87(3) [99.87(3)]° were determined at 80 [125] mm) and indicate that the structure is non-commensurate along the *c*-axis. A preliminary structure solution was obtained in the smaller sub-lattice. Conventional direct methods located the

general positions of two thallium atoms and four selenium atoms defining a crystallograhically well-behaved $[TlSe_{4/2}^{-}]_{\infty}^{1}$ polyanion, implying that the smaller sub-lattice is the anion sub-lattice. Successive Fourier syntheses located the general positions of the C, O, and N atoms of two severely disordered cations and unrecognizable solvent molecules. Crystals of the compound $(2,2,2\text{-crypt-Na}^{+})_4Tl_4Se_8^{4-}\cdot 0.5en$ were obtained from the same solution as were those of $(2,2,2\text{-crypt-Na}^{+})_x(18\text{-crown-6-Na}^{+})_y[TlSe_{4/2}^{-}]_{\infty}^{1}\cdot zTHF$ and contain only the 2,2,2-crypt-Na^{+} cation, even though both the 18-crown-6 and the 2,2,2-crypt ligands were used in the experiment (see **Crystal Growing**). Consequently, the disorder in the present structure was modeled by assuming two positionally-disordered 2,2,2-crypt-Na^{+} cations, but the attempt was unsuccessful. Interestingly, the calculated density of the hypothetical $(2,2,2\text{-crypt-Na}^{+})[TlSe_{4/2}^{-}]_{\infty}^{1}\cdot THF$ salt is 2.056 (Z = 4) and is greater than that deduced by floatation of the crystals in perfluorodecaline (< 1.92 g cm^{-1}; see **Crystal Isolation and Mounting**) and indicates that the compound contains both the 2,2,2-crypt-Na^{+} and the 18-crown-6-Na^{+} cations disordered on the cationic sites in the crystal lattice. A similar type of disorder has been reported for the anions in the compound $(2,2,2\text{-crypt-K}^{+})_3(TlSn_8^{3-})_{0.5}(TlSn_9^{3-})_{0.5}\cdot en$.[30] Attempts are currently being made to model the disorder and to solve the non-commensurate nature of the structure.

Raman Spectroscopy

$SnSe_4^{4-}$, $Sn_2Ch_6^{4-}$, and $Sn_4Ch_{10}^{4-}$ (Ch = Se or Te). Raman spectra were recorded on a Jobin-Yvon Mole S-3000 triple spectrograph system equipped with a 0.32-m prefilter,

adjustable 25-mm entrance slit, and a 1.00-m double monochromator. Holographic gratings were used for the prefilter (600 groves mm^{-1}, blazed at 500 nm) and for the monochromator (1800 groves mm^{-1}, blazed at 500 nm). An Olympus metallurgical microscope (model BHSM-L-2) was used to focus the excitation laser beam to a 1-μm spot on the sample. The 514.5-nm line of a Spectra Physics Model 2016 Ar^+ ion laser was used for the excitation of yellow and orange samples and the 647.1-nm line of a Lexel Laser Inc., Model 3500 Kr^+ ion laser was used for red samples. The Raman spectrometer frequencies were calibrated by using the 1018.3 cm^{-1} line of neat liquid indene. The spectra were recorded by signal averaging using a Spectraview-2D CCD detector equipped with a 25-mm chip (1152 × 298 pixels). Laser powers of 20 ($Sn_4Se_{10}^{4-}$), 100 ($SnSe_4^{4-}$, $Sn_2Te_6^{4-}$, and $Sn_4Te_{10}^{4-}$), and 200 ($Sn_2Se_6^{4-}$) mW and slit settings corresponding to a resolution of ±2 cm^{-1} were employed. A total of 15 reads having 60 s integration times were summed.

Raman spectra were recorded at ambient temperatures on microcrystalline or single crystal samples sealed in Pyrex melting-point capillaries which had been previously vacuum dried for 24 h at 250 °C.

$Tl_2Ch_2^{2-}$ (Ch = Se, Te). Raman spectra were recorded by Dr. Janice Helmann of Bruker Spectrospin, Milton, Ontario on a Bruker Equinox 55 FT-IR spectrometer equipped with an FRA 106/S FT-Raman accessory which employed a CaF_2 beamsplitter and a liquid-nitrogen-cooled Ge diode detector. The backscattered (180°) radiation was sampled. Rayleigh filters consisting of a series of transmission and reflection filters were used. The scanner velocity was 50 kHz and the wavelength range for acquisition was 5500–10,500 cm^{-1}

when shifted relative to the laser line at 9394 cm^{-1}, giving a spectral range of 3895 to –1105 cm^{-1}. The actual usable Stokes range was 50–3000 cm^{-1} with a spectral resolution of 4 cm^{-1}. The Fourier transformations were carried out by using a Blackman Harris 3-term apodization and a zero-filling factor of 2. The 1064-nm line of a Nd YAG laser (350 mW maximum output) was used for excitation of the samples with a laser spot of *ca.* 0.2 mm at the sample. The spectra were recorded at ambient temperatures on powdered samples by using laser powers of 40 mW for the Se compound and 70 mW for the Te analogue and were corrected for instrument response. The powdered samples were sealed in Pyrex melting point capillaries (*vide supra*), and samples of the Se compound were obtained from Janette Campbell, McMaster University.

Theoretical Calculations

Calculations were performed by Dr. David A. Dixon of the William R. Wiley Environmental Molecular Sciences Laboratory, Pacific Northwest National Laboratory, 906 Batelle Blvd., P.O. Box 999, KI-83 Richland, Washington 99352.

The initial calculations were performed with the density functional theory (DFT) program DGauss[92] on Silicon Graphics, Inc., Model 4600PC workstations at the local (LDFT) and at the gradient-corrected nonlocal (NLDFT) levels. Calculations were performed with a basis set in which the Tl core electrons were treated with an all-pseudopotential (PP/PP) basis set[93] and the valence electrons were treated with a double-zeta valence-polarized (DZVP) basis set. For the Se and Te atoms, calculations were performed with the

same type of PP/PP and DZVP basis sets as those used for thallium as well as with all-electron DZVP basis sets.[94] All-electron DZVP basis set calculations were also performed on the hitherto unknown isoelectronic $In_2Ch_2^{2-}$ (Ch = Se or Te) anions for comparison. The local potential fit of Vosko, Wilk, and Nusair[95] was used (VWN/PP/PP and VWN/PP /DZVP). The gradient-corrected NLDFT calculations were performed with the nonlocal exchange potential of Becke[96] together with the nonlocal correlation function of Perdew (BP/PP/PP and BP/PP/DZVP).[97] In order to check the dependence of the calculated results on the form of the treatment of the core electrons, additional calculations were carried out by using the effective core potentials (ECP) and the basis set of Stevens *et al.*[98] The ECP for Tl has the 4*d* and the 4*f* electrons in the core and the 5*s*, 5*p*, and 5*d* electrons in the valence space. For Se and Te, only the *ns* and the *np* (*n* = 4 for Se and 5 for Te) electrons are in the valence space. The *d* polarization functions were taken from Huzinaga's compilation.[99] The calculations were performed at the local level with the program Gaussian94.[100]

The geometries were optimized by using the analytic gradient methods. Second derivatives were calculated by numerical differentiation of the analytic first derivatives except for the all-electron calculations on the $In_2Ch_2^{2-}$ anions where analytic methods were used.[101] For the finite difference calculations, a two-point method with a finite difference of 0.01 a.u. was used. Bond orders and valencies were calculated by following Mayer's method.[102]

CHAPTER 3

DITIN(IV) CHALCOGENIDE ANIONS, $Sn_2Ch_6^{4-}$ AND $Sn_2Ch_7^{4-}$ (Ch = Se, Te)

Introduction

The first classically-bonded tin(IV) chalcogenide anion characterized in solution by ^{119}Sn and ^{125}Te NMR spectroscopy was the $SnTe_4^{4-}$ anion.[103] Schrobilgen and coworkers[56] subsequently characterized the complete series of classically-bonded tin(IV) anions, $SnSe_xTe_{4-x}^{4-}$ (x = 0–4) and $SnSe_xTe_{3-x}^{2-}$ (x = 0–3), by solution ^{77}Se, ^{119}Sn, and ^{125}Te NMR spectroscopy. The monomeric $SnCh_4^{4-}$ (Ch = Se,[58,104] Te[59]) anions have also been characterized in the solid state by X-ray crystallography; however, the monomeric $SnCh_3^{2-}$ (Ch = Se, Te) anions have not yet been isolated as salts but dimerize in the solid state to form $Sn_2Ch_6^{4-}$ anions.[60–68] Interestingly, the solution structures of the dimeric $Sn_2Ch_6^{4-}$ anions have never been reported. Moreover, several tin(IV) chalcogenide anions that are dinuclear in tin or have higher tin nuclearities have also been synthesized and characterized primarily by X-ray crystallography as structural units in Zintl phases[105] (e.g.,$[Sn_2Se_5^{2-}]_n$,[106,107] $Sn_2Se_7^{6-}$,[108,109] $Sn_2Te_6^{6-}$,[110] $Sn_3Se_8^{4-}$,[111] $[Sn_3Se_7^{2-}]_n$[112]) or as discrete units in Zintl salts (e.g., $Sn_4Se_{10}^{4-}$[113,114]). Of the higher nuclearity tin(IV) species, none has been structurally characterized in solution by multi-NMR spectroscopy. Nuclear magnetic resonance spectroscopy of the spin-½ nuclei ^{77}Se, $^{117,119}Sn$, and ^{125}Te is particularly well suited for the solution characterization of tin(IV) chalcogenide anions and can provide additional valuable structural information based upon

homo- and heteronuclear spin–spin couplings and may correlate with structural parameters and vibrational frequencies observed in the solid state.

A synthetic strategy leading to the preparation of classically-bonded Zintl anions in solution has usually involved preparing and extracting ternary MXCh alloys (M = Na, K; X = Sn, Pb, Tl; Ch = S, Se, Te) in a basic, non-aqueous medium such as en or liquid NH_3 and in the presence of a stoichiometric excess of the macrobicyclic ligand, 2,2,2-crypt, which serves to minimize ion-pairing by acting as a sequestering agent for M^+.[71] Under conditions involving minimum ion-pairing, solutions arising from extraction of the alloys $KSnCh_2$ (Ch = Se, Te) in en were shown by multi-NMR spectroscopy to contain only the monomeric $SnCh_3^{2-}$ anions.[56] It was therefore of interest to investigate, through the use of solution multi-NMR spectroscopy, the effect of varying the amounts of unsequestered M^+ on the extent of condensation of the monomeric $SnCh_3^{2-}$ anions.

Although the crystal structures of the $SnCh_3^{2-}$ anions remain uncharacterized, the X-ray crystal structure of the hydroxide derivative of the $SnTe_3^{2-}$ anion, $HOSnTe_3^{3-}$, is reported in this Chapter. The Raman spectra of the $Sn_2Ch_6^{4-}$ (Ch = Se, Te) anions are also reported and are interpreted in light of their crystal structures.

Results and Discussion

Synthesis of the $Sn_2Ch_6^{4-}$ and $Sn_2Ch_7^{4-}$ (Ch = Se, Te) Anions and Structural Characterization by ^{77}Se, ^{119}Sn, and ^{125}Te NMR Spectroscopy.

The experimental approach involved the synthesis of the ternary alloys $KSn_{0.67}Se_{1.93}$,

$Ksn_{0.63}Te_{1.70}$, and $NaSn_{0.43}Te$ by fusion of the elements followed by extraction of the powdered alloys in en or liquid NH_3 in the absence (Te) or presence (Se) of non-stoichiometric amounts of 2,2,2-crypt with respect to M^- (M = Na, K), where M^- : 2,2,2-crypt = 1.00 : 0.42.

The $Sn_2Ch_6^{4-}$ and $Sn_2Ch_7^{4-}$ (Ch = Se, Te) anions present in solutions containing K^- were identified by natural abundance ^{77}Se, ^{119}Sn, and ^{125}Te NMR spectroscopy. The experimental ^{77}Se, ^{119}Sn, and ^{125}Te NMR spectra and the simulated ^{119}Sn NMR spectra are depicted in Figures 3.1–3.4. The chemical shifts of the new ditin anions as well as of the previously characterized $SnCh_3^{2-}$ and $SnCh_4^{4-}$ anions[56] are listed in Table 3.1 together with the observed and calculated satellite/central peak (I_S/I_C) intensity ratios of the Se, Te, and Sn environments of the anions (Chapter 1). The scalar, J, the reduced, $^1K(Sn–Ch)$, and the relativistically corrected reduced, $^1K(Sn–Ch)_{RC}$, coupling constants for the $Sn_2Ch_6^{4-}$ and $Sn_2Ch_7^{4-}$ as well as for the previously characterized $SnCh_3^{2-}$ and $SnCh_4^{4-}$ anions are listed in Table 3.2. The number of observed environments, the satellite doublet spacings corresponding to $^1J(^{119}Sn–^{77}Se)$, $^1J(^{119}Sn–^{125}Te)$, and $^2J(^{119}Sn–^{117}Sn)$, and the I_S/I_C ratios are consistent with dimeric $SnCh_3^{2-}$ structures, namely $Sn_2Ch_6^{4-}$, and $Sn_2Ch_7^{4-}$ anion structures.

The ^{119}Sn and ^{77}Se NMR spectra of the yellow solutions obtained by extracting $KSn_{0.67}Se_{1.93}$ in en and liquid NH_3 in the presence of a 42 mole% deficit of 2,2,2-crypt were recorded at 0 and –50 °C and gave rise to several new signals (Figures 3.1 and 3.3). Although satellites were resolved in the ^{119}Sn NMR spectrum at both temperatures, the ^{119}Sn NMR resonances at 0 °C were broad and the ^{77}Se spectrum obtained at –50 °C contained a

Figure 3.1. NMR spectra of $Sn_2Se_6^{4-}$: (a) ^{119}Sn (186.504 MHz, –50 °C) and simulated spectrum (right-hand trace); (b) ^{77}Se (95.383 MHz, 0 °C). The peak labelling scheme is defined in Table 3.3 and in the text; (A) and (B) in the ^{77}Se NMR spectrum denote the terminal and bridging selenium environments of $Sn_4Se_{10}^{4-}$ (Chapter 4).

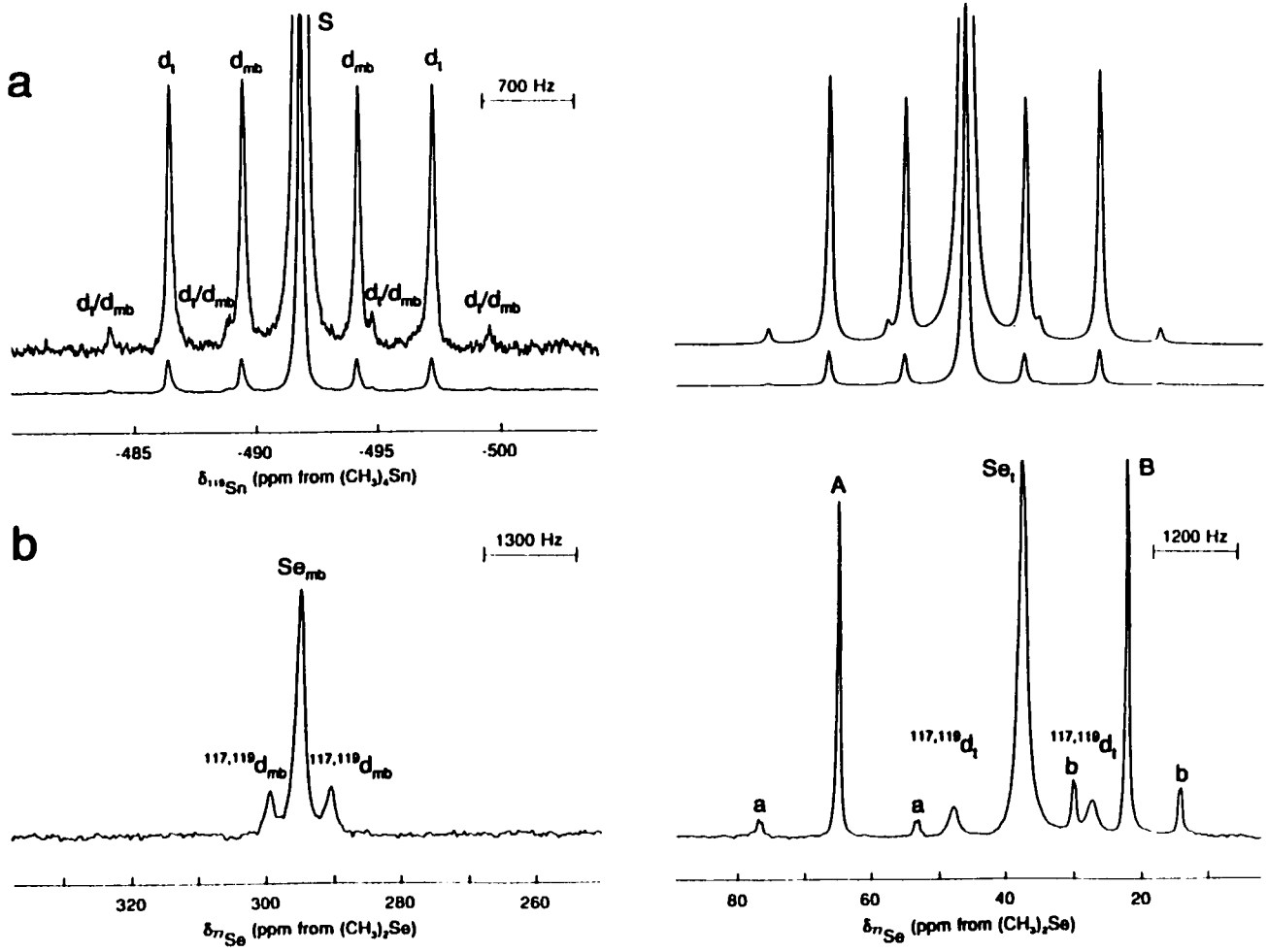
a
S
d_t
d_{mb}
d_{mb}
d_t
700 Hz
d_t/d_{mb}
d_t/d_{mb}
d_t/d_{mb}
d_t/d_{mb}
-485
-490
-495
-500
δ_{119}Sn (ppm from $(CH_3)_4Sn$)
b
1300 Hz
Se_{mb}
$^{117,119}d_{mb}$
$^{117,119}d_{mb}$
320
300
280
260
δ_{77}Se (ppm from $(CH_3)_2Se$)
A
Se_t
B
1200 Hz
a
a
$^{117,119}d_t$
b
$^{117,119}d_t$
b
80
60
40
20
δ_{77}Se (ppm from $(CH_3)_2Se$)

Figure 3.2. NMR spectra of $Sn_2Te_6^{4-}$: (a) ^{119}Sn (186.504 MHz, –70 °C) and simulated spectrum (right-hand trace); (b) ^{125}Te (157.794 MHz, –70 °C). The peak labelling scheme is defined in Table 3.3 and in the text; (C) in the ^{125}Te NMR spectrum denotes the terminal tellurium environment of $Sn_2Te_7^{4-}$ (see Figure 3.4).

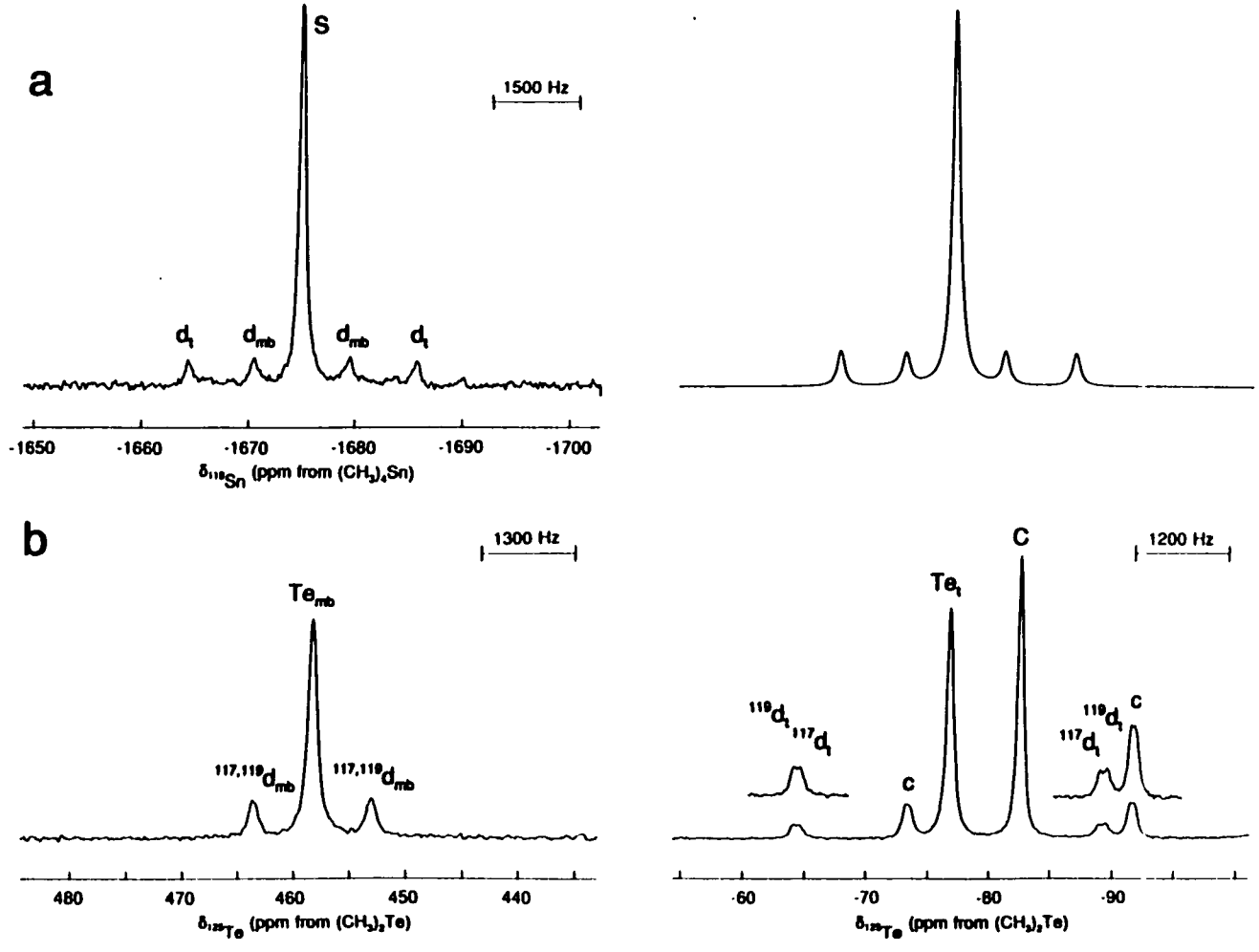
a
S
1500 Hz
d_t
d_{mb}
d_{mb}
d_t
-1650
-1660
-1670
-1680
-1690
-1700
δ_{119Sn} (ppm from $(CH_3)_4Sn$)
b
1300 Hz
Te_{mb}
$^{117,119}d_{mb}$
$^{117,119}d_{mb}$
480
470
460
450
440
δ_{125Te} (ppm from $(CH_3)_2Te$)
C
Te_t
1200 Hz
$^{119}d_t$ $^{117}d_t$
c
$^{117}d_t$
$^{119}d_t$
c
-60
-70
-80
-90
δ_{125Te} (ppm from $(CH_3)_2Te$)

Figure 3.3. NMR spectra of $Sn_2Se_7^{4-}$: (a) ^{119}Sn (186.504 MHz, –50 °C) and simulated spectrum (right-hand trace); (b) ^{77}Se (95.383 MHz, 0 °C). The peak labelling scheme is defined in Table 3.4 and in the text.

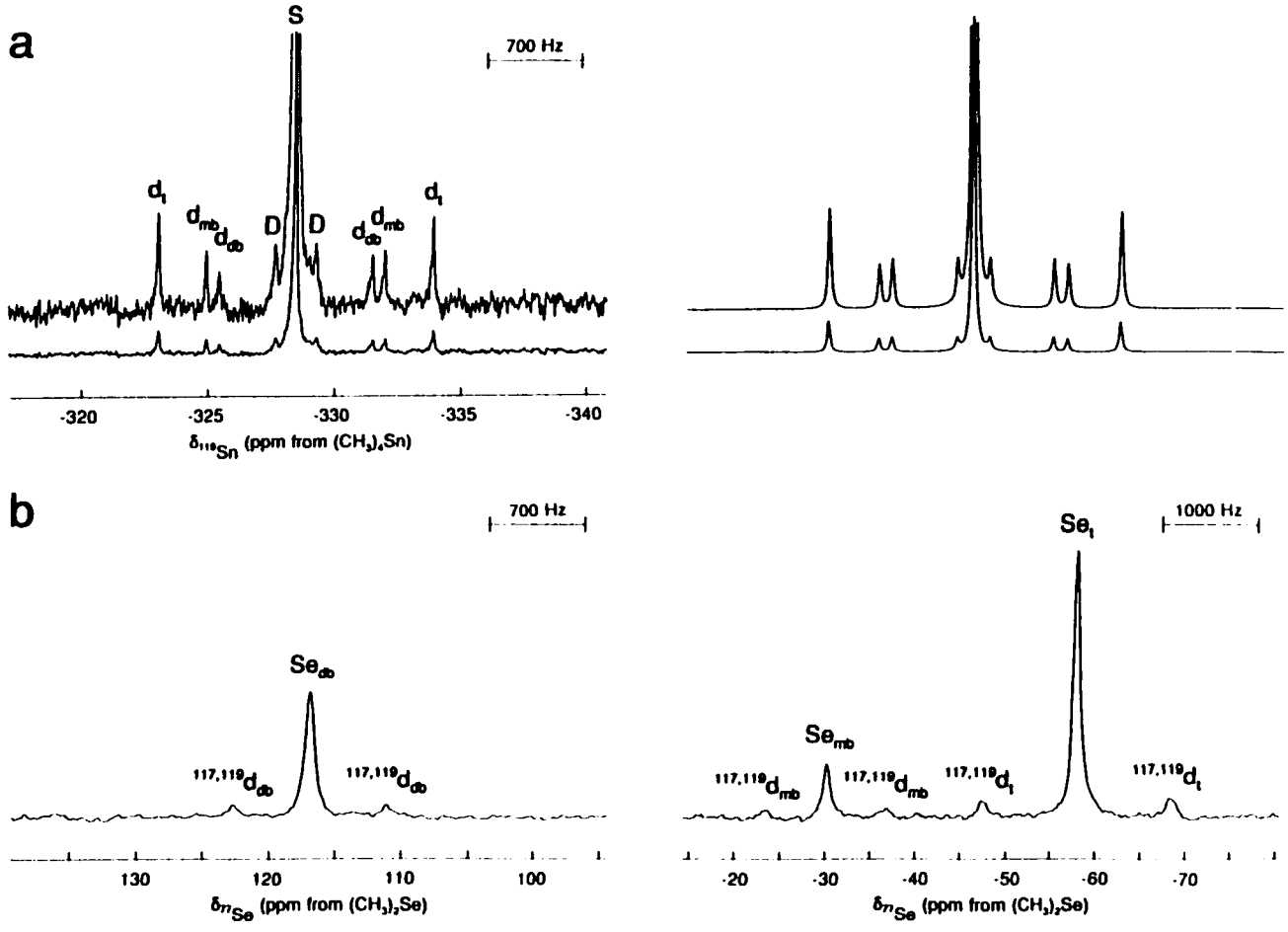
a
S
700 Hz
d_t
d_{mb} d_{db}
D
D
d_{db} d_{mb}
d_t
-320
-325
-330
-335
-340
$\delta_{^{119}Sn}$ (ppm from $(CH_3)_4Sn$)
b
700 Hz
Se_{db}
$^{117,119}d_{db}$
$^{117,119}d_{db}$
130
120
110
100
$\delta_{^{77}Se}$ (ppm from $(CH_3)_2Se$)
1000 Hz
Se_t
Se_{mb}
$^{117,119}d_{mb}$
$^{117,119}d_{mb}$
$^{117,119}d_t$
$^{117,119}d_t$
-20
-30
-40
-50
-60
-70
$\delta_{^{77}Se}$ (ppm from $(CH_3)_2Se$)

Figure 3.4. NMR spectra of $Sn_2Te_7^{4-}$: (a) ^{119}Sn (186.504 MHz, –70 °C) and simulated spectrum (right-hand trace); (b) ^{125}Te (157.794 MHz, –70 °C). The peak labelling scheme is defined in Table 3.4 and in the text; (E) in the ^{125}Te NMR spectrum denotes the terminal tellurium environment of $Sn_2Te_6^{4-}$ (see Figure 3.2) and (?) denotes an unassigned resonance.

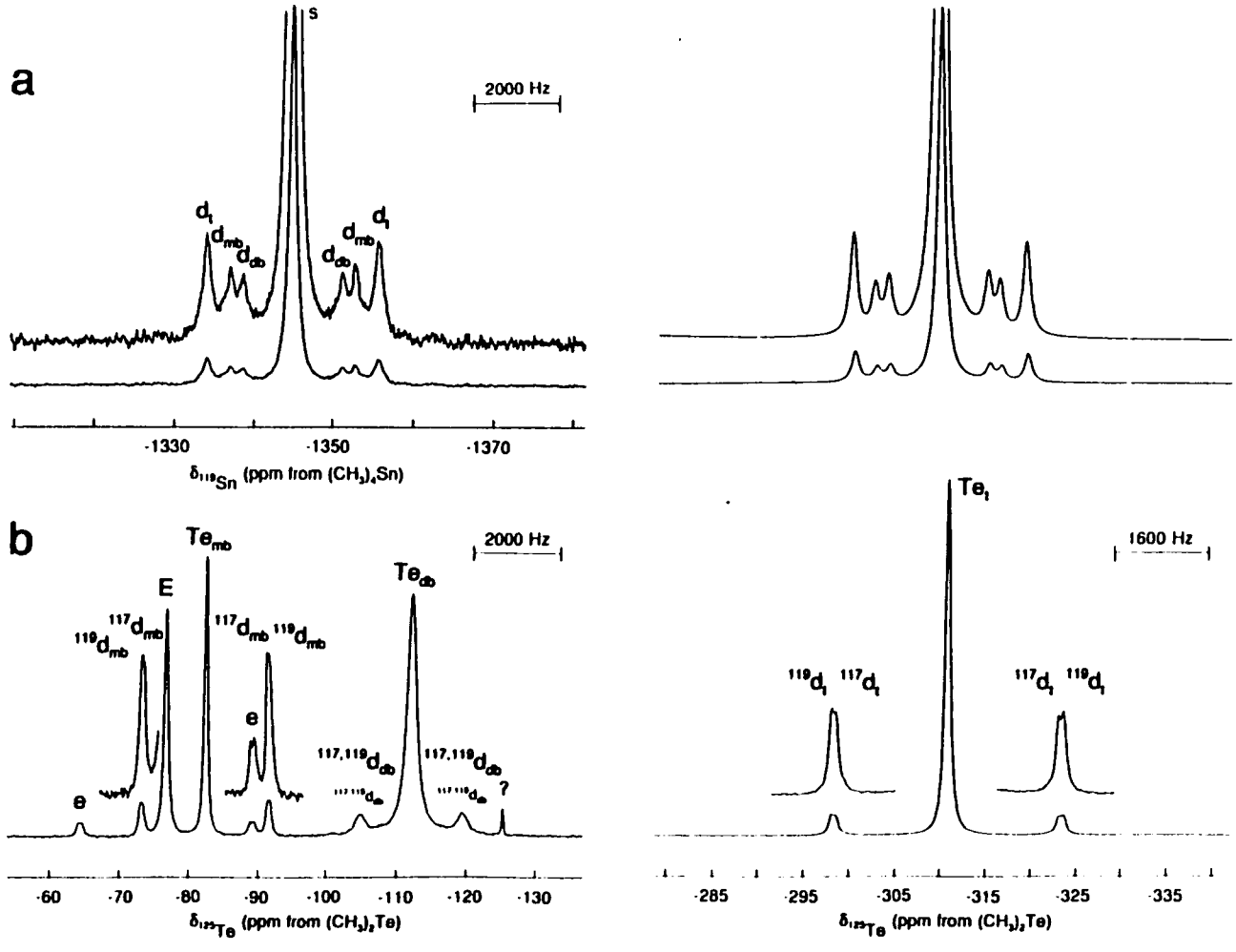
a
2000 Hz
S
d_t
d_{mb}
d_{db}
d_{db}
d_{mb}
d_t
-1330
-1350
-1370
δ_{119}Sn (ppm from $(CH_3)_4Sn$)
b
2000 Hz
Te_{mb}
E
Te_{db}
$^{119}d_{mb}$
$^{117}d_{mb}$
$^{117}d_{mb}$ $^{119}d_{mb}$
e
e
$^{117,119}d_{db}$
$^{117,119}d_{db}$
?
-60
-70
-80
-90
-100
-110
-120
-130
δ_{125}Te (ppm from $(CH_3)_2Te$)
Te_t
1600 Hz
$^{119}d_t$ $^{117}d_t$
$^{117}d_t$ $^{119}d_t$
-285
-295
-305
-315
-325
-335
δ_{125}Te (ppm from $(CH_3)_2Te$)

Table 3.1. Chemical Shifts and Satellite Intensities for the $SnCh_4^{4-}$, $Sn_2Ch_6^{4-}$, $Sn_2Ch_7^{4-}$, and $SnCh_3^{2-}$ (Ch = Se, Te) Anions.

	chemical shift (ppm)[a]			100 × Is/Ic [b]		
anion	^{119}Sn	^{125}Te	^{77}Se	Sn	Te	Se
$SnTe_4^{4-}$	−1824[c]	−203		15.5 (16.8)	9.1 (9.6)	
	−1749.8[d]	−281.8				
$Sn_2Te_6^{4-}$	−1675.0[c]	−89.3 (t)		6.2 (8.5)	17.2 (19.2)	
		458.3 (mb)		6.9 (8.5)	7.2 (9.6)	
$Sn_2Te_7^{4-}$	−1344.9[c]	−323.5 (t)		7.1 (8.5)	6.2 (9.6)	
		−95.1 (mb)		5.1 (4.3)	13.8 (19.2)	
		−124.8 (db)		4.6 (4.3)	10.3 (9.6)	
$SnTe_3^{2-}$	−1170[c]	−385		12.3 (11.3)	7.9 (9.6)	
	−1230.1[e]	−476.8				
	−1152.2[d]	−506.7				
$SnSe_4^{4-}$	−476.6[c]		−61.9			
$Sn_2Se_6^{4-}$	−499[f]		37.6 (t)			11.0 (9.6)
			295.1 (mb)			21.4 (19.2)
	−491.6[g]		9.2 (t)	7.2 (8.2)		
			266.4 (mb)	7.6 (8.2)		
$Sn_2Se_7^{4-}$	−388[f]		−58.1 (t)			20.1 (19.2)
			−30.2 (mb)			18.4 (19.2)
			116.8 (db)			10.0 (9.6)

Table 3.1. Continued.

anion	chemical shift (ppm)[a]			100 × Is/Ic[b]		
	^{119}Sn	^{125}Te	^{77}Se	Sn	Te	Se
$Sn_2Se_7^{4-}$	-328.4[g]		-88.8 (t)	7.4 (8.2)		
			-59.8 (mb)	3.8 (4.1)		
			106.4 (db)	3.5 (4.1)		
$SnSe_3^{2-}$	-264.3[c]		-92.16[c]			
	-299.5[g]		-91.0[g]			

[a] The symbols t, mb, and db denote the terminal chalcogen, monochalcogeno- and dichalcogeno-bridging environments.

[b] Calculated values are given in parentheses. [c] Recorded in en solvent (24 °C) containing a stoichiometric excess of 2,2,2-crypt with respect to K^+.[56 d,c] Recorded in NH_3 solvent (-70 °C) containing unsequestered Na^+ [K^+]. [f,g] Recorded in en [NH_3] solvent (0 [-50] °C) containing a K^+ : 2,2,2-crypt ratio of 1.00 : 0.42.

Table 3.2. Scalar, J, Reduced, K, and Relativistically Corrected Reduced, K_{RC}, Spin–Spin Coupling Constants for the $SnCh_4^{4-}$, $Sn_2Ch_6^{4-}$, $Sn_2Ch_7^{4-}$, and $SnCh_3^{2-}$ (Ch = Se, Te) Anions.[a]

	J (Hz)				K ($\times 10^{20}$ T^2 J^{-1})		K_{RC} ($\times 10^{20}$ T^2 J^{-1})	
anion	^{119}Sn–^{125}Te	^{117}Sn–^{125}Te	^{119}Sn–^{77}Se	^{117}Sn–^{77}Se	Sn–Te	Sn–Se	Sn–Te	Sn–Se
$SnTe_4^{4-}$	2851[b] 2960[c]	2727 2826			199.1 206.5		97.1 100.6	
$Sn_2Te_6^{4-}$ [d]	3998 (t) 1683 (mb)	3839 (t)			279.7 (t) 117.5 (mb)		136.4 (t) 57.3 (mb)	
$Sn_2Te_7^{4-}$ [d]	4023 (t) 2902 (mb) 2319 (db)	3946 (t)			284.5 (t) 202.6 (mb) 161.9 (db)		138.7 (t) 98.8 (mb) 80.0 (db)	
$SnTe_3^{2-}$	4535[b] 4487[d] 4376[c]	4335 4309			316.6 314.0 305.8		154.4 153.1 149.1	
$SnSe_4^{4-}$ [b]			1463	1398		169.8		103.1
$Sn_2Se_6^{4-}$			2014 (t)[e] 873 (mb)[e]			233.6 (t) 101.2 (mb)		141.9 (t) 61.5 (mb)
			2005 (t)[f] 888 (mb)[f]			232.5 (t) 103.0 (mb)		141.3 (t) 62.6 (mb)
$Sn_2Se_7^{4-}$ [g]			2045 (t)[e] 1306 (mb)[e] 1130 (db)[e]			237.2 (t) 151.4 (mb) 131.0 (db)		144.1 (t) 92.0 (mb) 62.6 (db)

Table 3.2. Continued.

	J (Hz)				K ($\times 10^{20}$ T^2 J^{-1})		K_{RC} ($\times 10^{20}$ T^2 J^{-1})	
anion	^{119}Sn–^{125}Te	^{117}Sn–^{125}Te	^{119}Sn–^{77}Se	^{117}Sn–^{77}Se	Sn–Te	Sn–Se	Sn–Te	Sn–Se
$Sn_2Se_7^{4-}$			2037(t)[f] 1324 (mb)[f] 1134 (db)[f]			236.2 (t) 153.5 (mb) 131.5 (db)		143.5 (t) 93.3 (mb) 80.0 (db)
$SnSe_3^{2-}$ [b]			2051			237.8		144.5

[a] The symbols t mb, and db denote the terminal chalcogen, monochalcogeno-, and dichalcogeno-bridging environments. [b] Recorded in en solvent (24 °C) containing a stoichiometric excess of 2,2,2-crypt with respect to K$^+$.[56] [c,d] Recorded in NH_3 solvent (–70 ° C) containing unsequestered Na$^+$ [K$^+$]. [e,f] Recorded in en [NH_3] solvent (0 [–50] °C) containing a K$^+$: 2,2,2-crypt ratio of 1.0 : 0.42. [g] $^2J(^{119}Sn–^{117}Sn)$ = 268 [302] Hz in en [NH_3] solvent (0 [–50] °C) containing a K$^+$: 2,2,2-crypt ratio of 1.0 : 0.42. The corresponding K, K_{RC} values are 16.60, 8.2 [18.70, 9.2] in en [NH_3] solvent.

number of overlapping peaks which precluded accurate satellite assignments and I_S/I_C determinations. Consequently, subsequent discussion of the NMR parameters refers to those obtained at –50 (^{119}Sn) and 0 °C (^{77}Se), although Table 3.1 lists the parameters obtained at both temperatures. Resonances observed in the ^{119}Sn NMR spectrum at –491.6 (57.0 %) and –328.4 ppm (15.0 %) were assigned to the $Sn_2Se_6^{4-}$ and $Sn_2Se_7^{4-}$ anions, respectively, and are discussed under their respective subheadings (*vide infra*). Resonances observed at –350.1 (27.0 %) and at –299.5 ppm (1.0 %) in the ^{119}Sn NMR spectrum were assigned to the novel adamantanoid $Sn_4Se_{10}^{4-}$ anion and to the known $SnSe_3^{2-}$ anion,[56] respectively. The structural characterization of the $Sn_4Se_{10}^{4-}$ anion by ^{77}Se and ^{119}Sn NMR spectroscopy, X-ray crystallography, and Raman spectroscopy is reported in Chapter 4. Selenium resonances were observed at 295.1 and 37.6 ppm for the $Sn_2Se_6^{4-}$ anion; at 116.8, –30.2, and –58.1 ppm for the $Sn_2Se_7^{4-}$ anion; at 65.0 and 22.2 ppm for the $Sn_4Se_{10}^{4-}$ anion; and at –91.0 ppm for the $SnSe_3^{2-}$ anion.

The ^{119}Sn and ^{125}Te NMR spectra of the dark red solution obtained by extracting $KSn_{0.63}Te_{1.70}$ in liquid NH_3 in the absence of 2,2,2-crypt (Chapter 2) were recorded at –70 °C (Figures 3.2 and 3.4). The signal at –1230.1 ppm (32.0 %[48]) in the ^{119}Sn NMR spectrum was assigned to the previously characterized trigonal-planar $SnTe_3^{2-}$ anion.[56] The ^{125}Te and the ^{123}Te satellites were well resolved [$^1J(^{119}Sn–^{125}Te)$ = 4487 Hz; $^1J(^{119}Sn–^{123}Te)$ = 3726 Hz], and the ratio $^1J(^{119}Sn–^{125}Te)/^1J(^{119}Sn–^{123}Te)$ = 1.204 (hereafter referred to as R_J) is in excellent agreement with the ratio $\gamma(^{125}Te)/\gamma(^{123}Te)$ = 1.206 (hereafter referred to as R_γ). In addition, the triplet subspectrum arising from coupling of the ^{119}Sn nucleus to two spin-active ^{125}Te

nuclei was observed. Three additional resonances were observed in the ^{119}Sn NMR spectrum at lower frequencies relative to the $SnTe_3^{2-}$ anion (–1675.0, 34.0 %; –1344.9, 28.0 %; and –1267.5 ppm, 6.0 %) and did not correspond to known species. The resonances at –1675.0 and –1344.9 ppm were assigned to the $Sn_2Te_6^{4-}$ and $Sn_2Te_7^{4-}$ anions, respectively, and are discussed under their respective subheadings (*vide infra*). The signal at –1267.5 ppm could not be assigned as ^{125}Te satellites were not observed. The ^{125}Te resonance of the $SnTe_3^{2-}$ anion was observed at –476.8 ppm, and the ^{125}Te signals associated with the ditin anions were observed at 458.3 and –89.3 ppm ($Sn_2Te_6^{4-}$) and at –323.5, –124.8, and –95.1 ppm ($Sn_2Te_7^{4-}$). The remaining weak resonances at –30.2, –137.9, and –161.2 ppm could not be assigned because ^{117,119}Sn satellites were not observed.

The ^{119}Sn and ^{125}Te NMR spectra (–70 °C) of the intense red liquid NH_3 extract of the $NaSn_{0.43}Te$ alloy in the absence of 2,2,2-crypt gave rise to two and four signals, respectively. The most intense signal in the ^{119}Sn NMR spectrum (–1749.8 ppm, 90.0 %) was assigned to the previously characterized tetrahedral $SnTe_4^{4-}$ anion.[56] The weaker signal (–1155.2 ppm, 10.0 %) consisted of a broad singlet flanked by a pair of ^{125}Te satellites [$^1J(^{119}Sn–^{125}Te)$ = 4376 Hz] and was assigned to the $SnTe_3^{2-}$ anion (see **The $SnCh_3^{2-}$ (Ch = Se, Te) Condensation Processes**). The ^{125}Te resonances of the $SnTe_4^{4-}$ [$^1J(^{125}Te–^{119}Sn)$ = 2960 Hz and $^1J(^{125}Te–^{117}Sn)$ = 2826 Hz; R_J = 1.045 and R_γ = 1.046)] and $SnTe_3^{2-}$ anions were observed at –281.8 and –506.7 ppm, respectively. The remaining weak signals in the ^{125}Te NMR spectrum (–370.4 and –591.9 ppm) could not be assigned.

Analysis of Spin–Spin Coupling Patterns. (a) $Sn_2Ch_6^{4-}$ (Ch = Se or Te). The ^{119}Sn

NMR spectrum of the $Sn_2Se_6^{4-}$ anion (Figure 3.1) consisted of a singlet (–491.6 ppm) flanked by two pairs of ^{77}Se satellites (d_{mb}, 888 Hz; d_t, 2005 Hz) in a 1.0 : 1.0 peak area ratio, indicating coupling to two chemically inequivalent selenium environments. In addition, four weaker satellites were observed in the ^{119}Sn NMR spectrum (d_t/d_{mb} in Figure 3.1) and their assignments are discussed below. The two associated selenium environments were observed in the ^{77}Se NMR spectrum at 295.1 and 37.6 ppm with a relative peak area ratio of 2.0 : 4.2. The I_S/I_C ratios of the accompanying tin satellites (Table 3.1) indicated that the two selenium environments were coupled to two and one tin atoms, respectively. These findings are consistent with the solid-state D_{2h} point symmetry of the $Sn_2Se_6^{4-}$ anion (see **X-ray Crystal Structures**). The ^{77}Se peaks at 295.1 and 37.6 ppm were assigned to the monoseleno-bridge, Se_{mb}, and terminal, Se_t, selenium environments of the anion, respectively. The smaller coupling was consequently assigned to $^1J(^{119}Sn–^{77}Se_{mb})$ and the larger to $^1J(^{119}Sn–^{77}Se_t)$. The coexistence of the $SnSe_3^{2-}$ and $Sn_2Se_6^{4-}$ anions implies that both anions are in equilibrium (eq. 3.1) and that the equilibrium is shifted toward the dimer under conditions allowing ion-pair

$$2SnSe_3^{2-} \rightleftharpoons Sn_2Se_6^{4-} \qquad (3.1)$$

formation (see **The $SnCh_3^{2-}$ (Ch = Se, Te) Condensation Processes**). This is noteworthy, because the $SnSe_3^{2-}$ anion is known as the only species in K/Sn/Se alloy extracts containing stoichiometric excesses of 2,2,2-crypt with respect to K^+.[56]

The ^{119}Sn and ^{125}Te NMR spectra of the $Sn_2Te_6^{4-}$ anion (Figure 3.2) were similar to those observed for the $Sn_2Se_6^{4-}$ anion. The ^{119}Sn NMR spectrum consisted of a singlet

(–1675.0 ppm) flanked by two sets of satellites arising from $^{1}J(^{119}Sn–^{125}Te)$ couplings (d_{mb}, 1683 Hz and d_t, 3998 Hz; peak area ratio, 1.1 : 1.0). The counterpart to the four weak satellites observed in the ^{119}Sn NMR spectrum of $Sn_2Se_6^{4-}$ were not observed for $Sn_2Te_6^{4-}$ because the NMR signals were broadened. The ^{125}Te resonances of $Sn_2Te_6^{4-}$ were observed at 458.3 (Te_{mb}) and at –89.3 ppm (Te_t) with a relative peak area ratio of 2.0 : 4.3.

(b) $Sn_2Ch_7^{4-}$ (Ch = Se or Te). The ^{119}Sn NMR spectrum of $Sn_2Se_7^{4-}$ (Figure 3.3) consisted of a singlet (–328.4 ppm) flanked by three sets of ^{125}Te satellites (d_{db}, 1134 Hz; d_{mb}, 1324 Hz; d_t, 2037 Hz) having relative peak areas of 1.0 : 1.2 : 2.1, which is consistent with coupling to three chemically distinct selenium environments. Satellites corresponding to a $^{2}J(^{119}Sn–^{117}Sn)$ coupling of 302 Hz were also observed in the ^{119}Sn NMR spectrum; this coupling is similar to that observed for $Sn_4Se_{10}^{4-}$ (342 Hz; Chapter 4). Comparable $^{2}J(^{119}Sn–^{117}Sn)$ values of 205, 235, and 263 Hz have been observed for the solution structures of the dimethyltin(IV) chalcogenides $[(CH_3)_2SnCh]_3$ (Ch = S, Se, Te), respectively.[115] The ^{77}Se signals corresponding to the three Se environments of $Sn_2Se_7^{4-}$ were observed at 116.8, –30.2 and –58.1 ppm, respectively (relative peak area ratio, 1.9 : 1.0 : 4.4). The I_S/I_C ratios of the accompanying ^{119}Sn satellites indicated that the Se environments were bonded to one, two and one Sn atoms, respectively. These findings are consistent with a ditin selenide anion, $Sn_2Se_7^{4-}$ (Structure **I**).

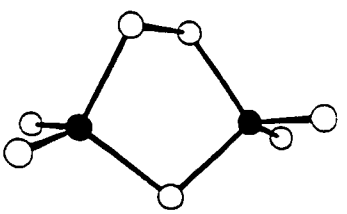

I

Although the crystal structure of the $Sn_2Se_7^{4-}$ anion is unknown, the telluride analog has been characterized by X-ray crystallography in $Cs_4Sn_2Te_7$.[116] The ^{77}Se peaks at 116.8, –30.2, and –58.1 ppm were assigned to Se_{db} (db, diseleno-bridge), Se_{mb}, and Se_t, respectively. The smallest coupling was consequently assigned to $^1J(^{119}Sn–^{77}Se_{db})$, the intermediate coupling to $^1J(^{119}Sn–^{77}Se_{mb})$, and the largest coupling to $^1J(^{119}Sn–^{77}Se_t)$.

By analogy with that of the $Sn_2Se_7^{4-}$ anion, the ^{119}Sn NMR spectrum of the $Sn_2Te_7^{4-}$ anion (Figure 3.4) consisted of a singlet (–1344.9 ppm) flanked by three pairs of ^{125}Te satellites (d_{db}, 2319 Hz, d_{mb}, 2902 Hz, and d_t, 4023 Hz with relative peak areas of 1.0 : 1.1 : 1.8). The ^{125}Te NMR spectrum consisted of three environments at –124.8 (Te_{db}), –95.1 (Te_{mb}), and –323.5 ppm (Te_t) with relative peak areas of 2.2 : 1.0 : 3.9.

Spectral Simulations. The ^{119}Sn NMR spectra of the $Sn_2Ch_6^{4-}$ and $Sn_2Ch_7^{4-}$ anions were simulated by using the natural abundances of the spin-½ nuclei ^{77}Se, ^{117}Sn, ^{119}Sn, and ^{125}Te;[74] the values of the observed coupling constants; and the total line intensities and multiplicities of the most abundant isotopomers (Tables 3.3 and 3.4) contributing significant first-order subspectra to the experimental ^{119}Sn NMR spectra. The resulting simulations (Figures 3.1–3.4) are in excellent agreement with the experimental spectra and account for all the observed satellite peaks. A singlet (S) is observed for the isotopomers in which no $^*Ch$ ($^*Ch$ = ^{77}Se or ^{125}Te) atoms are directly bonded to spin-active Sn atoms, namely, $^{119}Sn_xSn_{2-x}{}^*Ch_z{}^*Ch_{y-z}^{4-}$ [x = 1, 2; y = 6 ($Sn_2Ch_6^{4-}$), 7 ($Sn_2Ch_7^{4-}$); z = 0–2]. When one $^*Ch$ atom is in a terminal or bridging position directly bonded to a ^{119}Sn atom, a doublet (d_t, d_{mb}, or d_{db}) results which is symmetrically disposed about the central singlet (S) at a spacing

Table 3.3. Natural Abundance Isotopomers and Subspectra Used to Simulate the ^{119}Sn NMR Spectra of the $Sn_2Ch_6^{4-}$ (Ch = Se, Te) Anions.

$^{119}Sn_x{}^{117}Sn_y Sn_{2-x-y}{}^*Ch_z Ch_{6-z}{}^{4-}$ [a]			total intensity [b]		
x	y	z	Se	Te	subspectrum multiplicity [c]
1	0	0	8.962	8.880	S
1	0	1	1.470	1.501	S
1	0	1	1.470	1.501	d_t
1	0	1	1.470	1.501	d_{mb}
1	0	2	0.241	0.256	S
1	0	2	0.241	0.256	d_t
1	0	2	0.241	0.256	d_{mb}
1	0	2	0.060[d]	0.060[d]	d_t/d_{mb}[e]
1	1	0	0.814	0.799	D[f]
1	1	1	0.134	0.136	D[f]
1	1	1	0.134	0.136	D/d_t[f]
1	1	1	0.134	0.136	D/d_{mb}[f]
2	0	0	0.917	0.901	S
2	0	1	0.301	0.307	d_t
2	0	1	0.150	0.154	d_{mb}

[a] *Ch denotes ^{77}Se or ^{125}Te. [b] Natural abundances of spin-½ nuclides used to calculate isotopomer abundances were taken from ref. (74): ^{77}Se, 7.58%; ^{117}Sn, 7.61%; ^{119}Sn, 8.58%; ^{125}Te, 6.99%. The natural abundances of ^{115}Sn (0.35%) and ^{123}Te (0.87%) are too low to contribute detectable isotopomer subspectra and are combined with the spinless tin and nuclides, respectively. [c] S denotes a singlet; D denotes a DOUBLET arising from $^2J(^{119}Sn–^{117}Sn)$; and d_t and d_{mb} denote doublets arising from $^1J(^{119}Sn–^{77}Se_t)$ and $^1J(^{119}Sn–^{77}Se_{mb})$, respectively. The symbols D/d_t and D/d_{mb} denote DOUBLET-of-doublets, and d_t/d_{mb} denotes a doublet-of-doublets; see p. 86. [d] Isotopomers having multiplet line intensities below this value are too weak to be observed and are not included in the summation of the simulated subspectra. [e] Not observed for $Sn_2Te_6^{4-}$. [f] Not observed.

Table 3.4. Natural Abundance Isotopomers and Subspectra Used to Simulate the ^{119}Sn NMR Spectra of the $Sn_2Ch_7^{2-}$ (Ch = Se, Te) Anions.

$^{119}Sn_x{}^{117}Sn_ySn_{2-x-y}{}^*Ch_zCh_{7-z}{}^{2-}$ [a]			total intensity [b]		
x	y	z	Se	Te	subspectrum multiplicity [c]
1	0	0	8.283	8.109	S
1	0	1	2.038	2.075	S
1	0	1	1.359	1.383	d_t
1	0	1	0.679	0.692	d_{mb}
1	0	1	0.679	0.692	d_{db}
1	0	2	0.206	0.219	S
1	0	2	0.413	0.437	d_t
1	0	2	0.206	0.219	d_{mb}
1	0	2	0.206	0.219	d_{db}
1	1	0	0.752	0.736	D[d]
1	1	1	0.216	0.251	D/d_t[e]
1	1	1	0.108	0.126	D/d_{mb}[e]
1	1	1	0.108	0.126	D/d_{db}[e]
2	0	0	0.848	0.830	S
2	0	1	0.278	0.283	d_t
2	0	1	0.070[f]	0.071[f]	d_{mb}
2	0	1	0.139	0.142	d_{db}

[a] *Ch denotes ^{77}Se or ^{125}Te. [b] Natural abundances of spin-½ nuclides used to calculate isotopomer abundances were taken from ref. (74): ^{77}Se, 7.58%; ^{117}Sn, 7.61%; ^{119}Sn, 8.58%; ^{125}Te, 6.99%. The natural abundances of ^{115}Sn (0.35%) and ^{123}Te (0.87%) are too low to contribute detectable isotopomer subspectra and are combined with the spinless tin and nuclides, respectively. [c] S denotes a singlet; D denotes a DOUBLET arising from $^2J(^{119}Sn-^{117}Sn)$; and d_t and d_{mb} denote doublets arising from $^1J(^{119}Sn-^{77}Se_t)$ and $^1J(^{119}Sn-^{77}Se_{mb})$, respectively. The symbols D/d_t and D/d_{mb} denote DOUBLET-of-doublets, and d_t/d_{mb} denotes a doublet-of-doublets; see p. 86. [d] Not observed for $Sn_2Te_7^{2-}$. [e] Not observed. [f] Isotopomers having multiplet line intensities below this value are too weak to be observed and are not included in the summation of the simulated subspectra.

corresponding to $^1J(^{119}Sn–^{\bullet}Ch_t)$, $^1J(^{119}Sn–^{\bullet}Ch_{mb})$, or $^1J(^{119}Sn–^{\bullet}Ch_{db})$, respectively. The isotopomers, $^{119}Sn^{117}Sn^{\bullet}Ch_2Ch_{y-2}^{4-}$, give rise to a DOUBLET (D) resulting from $^2J(^{119}Sn–^{117}Sn)$ coupling when no $^{\bullet}Ch$ atoms are directly bonded to ^{119}Sn atoms. The presence of a $^{\bullet}Ch$ atom in a terminal (D/d_t), monochalcogeno (D/d_{mb})-, or dichalcogeno (D/d_{db})-bridging position directly bonded to a ^{119}Sn atom produces a DOUBLET-of-doublets whose transitions are symmetrically disposed about the binomial doublets d_t, d_{mb}, or d_{db}, respectively. The $^{119}Sn_xSn_{2-x}{}^{\bullet}Ch_2Ch_y^{4-}$ [y = 4 ($Sn_2Ch_6^{4-}$), 5 ($Sn_2Ch_7^{4-}$)] isotopomers result in a doublet-of-doublets (d_t/d_{mb}, d_t/d_{db}, or d_{mb}/d_{db}) when the $^{\bullet}Ch$ atoms are appropriately positioned and directly bonded to at least one ^{119}Sn atom, e.g., one $^{\bullet}Ch$ atom in a terminal position and one in a monochalcogeno-bridging position directly bonded to a ^{119}Sn atom produces a d_t/d_{mb} doublet-of-doublets. The transitions of the doublet-of-doublets are observed symmetrically disposed about the central singlet.

Scalar (J) and Reduced (K and K_{RC}) Coupling Constants. The scalar, J, the reduced, $^1K(Sn–Ch)$, and the relativistically corrected reduced, $^1K(Sn–Ch)_{RC}$, coupling constants for the $Sn_2Ch_6^{4-}$ and $Sn_2Ch_7^{4-}$ as well as for the previously characterized $SnCh_3^{2-}$ and $SnCh_4^{4-}$ anions[56] are listed in Table 3.2.

The large $^1K(Sn–Ch)_{RC}$ values for the $Sn_2Ch_6^{4-}$ and $Sn_2Ch_7^{4-}$ anions indicate a significant *s*-component to the bonding and contrast with the smaller values determined for the essentially pure *p*-bonded trigonal-bipyramidal $M_2Ch_3^{2-}$ [82] and $TlMTe_3^{3-}$ (Chapter 6) cages (M = Sn, Pb).The magnitudes of $^1K(Sn–Ch)_{RC}$ for the $Sn_2Ch_6^{4-}$ and $Sn_2Ch_7^{4-}$ anions can be correlated with the degree of hybridization at the Sn atoms, and hence the degree of *s*-

character in the Sn–Ch bonds, by comparison with analogous $^1K_{RC}$ values for the formally sp^2- and sp^3-hybridized $SnCh_3^{2-}$ and $SnCh_4^{4-}$ anions, respectively.[56] The $^1K(Sn–Ch)_{RC}$ values for $Sn_2Ch_6^{4-}$ and $Sn_2Ch_7^{4-}$ are similar to, but smaller than, those observed for the $SnCh_3^{2-}$ anions. The Sn hybrid orbitals involved in bonding to Ch_t can therefore be described as having less *s*-character than sp^2-hybrid orbitals. The larger $^1K(Sn–Ch)_{RC}$ values for Ch_t when compared to those for Ch_{mb} and Ch_{db} are consistent with higher relative bond orders in the $Sn–Ch_t$ bonds than in the $Sn–Ch_{mb}$ and $Sn–Ch_{db}$ bonds. This is reflected in the shorter $Sn–Ch_t$ bond distances [average: Se, 2.464(2) Å; Te, 2.669(5) Å] and longer $Sn–Ch_{mb}$ bond distances [average: Se, 2.590(4) Å; Te, 2.817(3) Å] observed for the $Sn_2Ch_6^{4-}$ anions (see **X-ray Crystal Structures**). The differences in the magnitudes of $^1K(Sn–Te)_{RC}$ determined for the $Sn_2Te_7^{4-}$ anion are also reflected in the $Sn–Te_t$ [2.683(3) Å], $Sn–Te_{mb}$ [2.808(2) Å], and $Sn–Te_{db}$ [2.800(2) Å] bond distances observed in $Cs_4Sn_2Te_7$.[116] The similarity between $^1K(Sn–Ch_{mb})_{RC}$ and $^1K(Sn–Ch)_{RC}$ for the $Sn_2Ch_7^{4-}$ and $SnCh_4^{4-}$ anions, respectively, suggests that the Sn(IV) orbitals involved in bonding to Ch_{mb} are essentially sp^3-hybridized. The smaller $^1K_{RC}$ values observed for $Sn–Ch_{mb}$ and $Sn–Ch_{db}$ in $Sn_2Ch_6^{4-}$ and $Sn_2Ch_7^{4-}$, respectively, indicate a substantial decrease in the *s*-character of the Sn hybrid orbitals. This is reflected in the $Ch_{mb}–Sn–Ch_{mb}$ bond angles [Se, 95.176(12)°; Te, 93.41(9)°] observed in the $Sn_2Ch_6^{4-}$ anions, which are considerably smaller than the ideal tetrahedral angle of 109.5° (see **X-ray Crystal Structures**).

Other than for $SnCh_3^{2-}$, $SnCh_4^{4-}$, and $Sn(Se_4)_3^{2-}$,[117] there is a lack of NMR data pertaining to classically-bonded Sn/Se or Sn/Te systems, and no scalar couplings have been

reported for the $Sn(Se_4)_3^{2-}$ anion. However, the magnitudes of $^1J(^{119}Sn–Ch_{mb})$ for $Sn_2Ch_6^{4-}$ and $Sn_2Ch_7^{4-}$ are comparable with those determined for substituted tin–chalcogen cages in which the tin atom environment is approximately tetrahedral and that about the chalcogens is bent: $[(CH_3)_2SnSe]_3$, $^1J(^{119}Sn–^{77}Se_b)$ = 1219 Hz; $[(CH_3)_2SnTe]_3$, $^1J(^{119}Sn–^{125}Te_b)$ = 3103 Hz.[115] Other compounds containing tetrahedral tin environments include $Sn(SePh)_4$ [$^1J(^{119}Sn–^{77}Se)$ = 1584 Hz] and $Sn(TePh)_4$ [$^1J(^{119}Sn–^{125}Te)$ = 3379 Hz].[118]

Chemical Shifts. The ^{119}Sn chemical shifts of the $Sn_2Ch_6^{4-}$ (Se, –491.6 ppm; Te, –1675.0 ppm) and $Sn_2Ch_7^{4-}$ (Se, –328.4 ppm; Te, –1344.9 ppm) anions appeared in the Sn(IV) region and were accompanied by the ^{119}Sn NMR resonances of the $SnCh_3^{2-}$ (Se, –299.5 ppm; Te, –1230.1 ppm). Similar ^{119}Sn chemical shifts have also been reported for the $SnCh_4^{4-}$, i.e., Se, –476.6 ppm and Te, –1749.8 ppm.[56] As expected, on the basis of the electronegativity difference between Se and Te,[119] the Sn resonances for the Se anions were more deshielded than those for the Te analogs.

For both the $Sn_2Ch_6^{4-}$ and $Sn_2Ch_7^{4-}$ anions, the signals corresponding to the terminal chalcogen, Ch_t, environments were found to be more shielded than the signals associated with the monochalcogeno-, Ch_{mb}, and dichalcogeno-bridging, Ch_{db}, environments (Table 3.1) and contrast with the order, $\delta(Se_t) > \delta(Se_{mb})$, observed for the $Sn_4Se_{10}^{4-}$ anion (Chapter 4). This difference can be rationalized using the rule of topological charge stabilization,[120] which predicts that the 4– charge of $Sn_4Se_{10}^{4-}$ is distributed over both the terminal and bridging atoms but is localized primarily on the terminal atoms in $Sn_2Ch_6^{4-}$ and $Sn_2Ch_7^{4-}$. For $Sn_2Se_7^{4-}$, the signal corresponding to Se_{mb} appeared at intermediate frequency, indicating a decrease

in the shielding of the different selenium environments in the order $Se_t > Se_{mb} > Se_{db}$. The monoseleno- and diseleno-bridges each formally contribute a charge of 2– to the anions as "Se^{2-}" and "Se_2^{2-}", respectively. The selenium chemical shift of Se_2^{2-} is therefore expected to be less shielded than that of Se^{2-}. Accordingly, the chemical shift difference (Δ_1) between $\delta(Se_t)$ and $\delta(Se_{mb})$ (27.9 ppm) was found to be significantly smaller than the corresponding difference (Δ_2) between $\delta(Se_t)$ and $\delta(Se_{db})$ (174.9 ppm). For $Sn_2Te_7^{4-}$, however, Δ_1 (228.4 ppm) was found to be comparable in magnitude to Δ_2 (198.7 ppm). The differences between the relative ^{77}Se and ^{125}Te chemical shift ranges are qualitatively consistent with the larger dynamic chemical shift range predicted for ^{125}Te by Ramsey's equation for nuclear shielding in which the paramagnetic term, σ^p, has a direct dependence on the radial term $\langle r^{-3} \rangle_{np}$ for the valence *p*-electrons (Chapter 1). However, the shielding order for $Sn_2Te_7^{4-}$ was found to be $Te_t > Te_{db} > Te_{mb}$ and is reversed relative to that of the Se analogs. The apparently anomolous chemical shift ordering may be attributed to shielding anisotropy (SA)[121] and may also account for the shielding order observed for the $Sn_4Se_{10}^{4-}$ anion (Chapter 4). However, in the absence of a knowledge of the ^{77}Se and ^{125}Te shielding tensors, the apparent anomalies in the ^{77}Se and ^{125}Te shielding trends are presently not fully understood.

The $SnCh_3^{2-}$ (Ch = Se, Te) Condensation Processes. Krebs and coworkers[48–54] observed a correlation between basicity and the extent of oligomerization of simple monomeric tin(IV) sulfide anions in aqueous solutions. For example, the monomeric SnS_4^{4-} anion was obtained from a strongly basic aqueous solution (pH = 11–12)[51] whereas the more condensed $Sn_2S_6^{4-}$ anion was obtained from a less basic solution (pH = 9–9.5).[50] The higher

charge density of the smaller SnS_4^{4-} anion apparently renders it more basic and a better proton acceptor than $Sn_2S_6^{4-}$ and consequently requires a more basic medium for its stabilization. A similar correlation was also observed in the study of the GeS_4^{4-}, $Ge_2S_6^{4-}$, $Ge_2S_7^{4-}$, and $Ge_4S_{10}^{4-}$ anions in aqueous solutions.[54] In view of these results, the influence of ion-pair formation on the condensation of the $SnCh_3^{2-}$ (Ch = Se, Te) and $SnTe_4^{4-}$ anions in basic, non-aqueous solvents was investigated. This was accomplished by varying the relative amounts of unsequestered M^+ (M = Na, K) present in en or liquid NH_3 solutions of these anions.

Solutions obtained by extraction of the alloys $KSnCh_2$ (Ch = Se, Te) and NaSnTe in en in the presence of a stoichiometric excess of 2,2,2-crypt have been shown by multi-NMR spectroscopy to contain only the $SnCh_3^{2-}$ and $SnTe_4^{4-}$ anions, respectively.[56] This study initially consisted of a systematic investigation by ^{119}Sn and ^{77}Se NMR spectroscopy of the extent of $SnSe_3^{2-}$ condensation in the presence of a non-stoichiometric amount of 2,2,2-crypt with respect to K^+. The en and liquid NH_3 extracts of the alloy $KSn_{0.67}Se_{1.93}$ containing a K^+ : 2,2,2-crypt stoichiometry of 1.00 : 0.42 were shown to contain the less basic $Sn_2Se_6^{4-}$, $Sn_2Se_7^{4-}$, and $Sn_4Se_{10}^{4-}$ anions as major species along with small amounts of the highly basic $SnSe_3^{2-}$ anion. This is consistent with the observation that the $Ge_2S_6^{4-}$ anion is always found in equilibrium with the $Ge_2S_7^{4-}$ and $Ge_4S_{10}^{4-}$ anions in strongly basic aqueous media.[54] The findings are supported by the X-ray crystal structure determinations of the $Sn_2Se_6^{4-}$ (*vide infra*) and $Sn_4Se_{10}^{4-}$ (Chapter 4) anions which were isolated from en extracts of the $KSn_{0.67}Se_{1.93}$ alloy. Nuclear magnetic resonance spectra of the liquid NH_3 extract of

$KSn_{0.63}Te_{1.70}$ in the absence of 2,2,2-crypt established the presence of $Sn_2Te_6^{4-}$ and $Sn_2Te_7^{4-}$ in solution along with comparable amounts of $SnTe_3^{2-}$. No conclusive evidence was found for the $Sn_4Te_{10}^{4-}$ anion. The liquid NH_3 extract of the alloy $NaSn_{0.43}Te$ in the absence of 2,2,2-crypt was shown to contain primarily the $SnTe_4^{4-}$ anion along with a small amount of $SnTe_3^{2-}$.

Condensation of the monomeric $SnCh_3^{2-}$ anions can be viewed as the nucleophilic attack of a Ch atom of one monomer on the Sn center of another and is sterically favored by the trigonal-planar (D_{3h}) geometry of the anions. The lack of condensation of the $SnTe_4^{4-}$ anion may be a consequence of the more sterically crowded tetrahedral environment as well as the higher anion charge. This process can also be rationalized in terms of ion-pairing and charge stabilization in the monomeric and oligomeric anions. Condensation according to eq. 3.2 results in the localization of the 4– charge at the Ch_t positions of the more condensed

$$n SnCh_3^{2-} (+ M^+) \rightleftharpoons SnCh_3^{2-} + Sn_2Ch_6^{4-} + Sn_2Ch_7^{4-} + Sn_4Ch_{10}^{4-} (+ M^+) \qquad (3.2)$$

anions. Formally, the charge per Ch_t atom is 1– in the oligomeric anions and ⅔– in $SnCh_3^{2-}$. The unsequestered M^+ cations strongly ion-pair with (a) the Ch atoms of $SnCh_3^{2-}$, reducing anionic–anionic repulsions and allowing the monomeric species to condense; and (b) the Ch_t atoms of the more condensed species, stabilizing the higher formal charges on these atoms. In essence, the M^+ cation plays the role of a proton in the condensation of the $SnCh_3^{2-}$ anions (cf. the condensation of SnS_4^{4-} and GeS_4^{4-} as a function of pH in aquous solutions; see above). The larger oligomeric : monomeric anion ratio observed in the Sn/Se system when

compared to that of the Sn/Te system can be explained in terms of the electronegativity difference between Se and Te.[119] The higher electronegativity of Se when compared to that of Te renders the Sn–Se bond more ionic and enhances the formation of oligomers by means of nucleophilic attack, and may account for the formation of the $Sn_4Ch_{10}^{4-}$ tetramer in the Sn/Se system but not in the Sn/Te system.

The differences between the present and previously reported[56] $\delta(^{119}Sn)$, $\delta(^{125}Te)$, and $^1J(^{119}Sn–^{125}Te)$ values for the $SnTe_3^{2-}$ anion (Table 1) can be attributed to strong ion-pairing between M^+ and $SnTe_3^{2-}$. Ion-pairing leads to deshielding of the Sn centre and shielding of the Te nucleus as well as to a decrease in $^1J(^{119}Sn–^{125}Te)$, indicating removal of *s*-electron density from the Sn–Te bonds. Moreover, $^1J(^{119}Sn–^{125}Te)$ was noted to be a function of ion-pairing and decreased according to the polarizing ability of M^+, i.e., $^1J(^{119}Sn–^{125}Te)$ decreased in the order 2,2,2-crypt-K^+···$[SnTe_3^{2-}]$ (negligible ion-pairing) > $[K^+···SnTe_3^{2-}]$ > $Na^+···[SnTe_3^{2-}]$. A similar trend in $\delta(^{119}Sn)$ and $^1J(^{119}Sn–^{117}Sn)$ was noted for the series of cluster anions $Sn_{9-n}Pb_n^{4-}$ and $Sn_{9-n}Ge_n^{4-}$ ($n = 0 – 8$) in en solutions containing unsequestered alkali-metal cations.[122]

The ^{119}Sn and ^{125}Te NMR spectra (–70 °C) of the $SnTe_3^{2-}$ anion in liquid NH_3 extracts of M/Sn/Ch (M = Na, K) alloys containing no 2,2,2-crypt were recorded at 11.744 and 7.0463 T and gave rise to significantly larger line widths ($\nu_{1/2}$) at the higher field strength (B_o), i.e., 75.5 (^{119}Sn) and 62.5 Hz (^{125}Te) at 11.744 T compared with 55.5 (^{119}Sn) and 32.8 Hz (^{125}Te) at 7.0463 T. This indicates that relaxation by means of the shielding anisotropy (SA) mechanism,[121] which varies with B_o^2 [$(11.744\ T)^2/(7.0463\ T)^2 = 2.78$], makes a significant

contribution to the relaxation mechanism of ^{119}Sn [(75.5 Hz)/(55.5 Hz) = 1.36] and of ^{125}Te [(62.5 Hz)/(32.8 Hz) = 1.91] in $SnTe_3^{2-}$. The influence of ion-pairing on line broadening is also known[71] and may also have contributed to the broadening of the ^{119}Sn and ^{125}Te signals of the $SnTe_3^{2-}$ anion by means of chemical exchange and/or other relaxation mechanisms.

Structural Characterization of the $Sn_2Ch_6^{4-}$ (Ch = Se, Te) and $HOSnTe_3^{3-}$ Anions by X-ray Crystallography.

A summary of the crystal data and the refinement results for $(K^+)_2$(18-crown-6-$K^+)_2Sn_2Se_6^{4-}$·4en (**1**), $(K^+)_2$(2,2,2-crypt-$K^+)_2Sn_2Te_6^{4-}$ (**2**), K^+(2,2,2-crypt-$K^+)_2HOSnTe_3^{3-}$ (**3**) and K^+(2,2,2-crypt-$K^+)_2HOSnTe_3^{3-}$·en (**4**) is given in Table 3.5. The final atomic coordinates and equivalent isotropic thermal parameters for the anion and K atoms are summarized in Table 3.6. The most significant bond distances and angles in the $Sn_2Ch_6^{4-}$ (Ch = Se, Te) anions, the long contact distances in the $K^+\cdots Sn_2Ch_6^{4-}$ units, and the significant bond distances and angles in the $HOSnTe_3^{3-}$ anion are listed in Table 3.7. Table 3.8 lists the Sn···Sn, Sn–Ch_{mb}–Sn, Ch_{mb}–Sn–Ch_{mb}, and Ch_t–Sn–Ch_t parameters observed in the present and previously characterized $Sn_2Ch_6^{4-}$ (Ch = Se, Te) anions.

In the four compounds, the structures of the 18-crown-6-K^+ and 2,2,2-crypt-K^+ cations are similar to those determined previously in K^+(18-crown-6-$K^+)_2GaTe_3^{2-}$,[123] K^+(2,2,2-crypt-$K^+)_3Pb_9^{4-}$,[29] and (2,2,2-crypt-$K^+)_2Sn_2Se_3^{2-}$ [82] with average K···O distances of 2.96(4) Å for (**1**) and average K···O, K···N distances of 2.82(2), 3.001(1) Å for (**2**) and 2.81(2) [2.81(1)], 2.96(2) [2.96(1)] Å for (**3**) [(**4**)].

Table 3.5. Summary of Crystal Data and Refinement Results for $(K')_2(18\text{-crown-6-}K')_2Sn_2Se_6^{4-}$ (**1**), $(K')_2(2,2,2\text{-crypt-}K')_2Sn_2Te_6^{4-}$ (**2**), $K'(2,2,2\text{-crypt-}K')_2HOSnTe_3^{3-}$ (**3**), and $K'(2,2,2\text{-crypt-}K')_2HOSnTe_3^{3-}\cdot en$ (**4**).

	(**1**)	(**2**)	(**3**)	(**4**)
formula	$C_{32}H_{80}N_8O_{12}K_4Sn_2Se_6$	$C_{32}H_{76}N_2O_{12}K_4Sn_2Te_6$	$C_{36}H_{73}N_4O_{13}K_3SnTe_3$	$C_{38}H_{81}N_6O_{13}K_3SnTe_3$
space group (No.)	$P2_1/c$ (15)	$P\bar{1}$ (2)	$P\bar{1}$ (2)	$P\bar{1}$ (2)
a, Å	15.634(2)	11.025(5)	11.670(2)	14.774(6)
b, Å	8.4790(10)	11.118(7)	12.977(4)	15.161(5)
c, Å	23.404(3)	17.137(9)	18.628(5)	16.744(5)
α, deg	90.00	95.09(5)	94.14(2)	71.25(3)
β, deg	108.600(10)	107.22(4)	106.21(2)	68.41(3)
γ, deg	90.00	109.49(4)	100.49(2)	62.41(3)
V, Å^3	2940.4(6)	1850.0(17)	2640.9(11)	3038.4(18)
Z	2	1	2	2
mol. wt.	1636.58	1912.36	1388.77	1448.88
ρ, g cm^{-3}	1.848	1.717	1.746	1.584
morphology	platelet	platelet	platelet	prism
dimensions, mm	0.35 × 0.32 × 0.12	0.29 × 0.26 × 0.35	0.39 × 0.19 × 0.28	0.43 × 0.21 × 0.30
colour	yellow	deep red	orange	deep red
refinement method	F^2	F^2	F^2	F^2
reflections used	7733	4510	10084	8256
reflections suppressed ($F^2 < -2\sigma F^2$)	61	45	25	0

Table 3.5. Continued.

	(1)	(2)	(3)	(4)
parameters refined	449	61	541	557
H-atom method	refined s.o.f., U_{eq}	calculated	calculated	calculated
R_1 ($F^2 > 2\sigma F^2$)	0.0298	0.1172	0.0554	0.0554
wR_2 (F^2)	0.0800	0.4022 [a]	0.1101	0.1758
S ($F^2 > 2\sigma F^2$)	1.033	0.880	1.179	1.243
$\Delta\rho_{max}$, e Å^{-3}	1.513	2.159	1.065	2.538
$\Delta\rho_{min}$, e Å^{-3}	–0.961	–1.562	–0.862	–0.666
w,	$w_1 = 0.0480$ $w_2 = 0.4810$	$w_1 = 0.2669$ $w_2 = 0.0000$	$w_1 = 0.0163$ $w_2 = 0.0000$	$w_1 = 0.0931$ $w_2 = 0.0000$

[a] The high wR_2 value is a consequence of the severe disorder in the 2,2,2-crypt-K$^+$ cations; see Chapter 2, pp. 56–57.

Table 3.6. Atomic Coordinates and Equivalent Isotropic Thermal Parameters ($Å^2$) for the Anions and K atoms in $(K^+)_2$(18-crown-6-$K^+)_2Sn_2Se_6^{4-}$ (**1**), $(K^+)_2$(2.2.2-crypt-$K^+)_2Sn_2Te_6^{4-}$ (**2**), K^+(2.2.2-crypt-$K^+)_2HOSnTe_3^{3-}$ (**3**), and K^+(2.2.2-crypt-$K^+)_2HOSnTe_3^{3-}$·en (**4**).

	x	*y*	*z*	U_{eq} [a]
		(**1**)		
Sn(1)	0.60652(1)	0.58420(2)	0.01318(1)	0.01411(5)
Se(1)	0.65022(2)	0.83161(3)	0.07053(1)	0.01900(6)
Se(2)	0.71568(2)	0.46461(3)	–0.02996(1)	0.02071(7)
Se(3)	0.54618(2)	0.37177(3)	0.07034(1)	0.01831(6)
K(1)	0.13731(4)	0.39529(7)	0.87592(3)	0.02054(11)
		(**2**)		
Sn(1)	0.4260(2)	0.4322(2)	0.8809(1)	0.066(1)
Te(1)	0.3619(2)	0.3365(2)	1.0166(1)	0.086(1)
Te(2)	0.5261(2)	0.2805(2)	0.8112(1)	0.082(1)
Te(3)	0.2250(2)	0.4925(3)	0.7847(1)	0.099(1)
K(1)	–0.1850(6)	–0.1651(6)	0.6377(3)	0.082(2)
K(2)	0.1770(11)	0.5493(14)	0.9924(6)	0.065(4)
		(**3**)		
Sn(1)	0.85392(5)	0.40879(5)	0.81703(3)	0.0221(2)
Te(1)	1.07879(5)	0.53474(5)	0.84824(4)	0.0319(2)
Te(2)	0.66705(5)	0.50640(5)	0.81437(4)	0.0304(2)
Te(3)	0.80958(5)	0.23173(5)	0.72204(3)	0.0285(2)
O(1)	0.8761(5)	0.3662(4)	0.9249(3)	0.0295(15)
K(1)	0.8342(2)	0.76665(14)	0.50943(10)	0.0248(4)
K(2)	0.6850(2)	0.86054(15)	0.93475(11)	0.0257(4)
K(3)	0.8954(2)	0.5836(2)	0.98600(11)	0.0326(5)
		(**4**)		
Sn(1)	0.02188(7)	0.15057(6)	0.29543(5)	0.0463(3)
Te(1)	–0.01466(8)	0.23815(7)	0.42741(6)	0.0654(3)
Te(2)	0.22836(7)	0.04087(7)	0.22759(6)	0.0632(3)
Te(3)	–0.11095(9)	0.24768(8)	0.19205(7)	0.0750(3)
O(1)	–0.0166(6)	0.0323(6)	0.3718(5)	0.057(2)
K(1)	0.3168(2)	0.5158(2)	0.1977(2)	0.0506(7)
K(2)	0.7701(2)	0.7848(2)	0.2414(2)	0.0515(7)
K(3)	0.8580(3)	0.0545(3)	0.5352(2)	0.0972(13)

[a] U_{eq} is defined as one-third of the trace of the orthogonalized U_{ij} tensor.

Table 3.7. Selected Bond Lengths (Å), Significant Long Contacts (Å), and Bond Angles (deg) for $(K^+)_2$(18-crown-6-K^+)$_2Sn_2Se_6^{4-}$ (**1**), $(K^+)_2$(2,2,2-crypt-K^+)$_2Sn_2Te_6^{4-}$ (**2**), K^+(2,2,2-crypt-K^+)$_2HOSnTe_3^{3-}$ (**3**), and K^+(2,2,2-crypt-K^+)$_2$-$HOSnTe_3^{3-}$·en (**4**).

(1)		(2)	
Sn(1)–Se(1)	2.4665(4)	Sn(1)–Te(1)	2.820(3)
Sn(1)–Se(2)	2.4616(4)	Sn(1)–Te(1A)	2.814(3)
Sn(1)–Se(3)	2.5941(4)	Sn(1)–Te(2)	2.674(3)
Sn(1)–Se(3A)	2.5852(5)	Sn(1)–Te(3)	2.664(3)
Sn(1)···Sn(1A)	3.4930(9)	Sn(1)···Sn(1A)	3.865(3)
K(1)···Se(1)	3.6946(7)	K(2)···Te(1)	3.580(11)
K(1)···Se(2)	3.7952(8)	K(2)···Te(2)	3.719(11)
K(2)···Se(1)	3.4534(8)	K(2)···Te(3)	3.778(11)
K(2)···Se(3A)	3.6030(8)		
K(2A)···Se(2)	3.5723(8)		
Sn(1)–Se(3)–Sn(1A)	84.823(12)	Sn(1)–Te(1)–Sn(1A)	86.59(9)
Se(3)–Sn(1)–Se(3A)	95.176(12)	Te(1)–Sn(1)–Te(1A)	93.41(9)
(3)		**(4)**	
Sn(1)–Te(1)	2.710(1)	Sn(1)–Te(1)	2.669(1)
Sn(1)–Te(2)	2.705(1)	Sn(1)–Te(2)	2.707(2)
Sn(1)–Te(3)	2.674(1)	Sn(1)–Te(3)	2.683(2)
Sn(1)–O(1)	2.081(5)	Sn(1)–O(1)	2.027(8)
Te(1)–Sn(1)–Te(2)	116.71(3)	Te(1)–Sn(1)–Te(2)	114.54(5)
Te(1)–Sn(1)–Te(3)	116.25(3)	Te(1)–Sn(1)–Te(3)	117.38(5)
Te(2)–Sn(1)–Te(3)	118.21(3)	Te(2)–Sn(1)–Te(3)	119.82(5)
O(1)–Sn(1)–Te(1)	96.1(2)	O(1)–Sn(1)–Te(1)	96.2(2)
O(1)–Sn(1)–Te(2)	96.1(2)	O(1)–Sn(1)–Te(2)	96.9(2)
O(1)–Sn(1)–Te(3)	107.6(2)	O(1)–Sn(1)–Te(3)	105.5(2)

Table 3.8. $Sn–Ch_t$, $Sn–Ch_{mb}$, and Sn···Sn Distances (Å) and $Sn–Ch_{mb}–Sn$, $Ch_{mb}–Sn–Ch_{mb}$, and $Ch_t–Sn–Ch_t$ Bond Angles (deg) Observed in Known $Sn_2Ch_6^{4-}$ Salts.[a]

Counter Cation	$Sn–Ch_t$	$Sn–Ch_{mb}$	Sn Sn	$Sn–Ch_{mb}–Sn$	$Ch_{mb}–Sn–Ch_{mb}$	$Ch_t–Sn–Ch_t$	Ref.
				$Sn_2Se_6^{4-}$			
$(K^+)_2$(18-crown-6-$K^+)_2$	2.464(2)	2.590(4)	3.4930(9)	84.823(12)	95.176(12)	117.748(12)	present work
$(enH^+)_2$(2,2,2-crypt-$K^+)_2$	2.460(8)	2.582(12)	3.557(1)	87.05(2)	92.95(2)	119.41(2)	60
$K^+(N(CH_3)^+)_3$	2.460(6)	2.598(6)	3.578(24)	87.1(5)	92.9(5)	118.53(3)	60
Na^+	2.470(5)	2.586(2)	3.529(25)	86.1(7)	93.9(7)	117.7(2.8)	61
K^+	2.461	2.588	3.514	85.5	94.5	121.2	62
Rb^+	2.462(3)	2.594(11)	3.518	85.4(1)	94.6(1)	120.1(1)	63
Cs^+	2.450(3)	2.587(1)	3.504(1)	85.26(5)	94.74(5)	118.91(6)	64
$(enH^+_2)_2$	2.460(9)	2.579(14)	3.480(1)	84.9(1)	95.1(1)	115.1(1)	65
				$Sn_2Te_6^{4-}$			
$(K^+)_2$(2,2,2-crypt-$K^+)_2$	2.669(5)	2.817(3)	3.865(3)	86.59(9)	93.41(9)	119.59(9)	present work
$N(CH_3)^+$	2.685(1)	2.809(4)	3.781(2)	84.6(2)	95.4(1)	113.7(1)	66
$N(C_2H_5)^+$	2.695(6)	2.779(5)	3.782(2)	85.0(1)	95.0(1)	120.5(1)	67
$Zn(en)_3^{2+}$	2.6824(6)	2.788(1)	3.786	85.53(3)	94.47(3)	113.62(3)	68

[a] The symbols t and mb denote the terminal chalcogen and monochalcogeno-bridging environments, respectively.

$Sn_2Ch_6^{4-}$ (Ch = Se, Te) (1) and (2). The crystal structures of compounds (**1**) and (**2**) consist of a centrosymmetric $Sn_2Ch_6^{4-}$ anion (Figures 3.5 and 3.7) bridging two symmetry-related unsequestered K^+ cations, forming layers of $K\cdots Sn_2Ch_6^{4-}\cdots K$. In the structure of the Te compound, the layers are well separated from the 2,2,2-crypt-K^+ cations, whereas in the structure of the Se analog, the layers are sandwiched between two symmetry-related 18-crown-6-K^+ cations and are bridged to these cations by en solvent molecules. The unsequestered K^+ cations in the Se compound are coordinated to additional en solvent molecules (Figure 3.6), completing a distorted octahedral environment about the K^+ atoms. The K···Se [K···Te] distances are in the range 3.4534(8)–3.7952(8) [3.580(11)–3.778(11)] Å and are longer than the sum of the K^+ ionic radius (1.33 Å)[124] and the Se [Te] van der Waals radius (2.0 [2.2] Å)[124] of 3.33 [3.53] Å. The K···K distance between the $K\cdots Sn_2Ch_6^{4-}\cdots K$ units is 4.241(2) [3.79(1)] Å in the Se [Te] compound, and the distance within a unit is 7.429(2) [7.48(1)] Å.

The structure of the $Sn_2Ch_6^{4-}$ anions (Ch = Se, Te) is based on two edge-sharing distorted $SnCh_4$ tetrahedra and is therefore isostructural with B_2H_6,[125] $W_2Se_6^{2-}$,[126] and $Ge_2Ch_6^{4-}$ (Ch = S,[53] Se[114,127]). Two distinct Sn–Ch bond distances are apparent in the structures, i.e., Sn–Ch_t and Sn–Ch_{mb}, and are slightly shorter or longer, respectively, than those found in the crystal structures of $SnCh_4^{4-}$ [Se, 2.494(1)–2.536(1) Å;[104] Te, 2.710(3)–2.819(2) Å[59]]. The average Sn–Ch_t distance [Se, 2.464(2) Å; Te, 2.669(5) Å] is significantly shorter than the average Sn–Ch_{mb} distances [Se, 2.590(4) Å; Te, 2.817(3) Å] and is consistent with the expected higher relative bond order of the Sn–Ch_t bonds. Similar

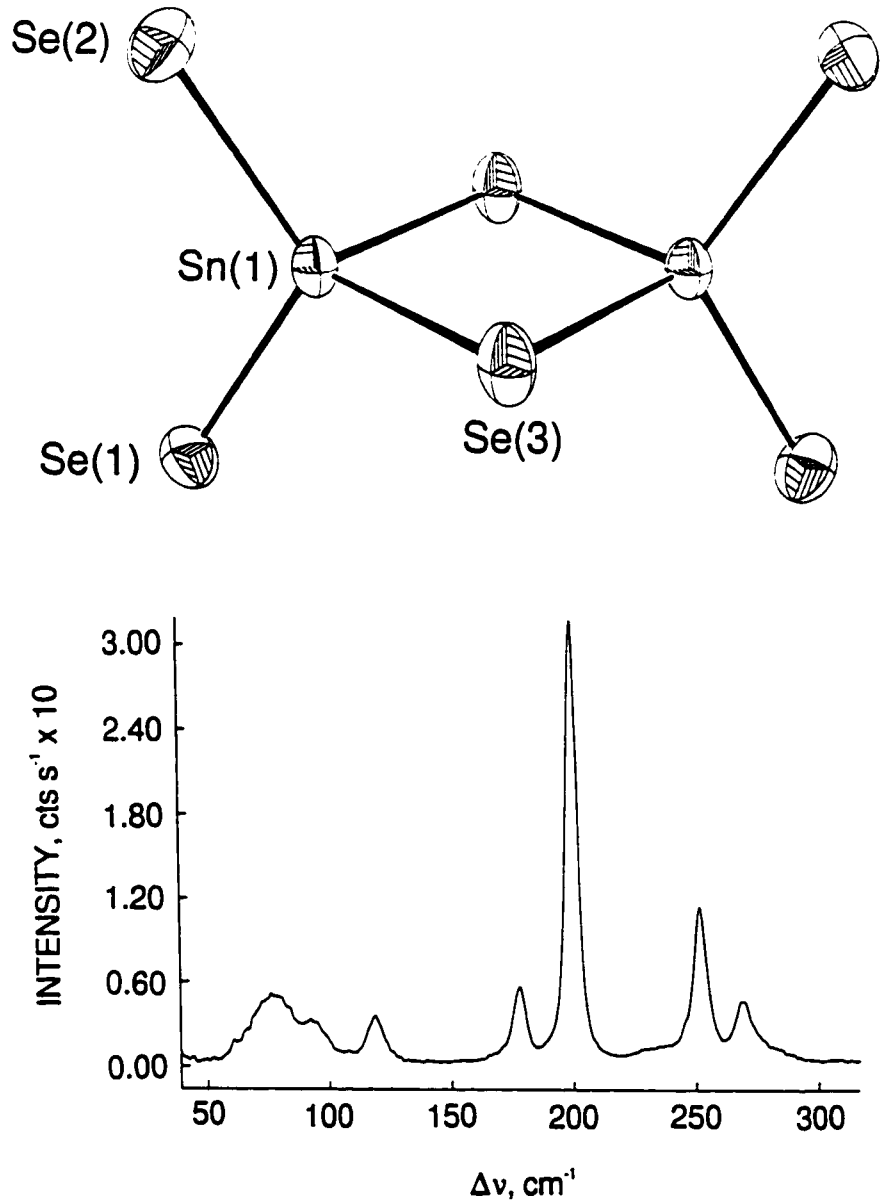

Figure 3.5. View and Raman spectrum of $Sn_2Se_6^{4-}$ in $(K^+)_2(18\text{-crown-6-}K^+)_2Sn_2Se_6^{4-}\cdot 4en$ with displacement ellipsoids drawn at the 70% probability level.

Figure 3.6. View of the (18-crown-6-K^+)···en···K^+(en)···$Sn_2Se_6^{4-}$···K^+(en)···en···(18-crown-K^+) structural unit in $(K^+)_2$(18-crown-6-K^+)$_2Sn_2Se_6^{4-}$·4en with displacement ellipsoids drawn at the 70% probability level. Hydrogen atoms have been omitted for clarity.

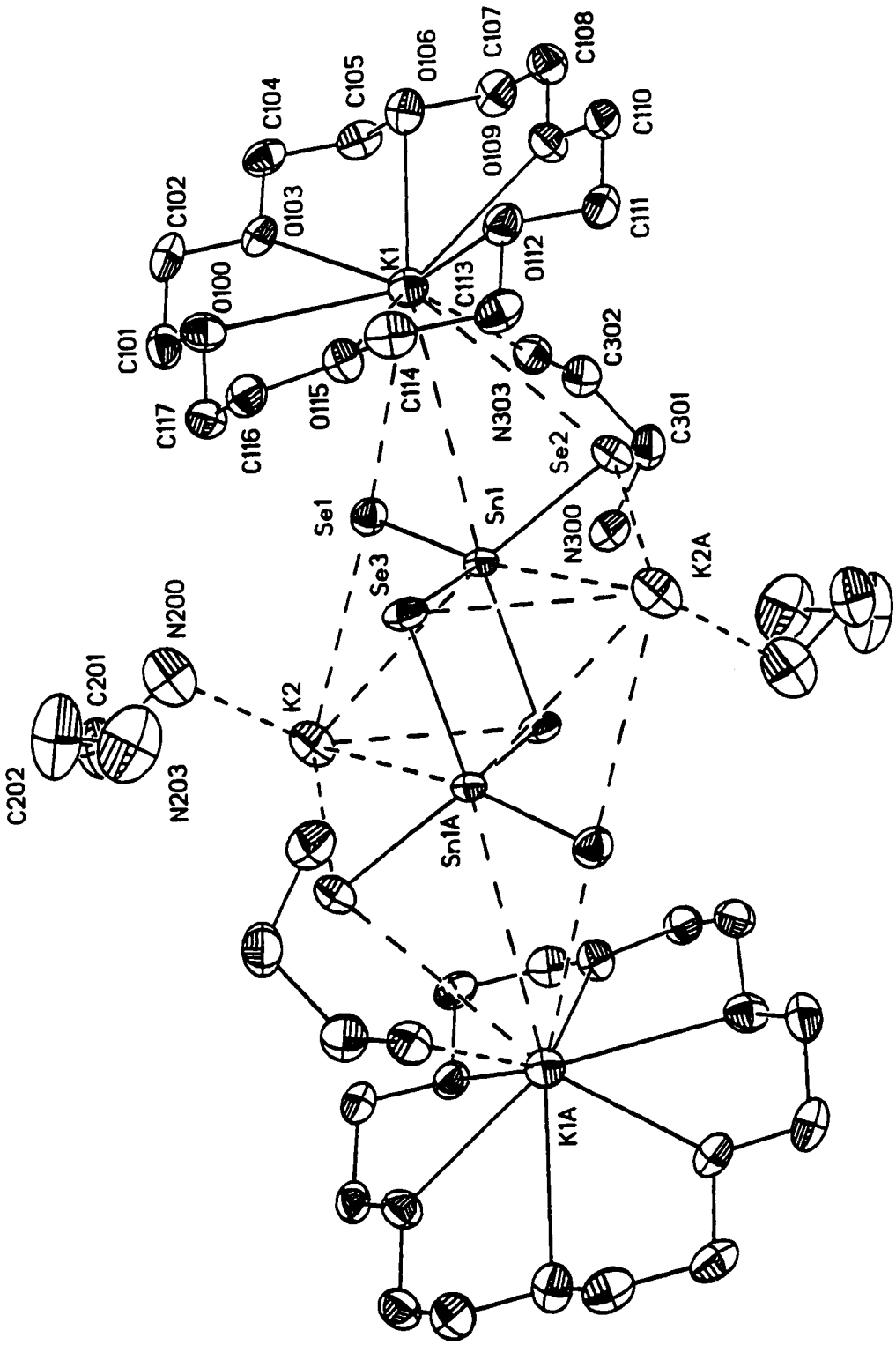
C107
C108
O106
C105
C104
C110
O109
C102
O103
C111
K1
O112
O100
C113
C101
C302
C114
O115
N303
C117
C116
C301
Se2
Se1
Sn1
N300
Se3
K2A
N200
C201
K2
C202
N203
Sn1A
K1A

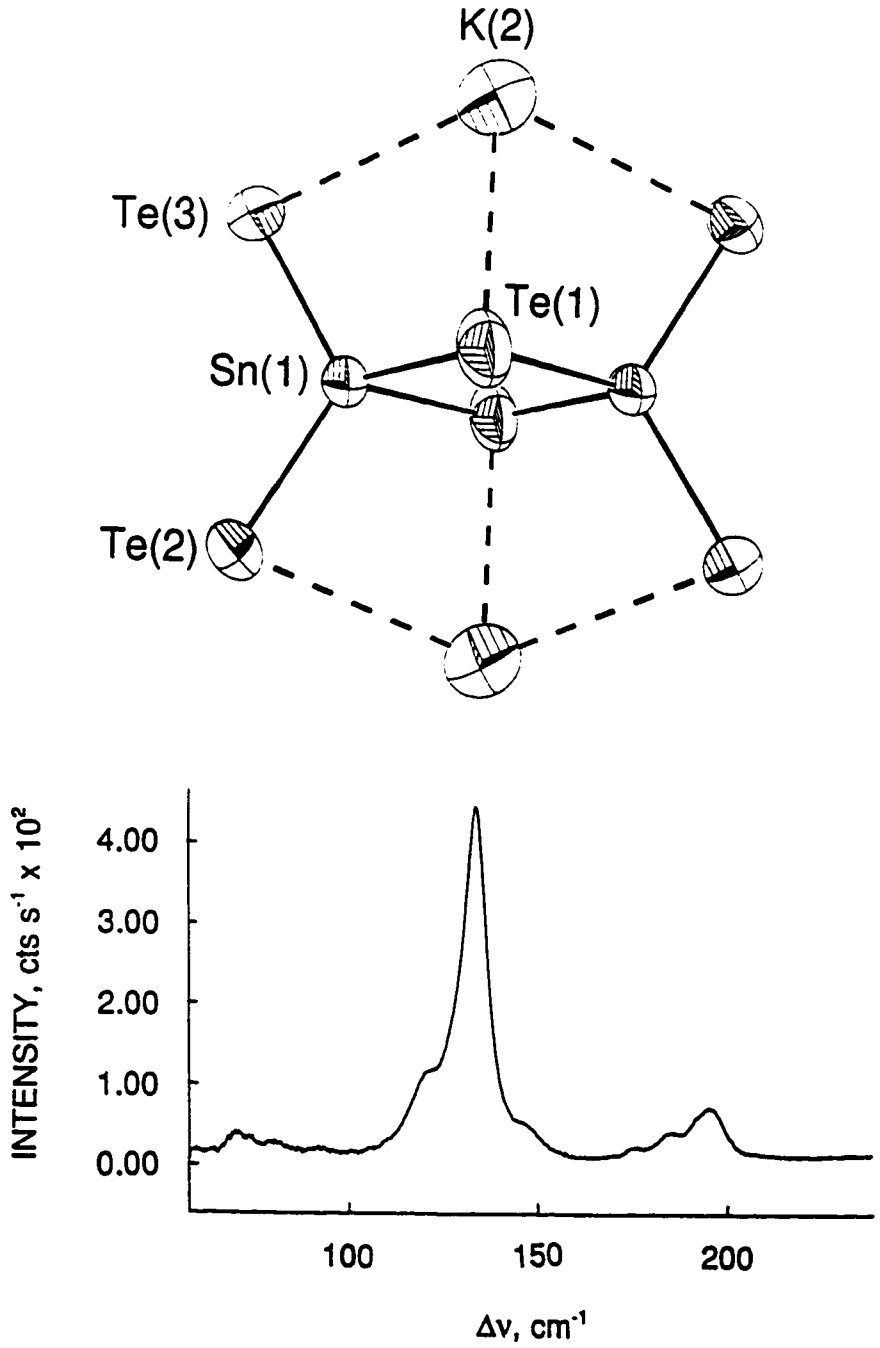

Figure 3.7. View and Raman spectrum of $Sn_2Te_6^{4-}$ in $(K^+)_2(2,2,2\text{-crypt-}K^+)_2Sn_2Te_6^{4-}$ with displacement ellipsoids drawn at the 30% probability level.

average Sn–Ch_t [Se, 2.461(3) Å; Te, 2.687(3) Å] and Sn–Ch_{mb} [Se, 2.590(3) Å; Te, 2.801(4) Å] bond distances have also been observed in the previously reported $Sn_2Ch_6^{4-}$ structures (Table 3.8). These distances correlate well with the larger $^1K(Sn–Ch_t)_{RC}$ and smaller $^1K(Sn–Ch_{mb})_{RC}$ couplings determined for the $Sn_2Ch_6^{4-}$ anions (see **Coupling Constants**).

In the present $Sn_2Se_6^{4-}$ anion structure, the Sn···Sn distances is 3.4930(9) Å and is significantly shorter than those observed in the previously characterized anions [average, 3.538(12) Å], and the Sn–Se_{mb}–Sn [84.823(12)°] and Se_{mb}–Sn–Se_{mb} [95.176(12)°] bond angles are significantly smaller and larger, respectively, than in the known structures (Table 3.8).[60–64] The Se_t–Sn–Se_t bond angle in the present $Sn_2Se_6^{4-}$ anion is similar only to that observed in $Na_4Sn_2Se_6 \cdot 13H_2O$.[61] In contrast, the Sn···Sn distance in the present $Sn_2Te_6^{4-}$ anion [3.865(3) Å] is significantly longer than those reported for the anion in the $N(CH_3)_4^+$,[66] $N(C_2H_5)_4^+$,[67] and $Zn(en)_3^{2+}$ [68]salts (Table 3.8). The present Sn–Te_{mb}–Sn and Te_{mb}–Sn–Te_{mb} bond angles are larger and smaller, respectively, than those observed in the previously reported structures (Table 3.8).

It should be noted that the $Sn_2Se_6^{4-}$ anion has also been characterized by X-ray crystallography in $(enH_2^{2+})_2Sn_2Se_6^{4-}$.[65] Although the Se_{mb}–Sn–Se_{mb} bond angle [95.1(1)°] in this compound is similar to that in the present anion, the Sn–Se_{mb}–Sn bond angle [84.91(1)°] is larger and the Sn···Sn distance, which is anticipated to be slightly larger, is actually shorter [3.480(1) Å] than in the present and in the previously reported structures (Table 3.8). The average Sn–Se_t and Sn–Se_{mb} distances in $(enH_2^{2+})_2Sn_2Se_6^{4-}$ are 2.460(9) and 2.579(14) Å, respectively, and are similar to those observed in the present and previously reported

structures.

$HOSnTe_3^{3-}$ (3) and (4). The $HOSnTe_3^{3-}$ anion was obtained during an attempt to obtain crystals of the trigonal-bipyramidal cage anion $TlSnTe_3^{3-}$ from an en solution prepared by reacting the alloys $Tl_2Sn_2Te_3$ and K_2Te (Chapter 6) in the presence of a stoichiometric excess of 2,2,2-crypt with respect to K^+. The en solution was shown by ^{119}Sn and ^{125}Te NMR spectroscopy to contain small amounts of the $Tl_2Te_2^{2-}$, $SnTe_3^{2-}$, and HTe^- anions as well as larger amounts of $TlSnTe_3^{3-}$ and a new Sn(IV)/Te anion. The structure of the new Sn(IV)/Te anion could not be determined, but the observed I_S/I_C intensity ratio and the magnitude of $^1K(Sn–Te)_{RC}$, 146.6 T^2J^{-1} x 10^{20}, which is comparable to the $^1K(Sn–Te)_{RC}$ value determined for $SnTe_3^{2-}$ (154.4 T^2J^{-1} x 10^{20}), suggested that the anion contains $SnTe_3$ units. Only the $HOSnTe_3^{3-}$ anion was characterized by X-ray crystallography in the crystalline material obtained from the en solution. It is therefore reasonable to speculate that the solution species is $HOSnTe_3^{3-}$.

Although the synthesis of the $HOSnTe_3^{3-}$ anion appears to be adventitious, reduction of 2,2,2-crypt by the strong reducing agent, K_2Te, has been noted before[71] and likely serves as a hydroxide source leading to the formation of compounds (3) and (4). Compounds (3) and (4) were obtained from a solution prepared by using a slight excess of 2,2,2-crypt with respect to K^+, yet both structures contain unsequestered K^+, which is consistent with attack on the cryptand.

The Sn–Te distances in the $HOSnTe_3^{3-}$ anion (Figure 3.8) range from 2.6735(11)–2.7103(11) [average, 2.696(11)] Å in (3) and 2.683(2)–2.707(2) [average, 2.696(7)] Å in (4).

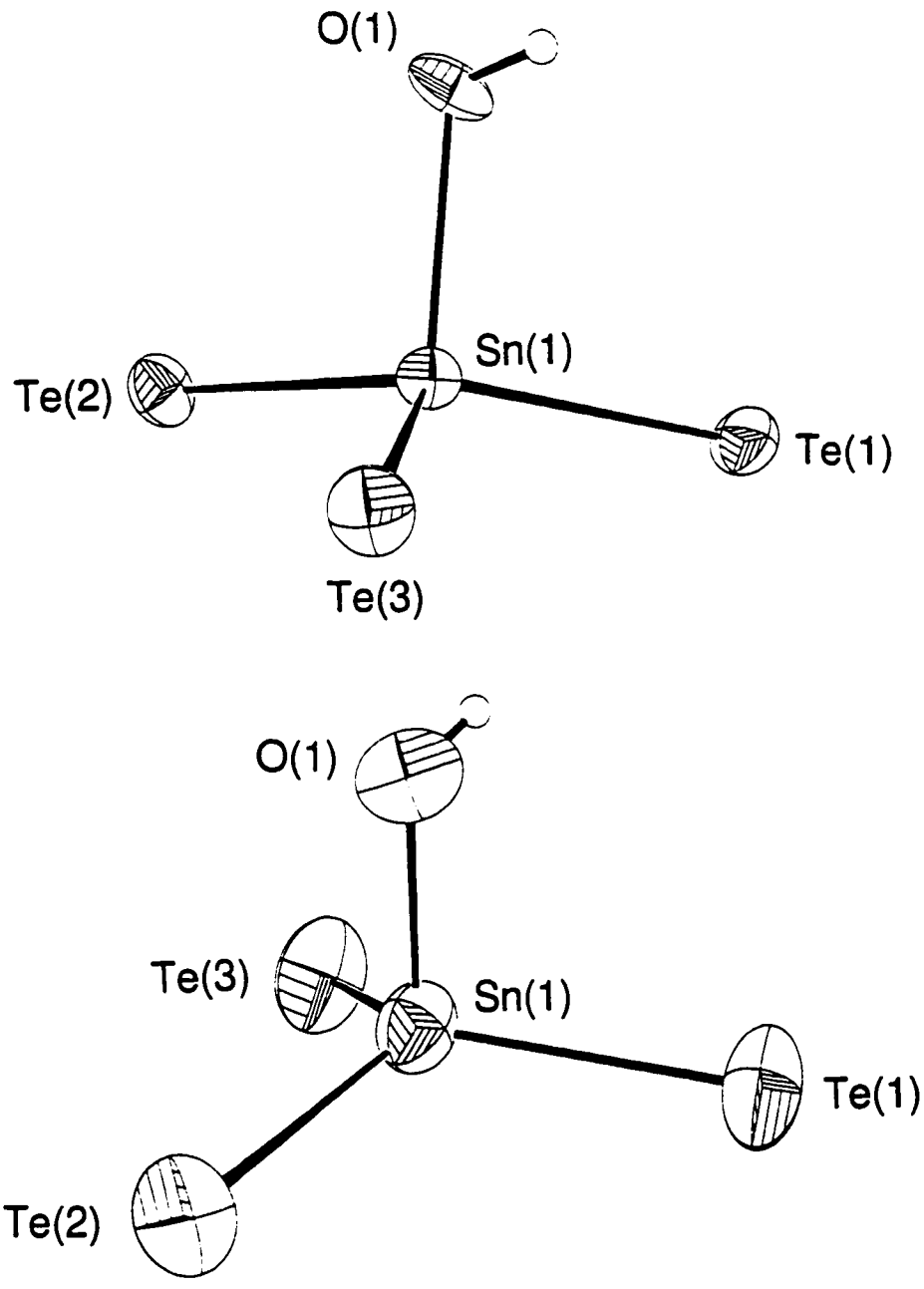

Figure 3.8. View of the $HOSnTe_3^{3-}$ anion in (a) $K^+(2,2,2\text{-crypt-}K^+)_2HOSnTe_3^{3-}$ and (b) $K^+(2,2,2\text{-crypt-}K^+)_2HOSnTe_3^{3-}\cdot en$ with displacement ellipsoids drawn at the 50% probability level.

The average Sn–Te bond distance is shorter than the average Sn–Te_t distance in $Sn_2Te_6^{6-}$ [2.727(2) Å][93] and those in $SnTe_4^{4-}$ [2.710(3)–2.819(2) Å][59] and is comparable to the average Sn–Te_t distance in $Sn_2Te_6^{4-}$ [2.669(5) Å] and in $Sn_2Te_7^{4-}$ [2.683(3) Å].[116] In addition, the present Sn–Te distances are shorter than the sum of the Te colavent radius (1.37 Å)[124] and the Sn(IV) metallic radius (1.399 Å)[124] of 2.77 Å. The Sn–O distance [2.081(5) Å in (**3**) and 2.027(8) Å in (**4**)] is longer than the average Sn–O bond distance [1.948(3) Å] observed in the crystal structure of Sn(O-*t*-Bu)$_4$,[128] but is comparable to the sum of the O single-bond covalent radius (0.66 Å)[124] and the Sn(IV) metallic radius (1.399 Å) of 2.06 Å. The Te–Sn–Te bond angles range from 116.25(3)–118.21(3)° in (**3**) and from 114.54(5)–119.82(5)° (**4**), and the Te–Sn–O bond angles are in the range 96.1(2)–107.6(2)° in (**3**) and 96.2(2)–105.5(2)° in (**4**).

The $HOSnTe_3^{3-}$ anion is the first example of a simple mixed hydroxytellurate anion of tin and is structurally related to $OWTe_3^{2-}$ [129] and is isostructural with $HOGeS_3^{3-}$.[91] The $HOSnTe_3^{3-}$ anion can be formally viewed as being obtained by the nucleophilic attack of OH^- on the Sn atom of the trigonal-planar (D_{3h}) $SnTe_3^{2-}$ anion. The nucleophilic attack induces a change in the hybridization of the Sn atom from pure sp^2 in the $SnTe_3^{2-}$ anion to ca. sp^3 in $HOSnTe_3^{3-}$ and is accompanied by a slight distortion of the D_{3h} geometry towards C_{3v} point symmetry (the tin atoms are 0.4677 (**3**) and 0.4519 Å (**4**) above the center of the plane containing the three Te atoms). This distortion is reflected in the magnitudes of the average Te–Sn–Te bond angles [117.1(6)° in (**3**) 117.2(1.5)° in (**4**)], which are smaller than the ideal D_{3h} angles of 120°. By analogy with the $Sn_2Ch_6^{4-}$ and $Sn_2Ch_7^{4-}$ (Ch = Se, Te) anions, the 3–

charge on the $HOSnTe_3^{3-}$ anion is expected to be concentrated on the Te atoms.

Structural Characterization of the $Sn_2Ch_6^{4-}$ (Ch = Se, Te) Anions by Raman Spectroscopy.

The solid-state Raman spectra of the $Sn_2Se_6^{4-}$ and $Sn_2Te_6^{4-}$ anions in $(K^+)_2$(18-crown-6-$K^+)_2Sn_2Se_6^{4-}$·4en and in $(K^+)_2$(2,2,2-crypt-$K^+)_2Sn_2Te_6^{4-}$, respectively, are shown in Figure 3.5 and 3.7. The observed frequencies and their assignments are summarized in Tables 3.9–3.10. The vibrational modes of the $Sn_2Se_6^{4-}$ and $Sn_2Te_6^{4-}$ anions were assigned under D_{2h} point symmetry and belong to the irreducible representations $4A_g + 2B_{1g} + 2B_{2g} + B_{3g} + A_u + 3B_{1u} + 2B_{2u} + 3B_{3u}$. A total of 18 vibrational bands are expected, of which nine modes (A_g, B_{1g}, B_{2g} and B_{3g}) are Raman active, eight modes are infrared active (B_{1u}, B_{2u} and B_{3u}), and the A_u mode is inactive.

$Sn_2Se_6^{4-}$. The Raman spectra of $Sn_2Se_6^{4-}$ in $Na_4Sn_2Se_6 \cdot 13H_2O$,[61] $(enH^+)_2$(2,2,2-crypt-$K^+)_2Sn_2Se_6^{4-}$,[60] and $K^+(N(CH_3)_4^+)_3Sn_2Se_6^{4-}$ [60] have been reported and are in agreement with the anion frequencies in $(K^+)_2$(18-crown-6-$K^+)_2Sn_2Se_6^{4-}$·4en. However, only six of the possible nine Raman-active anion modes could be observed for $Na_4Sn_2Se_6 \cdot 13H_2O$, and only the totally symmetric modes, $\nu_1(A_g)$ and $\nu_2(A_g)$, were assigned.[61] An unassigned Raman spectrum of $Sn_2S_6^{4-}$ in $Na_4Sn_2S_6 \cdot 14H_2O$ has also been reported.[130]

The $Sn_2Se_6^{4-}$ anion vibrational modes in $(enH^+)_2$(2,2,2-crypt-$K^+)_2Sn_2Se_6^{4-}$ and in $K^+(N(CH_3)_4^+)_3Sn_2Se_6^{4-}$ were assigned by analogy with those of Ga_2Br_6,[131] for which both the infrared and Raman spectra, including Raman polarization measurements, have been

Table 3:9. Raman Vibrational Frequencies and Assignments for the $Sn_2Se_6^{4-}$ anion in the 18-crown-6-K$^+$, $(enH^+)_2$(2,2,2-crypt-$K^+)_2$, and $K^+(N(CH_3)_4^+)_3$ Salts and for the Related Ga_2X_6 (X = Cl or Br) Molecules.[a,b]

frequencies (cm^{-1})					frequencies (cm^{-1})	
		$Sn_2Se_6^{4-}$				
Ga_2Cl_6 [c]	Ga_2Br_6 [d]	18-crown-6-K^+ [e]	$(enH^+)_2$(2,2,2-crypt-$K^+)_2$ [f]	assign.	$K^+(N(CH_3)_4^+)_3$ [f]	assign.
462(m)	339(0.2)	270(100)	270(20)	$\nu_{11}(B_{2g})$	280(13), 260(12)	$\nu_{11}(B_{2g})$, $\nu_8(B_{1u})$
413(s)	291(1.5)	251(38)	248(25)	$\nu_1(A_g)$	255(14), 249(12)	$\nu_1(A_g)$, $\nu_{16}(B_{3u})$, $\nu_{13}(B_{2u})$
243(w)	241(0.2)	~179	~185(sh)	$\nu_6(B_{1g})$		
318(mw)	204(6)	201(100)	202(100)	$\nu_2(A_g)$	200(100)	$\nu_2(A_g)$
215(sh)	158(0.2)	179(19)	179(15)	$\nu_{15}(B_{3g})$	178(7), 173(8)	$\nu_{15}(B_{3g})$, $\nu_{17}(B_{3u})$
167(m)	119(4)	119(12)	118(8)	$\nu_3(A_g)$	121(4), 118(6)	$\nu_3(A_g)$, $\nu_9(B_{1u})$
125(sh)	85(5.5)	~104(sh)	104(14)	$\nu_7(B_{1g})$	90(11), 75(13), 67(10), 62(7)	$\nu_4(A_g)$, $\nu_5(A_u)$, $\nu_7(B_{1g})$, $\nu_{12}(B_{2g})$, $\nu_{14}(B_{2u})$, $\nu_{18}(B_{3u})$
117(w)	74(10)	91(11)	87(8)	$\nu_{12}(B_{2g})$		
100(s)	64(?)	77(17)	74(14)	$\nu_4(A_g)$		

[a] Relative line intensities are given in parentheses. [b] Assignments are made under D_{2h} point symmetry. [c] Ref. (132). [d] Ref (131).

[e] Present work. [f] Ref (60).

Table 3.10. Raman Vibrational Frequencies and Assignments for the $Sn_2Te_6^{+-}$ Anion in $(K^+)_2(2,2,2\text{-crypt-}K^+)_2Sn_2Te_6^{+-}$ and for the Related In_2I_6 Molecule.[a,b]

In_2I_6 [c]		$Sn_2Te_6^{+-}$ [d]	
freq. (cm^{-1})	assign.	freq. (cm^{-1})	assign.
232(0.5)	$\nu_{11}(B_{2g})$	196(15)	$\nu_{11}(B_{2g})$
187(1.5)	$\nu_1(A_g)$	185(8)	$\nu_1(A_g)$
134(100)	$\nu_2(A_g)$	176(3)	unassigned
114(10)	$\nu_6(B_{1g})$	147(11, sh)	$\nu_6(B_{1g})$
69(5)	$\nu_3(A_g)$	134(100)	$\nu_2(A_g)$
55(1)	$\nu_7(B_{1g})$	121 (25, sh)	$\nu_{15}(B_{3g})$
49(8)	$\nu_{12}(B_{2g})$	92(3), 82(4), 71(8)	$\nu_3(A_g)$, $\nu_4(A_g)$, $\nu_7(B_{1g})$, $\nu_{12}(B_{2g})$
44(6.5)	$\nu_{15}(B_{3g})$		
40(0.5)	$\nu_4(A_g)$		

[a] Relative line intensities are given in parentheses. [b] Assignments are made under D_{2h} point symmetry. [c] Ref. (133). [d] Present work.

obtained and the assignments have been confirmed by a normal coordinate analysis.[134] A normal-coordinate analysis of Ga_2Cl_6 has been reported[132] and was also used to assign the anion vibrational modes in $(enH^+)_2(2,2,2\text{-crypt-}K^+)_2Sn_2Se_6^{4-}$ and in $K^+(N(CH_3)_4^+)_3Sn_2Se_6^{4-}$. The $Sn_2Se_6^{4-}$ vibrational modes in the 18-crown-6-K^+ salt were therefore assigned by direct analogy with the previously reported values.[60] A factor-group analysis was also performed for the present $Sn_2Se_6^{4-}$ anion structure. The correlations are given in Table 3.11 and indicate that each Raman band of the anion is split into an A_g and a B_g component (A_u and B_u in the infrared spectrum) under C_{2h} crystal symmetry. However, the splittings were too small to be resolved.

The $Sn_2Se_6^{4-}$ anion modes are shifted to lower frequency relative to those of Ga_2Cl_6 and Ga_2Br_6 by virtue of the reduced mass effect. The most intense peak (201 cm^{-1}) was assigned to the symmetric ring mode, $\nu_2(A_g)$. The symmetric terminal Sn–Se stretching mode, $\nu_1(A_g)$, is expected to be similar to the symmetric stretching mode, $\nu_1(A_1)$, of $SnSe_4^{4-}$ (239, 247 cm^{-1}) (Chapter 4) and was assigned to the band at 250 cm^{-1}. A similar trend has been noted for $Ge_2S_6^{4-}$ (416 cm^{-1})[53] and GeS_4^{4-} (417 cm^{-1}).[135] The symmetric deformation mode, $\nu_3(A_g)$, of the terminal $SnSe_2$ groups was assigned to the line at 118(8) cm^{-1}. The ring deformation mode, $\nu_4(A_g)$, was assigned to the line at 77 cm^{-1}. The asymmetric Sn–Se stretching mode, $\nu_6(B_{1g})$, is expected to be weak in the Raman spectrum and likely overlaps with the terminal $SnSe_2$ bending mode, $\nu_{15}(B_{3g})$, at 179 cm^{-1}. The highest frequency band at 270 cm^{-1} was assigned to the asymmetric Sn–Se terminal stretching mode, $\nu_{11}(B_{2g})$. The remaining torsional modes, $\nu_7(B_{1g})$ and $\nu_{12}(B_{1g})$, were assigned to bands at 104 and 91 cm^{-1},

Table 3.11. Correlation Diagrams for the Vibrational Modes of the $Sn_2Ch_6^{4-}$ (Ch = Se or Te) Anions in $(K^+)_2$(18-crown-6-K^+)$_2Sn_2Se_6^{4-}$·4en and in $(K^+)_2$(2,2,2-crypt-K^+)$_2Sn_2Te_6^{4-}$.[a]

$(K^+)_2$(18-crown-6-K^+)$_2Sn_2Se_6^{4-}$·4en ($P2_1/c$, Z = 2)

	mol. symm.	site symm.	crystal symm.	
	D_{2h}	C_1	C_{2h}	
$2\nu_1 - 2\nu_4$	A_g			
$2\nu_5 - 2\nu_6$, 2R	B_{1g}	A_g	A_g (R)	$\nu_1 - \nu_9$ 3R
$2\nu_7 - 2\nu_8$, 2R	B_{2g}			
$2\nu_9$, 2R	B_{3g}		B_g (R)	$\nu_1 - \nu_9$, 3R
$2\nu_{10}$	A_u			
$2\nu_{11} - 2\nu_{13}$, 2T	B_{1u}	A_u	B_u (IR)	$\nu_{10} - \nu_{11}$, 3T
$2\nu_{14} - 2\nu_{15}$, 2T	B_{2u}			
$2\nu_{16} - 2\nu_{18}$, 2T	B_{3u}		A_u (IR)	$\nu_{10} - \nu_{18}$, 3T

$(K^+)_2$(2,2,2-crypt-K^+)$_2Sn_2Te_6^{4-}$ ($P\bar{1}$, Z = 1)

	mol. symm.	site symm.	crystal symm.	
	D_{2h}	C_1	C_i	
$\nu_1 - \nu_4$	A_g			
$\nu_5 - \nu_6$, R	B_{1g}	A_g	A_g (R)	$\nu_1 - \nu_9$, 3R
$\nu_7 - \nu_8$, R	B_{2g}			
ν_9, R	B_{3g}			
ν_{10}	A_u			
$\nu_{11} - \nu_{13}$, T	B_{1u}	A_u	A_u (IR)	$\nu_{10} - \nu_{18}$, 3T
$\nu_{14} - \nu_{15}$, T	B_{2u}			
$\nu_{16} - \nu_{18}$, T	B_{3u}			

[a] R and T denote rotatory and translatory (external) modes, respectively, and (R) and (IR) denote Raman and infrared activity, respectively.

respectively. It should be noted that while the A_g, B_{1g}, B_{2g} and B_{3g} anion modes in the $K^+(N(CH_3)_4^+)_3Sn_2Se_6^{4-}$ salt are in agreement with those observed in the 18-crown-6-K^+ and $(enH^+)_2$(2,2,2-crypt-K^+)$_2$ salts, additional modes were observed in the Raman spectrum of the $K^+(N(CH_3)_4^+)_3$ salt and were assigned to the formally Raman inactive (infrared active) modes $\nu_5(A_u)$, $\nu_8(B_{1u})$, $\nu_9(B_{1u})$, $\nu_{13}(B_{2u})$, $\nu_{14}(B_{2u})$, $\nu_{16}(B_{3u})$, $\nu_{17}(B_{3u})$ and $\nu_{18}(B_{3u})$, which become Raman active under the C_i crystal symmetry of the salt. Tentative assignments of the additional modes were based on the frequency ordering of the infrared active modes in Ga_2Br_6 and are given in Table 3.9.

$Sn_2Te_6^{4-}$. The spectrum of the $Sn_2Te_6^{4-}$ anion consists of several overlapping bands and is attributed to the similarity in the masses of tin and tellurium. Moreover, because of the small mass difference, the vibrational modes are expected to be even more strongly coupled than in $Sn_2Se_6^{4-}$. A factor-group analysis has been performed by using the site symmetry, C_1, of the $Sn_2Te_6^{4-}$ anions within the primitive unit cell. The correlations are given in Table 3.11 and indicate that each Raman band of the anion correlates to A_g symmetry and each infrared band to A_u symmetry under C_i crystal symmetry so that no factor-group splitting is expected in either the Raman or infrared spectrum. Tentative assignments (Table 3.10) have been made by analogy with the $Sn_2Se_6^{4-}$ anion and the isoelectronic In_2I_6;[133] the latter has been fully assigned on the basis of a normal coordinate analysis.[134] Because of the reduced mass effect, the vibrational modes of the $Sn_2Te_6^{4-}$ anion occur at lower frequency than those of the $Sn_2Se_6^{4-}$ anion. The most intense peak 134 cm^{-1} was assigned to the symmetric ring mode, $\nu_2(A_g)$, and the totally symmetric Sn–Te stretching mode, $\nu_1(A_g)$, was assigned to the band

at 185 cm^{-1}. The highest frequency band at 196 cm^{-1} was assigned to the asymmetric Sn–Te stretching mode, $\nu_{11}(B_{2g})$, and an intense shoulder at 121 cm^{-1} was assigned to $\nu_{15}(B_{3g})$. The remaining assignments for $\nu_3(A_g)$, $\nu_4(A_g)$, $\nu_6(B_{1g})$, $\nu_7(B_{1g})$, and $\nu_{12}(B_{2g})$ are deemed more tentative.

Conclusion

The molecular structures of the $Sn_2Ch_6^{4-}$ (Ch = Se or Te) and $Sn_2Te_7^{4-}$ have been known for some time. This work reports the first characterization of the the $Sn_2Ch_6^{4-}$, $Sn_2Te_7^{4-}$, and the novel $Sn_2Se_7^{4-}$ anion in solution by natural abundance ^{77}Se, ^{119}Sn, and ^{125}Te NMR spectroscopy. The solution structures were confirmed by a detailed analysis of the first-order ^{119}Sn NMR subspectra arising from natural abundance isotopomer distributions, and the $^1K(Sn–Ch_t)_{RC}$, $^1K(Sn–Ch_{mb})_{RC}$, and $^1K(Sn–Ch_{db})_{RC}$ coupling constants were shown to correlate with the Sn–Ch_t, Sn–Ch_{mb}, and Sn–Ch_{db} bond distances. Although previous NMR studies have systematically dealt with simple main-group polychalcogenide anions, the present findings represent the first multi-NMR speciation study of factors influencing the condensation processes of simple polychalcogenide anions in non-aqueous solvents. The condensation equilibria among $SnCh_3^{2-}$, $Sn_2Ch_6^{4-}$, $Sn_2Ch_7^{4-}$, and $Sn_4Ch_{10}^{4-}$ were shown to be influenced by the relative amounts of uncryptated alkali-metal cations present in solution, establishing that oligomerization is promoted by ion-pair formation. The hydroxide derivative of the $SnTe_3^{2-}$ anion, $HOSnTe_3^{3-}$, was characterized in the solid-state by X-ray crystallography and represents the second example of a simple mixed hydroxytelluride anion

of a group 14 metal.

CHAPTER 4

TETRATIN(IV) CHALCOGENIDE ANIONS, $Sn_4Ch_{10}^{4-}$ (Ch = Se, Te) and $Sn_4Se_9^{4-}$

Introduction

A structural unit frequently encountered in the chemistry of heavy main-group metal chalcogenide anions is the adamantanoid M_4Ch_{10} or $M_4Ch_6R_4$ cage (R = Ch, halide (X), organic, or organometallic fragments). The structural unit comprises M_4Ch_6 cores with the Ch, X, or R substituents in terminal positions. To date, adamantanoid compounds containing Group 12 [$Hg_4(\mu\text{-ChR})_6X_4^{2-}$,[136] $M_4(\mu\text{-SePh})_6(SePh)_4^{2-}$,[137] $Hg_4(\mu\text{-SR})_{6-m}(\mu\text{-X})_mX_4^{2-}$ [138] (M = Zn, Cd; Ch = S, Se, Te; R = Et, *n*-Pr, *i*-Pr, *n*-Bu; X = Cl, Br; m = 0–2], Group 13 [$Ga_4S_{10}^{4-}$, $In_4Ch_{10}^{4-}$ (Ch = S, Se)[139]], and Group 14 [$Si_4S_{10}^{4-}$,[140] $Ge_4Ch_{10}^{4-}$ (Ch = S,[140–142] Se,[46,143] Te[86]), $(CH_3)_4Sn_4Ch_6$ (Ch = S,[144] Se[145]), $\{Cp(CO)_2Fe\}_4Sn_4Se_6$,[146] $\{Cp(CO)_3Mo\}_4Sn_4Te_6$[147]] metals have been synthesized and characterized primarily by X-ray crystallography and, to a lesser extent, by vibrational spectroscopy. Dean and coworkers[136–138] have used ^{77}Se, ^{125}Te, ^{111}Cd, ^{113}Cd, and ^{199}Hg NMR spectroscopy to characterize Group 12 adamantanoid cages in solution. Multi-NMR studies of adamantanoid M_4Ch_{10} cages have the potential to provide corroborating structural information in solution in the form of chemical shifts and M–Ch spin–spin coupling constants which may correlate with structural parameters and vibrational frequencies observed in the solid state.

Chapter 3 discussed the multi-NMR spectroscopic characterizations of the classically-

bonded tin(IV) chalcogenide anions, $Sn_2Ch_6^{4-}$ and $Sn_2Ch_7^{4-}$ (Ch = Se, Te), as well as the X-ray crystallographic and solid-state Raman spectroscopic investigations of the $Sn_2Ch_6^{4-}$ anions, which were obtained by extracting ternary K/Sn/Ch (Ch = Se, Te) alloys in en and in liquid NH_3 and in the absence or presence of non-stoichiometric amounts of 2,2,2-crypt or 18-crown-6 with respect to K^+. The present Chapter reports the syntheses and the structural characterization by ^{119}Sn, ^{77}Se, and ^{125}Te NMR spectroscopy, X-ray crystallography, and Raman spectroscopy of the novel $Sn_4Ch_{10}^{4-}$ (Ch = Se, Te) anions, where the tellurium analogue represents the first example of an adamantanoid cage containing only tin and tellurium. The Raman spectrum of the $SnSe_4^{4-}$ anion in $(Na^+)_4SnSe_4^{4-}\cdot 2en$[148] is also reported and compared with those of $Sn_4Se_{10}^{4-}$ and the isovalent SnS_4^{4-} anion. The X-ray crystal structure of the novel adamantanoid anion, $Sn_4Se_9^{4-}$, is also reported.

Results and Discussion

Synthesis of $Sn_4Ch_{10}^{4-}$ (Ch = Se, Te)

Solutions of the $Sn_4Se_{10}^{4-}$ anion were prepared by extracting the ternary alloy $KSn_{0.67}Se_{1.93}$ in en and in liquid NH_3 in the presence of non-stoichiometric amounts of 2,2,2-crypt with respect to K^+, where K^+ : 2,2,2-crypt = 1.00 : 0.42. Single crystals of $(18\text{-crown-6-}K^+)_4Sn_4Se_{10}^{4-}\cdot 5en$ were isolated upon addition of THF to an en solution of the alloy $KSn_{0.90}Se_{1.93}$ containing a stoichiometric deficit of 18-crown-6 with respect to K^+. Since no conclusive evidence was found by ^{119}Sn and ^{125}Te NMR spectroscopy for the $Sn_4Te_{10}^{4-}$ anion in en or in liquid NH_3 extracts of the $KSn_{0.63}Te_{1.70}$ alloy (Chapter 3), the $Sn_4Te_{10}^{4-}$ anion was

prepared by extracting the alloy $K_4Sn_4Te_{10}$ in liquid NH_3 in the absence of 2,2,2-crypt. This synthesis is analogous to the one used to prepare the isostructural $Ge_4Te_{10}^{4-}$ anion[86] which involved extracting the alloy $K_4Ge_4Te_{10}$ in en in the presence of $(C_2H_5)_4N^+Br^-$. Crystals of the compound $((C_2H_5)_4N^+)_4Ge_4Te_{10}^{4-}$ were isolated upon addition of diethyl ether to the en solution. However, analogous attempts at preparing crystals of (2,2,2-crypt-K^+)$_4Sn_4Te_{10}^{4-}$ by addition of THF to an en extract of $K_4Sn_4Te_{10}$ containing a 50 mole% deficit of 2,2,2-crypt resulted in the isolation and subsequent characterization by X-ray crystallography of (2,2,2-crypt-K^+)$_2(Te_4^{2-})_{0.5}(Te_6^{2-})_{0.5}$.[43] Crystals of (18-crown-6-K^+)$_4Sn_4Te_{10}^{4-}$·3en·2THF were isolated by addition of THF to an en solution of $K_4Sn_4Te_{10}$ containing a 25 mole% deficit of 18-crown-6 with respect to K^+.

Structural Characterization of the $Sn_4Ch_{10}^{4-}$ (Ch = Se, Te) Anions by X-ray Crystallography

A summary of the crystal data and refinement results are given in Table 4.1. The final atomic coordinates and equivalent isotropic thermal parameters for the Sn, Ch, and K atoms are summarized in Tables 4.2 and 4.3. The most significant bond distances and angles in the $Sn_4Ch_{10}^{4-}$ anions are given in Tables 4.4 and 4.5. The structure of the 18-crown-6-K^+ cations in the title compounds is similar to that observed in K^+(18-crown-6-K^+)$GaTe_3^-$,[123] with average K···O distances of 2.815(12) [2.823(19)] Å in the Se [Te] compound.

The most interesting aspect of the structures is the adamantanoid geometry of the anions (~T_d point symmetry) in which the tin atoms occupy the bridgehead positions and the

Table 4.1. Summary of Crystal Data and Refinement Results for (18-crown-6-K^+)$_4$-$Sn_4Se_{10}^{4-}$·5en (**1**), (18-crown-6-K^+)$_4Sn_4Te_{10}^{4-}$·3en·2THF (**2**), and (2,2,2-crypt-K^+)$_4Sn_4Se_9^{4-}$·en·THF (**3**).[a]

	(1)	(2)	(3)
Formula	$C_{58}H_{136}N_{10}O_{24}K_4Sn_4Se_{10}$	$C_{62}H_{136}N_6O_{26}K_4Sn_4Te_{10}$	$C_{78}H_{160}N_{10}O_{25}K_3Sn_4Se_9$
Space group (No.)	$P2_1/n$	$P2_1/n$	$P2_1/c$
a, Å	22.033(2)	22.420(5)	24.194(5)
b, Å	18.966(2)	19.570(4)	17.187(3)
c, Å	24.392(2)	24.680(5)	27.254(6)
α, deg	90.00	90.00	90.00
β, deg	97.548(8)	96.90(3)	92.48(3)
γ, deg	90.00	90.00	90.00
V, Å^{-3}	10091.0(17)	10750.2(37)	11320.4(39)
Z	4	4	4
mol. wt.	2778.53	3288.93	2979.96
ρ, g cm^{-3}	1.829	2.032	1.748
morphology	parallelepiped	platelet	platelet
dimensions, cm	0.16 × 0.32 × 0.28	0.19 × 0.45 × 0.38	0.26 × 0.11 × 0.36
colour	orange	deep red	orange
refinement method	F^2	F^2	F^2
refl.used	15235	16713	24265
refl.suppressed ($F^2 < -2\sigma F^2$)	35	34	244
parameters refined	1021	1015	1126
H-atom method	calculated	calculated	calculated
R_1 ($F^2 > 2\sigma F^2$)	0.0843	0.0458	0.1028
wR_2 (F^2)	0.1859	0.1780	0.3156
S ($F^2 > 2\sigma F^2$)	1.133	1.508	1.075
$\Delta\rho_{max}$, e Å^{-3}	0.890	2.863	17.777
$\Delta\rho_{min}$, e Å^{-3}	–0.359	–2.392	–6.161
w	$w_1 = 0.0459$	$w_1 = 0.1000$	$w_1 = 0.1860$
	$w_2 = 26.7015$	$w_2 = 0.0000$	$w_2 = 301.2744$

[a] The results for (2,2,2-crypt-K^+)$_4Sn_4Se_9^{4-}$·en·THF (**3**) are preliminary.

Table 4.2. Atomic Coordinates and Equivalent Isotropic Thermal Parameters ($Å^2$) for the Sn, Se, and K atoms in (18-crown-6-K^+)$_4Sn_4Se_{10}^{4-}$·5en.

	x	*y*	*z*	U_{eq} [a]
Sn(1)	0.70945(2)	0.26633(2)	1.07993(2)	0.02353(12)
Sn(2)	0.64713(2)	0.38702(2)	0.94294(15)	0.01928(11)
Sn(3)	0.64273(2)	0.16800(2)	0.93419(2)	0.02039(11)
Sn(4)	0.80819(2)	0.27158(2)	0.94692(2)	0.02168(11)
Se(1)	0.65137(3)	0.15812(3)	1.03903(2)	0.02615(14)
Se(2)	0.65118(3)	0.37788(3)	1.04764(2)	0.02246(14)
Se(3)	0.81738(3)	0.27050(3)	1.05197(3)	0.02851(19)
Se(4)	0.75407(3)	0.38508(3)	0.91317(2)	0.02202(14)
Se(5)	0.58740(3)	0.28063(3)	0.89956(2)	0.02143(13)
Se(6)	0.75079(3)	0.16274(3)	0.90654(3)	0.02489(14)
Se(7)	0.59538(3)	0.49553(3)	0.91290(3)	0.0318(2)
Se(8)	0.58523(3)	0.06930(3)	0.88999(3)	0.0356(2)
Se(9)	0 90999(3)	0.27406(3)	0.91856(3)	0.0358(2)
Se(10)	0.71934(4)	0.25849(4)	1.17980(3)	0.0457(2)
K(1)	0.03909(7)	0.98100(8)	0.85743(6)	0.0358(3)
K(2)	0.05745(7)	0.48859(9)	0.82253(6)	0.0394(3)
K(3)	–0.24608(7)	0.75776(7)	0.84898(6)	0.0331(3)
K(4)	0.09932(8)	0.72484(7)	0.58397(6)	0.0354(3)

[a] U_{eq} is defined as one-third of the trace of the orthogonalized U_{ij} tensor.

Table 4.3. Atomic Coordinates and Equivalent Isotropic Thermal Parameters ($Å^2$) for the Sn, Te, and K atoms in (18-crown-6-K^+)$_4$$Sn_4Te_{10}^{4-}$·3en·2THF.

	x	*y*	*z*	U_{eq}[a]
Sn(1)	0.64207(2)	0.33498(2)	–0.06479(2)	0.02074(14)
Sn(2)	0.81586(2)	0.23002(2)	–0.04478(2)	0.02456(11)
Sn(3)	0.64564(2)	0.10715(2)	–0.05882(2)	0.02124(14)
Sn(4)	0.70307(2)	0.22631(2)	0.08875(2)	0.02715(15)
Te(1)	0.58174(2)	0.21904(2)	–0.10331(2)	0.02096(13)
Te(2)	0.75787(2)	0.34367(2)	–0.09134(2)	0.02515(14)
Te(3)	0.64438(2)	0.34225(2)	0.04673(2)	0.02817(14)
Te(4)	0.82040(2)	0.22551(3)	0.06667(2)	0.03272(14)
Te(5)	0.76076(2)	0.11300(2)	–0.08767(2)	0.02418(14)
Te(6)	0.64421(2)	0.10927(2)	0.05235(2)	0.02364(14)
Te(7)	0.92832(2)	0.23057(3)	–0.06668(3)	0.0431(2)
Te(8)	0.59317(3)	–0.00720(3)	–0.09500(2)	0.0454(2)
Te(9)	0 70751(4)	0.23070(3)	0.19577(2)	0.0520(2)
Te(10)	0.58349(2)	0.43924(2)	–0.11477(2)	0.0288(2)
K(1)	1.09809(7)	–0.22368(7)	0.57994(6)	0.0277(3)
K(2)	1.05642(7)	0.02293(8)	0.82440(7)	0.0338(4)
K(3)	0.45304(10)	0.02938(11)	0.64358(8)	0.0501(5)
K(4)	0.73258(11)	0.24012(9)	0.64597(8)	0.0510(6)

[a] U_{eq} is defined as one-third of the trace of the orthogonalized U_{ij} tensor.

Table 4.4. Selected Bond Lengths (Å) and Bond Angles (deg) for (18-crown-6-K^+)$_4$-$Sn_4Se_{10}^{4-}$·5en.

Bond Lengths (Å)			
Sn(1)–Se(1)	2.5507(7)	Sn(3)–Se(1)	2.5461(7)
Sn(1)–Se(2)	2.5446(7)	Sn(3)–Se(5)	2.5472(6)
Sn(1)–Se(3)	2.5566(8)	Sn(3)–Se(6)	2.5572(7)
Sn(1)–Se(10)	2.4217(8)	Sn(3)–Se(8)	2.4310(7)
Sn(2)–Se(2)	2.5489(7)	Sn(4)–Se(3)	2.5439(8)
Sn(2)–Se(4)	2.5526(7)	Sn(4)–Se(4)	2.5438(7)
Sn(2)–Se(5)	2.5600(6)	Sn(4)–Se(6)	2.5493(7)
Sn(2)–Se(7)	2.4187(7)	Sn(4)–Se(9)	2.4302(8)
Bond Angles (deg)			
Se(1)–Sn(1)–Se(2)	109.98(2)	Se(5)–Sn(3)–Se(6)	111.45(2)
Se(1)–Sn(1)–Se(3)	110.84(2)	Se(5)–Sn(3)–Se(8)	107.48(3)
Se(1)–Sn(1)–Se(10)	108.56(3)	Se(6)–Sn(3)–Se(8)	107.50(2)
Se(2)–Sn(1)–Se(3)	109.85(2)	Se(3)–Sn(4)–Se(4)	107.74(2)
Se(2)–Sn(1)–Se(10)	109.72(3)	Se(3)–Sn(4)–Se(6)	110.64(2)
Se(3)–Sn(1)–Se(10)	107.84(3)	Se(3)–Sn(4)–Se(9)	109.43(3)
Se(2)–Sn(2)–Se(4)	111.83(3)	Se(4)–Sn(4)–Se(6)	111.91(2)
Se(2)–Sn(2)–Se(5)	108.01(2)	Se(4)–Sn(4)–Se(9)	107.53(3)
Se(2)–Sn(2)–Se(7)	108.34(2)	Se(6)–Sn(4)–Se(9)	109.52(3)
Se(4)–Sn(2)–Se(5)	108.25(2)	Sn(3)–Se(1)–Sn(1)	107.52(2)
Se(4)–Sn(2)–Se(7)	109.93(2)	Sn(1)–Se(2)–Sn(2)	108.45(2)
Se(5)–Sn(2)–Se(7)	110.46(2)	Sn(4)–Se(3)–Sn(1)	108.37(3)
Se(1)–Sn(3)–Se(5)	111.36(2)	Sn(4)–Se(4)–Sn(2)	109.26(2)
Se(1)–Sn(3)–Se(6)	108.22(2)	Sn(3)–Se(5)–Sn(2)	109.07(2)
Se(1)–Sn(3)–Se(8)	110.77(3)	Sn(4)–Se(6)–Sn(3)	107.28(2)

Table 4.5. Selected Bond Lengths (Å) and Bond Angles (deg) for (18-crown-6-K^+)$_4$-$Sn_4Te_{10}^{4-}$·3en·2THF.

Bond Lengths (Å)			
Sn(1)–Te(1)	2.7519(7)	Sn(3)–Te(1)	2.7705(7)
Sn(1)–Te(2)	2.7582(9)	Sn(3)–Te(5)	2.7590(9)
Sn(1)–Te(3)	2.7502(8)	Sn(3)–Te(6)	2.7480(8)
Sn(1)–Te(10)	2.6506(8)	Sn(3)–Te(8)	2.6337(8)
Sn(2)–Te(2)	2.7566(8)	Sn(4)–Te(3)	2.7618(8)
Sn(2)–Te(4)	2.7416(9)	Sn(4)–Te(4)	2.7497(9)
Sn(2)–Te(5)	2.7536(8)	Sn(4)–Te(6)	2.7405(8)
Sn(2)–Te(7)	2.6413(9)	Sn(4)–Te(9)	2.6325(9)
Bond Angles (deg)			
Te(1)–Sn(1)–Te(2)	113.98(2)	Te(5)–Sn(3)–Te(6)	112.36(3)
Te(1)–Sn(1)–Te(3)	109.74(2)	Te(5)–Sn(3)–Te(8)	109.94(2)
Te(1)–Sn(1)–Te(10)	106.14(3)	Te(6)–Sn(3)–Te(8)	107.04(3)
Te(2)–Sn(1)–Te(3)	109.24(3)	Te(3)–Sn(4)–Te(4)	110.75(2)
Te(2)–Sn(1)–Te(10)	105.64(2)	Te(3)–Sn(4)–Te(6)	112.00(3)
Te(3)–Sn(1)–Te(10)	112.06(3)	Te(3)–Sn(4)–Te(9)	107.99(3)
Te(2)–Sn(2)–Te(4)	113.77(3)	Te(4)–Sn(4)–Te(6)	111.39(2)
Te(2)–Sn(2)–Te(5)	110.07(3)	Te(4)–Sn(4)–Te(9)	106.10(4)
Te(2)–Sn(2)–Te(7)	108.99(2)	Te(6)–Sn(4)–Te(9)	108.35(3)
Te(4)–Sn(2)–Te(5)	108.64(2)	Sn(3)–Te(1)–Sn(1)	107.79(3)
Te(4)–Sn(2)–Te(7)	106.51(4)	Sn(1)–Te(2)–Sn(2)	105.16(2)
Te(5)–Sn(2)–Te(7)	108.70(3)	Sn(4)–Te(3)–Sn(1)	106.51(2)
Te(1)–Sn(3)–Te(5)	108.65(2)	Sn(4)–Te(4)–Sn(2)	106.11(4)
Te(1)–Sn(3)–Te(6)	108.44(2)	Sn(3)–Te(5)–Sn(2)	109.03(2)
Te(1)–Sn(3)–Te(8)	110.40(3)	Sn(4)–Te(6)–Sn(3)	106.08(2)

chalcogen atoms occupy the bridging and terminal sites (Figures 4.1 and 4.2). The Ch–Sn–Ch bond angles range from 107.48(2)–111.91(2)° in the Se compound and from 105.64(2)– 113.98(2)° in the Te compound, so that the $Sn_4Ch_{10}^{4-}$ anions can be described as composed of four nearly tetrahedral Sn(IV) centres to which are bonded four Ch_t (t, terminal) atoms and six Ch_{mb} (mb, monobridging) atoms. The average bond angle within the central Sn_4Ch_6 core, Ch_{mb}–Sn–Ch_{mb}, is 110.0(4) [110.8(6)]° in the Se [Te] compound and is slightly larger than the average bond angle involving terminal bonds, i.e., Ch_t–Sn–Ch_{mb} [Se, 108.9(3)°; Te, 108.1(6)°], a trend common to all known $M_4Ch_{10}^{4-}$ adamantanoid anions.[46,86,139–143] The Ch_t–Sn–Ch_{mb} angles are close to the ideal tetrahedral angles observed in $SnCh_4^{4-}$ [Se, 109.5(12)° in Na_4SnSe_4[104]and 109.5(3)° in K_4SnSe_4;[104] Te, 109.4(19)],[59] and the Ch_{mb}–Sn–Ch_{mb} angles are comparable to those observed in other systems containing the Sn_4Ch_6 cores, i.e., $(CH_3)_4Sn_4Se_6$ [110.13(4)–115.19(4)°],[145] $\{Cp(CO)_2Fe\}_4Sn_4Se_6$ [108.8(1)–111.8(1)°],[146] and $\{Cp(CO)_3Mo\}_4Sn_4Te_6$ [108.0(1)–114.4(1)°].[147] The average Sn–Ch_{mb}–Sn bond angles [Se, 108.3(3)°; Te, 106.8(8)°] are comparable to those observed in the compounds $(CH_3)_4Sn_4Se_6$ [102.13(4)–103.75(4)°], $\{Cp(CO)_2Fe\}_4Sn_4Se_6$ [107.3(1)–109.0(1)°], and $\{Cp(CO)_3Mo\}_4Sn_4Te_6$ [104.4(1)–108.1(1)°].

As observed in other adamantanoid structures of Group 14, i.e., $Si_4S_{10}^{4-}$ [140] and $Ge_4Ch_{10}^{4-}$ (Ch = S, Se, Te),[46,86,140–143] the average Sn–Ch_t bond length in $Sn_4Ch_{10}^{4-}$ [Se, 2.425(3) Å; Te, 2.639(4) Å] is significantly shorter than the average Sn–Ch_{mb} bond length [Se, 2.550(2) Å; Te, 2.753(2) Å]. This trend has also been observed in the related $Sn_2Ch_6^{4-}$ (Ch = S,[20] Se,[21] Te [22,23]) and $Sn_2Te_7^{4-}$ [116] anions and in the adamantanoid structures of Group

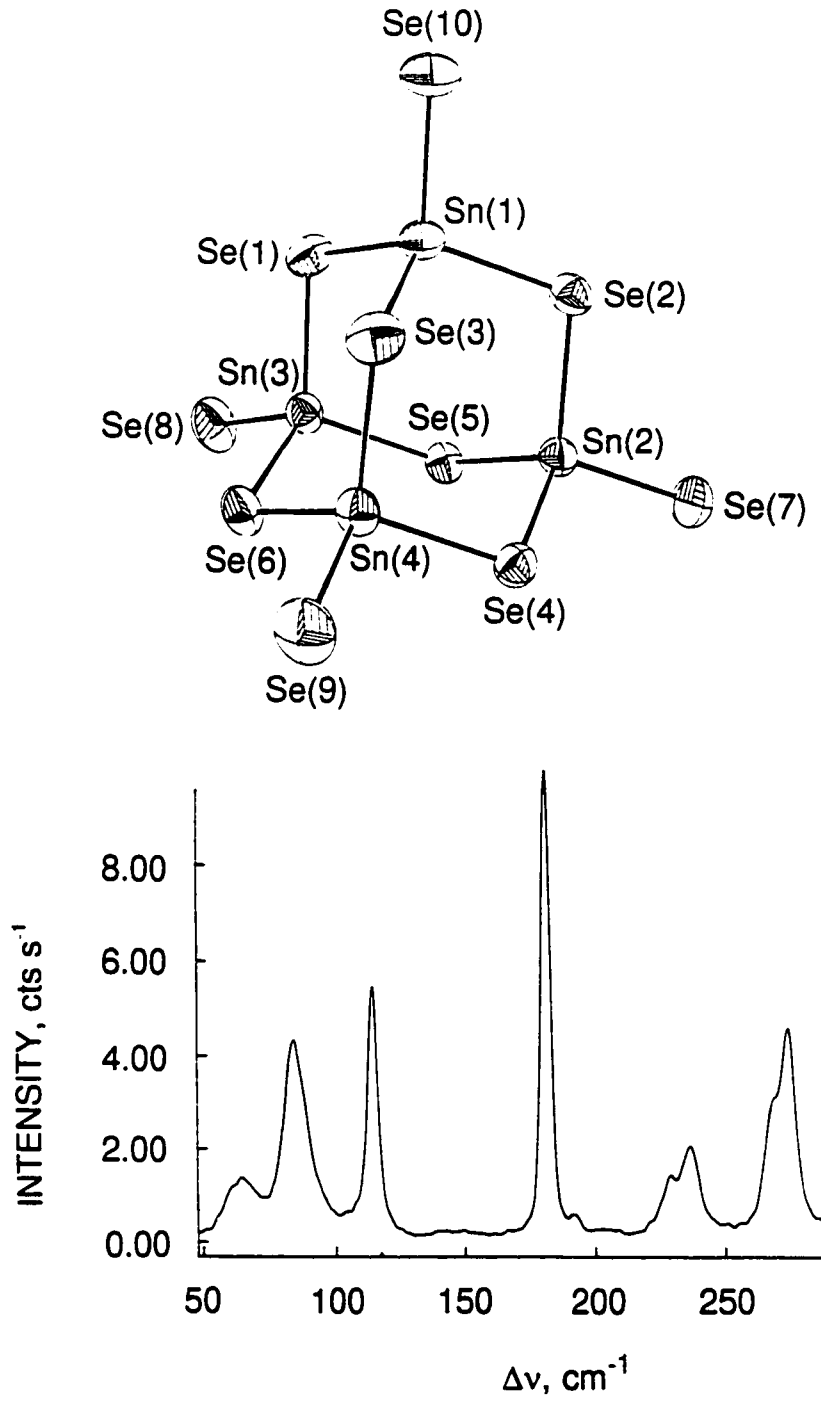

Figure 4.1. View and Raman spectrum of $Sn_4Se_{10}^{4-}$ in (18-crown-6-K^+)$_4Sn_4Se_{10}^{4-}$·5en with displacement ellipsoids drawn at the 70% probability level.

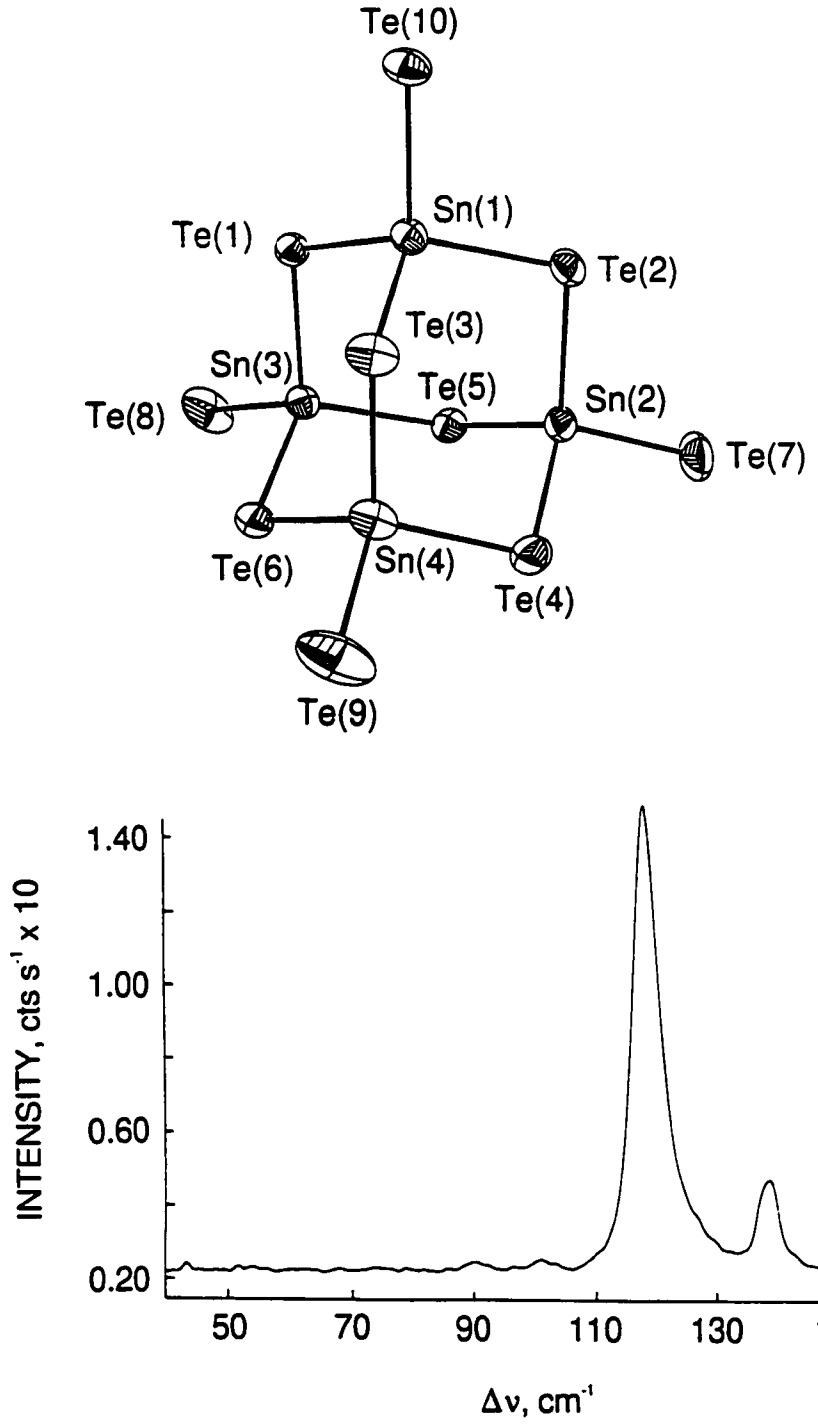

Figure 4.2. View and Raman spectrum of $Sn_4Te_{10}^{4-}$ in (18-crown-6-K^+)$_4Sn_4Te_{10}^{4-}$·3en·2THF with displacement ellipsoids drawn at the 70% probability level.

13, i.e., in $Ga_4S_{10}^{8-}$ and $In_4Ch_{10}^{8-}$ (Ch = S, Se).[139] However, the difference between M–Ch_t and M–Ch_{mb} is more pronounced in $Sn_4Ch_{10}^{4-}$, indicating stronger bonding to the terminal chalcogen atoms, but longer and more polar M–Ch_t bonds have been observed in the Group 13 analogues by virtue of the higher charge on the terminal chalcogen atoms. The average Sn–Ch_t bond length is shorter than those found in the tetrahedral $SnCh_4^{4-}$ anions [Se, 2.523(1) Å in Na_4SnSe_4[104] and 2.510(10) Å in K_4SnSe_4;[104] Te, 2.751(4) Å[59]], and the average Sn–Ch_{mb} bond length is comparable to those in $(CH_3)_4Sn_4Se_6$ [2.513(1)–2.541(1) Å],[144] $\{Cp(CO)_2Fe\}_4Sn_4Se_6$ [2.524(5)–2.554(4) Å],[145] and $\{Cp(CO)_3Mo\}_4Sn_4Te_6$ [2.740(2)–2.774(2)].[146] The Sn···Sn distances in $Sn_4Ch_{10}^{4-}$ range from 4.111(1)–4.160(1) [4.380(1)–4.489(1)] Å in the Se [Te] compound and are significantly longer than the corresponding distance observed for the $Sn_2Se_6^{4-}$ anion in $(K^+)_2(18\text{-crown-6-}K^+)_2Sn_2Se_6^{4-}\cdot 4en$ [3.4930(9) Å].

It should be noted that the $Sn_4Se_{10}^{4-}$ anion has also been characterized by X-ray crystallography in $(2,2,2\text{-crypt-}K^+)_4Sn_4Se_{10}^{4-}$ [113] and in $(N(C_2H_5)^+)_4Sn_4Se_{10}^{4-}$.[114] The bond distances and angles observed for the anion in both salts are identical to those reported in the present work.

Structural Characterization of $Sn_4Se_{10}^{4-}$ by NMR Spectroscopy

The $Sn_4Se_{10}^{4-}$ anion was identified in solution by natural abundance ^{77}Se and ^{119}Sn NMR spectroscopy.[26] The experimental ^{119}Sn and ^{77}Se NMR spectra and the simulated ^{119}Sn NMR spectrum are depicted in Figures 4.3 and 4.4. The chemical shifts and spin–spin coupling constants (scalar, J; reduced, K; and relativistically corrected reduced, K_{RC}) are

Figure 4.3. Observed (upper trace) and simulated (lower trace) ^{119}Sn NMR spectrum (186.504 MHz, –50 °C) $Sn_4Se_{10}^{4-}$. The peak labelling scheme is defined in Table 4.7 and in the text.

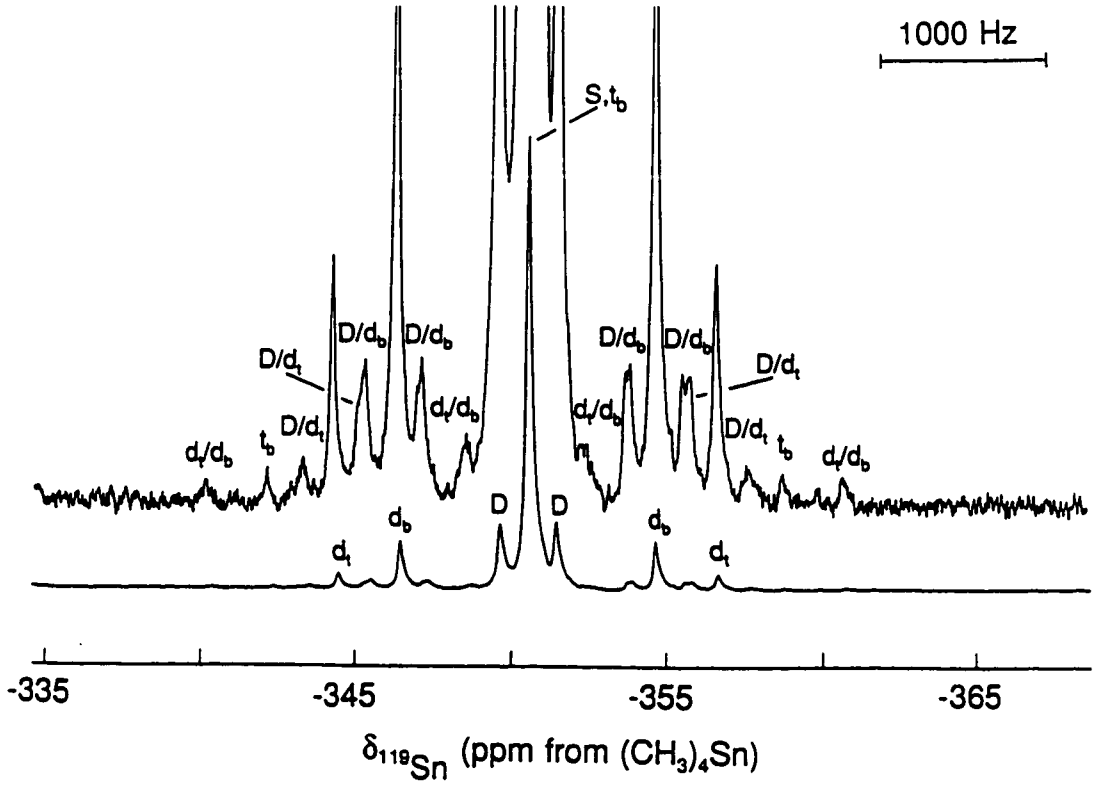
1000 Hz
S.t$_b$
D/d$_t$
D/d$_b$
D/d$_b$
d$_t$/d$_b$
D/d$_t$
t$_b$
d$_t$/d$_b$
D/d$_b$
D/d$_b$
d$_t$/d$_b$
D/d$_t$
D/d$_t$
t$_b$
d$_t$/d$_b$
d$_t$
d$_b$
D
D
d$_b$
d$_t$
-335
-345
-355
-365
$\delta_{^{119}Sn}$ (ppm from $(CH_3)_4Sn$)

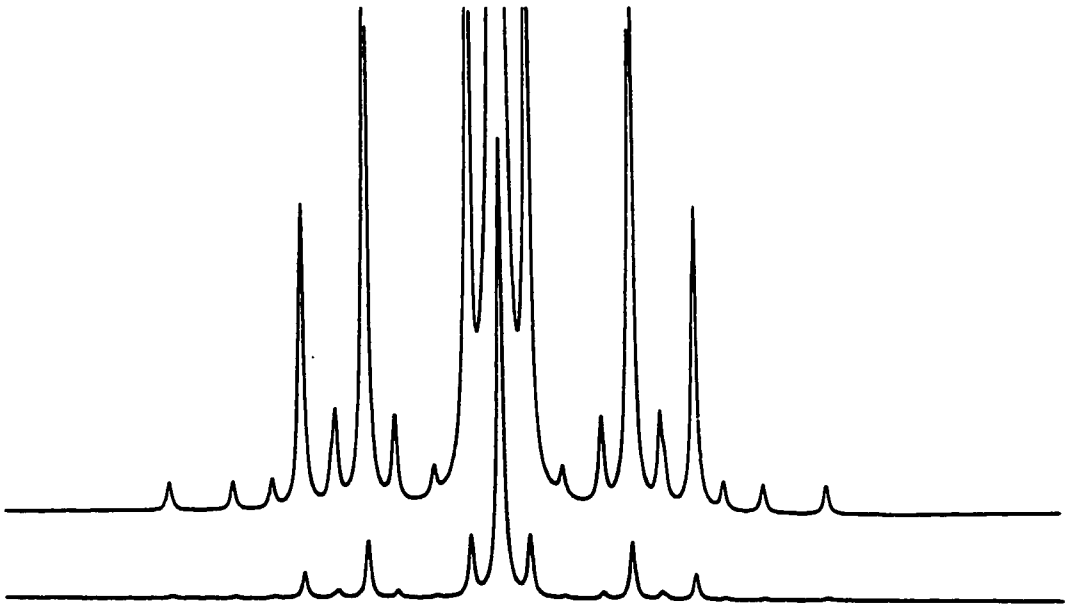

Figure 4.4. The ^{77}Se NMR spectrum (95.383 MHz, 0 °C) of $Sn_4Se_{10}^{4-}$. The peak labelling scheme is defined in Table 4.7 and in the text; (A) denotes the Se_t environment of the $Sn_2Se_6^{4-}$ anion (Chapter 3) and (a) denotes the associated unresolved ^{117}Sn and ^{119}Sn satellites.

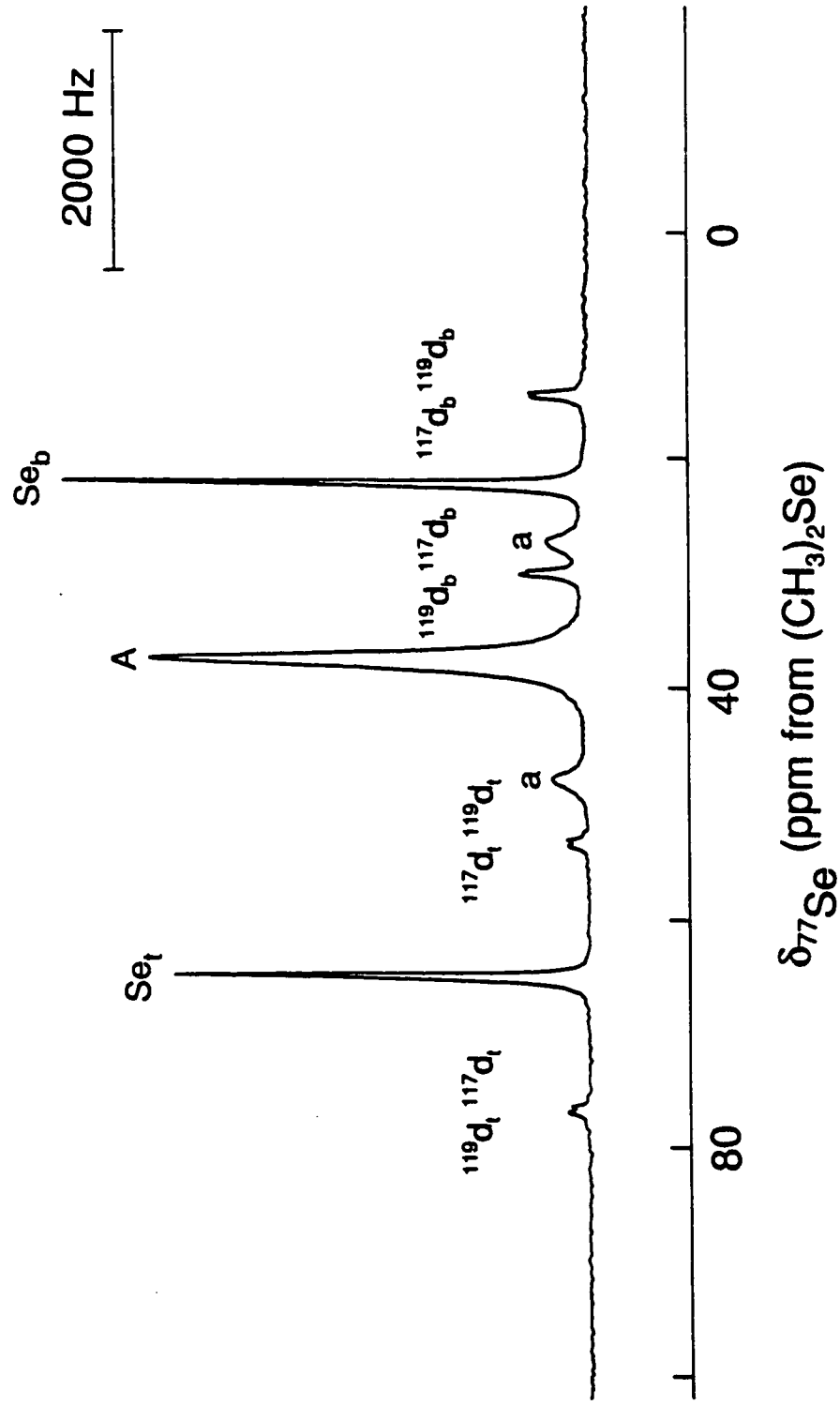
2000 Hz
Se_b
A
Se_t
$^{119}d_b\ ^{117}d_b$
a
$^{117}d_b\ ^{119}d_b$
$^{117}d_t\ ^{119}d_t$
a
$^{119}d_t\ ^{117}d_t$
80
40
0
$\delta_{77}Se$ (ppm from $(CH_3)_2Se$)

summarized in Table 4.6 together with the observed and calculated satellite/central peak (I_S/I_C) intensity ratios of the Sn and Se environments of the anion. The number of observed environments, the satellite doublet spacings corresponding to $^1J(^{119}Sn–^{77}Se)$ and $^2J(^{119}Sn–^{117}Sn)$, and the I_S/I_C ratios are consistent with the crystal structures of the adamantanoid $Sn_4Ch_{10}^{4-}$ anions and indicate that the solid-state molecular geometry is retained in solution.

Analysis of Spin–Spin Coupling Patterns. In addition to the resonances associated with the $SnSe_3^{2-}$ (–299.5 ppm, 1.0%), $Sn_2Se_6^{4-}$ (–491.6 ppm, 57.0%), and $Sn_2Se_7^{4-}$ (–328.4 ppm, 15.0%) anions, the ^{119}Sn NMR spectrum (–50 °C) consisted of a singlet (–350.1 ppm, 27.0%) flanked by two sets of symmetric ^{77}Se satellites (d_t, 2274 Hz; d_{mb}, 1536 Hz) in a 1.0 : 3.2 peak area ratio, indicating coupling to two chemically inequivalent selenium environments (Figure 4.3). Satellites corresponding to a $^2J(^{119}Sn–^{117}Sn)$ coupling of 342 Hz were also observed in the ^{119}Sn NMR spectrum; this coupling is similar to that observed for the $Sn_2Se_7^{4-}$ anion (302 Hz; Chapter 3). Comparable $^2J(^{119}Sn–^{117}Sn)$ couplings of 205, 235, and 263 Hz have been observed for the solution structures of the dimethyltin(IV) chalcogenides $[(CH_3)_2SnCh]_3$ (Ch = S, Se, Te), respectively.[115] In addition, several weaker satellites were observed in the ^{119}Sn NMR spectrum (D/d_{mb}, D/d_t, d_t/d_{mb}, and t_b in Figure 4.3) and their assignments are discussed below.

Assigments of $^1J(^{119}Sn–^{77}Se)$ couplings observed in the ^{119}Sn NMR spectrum were confirmed by observing the $^1J(^{77}Se–^{119}Sn)$ couplings in the ^{77}Se NMR spectrum. Selenium resonances corresponding to the two environments were observed in a 4.0 : 6.3 peak area

Table 4.6. Chemical Shifts, Spin–Spin Coupling Constants, and Satellite Intensities for the $Sn_4Se_{10}^{4-}$ Anion.

chemical shift, ppm [a]		spin-spin coupling contstants							
		J, Hz		K, $T^2J^{-1} \times 10^{20}$		K_{RC}, $T^2J^{-1} \times 10^{20}$		$100 \times I_S/I_C$ [b]	
^{119}Sn	^{77}Se [c]	^{119}Sn–^{77}Se	^{119}Sn–^{117}Sn	Sn–Se	Sn–Sn	Sn–Se	Sn–Se	Sn	Se
–350.1[d]	30.7(t)	2274	342	263.7	21.8	160.2	10.4	3.5(4.1)	
	7.1(mb)	1536		178.1		108.2		10.4(12,2)	
–359.3[e]	65.0(t)	2276	333	263.9	20.6	160.4	10.2		8.5(9.6)
	22.2(mb)	1532		177.7		107.9			17.5(19.2)

[a] Satellites were resolved in the ^{119}Sn NMR spectrum at both –50 and 0 °C; however, the ^{119}Sn NMR spectrum obtained at 0 °C was broad and the ^{77}Se NMR spectrum obtained at –50 °C contained a number of overlapping peaks which precluded accurate satellite assignments and I_S/I_C calculations. Consequently, the discussion of the NMR parameters (see Text) refers to those obtained at –50 (^{119}Sn) and 0 (^{77}Se) °C. [b] Calculated values are given in parentheses. [c] The symbols t and mb refer to the terminal chalcogen and monochalcogeno-bridging environments, respectively. [d] Recorded in liquid NH_3 at –50 °C. [e] Recorded in en at 0 °C.

ratio at 65.0 and 22.2 ppm, respectively (Figure 4.4). The I_S/I_C intensity ratios indicated that the two selenium environments were coupled to one and two tin atoms, respectively, and are consistent with the adamantanoid $Sn_4Se_{10}^{4-}$ structure.

The ^{119}Sn NMR spectrum of the $Sn_4Se_{10}^{4-}$ anion was simulated using the natural abundances of the spin-½ nuclides ^{117}Sn, ^{119}Sn, and ^{77}Se;[74] the values of the observed coupling constants; and the total line intensities and multiplicities of the most abundant (> 0.024%) isotopomers (Table 4.7) contributing significant first-order subspectra to the experimental ^{119}Sn NMR spectrum. The resulting simulation (Figure 4.3) is in excellent agreement with the experimental spectrum and accounts for all the observed satellite peaks. A singlet (S) is observed for the isotopomers in which no ^{77}Se atoms are directly bonded to spin-active Sn atoms, namely, $^{119}Sn_xSn_{4-x}{}^{77}Se_zSe_{10-z}^{4-}$ (x = 1–3; z = 0–2). When one terminal or one bridging ^{77}Se atom is directly bonded to a spin-active Sn atom, a doublet (d_t or d_{mb}) results which is symmetrically disposed about the central singlet (S) at a spacing corresponding to $^1J(^{119}Sn–^{77}Se_t)$ or $^1J(^{119}Sn–Se_{mb})$, respectively. The isotopomers, $^{119}Sn_x{}^{117}SnSn_{3-x}{}^{77}Se_zSe_{10-z}^{4-}$ (x = 1, 2; z = 0–2), give rise to a DOUBLET (D) arising from $^2J(^{119}Sn–^{117}Sn)$ coupling when no ^{77}Se atoms are bonded to ^{119}Sn atoms. The presence of a ^{77}Se atom in a terminal or a bridging position directly bonded to a ^{119}Sn atom gives rise to a DOUBLET-of-doublets (D/d_t or D/d_{mb}) whose transitions are symmetrically disposed about the binomial doublets d_t or d_{mb}, respectively (Figure 4.3). The lowest abundance isotopomers that are detectable are $^{119}Sn_xSn_{4-x}{}^{77}Se_2Se_8$ (x = 1, 2) and give rise to either a 1 : 2 : 1 triplet (t_{mb}), when both ^{77}Se atoms are bridged to at least one ^{119}Sn atom, or to a doublet-of-doublets

Table 4.7. Natural Abundance Isotopomers and Subspectra Used to Simulate the ^{119}Sn NMR Spectrum of the $Sn_4Se_{10}^{4-}$ Anion.

$^{119}Sn_x{}^{117}Sn_y Sn_{4-x-y}{}^{77}Se_z{}^{0}Se_{10-z}{}^{4-}$ [a]			total intensity [a]	
				subspectrum
x	y	z	Se	multiplicity [b]
1	0	0	8.962	S
1	0	1	4.531	S
			2.265	d_{mb}
			0.755	d_t
1	0	2	1.223	S
			0.524	d_b
			0.524	d_t
			0.262	d_t/d_{mb}
			0.262	t_b
1	1	0	2.499	D
1	1	1	1.233	D
			0.617	D/d_t
			0.206	D/d_{mb}
1	1	2	0.318	D/d_{mb}
			0.283	D
			0.106	D/d_t
2	0	0	2.828	S
2	0	1	1.163	d_{mb}
			0.698	S
			0.465	d_t
2	0	2	0.349	d_{mb}
			0.163	d_t
			0.140	d_t/d_{mb}
			0.140	t_b
			0.070	S
2	1	0	0.513	D
2	1	1	0.195	D
			0.162	D/d_{mb}
			0.065	D/d_t
3	0	0	0.290	S

Table 4.7. Continued.

$^{119}Sn_x{}^{117}Sn_y Sn_{4-x-y}{}^{77}Se_z{}^{0}Se_{10-z}$ [a]			total intensity [a]	
				subspectrum
x	y	z	Se	multiplicity [b]
3	0	1	0.143	d_{mb}
			0.072	d_t
			0.024[c]	S

[a] Natural abundances of the spin-½ nuclides used to calculate the isotopomer abundances were taken from ref. (74); ^{77}Se, 7.58%; ^{117}Sn, 7.61%; and ^{119}Sn, 8.58%. The natural abundance of ^{115}Sn (0.35%) is too low to contribute detectable isotopomer subspectra and is combined with the spinless tin nuclides. [b] S denotes a singlet; D denotes a DOUBLET arising from $^{2}J(^{119}Sn–^{117}Sn)$; d_t and d_{mb} denote doublets arising from $^{1}J(^{119}Sn–^{77}Se_t)$ and $^{1}J(^{119}Sn–^{77}Se_{mb})$, respectively; and t_b denotes at triplet arising from $^{1}J(^{119}Sn–^{77}Se_b)$. The symbols D/d and d/d generally denote DOUBLET-of-doublets and doublet-of-doublets, respectively; see text, p. 134. [c] Isotopomers having multiplet line intensities below this value are too weak to be observed and are not included in the summation of the simulated subspectra.

(d_t/d_{mb}), when one ^{77}Se atom is terminal and the other is bridging and directly bonded to at least one ^{119}Sn atom. The central transition of the triplet lies under the central singlet (S), while the outer two transitions are observed at a spacing corresponding to $^1J(^{119}Sn–^{77}Se_{mb})$ on either side of the central singlet. The transitions of the doublet-of-doublets are observed symmetrically disposed about the central singlet.

Coupling Constants. As expected, $^1J(^{119}Sn–^{77}Se_t)$ was found to be larger than $^1J(^{119}Sn–^{77}Se_{mb})$ and indicates a higher bond order for the Sn–Se_t bond than for the Sn–Se_{mb} bond and is consistent with the shorter Sn–Ch_t bonds [average: Se, 2.425(3) Å; Te, 2.639(4) Å] and the longer Sn–Se_{mb} bonds [average: Se, 2.550(2) Å; Te, 2.753(2) Å] observed for the $Sn_4Ch_{10}^{4-}$ anion. The magnitude of $^1J(^{119}Sn–^{77}Se_{mb})$, 1536 Hz, is similar to those determined for $Sn_2Se_7^{4-}$ (Chapter 3) and for the Se-bridged compound $[(CH_3)_2SnSe]_3$ (1219 Hz),[115] and the $^1J(^{119}Sn–^{77}Se_t)$ value of 2274 Hz agrees with analogous values determined for $SnSe_3^{2-}$ (2051 Hz),[56] $Sn_2Se_6^{4-}$ (2005 Hz), and $Sn_2Se_7^{4-}$ (2037 Hz) (Chapter 3).

Chemical Shifts. In the $Sn_4Se_{10}^{4-}$ anion, the ^{77}Se NMR signal corresponding to the terminal selenium, Se_t, environment was found to be more deshielded (65.0 ppm) than the signal associated with the bridging selenium, Se_{mb}, environment (22.2 ppm). The small chemical shift difference (Δ) between the two chalcogen environments in $Sn_4Se_{10}^{4-}$ (42.8 ppm) can be rationalized by using the rule of topological charge stabilization.[120] This rule has been applied to adamantanoid structures, M_4X_6, as well as to bridgehead substituted adamantanoids, $M_4X_6R_4$, and when extended to the isostructural $Sn_4Se_{10}^{4-}$ anion predicts that the 4– charge is distributed over both the Se_t and Se_{mb} atoms. This gives rise to a smaller Δ

which contrasts with the larger values observed for the dimeric $Sn_2Ch_6^{4-}$ and $Sn_2Ch_7^{4-}$ (Ch = Se, Te) anions where the 4– charge is primarily localized on the terminal atoms (Chapter 3). Interestingly, the chemical shift order in $Sn_2Te_7^{4-}$ was found to be $\delta(Te_{mb}) > \delta(Te_{db})$, which is the reverse of the order predicted by charge topology arguments and may be attributed to shielding anisotropy,[121] which may also account for the order, $\delta(Se_{mb}) < \delta(Se_t)$, observed for the $Sn_4Se_{10}^{4-}$ anion. However, in the absence of a knowledge of the ^{77}Se and ^{125}Te shielding tensors, the apparent anomalies in the ^{77}Se and ^{125}Te shielding trends are presently not fully understood.

Structural Characterization of $Sn_4Te_{10}^{4-}$ by NMR Spectroscopy

The ^{119}Sn NMR spectrum of the dark red solution obtained by extracting the alloy $K_4Sn_4Te_{10}$ in liquid NH_3 in the absence of 2,2,2-crypt was recorded at –70 °C (Figure 4.5) and was identical to that previously recorded for the liquid NH_3 extract of $KSn_{0.63}Te_{1.70}$ (Chapter 3). Three of the four ^{119}Sn resonances were assigned to the $SnTe_3^{2-}$ [$\delta(^{119}Sn)$ = –1230.1 ppm; $^1J(^{119}Sn–^{125}Te)$ = 4487 Hz], $Sn_2Te_6^{4-}$ [$\delta(^{119}Sn)$ = –1675.0 ppm; $^1J(^{119}Sn–^{125}Te)$ = 1683 (Te_{mb}) and 3998 Hz (Te_t)], and $Sn_2Te_7^{4-}$ [$\delta(^{119}Sn)$ = –1344.9 ppm; $^1J(^{119}Sn–^{125}Te)$ = 2319 (Te_{db}), 2902 (Te_{mb}), and 4032 Hz (Te_t)] anions. Whereas the singlet at –1267.5 ppm was poorly resolved in the previouly recorded ^{119}Sn NMR spectrum, the singlet in the present ^{119}Sn NMR spectrum was flanked by symmetric doublet satellites arising from $^1J(^{119}Sn–^{125}Te)$ = 3200 Hz. The observation of the ^1J coupling resulted in the correlation of this ^{119}Sn NMR resonance with one of the two previously unassigned ^{125}Te resonances [$\delta(^{125}Te)$ = –15.1 ppm;

Figure 4.5. The ^{119}Sn NMR spectrum (186.504 MHz, –70 °C) of a liquid NH_3 extract of $K_4Sn_4Te_{10}$ in the absence of 2,2,2-crypt. (A), $Sn_4Te_{10}^{4-}$; (a_1) denotes ^{125}Te satellites.

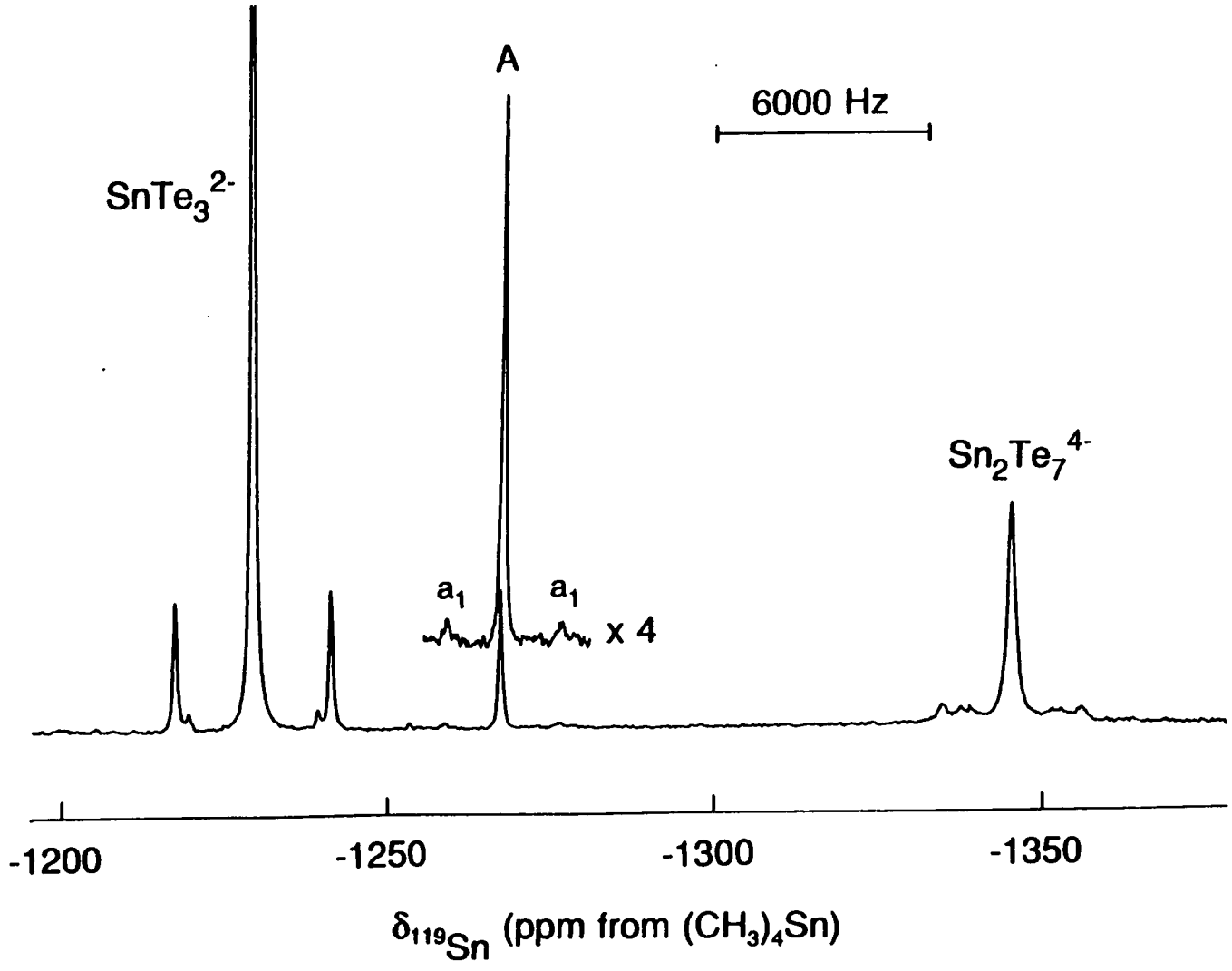
A
6000 Hz
$SnTe_3^{2-}$
$Sn_2Te_7^{4-}$
a_1
a_1
x 4
-1200
-1250
-1300
-1350
$\delta_{^{119}Sn}$ (ppm from $(CH_3)_4Sn$)

$^1J(^{125}Te-^{119}Sn)$ = 3200 Hz] observed in the ^{125}Te NMR spectrum of the $KSn_{0.63}Te_{1.70}$ alloy extract (Figure 4.6). It is therefore reasonable to conclude that the ^{119}Sn and ^{125}Te signals are associated with the same polyanion. It should be noted, however, that the ^{125}Te signal at 177.3 ppm was poorly resolved (Figure 4.6) precluding an accurate determination of the corresponding $^1J(^{125}Te-^{119}Sn)$ coupling. However, a $^1J(^{125}Te-^{119}Sn)$ value of ~3800 Hz could be measured.

Interestingly, the peak area ratio of the two ^{125}Te NMR resonances [4.2 (177.3 ppm) : 6.8 (–15.1 ppm)] is similar to that observed for the terminal selenium, Se_t, and bridging selenium, Se_{mb}, environments of the $Sn_4Se_{10}^{4-}$ anion (4.0 : 6.3; Figure 4.4). Moreover, the observed $^1J(^{119}Sn-^{125}Te)$ value of 3200 Hz corresponds to a $^1K(Sn-Te)_{RC}$ value of 108.9 × 10^{20} T^2 J^{-1} and is identical to that determined for $^1K(Sn-Se_{mb})_{RC}$ (108.2 × 10^{20} T^2 J^{-1}) in $Sn_4Se_{10}^{4-}$, suggesting the presence of a solution species isostructural with $Sn_4Se_{10}^{4-}$. Identical K_{RC} values have also been determined for $Sn–Ch_t$ and $Sn–Ch_{mb}$ in the isostructural $Sn_2Ch_6^{4-}$ and $Sn_2Ch_7^{4-}$ (Ch = Se or Te) anions (Chapter 3). It is therefore reasonable to speculate that the solution species is $Sn_4Te_{10}^{4-}$ and is supported by the X-ray crystal structure determination of the $Sn_4Te_{10}^{4-}$ anion which was obtained from an analogous en extract of $K_4Sn_4Te_{10}$. The the ^1J value of 3200 Hz can therefore be assigned to $^1J(^{119}Sn-^{125}Te_{mb})$ in $Sn_4Te_{10}^{4-}$ and the two ^{125}Te NMR resonances as the Te_{mb} (–15.1 ppm) and Te_t (177.3 ppm) environments of $Sn_4Te_{10}^{4-}$. Interestingly, $\delta(^{125}Te_{mb}) < \delta(^{125}Te_t)$ according to this assignment and is identical to the chemical shift order observed in $Sn_4Se_{10}^{4-}$ (*vide supra*).

By analogy with that of the $Sn_4Se_{10}^{4-}$ anion, the complete ^{119}Sn NMR spectrum of

Figure 4.6. The ^{125}Te NMR spectrum (157.794 MHz, –70 °C) of a liquid NH_3 extract of $KSn_{0.63}Te_{1.70}$ in the absence of 2,2,2-crypt. The symbols (a_1) and (a_2) denote the Te_t and Te_{mb} environments of $Sn_4Te_{10}^{4-}$ and (a_1') and (a_2') denote the associated ^{119}Sn satellites.

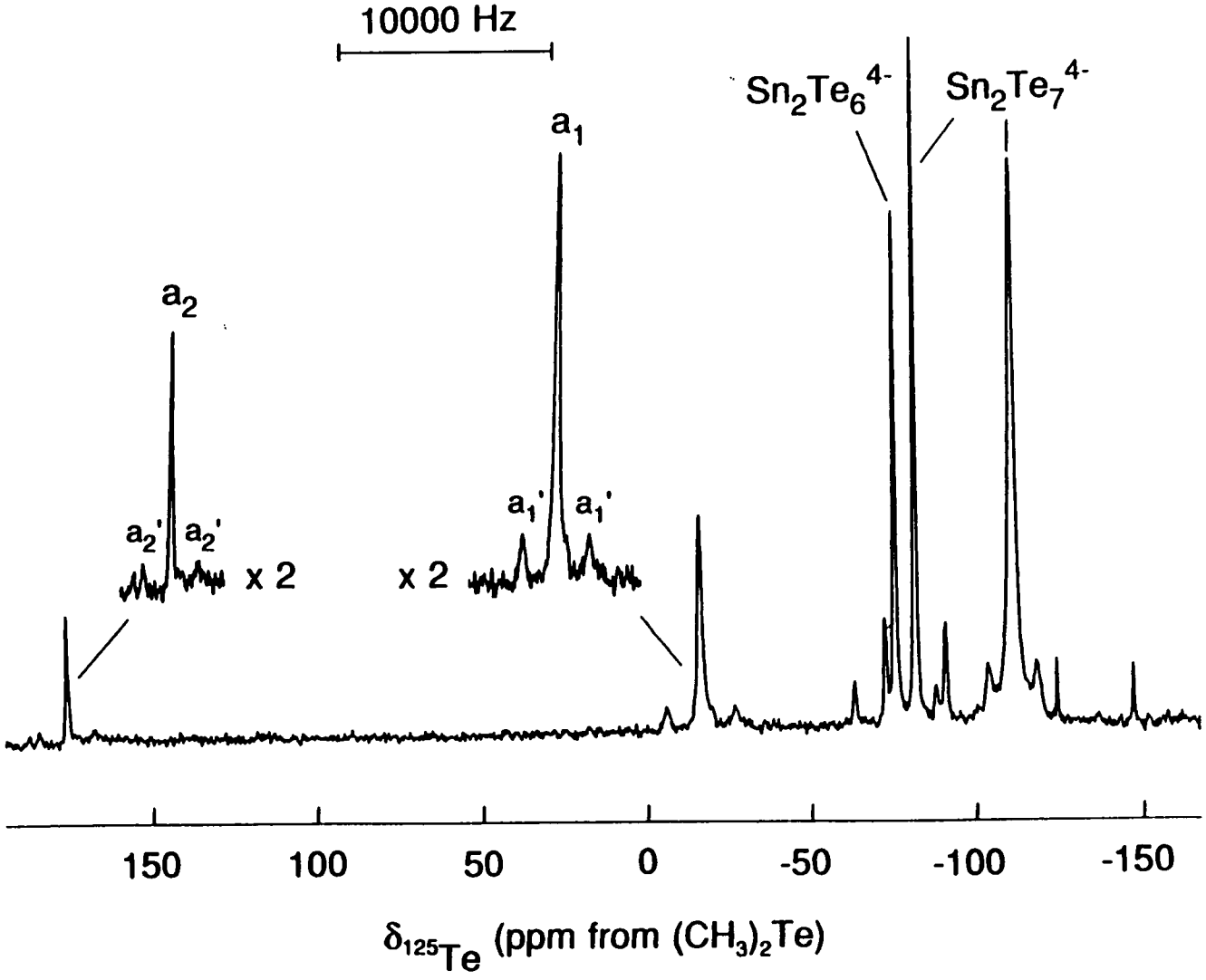
10000 Hz
$Sn_2Te_6^{4-}$
$Sn_2Te_7^{4-}$
a_1
a_2
a_2'
a_2'
x 2
a_1'
a_1'
x 2
150
100
50
0
-50
-100
-150
δ_{125}Te (ppm from $(CH_3)_2Te$)

$Sn_4Te_{10}^{4-}$ should consist of a singlet symmetrically flanked by two pairs of doublet satellites in a 1 : 3 peak intensity ratio corresponding to Te_t and Te_{mb}, respectively. Since the observed ^{119}Sn NMR resonance of $Sn_4Te_{10}^{4-}$ was extremely weak, only satellites corresponding to $^1J(^{119}Sn–^{125}Te_{mb})$ could be observed, and those associated with $^1J(^{119}Sn–^{125}Te_t)$, which are expected to be ⅔ less intense than those corresponding to $^1J(^{119}Sn–^{125}Te_{mb})$, could not be observed. However, based on the $^1K(Sn–Se_t)_{RC}$ value of 160.2 $T^2 J^{-1} \times 10^{20}$ determined for $Sn_4Se_{10}^{4-}$, $^1K(Sn–Te_t)$ and $^1J(^{119}Sn–^{125}Te_t)$ values of 328.6 $\times 10^{20}$ $T^2 J^{-1}$ and 4707 Hz, respectively, have been calculated for the $Sn_4Te_{10}^{4-}$ anion. The calculated ^1J value of 4707 Hz is in reasonable agreement with the approximate value measured from the ^{125}Te NMR spectrum (*vide supra*) and is similar to $^1J(^{119}Sn–^{125}Te_t)$ observed for $Sn_2Te_6^{4-}$ (3998 Hz), $Sn_2Te_7^{4-}$ (4023 Hz) (Chapter 3), and $SnTe_3^{2-}$ (4535 Hz).[56]

An attempt was made to prepare a solution of the $Sn_4Te_{10}^{4-}$ anion for NMR spectroscopy by dissolving crystals of the compound (18-crown-6-K^+)$_4Sn_4Te_{10}^{4-}$·3en·2THF in liquid NH_3. However, the resulting brownish-red solution was shown by ^{119}Sn NMR spectroscopy (–70 °C) to contain $SnTe_3^{2-}$ ($\delta(^{119}Sn)$ = –1181.7 ppm; $^1J(^{119}Sn–^{125}Te)$ = 3378 Hz) and two broad, featureless peaks at *ca.* –1225 ppm and –1130 ppm.

Raman Spectra of the $SnSe_4^{4-}$ and $Sn_4Ch_{10}^{4-}$ (Ch = Se, Te) Anions.

The solid state Raman spectra of, (18-crown-6-K^+)$_4Sn_4Se_{10}^{4-}$·5en, (18-crown-6-K^+)$_4Sn_4Te_{10}^{4-}$·3en·2THF, and (Na^+)$_4SnSe_4^{4-}$· 2en[148] are shown in Figures 4.1, 4.2, and 4.7, respectively, and the Raman frequencies and their assignments are listed in Table 4.8.

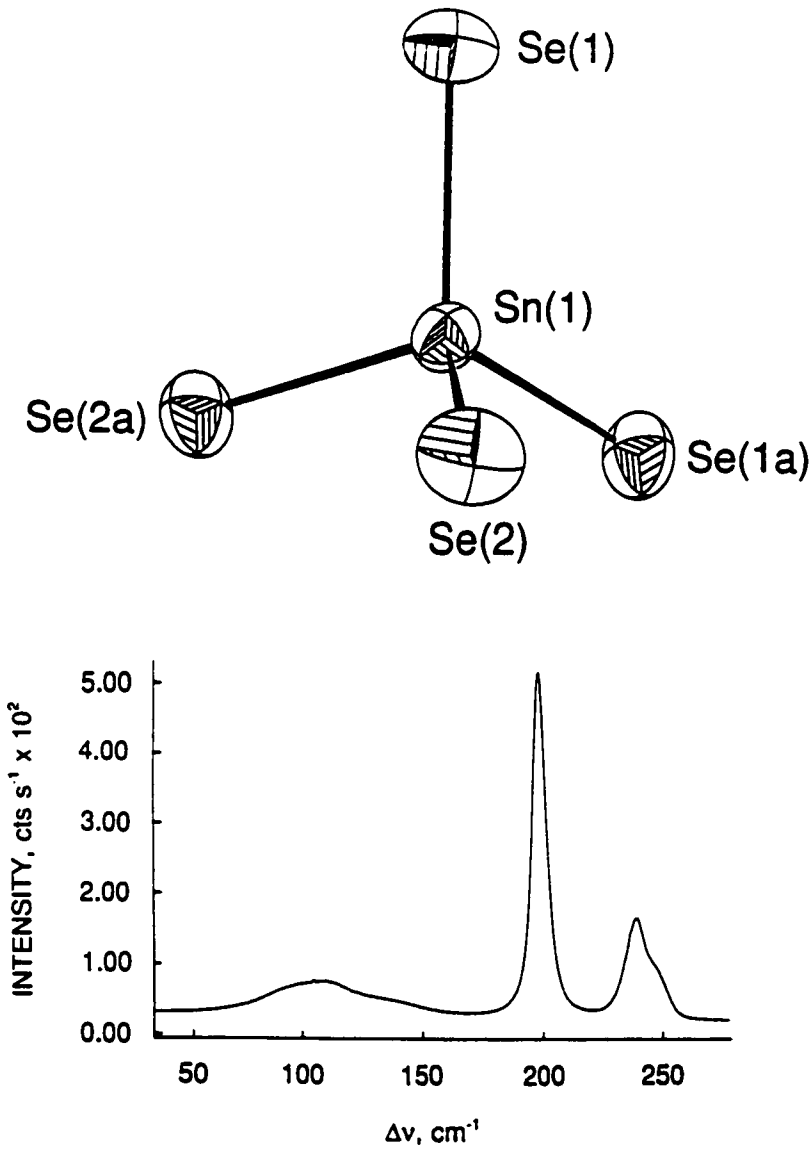

Figure 4.7. View and Raman spectrum of the $SnSe_4^{4-}$ anion in $(Na^+)_4SnSe_4^{4-}\cdot 2en$ with displacement ellipsoids drawn at the 50% probability level.

Table 4.8. Raman Frequencies and Assignments for $SnSe_4^{4-}$ and $Sn_4Ch_{10}^{4-}$ (Ch = Se, Te) and the Related SnS_4^{4-} and $Ge_4S_{10}^{4-}$.

frequency, cm^{-1}			frequency, cm^{-1}				
SnS_4^{4-} [a]	$SnSe_4^{4-}$	assignments	$Ge_4S_{10}^{4-}$ [b]	$Sn_4Se_{10}^{4-}$ [c]	$Sn_4Se_{10}^{4-}$ [d]	$Sn_4Te_{10}^{4-}$	assignments
150 [e]	109(10)	$\nu_2(E)$	112(5)	59(12)	54(13)		$\nu_{15}(T_2)$
170 [e]	136(5)	$\nu_4(T_2)$	148(14)	74(40)	75(44)	90(3)	$\nu_{14}(T_2)$
348(st)	199(100)	$\nu_1(A_1)$	160 [e]	81 sh	81sh		$\nu_5(E)$
344 (m)	239(29), 247 sh	$\nu_3(T_2)$	193(29)	108(58)	109(55)	102(3)	$\nu_3(A_1)$
			210(2)				$\nu_{13}(T_2)$
			346(100)	178(100)	178(100)	118(100)	$\nu_2(A_1)$
			378(4)	188(9), 200(4)	190(5)		$\nu_{12}(T_2)$
			405(10)	227(4), 238(11)	229(13), 237(20)		$\nu_{11}(T_2)$
			446sh	268sh	271sh		$\nu_{10}(T_2)$
			457(22)	274(51)	275(48)	139(20)	$\nu_1(A_1)$
			410 [e]	290sh	290sh		$\nu_5(E)$

[a] Reference (135). [b] Reference (149). [c] Reference (113). [d] Present work. [e] Obtained from a normal coordinate analysis.

$SnSe_4^{4-}$. The vibrational modes of the $SnSe_4^{4-}$ anion were assigned under T_d point symmetry and belong to the irreducible representations $A_1 + E + 2T_2$. A total of four vibrational bands are expected, $\nu_1(A_1)$, $\nu_2(E)$, $\nu_3(T_2)$ and $\nu_4(T_2)$, all of which are Raman active, while the $\nu_3(T_2)$ and $\nu_4(T_2)$ bands are also infrared active. Assignments were made by analogy with the isovalent SnS_4^{4-} anion.[135] Among the four bands expected for SnS_4^{4-}, only the two high-frequency modes, $\nu_1(A_1)$ and $\nu_2(E)$, were observed. Their assignment was confirmed by using polarization measurements and normal coordinate analyses, which also calculated the frequencies for $\nu_3(T_2)$ and $\nu_4(T_2)$.

Two sharp and two broad bands were observed in the Raman spectrum of $SnSe_4^{4-}$. The most intense peak (199 cm^{-1}) was assigned to the totally symmetric Sn–Se stretch, $\nu_1(A_1)$. A peak at 239 cm^{-1} was assigned to the asymmetric Sn–Se stretch, $\nu_3(T_2)$, and was split due to site symmetry lowering in the crystal (C_2 crystal site symmetry). The broad bands at lower wave numbers (109 and 136 cm^{-1}) were assigned to the partially overlapping antisymmetric Se–Sn–Se bends, $\nu_2(E)$ and $\nu_4(T_2)$, respectively. As expected, the stretching frequencies decrease from SnS_4^{4-} to $SnSe_4^{4-}$ in accord with the reduced mass effect (Table 4.8).

$Sn_4Se_{10}^{4-}$. The fundamental modes of the $Sn_4Se_{10}^{4-}$ anion were assigned under T_d point symmetry and belong to the irreducible representations $3A_1 + 3E + 3T_1 + 6T_2$. Modes belonging to the A_1, E, and T_2 representations are Raman active, the T_1 modes are inactive, and the T_2 modes are also infrared active. A factor-group analysis was performed by using the site symmetry of the $Sn_4Se_{10}^{4-}$ anion within the primitive unit cell. Correlation of the free

anion symmetry (T_d) with its site symmetry (C_1) to the crystal symmetry (C_{2h}) revealed that each band of the anion is split into an A_g and a B_g component (A_u and B_u in the infrared spectrum) under C_{2h} crystal symmetry (Table 4.9). Only 9 of the possible 15 bands were observed, and the factor-group splittings are too small to be resolved.

The Raman spectrum for $Sn_4Se_{10}^{4-}$ [113] has been reported for (2,2,2-crypt-K^+)$_4Sn_4Se_{10}^{4-}$ and is in agreement with the anion frequencies in (18-crown-K^+)$_4Sn_4Se_{10}^{4-}$·5en. The $Sn_4Se_{10}^{4-}$ vibrational modes in the 2,2,2-crypt-K^+ salt were made by analogy with those of $Ge_4S_{10}^{4-}$,[149] which was assigned on the basis of polarization measurements and a normal coordinate analysis, and those of the Sn_4Se_6 fragment of $(CH_3)_4Sn_4Se_6$,[145] which was assigned on the basis of a normal coordinate analysis. Overall, the $Sn_4Se_{10}^{4-}$ anion modes were shifted to lower frequency relative to those of $Ge_4S_{10}^{4-}$ by virtue of the reduced mass effect (Table 4.8). The most intense band at 178 cm^{-1} was assigned to $\nu_2(A_1)$, the totally symmetric breathing mode of the Sn_4Se_6 cage. The intense band at 275 cm^{-1} was assigned to the totally symmetric stretching mode, $\nu_2(A_1)$, associated with the terminal Sn–Se bonds and was significantly higher in frequency than $\nu_1(A_1)$ in $SnSe_4^{4-}$ (199 cm^{-1}). An analogous trend has been observed for $Ge_4S_{10}^{4-}$ (457 cm^{-1})[149] and GeS_4^{4-} (386 cm^{-1}).[135] In $SnSe_4^{4-}$ and GeS_4^{4-}, the negative charge of the anion is localized on the chalcogens, whereas in the adamantanoid $Ge_4S_{10}^{4-}$ and $Sn_4Se_{10}^{4-}$ cages, a significant portion of the negative charge also resides on the bridging chalcogens. Thus, the M–Ch bond lengths in GeS_4^{4-} [2.20(5) Å][150] and in $SnSe_4^{4-}$ [2.523(1)–2.516(1) Å][104] are significantly longer than the corresponding terminal M–Ch bond lengths in $Ge_4S_{10}^{4-}$ [2.108(11) Å][141] and $Sn_4Se_{10}^{4-}$ [2.4187(7)–2.4310(7) Å] and are in accord

Table 4.9. Correlation Diagrams for the Vibrational Modes of the $Sn_4Ch_{10}^{2+}$ (Ch = Se or Te) Anions in (18-crown-6-K^+)$_4Sn_4Se_{10}^{2+}$·5en and (18-crown-6-K^+)$_4$-$Sn_4Te_{10}^{2+}$·3en·2THF. [a]

	mol. symm.	site symm.	crystal symm.	
	T_d	C_1	C_{2h}	
$4\nu_1 - 4\nu_3$	A_1	A	A_g (R)	$\nu_1 - \nu_{15}$, 3R, 3T
$4\nu_4 - 4\nu_6$	E		B_g (R)	$\nu_1 - \nu_{15}$, 3R, 3T
$4\nu_7 - 4\nu_9$, 12R	T_1		A_u (IR)	$\nu_1 - \nu_{15}$, 3R, 3T
$4\nu_{10} - 4\nu_{15}$, 12T	T_2		B_u (IR)	$\nu_1 - \nu_{15}$, 3R, 3T

[a] Both compounds crystallize in the monoclinic $P2_1/n$ space group with Z = 4. R and T denote rotatory and translatory (external) modes, respectively, and (R) and (IR) denote Raman and infrared activity, respectively.

with the observed frequency order.

Assignments of the A_1 and T_2 fundamentals of the Sn_4Se_6 cage of $Sn_4Se_{10}^{4-}$ are in agreement with those observed for $(CH_3)_4Sn_4Se_6$, where the $\nu_2(A_1)$ and $\nu_3(A_1)$ counterparts occur at 191(vs) and 80(vs) cm^{-1}, respectively, and the $\nu_{11}(T_2)$ and $\nu_{12}(T_2)$ counterparts occur as site symmetry split bands at 252(s), 248(s) cm^{-1} and 210(m), 208.5(m) cm^{-1}, respectively.

The E fundamentals were difficult to assign as they should have low intensities in the Raman spectrum and were not observed for $Ge_4S_{10}^{4-}$ or for the Sn_4Se_6 cage of $(CH_3)_4Sn_4Se_6$, but have been calculated. Consequently, the shoulders at 81 and 290 cm^{-1} were tentatively assigned to the $\nu_4(E)$ and $\nu_5(E)$ modes of $Sn_4Se_{10}^{4-}$. Assignments of the T_2 fundamentals also follow those of $Ge_4S_{10}^{4-}$ except that two components are resolved for the broad weak feature assigned to $\nu_{11}(T_2)$. The splitting is consistent with site symmetry lowering which leads to removal and partial resolution of the triple degeneracy.

$Sn_4Te_{10}^{4-}$. The Raman spectrum of $Sn_4Te_{10}^{4-}$ consists of several overlapping peaks and is attributed to the similarity in the masses of tin and tellurium. Moreover, because of the small mass difference, the vibrational modes are expected to be even more strongly coupled than in $Sn_4Se_{10}^{4-}$ and in $Ge_4S_{10}^{4-}$. A similar pattern has been observed in the Raman spectrum of $Sn_2Te_6^{4-}$ when compared to that of $Sn_2Se_6^{4-}$ (Chapter 3). A factor-group analysis was performed for the $Sn_4Te_{10}^{4-}$ (Table 4.9). Only 4 of the expected 15 bands were observed, and the factor-group splittings are too small to be resolved. Tentative assignments have been made by analogy with the Raman spectrum of $Sn_4Se_{10}^{4-}$. Because of the reduced mass effect, the vibrational modes of $Sn_4Te_{10}^{4-}$ are shifted to lower frequencies relative to those of

$Sn_4Se_{10}^{4-}$. The most intense peak at 119 cm^{-1} was assigned to $\nu_2(A_1)$, the totally symmetric breathing mode of the Sn_4Te_6 cage. The intense band at 139 cm^{-1} was assigned to the totally symmetric stretching mode, $\nu_2(A_1)$, associated with the terminal Sn–Te bonds. The remaining weak bands were assigned to the A_1 and T_2 fundamentals.

X-ray Crystal Structure of $Sn_4Se_9^{4-}$.

As mentioned in the Experimental Section, the exact composition of the title compound is still under investigation. The ensuing discussion will therefore only describe the $Sn_4Se_9^{4-}$ anion, whose geometry has been satisfactorily modeled at the present stage in the refinement of the structure.

A summary of the crystal data and preliminary refinement results are given in Table 4.1. The atomic coordinates and equivalent isotropic thermal parameters for the Sn, Se, and K atoms are summarized in Table 4.10. The most significant bond distances and angles in the $Sn_4Se_9^{4-}$ anions are listed in Table 4.11. The structure of the 2,2,2-crypt-K^+ cations in the title compound is similar to that observed in $K^+(2,2,2\text{-crypt-}K^+)_3Pb_9^{4-}$ and in $(2,2,2\text{-crypt-}K^+)_3Pb_9^{3-}$,[29] with an average K···O [K···N] distance of 2.835(8) [2.972(15)] Å.

The compound contains a novel adamantanoid $Sn_4Se_9^{4-}$ anion of ~C_{3v} point symmetry (Figure 4.8) making it isostructural with P_4S_9[151] and P_4O_9.[152,153] The $Sn_4Se_9^{4-}$ anion can be viewed as being obtained by the removal of an Se_t atom from $Sn_4Se_{10}^{4-}$ and contains tin in its two formal oxidations states, i.e., +II (× 1) and +IV (× 3). As in the $Sn_4Ch_{10}^{4-}$ anion structures, the geometry about the Sn(IV) atoms is tetrahedral [average Se–Sn(IV)–Se,

Table 4.10. Atomic Coordinates and Equivalent Isotropic Thermal Parameters ($Å^2$) for the Sn, Se, and K atoms in (2,2,2-crypt-K^+)$_4$$Sn_4Se_9^{4-}$·en·THF.

	x	*y*	*z*	U_{eq} [a]
Sn(1)	0.12652(5)	0.98741(7)	0.19227(4)	0.0470(3)
Sn(2)	0.25382(3)	1.08505(5)	0.10460(3)	0.0279(2)
Sn(3)	0.27979(3)	0.86903(5)	0.16291(3)	0.0224(2)
Sn(4)	0.28900(3)	1.05931(4)	0.25479(3)	0.0223(2)
Se(1)	0.17624(6)	0.86054(9)	0.16622(5)	0.0357(3)
Se(2)	0.15095(6)	1.07156(10)	0.11744(5)	0.0390(3)
Se(3)	0.18588(5)	1.04835(8)	0.26632(5)	0.0331(3)
Se(4)	0.30254(6)	1.14849(7)	0.18049(4)	0.0299(3)
Se(5)	0.32569(5)	0.92106(7)	0.24221(4)	0.0249(2)
Se(6)	0.32569(5)	0.92106(7)	0.24221(4)	0.0249(2)
Se(7)	0.25845(6)	1.16079(9)	0.02917(5)	0.0356(3)
Se(8)	0.31434(7)	0.73712(8)	0.15071(5)	0.0390(3)
Se(9)	0.34221(6)	1.11289(8)	0.32482(5)	0.0377(5)
K(1)	0.48248(10)	0.81685(14)	0.46196(8)	0.0222(5)
K(2)	0.40157(10)	1.49588(15)	0.32470(9)	0.0245(5)
K(3)	0.09085(11)	1.45990(2)	0.15142(10)	0.0287(5)
K(4)	0.14626(10)	0.65710(2)	0.39202(9)	0.0269(5)

[a] U_{eq} is defined as one-third of the trace of the orthogonalized U_{ij} tensor.

Table 4.11. Selected Bond Lengths (Å) and Bond Angles (deg) for (2.2.2-crypt-K^+)$_4Sn_4Se_9^{4-}$·en·THF.

Bond Lengths (Å)			
Sn(1)–Se(1)	2.604(2)	Sn(3)–Se(1)	2.515(2)
Sn(1)–Se(2)	2.583(2)	Sn(3)–Se(5)	2.5622(14)
Sn(1)–Se(3)	2.642(2)	Sn(3)–Se(6)	2.5487(14)
Sn(3)–Se(8)	2.444(2)	Sn(2)–Se(2)	2.540(2)
Sn(4)–Se(3)	2.535(2)	Sn(2)–Se(4)	2.578(2)
Sn(4)–Se(4)	2.5719(14)	Sn(2)–Se(5)	2.563(2)
Sn(4)–Se(6)	2.5644(15)	Sn(2)–Se(7)	2.440(2)
Sn(4)–Se(9)	2.436(2)		
Bond Angles (deg)			
Se(1)–Sn(1)–Se(2)	97.48(6)	Se(5)–Sn(3)–Se(6)	108.43(5)
Se(1)–Sn(1)–Se(3)	107.33(6)	Se(5)–Sn(3)–Se(8)	110.48(5)
Se(6)–Sn(3)–Se(8)	107.56(5)	Se(2)–Sn(1)–Se(3)	104.09(6)
Se(3)–Sn(4)–Se(4)	107.55(6)	Se(3)–Sn(4)–Se(6)	107.22(5)
Se(3)–Sn(4)–Se(9)	114.87(6)	Se(2)–Sn(2)–Se(4)	110.02(6)
Se(4)–Sn(4)–Se(6)	112.96(5)	Se(2)–Sn(2)–Se(5)	115.83(6)
Se(4)–Sn(4)–Se(9)	108.11(6)	Se(2)–Sn(2)–Se(7)	104.38(6)
Se(6)–Sn(4)–Se(9)	106.29(5)	Se(4)–Sn(2)–Se(5)	104.83(5)
Sn(3)–Se(1)–Sn(1)	115.71(6)	Se(4)–Sn(2)–Se(7)	114.48(5)
Sn(1)–Se(2)–Sn(2)	114.89(7)	Se(5)–Sn(2)–Se(7)	107.61(5)
Sn(4)–Se(3)–Sn(1)	116.11(6)	Se(1)–Sn(3)–Se(5)	110.16(6)
Sn(4)–Se(4)–Sn(2)	108.08(5)	Se(1)–Sn(3)–Se(6)	112.84(6)
Sn(3)–Se(5)–Sn(2)	105.36(5)	Se(1)–Sn(3)–Se(8)	107.35(6)
Sn(4)–Se(6)–Sn(3)	107.32(5)		

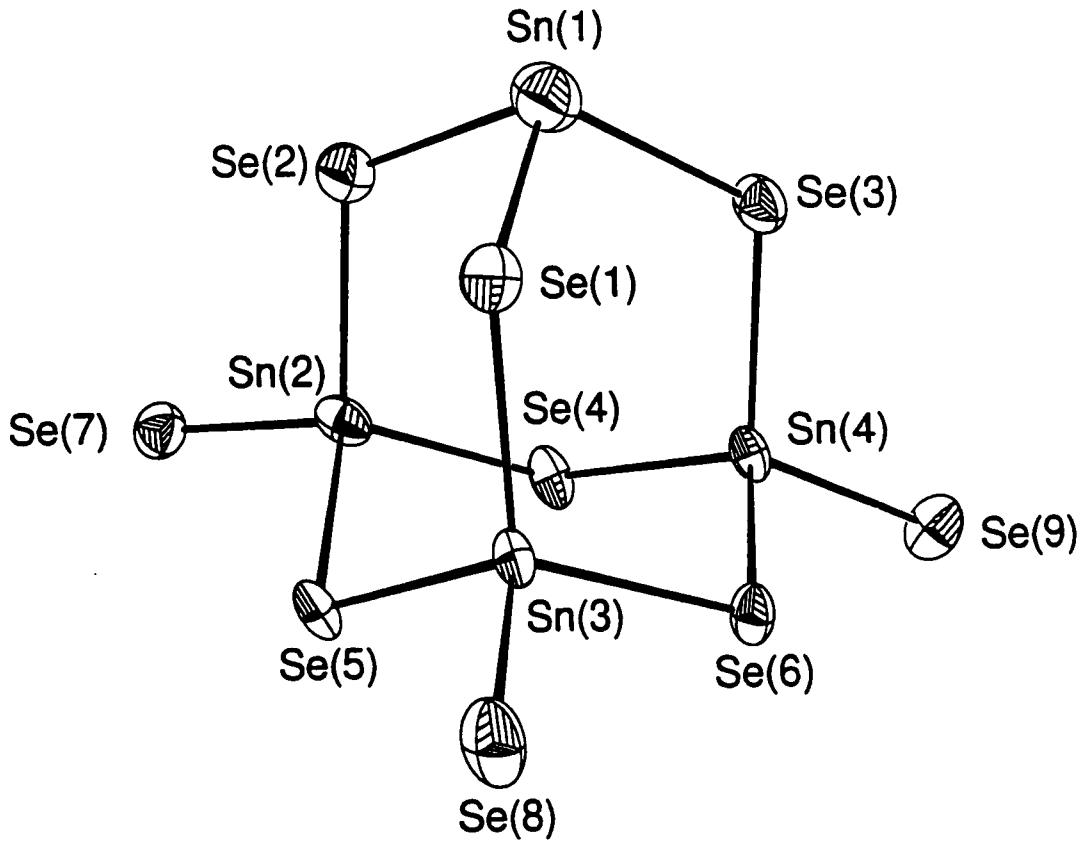

Figure 4.8. View of the $Sn_4Se_9^{4-}$ anion in (2,2,2-crypt-K^+)$_4Sn_4Se_9^{4-}$·en·THF. The displacement ellipsoids are drawn at the 50% probability level.

109.5(8)°] and the environment about the Sn(II) atoms is trigonal pyramidal [average Se–Sn(IV)–Se, 103.0(28)°]. The average Ch–Sn–Ch bond angle in the trigonal-pyramidal $Sn(II)Se_3$-fragment is larger than those in the trigonal-bipyramidal $Sn_2Ch_3^{2-}$ (Ch = Se, Te) anion structures: Se, 87.9(1)–92.1(1)° and Te, 90.8(2)–90.9(1)° . As expected, the Sn–Se_t bond distances in $Sn_4Se_9^{4-}$ are considerably shorter than the Sn–Se_{mb} distances. The average Sn–Se_t [2.440(2) Å] and Sn–Se_{mb} [2.567(10) Å] bond distances are comparable to those observed in $Sn_4Se_{10}^{4-}$ [2.425(3) and 2.550(2) Å, respectively].

Conclusion

The $Sn_4Ch_{10}^{4-}$ anions have been synthesized as their 18-crown-6-K^+ salts. The adamantanoid geometry (T_d point symmetry) of the anions was established in the solid state by X-ray crystallography and Raman spectroscopy and in solution by ^{119}Sn, ^{77}Se, and ^{125}Te NMR spectroscopy. The solution structure of the $Sn_4Se_{10}^{4-}$ anion was confirmed by a detailed analysis of the ^{119}Sn NMR subspectra arising from natural abundance isotopomer distributions, and the $^1J(^{119}Sn–^{77}Se_t)$ and $^1J(^{119}Sn–^{125}Te_{mb})$ coupling constants were shown to correlate with the Sn–Se_t and Sn–Se_{mb} bond lengths. The terminal Sn–Ch stretching frequencies observed for the $SnSe_4^{4-}$ and $Sn_4Se_{10}^{4-}$ are in accord with the relative lengths of the terminal Sn–Se bonds. The novel $Sn_4Se_9^{4-}$ anion has also been structurally characterized by X-ray crystallography and represents the first P_4O_9-type anion containing tin and a chalcogen.

CHAPTER 5

THE $Tl_2Ch_2^{2-}$ (Ch = Se and/or Te) ANIONS

Introduction

It has been recognized for some time that many Zintl-type anions are analogous to better known compounds formed by the elements from the first and second rows of the periodic table. For example, the homopolyatomic E_5^{2-} (E = Ge,[24] Sn,[25] Pb[25]) clusters possess skeletal bonding arrangments similar to those exhibited by $B_5H_5^{2-}$ and $C_2B_3H_5$,[35,154] and the square-planar 6π-electron quasi-aromatic Sb_4^{2-} [155] and Bi_4^{2-} [156] anions with 22 valence electrons possess bonding arrangements similar to those of P_4^{2-} [157] and $C_4H_4^{2-}$ [35]. The 20 valence electron Pb_4^{4-},[158] Tl_4^{8-},[159] $Sn_2Bi_2^{2-}$,[160] and $Pb_2Sb_2^{2-}$ [161] anions exhibit tetrahedral geometries that are isovalent with P_4,[162] As_4,[163] and Sb_4[163] and are consistent with localized electron precise valence structures having covalent 2-centre-2-electron bonds directed along the six edges of the tetrahedron and one valence lone electron pair on each atom.[164] The bonding molecular orbitals have been shown to consist of a combination of essentially pure *p* atomic orbitals, whereas the lone-electron pair molecular orbitals are comprised of valence *s* atomic orbitals.[164,165] The HOMO's were shown to be composed primarily of atomic *p* orbitals on the electropositive atoms, and the LUMO's, which possess antibonding character, were shown to be localized primarily on the more electronegative atoms. Interestingly, the $Tl_2Te_2^{2-}$ anion,[44] which is isovalent with $Sn_2Bi_2^{2-}$, $Pb_2Sb_2^{2-}$ and P_4, exhibits an unique

butterfly geometry in which the thallium atoms lie along the fold of the wings and is intermediate between the tetrahedral geometry adopted by 20-valence-electron systems and the square-planar geometry associated with tetranuclear species having 22 valence electrons. The departure from the anticipated tetrahedral geometry has been attributed to the large electronegativity difference between the Tl and Te atoms.[119,164,165] A purely ionic model describing the bonding in $Tl_2Te_2^{2-}$ as the coordination of two Tl^+ cations and two Te^{2-} anions has therefore been proposed.[164] In contrast, a covalent model, as in P_4, has been used to describe the bonding in $Sn_2Bi_2^{2-}$ and $Pb_2Sb_2^{2-}$ which contain atoms that are closer to one another in the periodic table and have similar electronegativities.[119,164] The puckering observed for the $Tl_2Te_2^{2-}$ anion (2,2,2-crypt-K^+)$_2Tl_2Te_2^{2-}\cdot$ en is, however, inconsistent with a purely ionic model because the arrangement of ions in ionic compounds tends to minimize Coulombic repulsions by maximizing interatomic distances between centres having the same charges and would therefore be expected to give a planar structure for $(Tl^+)_2(Te^{2-})_2^{2-}$. The distortion from planarity has been attributed, using spin-restricted scattered-wave Xα calculations, to the repulsive interaction between the antisymmetric combination of the Tl 6*s* atomic orbital and the occupied molecular orbital composed primary of Te 5*p* atomic orbitals. *Ab initio* and extended Hückel calculations on tetranuclear 20-electron systems[165] have indicated that an energetic interchange of the frontier molecular orbitals associated with a greater electronegativity difference between the bonding atoms can account for the preference of the butterfly geometry adopted by $Tl_2Te_2^{2-}$ over the tetrahedral one. *Ab initio* and extended Hückel calculations predict a planar structure for the isoelectronic 20 valence-

electron system, Tl_2I_2, in which the electronegativity difference between the atoms is larger when compared to that in the $Tl_2Te_2^{2-}$ anion. Accordingly, a more planar structure is anticipated and has been observed and calculated for the $Tl_2Se_2^{2-}$ anion[33,166] when compared to that of the Te analog.

Although the $Tl_2Ch_2^{2-}$ (Ch = Se and/or Te) anions have been characterized by solution multi-NMR spectroscopy[56] and the $Tl_2Te_2^{2-}$ anion by X-ray crystallography in (2,2,2-crypt-K^+)$_2Tl_2Te_2^{2-}\cdot$ en,[44] the X-ray crystal structure of $Tl_2Se_2^{2-}$ has only recently been reported,[33,166] and attempts to study these anions by vibrational spectroscopy have never been published. The $Tl_2Ch_2^{2-}$ anion vibrational modes, including that associated with inversion mode of the anions along the fold angle (the dihedral angle between the two Tl_2Ch-planes in the anion structures), are anticipated to be extremely low in energy. The anticipated deformability of the $Tl_2Ch_2^{2-}$ anions about the fold angle may be strongly influenced by environmental effects such as crystal packing and solvent coordination and may give rise to energy-minimized geometries in the gas phase having significantly different Tl···Tl distances and fold angles than in the solid state. Only single-point theoretical calculations have been reported for the experimental $Tl_2Te_2^{2-}$ anion geometry in (2,2,2-crypt-K^+)$_2Tl_2Te_2^{2-}\cdot$ en, and no attempts have been made to optimize the gas-phase geometry of the anion. A comparison of the gas-phase geometry with the experimental one should provide a means to assess the extent to which environmental factors influence the geometries of the $Tl_2Ch_2^{2-}$ anions.

The present Chapter reports a variable-temperature solution multi-NMR study of the $Tl_2Te_2^{2-}$ anion in en and liquid ammonia solvents and the X-ray crystal structure of the

$Tl_2Te_2^{2-}$ anion in the absence of solvent in the crystal lattice. Density functional theory calculations at the local and non-local levels have been used to derive the energy-minimized geometries of the $Tl_2Ch_2^{2-}$ (Ch = Se and/or Te) anions and to study the nature of the bonding in these anions. Density functional theory calculations have also been used to assign the vibrational spectra of the $Tl_2Ch_2^{2-}$ (Ch = Se or Te) anions.

Results and Discussion

Synthesis of the $Tl_2Te_2^{2-}$ Anion.

The experimental approach involved the synthesis of the ternary MTlTe (M = Na, K) alloys by fusion of the elements followed by extraction of the powdered alloys in en or liquid NH_3 in the presence of a molar excess of 2,2,2-crypt with respect to M^+. All attempts to obtain crystals of $(2,2,2\text{-crypt-}K^+)_2Tl_2Te_2^{2-}$ from an en solution of NaTlTe containing a 20 mole% excess of 2,2,2-crypt with respect to Na^+ resulted in the formation of microcrystalline material. Crystals of $(2,2,2\text{-crypt-}K^+)_2Tl_2Te_2^{2-}$ suitable for an X-ray structure determination were obtained upon addition of THF to a dark green en/ethylamine (1:1 v/v) solution resulting from the reaction of K_2Te and Tl_2Te in a 1:2 molar ratio in the presence of a 37 mole% deficit of 2,2,2-crypt with respect to K^+. The dark green solution had previously been shown by $^{203,205}Tl$ NMR spectroscopy to contain the $Tl_2Te_2^{2-}$ anion as the major species in solution along with small amounts of $TlTe_3^{3-}$ and $TlTe_2^{3-}$.[85]

X-ray Crystal Structure of (2,2,2-crypt-K^+)$_2Tl_2Te_2^{2-}$.

A summary of the refinement results and other crystallographic information are given in Table 5.1. The final atomic coordinates and equivalent isotropic thermal parameters for the Tl, Te, and K atoms are summarized in Table 5.2. The most significant interatomic and transannular distances and the most significant bond angles in $Tl_2Te_2^{2-}$ and in $Tl_2Se_2^{2-}$, including the fold angles, are listed in Table 5.3 along with the calculated values (see **Computational Results**). The structure of the 2,2,2-crypt-K^+ cations in the title compound is similar to those previously determined in (2,2,2-crypt-K^+)$_2Tl_2Se_2^{2-}$ [33,166] and in (2,2,2-crypt-K^+)$_2Tl_2Te_2^{2-}$·en,[44] with K···O [K···N] distances ranging from 2.697(5)–2.791(5) [2.933(5)–2.955(6)] Å.

The crystal structure of the title compound consists of ordered 2,2,2-crypt-K^+ cations and $Tl_2Te_2^{2-}$ anions disordered about a centre of symmetry and contrasts with the crystal structure of the Se analogue which consists of ordered $Tl_2Se_2^{2-}$ anions and disordered 2,2,2-crypt-K^+ cations. The most interesting aspect of the structure is the butterfly-shaped geometry of the anion (~C_{2v} point symmetry) in which the thallium atoms are located along the fold of the wings (Figure 5.1). This geometry has been previously observed in (2,2,2-crypt-K^+)$_2Tl_2Se_2^{2-}$ and in (2,2,2-crypt-K^+)$_2Tl_2Te_2^{2-}$·en. The fold angle in $Tl_2Se_2^{2-}$ (9.6°) is significantly smaller than that in $Tl_2Te_2^{2-}$ (17.4°) and is consistent with the higher electronegativity of Se when compared with that of Te.[119] Interestingly, the fold angle in the present $Tl_2Te_2^{2-}$ anion is considerably smaller than in the previously characterized salt (39.9°) and is discussed in a subsequent section (see **Computational Results**).

Table 5.1. Summary of Crystal Data and Refinement Results for $(2.2.2\text{-crypt-}K^+)_2\text{-}Tl_2Te_2^{2-}$.

Formula	$C_{36}H_{72}N_4O_{11}K_2Tl_2Te_2$
Space group (No.)	$P\bar{1}$ (No. 2)
a, Å	10.976(2)
b, Å	11.112(2)
c, Å	11.629(2)
α, deg	64.05(3)
β, deg	84.29(3)
γ, deg	81.47(3)
V, $Å^{-3}$	1260.3(4)
Z	1
mol. wt.	1495.12
ρ, g cm^{-3}	1.970
morphology	platelet
dimensions, cm	0.45 × 0.12 × 0.28
colour	deep red
refinement method	F^2
reflections used	6111
reflections suppressed ($F^2 < -2\sigma F^2$)	44
parameters refined	268
H-atom method	calculated
R_1 ($F^2 > 2\sigma F^2$)	0.0743
wR_2 (F^2)	0.2030
S ($F^2 > \sigma F^2$)	1.170
$\Delta\rho_{max}$, e $Å^{-3}$	5.076
$\Delta\rho_{min}$, e $Å^{-3}$	–4.774
w	$w_1 = 0.1080$
	$w_2 = 6.5603$

Table 5.2. Atomic Coordinates and Equivalent Isotropic Thermal Parameters ($Å^2$) for the Tl, Te, and K atoms in $(2,2,2\text{-crypt-}K^+)_2Tl_2Te_2^{2-}$.

	x	*y*	*z*	U_{eq}[a]
Tl(1A)	0.3428(3)	0.9985(3)	0.4459(2)	0.0399(4)
Tl(1B)	0.3605(3)	0.9974(3)	0.4269(2)	0.0399(4)
Te(1A)	0.4871(4)	0.7880(6)	0.6639(4)	0.0435(7)
Te(1B)	0.5070(3)	0.7843(6)	0.6471(4)	0.0435(7)
K(1)	0.10744(11)	1.32041(12)	–0.18028(12)	0.0199(3)

[a] U_{eq} is defined as one-third of the trace of the orthogonalized U_{ij} tensor.

Table 5.3. Experimental and Calculated Geometries for the $Tl_2Ch_2^{2-}$ (Ch = Se and/or Te) Anions.[a]

exp.		LDFT		NLDFT		LDFT
		PP/PP	PP/DZVP	PP/PP	PP/DZVP	ECP
			$Tl_2Se_2^{2-}$ (C_{2v})			
Tl···Tl (Å)	3.698(2)	3.540	3.629	3.561	3.674	3.555
Tl–Se (Å)	2.781(3)	2.736	2.943	2.755	2.966	2.821
Se···Se (Å)	4.140(3)	3.993	4.555	4.024	4.587	4.219
Tl–Se–Tl (°)	83.34(1)	80.6	76.1	80.5	75.9	78.1
Se–Tl–Se (°)	96.21(7)	93.7	101.4	93.8	101.3	96.8
fold angle (°)	9.6	33.8	21.3	33.8	22.6	31.2
			$Tl_2Te_2^{2-}$ (C_{2v})[b]			
Tl···Tl (Å)	3.798(2) [3.600(3)]	3.655	3.727	2.681	3.768	3.675
Tl–Te (Å)	2.956(2) [2.954(11)]	2.913	3.111	2.936	3.139	3.040
Te···Te (Å)	4.552(2) [4.414(3)	4.302	4.813	4.337	4.851	4.690
Tl–Te–Tl (°)	79.1(2) [75.1(3)]	77.7	73.6	77.7	73.8	74.0
Te–Tl–Te (°)	97.7(2) [96.6(2)	95.2	101.4	95.2	101.2	101.0
fold angle (°)	17.4 [39.9]	37.1	29.9	37.0	29.9	30.0

Table 5.3. Continued.

	Tl_2SeTe^{2-} (C_s)		
	LDFT PP/PP	NLDFT PP/PP	LDFT ECP/DZVP
Tl···Tl (Å)	3.583	3.612	3.600
Tl–Se (Å)	2.720	2.735	2.802
Tl–Te (Å)	2.934	2.962	3.060
Te···Se (Å)	4.155	4.198	4.455
Tl–Se–Tl (°)	82.4	82.6	79.9
Tl–Te–Tl (°)	75.3	75.1	72.1
Te–Tl–Se (°)	94.5	94.9	98.8
fold angle (°)	38.7	35.1	31.0

[a] The fold angle in the $Tl_2Ch_2^{2}$ anion structures is the dihedral angle between the two Tl_2Ch-planes. [b] Values reported in square brackets refer to the $Tl_2Te_2^{2}$ anion structure in (2,2,2-crypt-K$^+$)$_2$ $Tl_2Te_2^{2}$ · en and are taken from ref. (44). The fold angle reported for the $Tl_2Te_2^{2}$ anion in ref. (44), 49.9°, is incorrect and has been redetermined to be 39.9°.

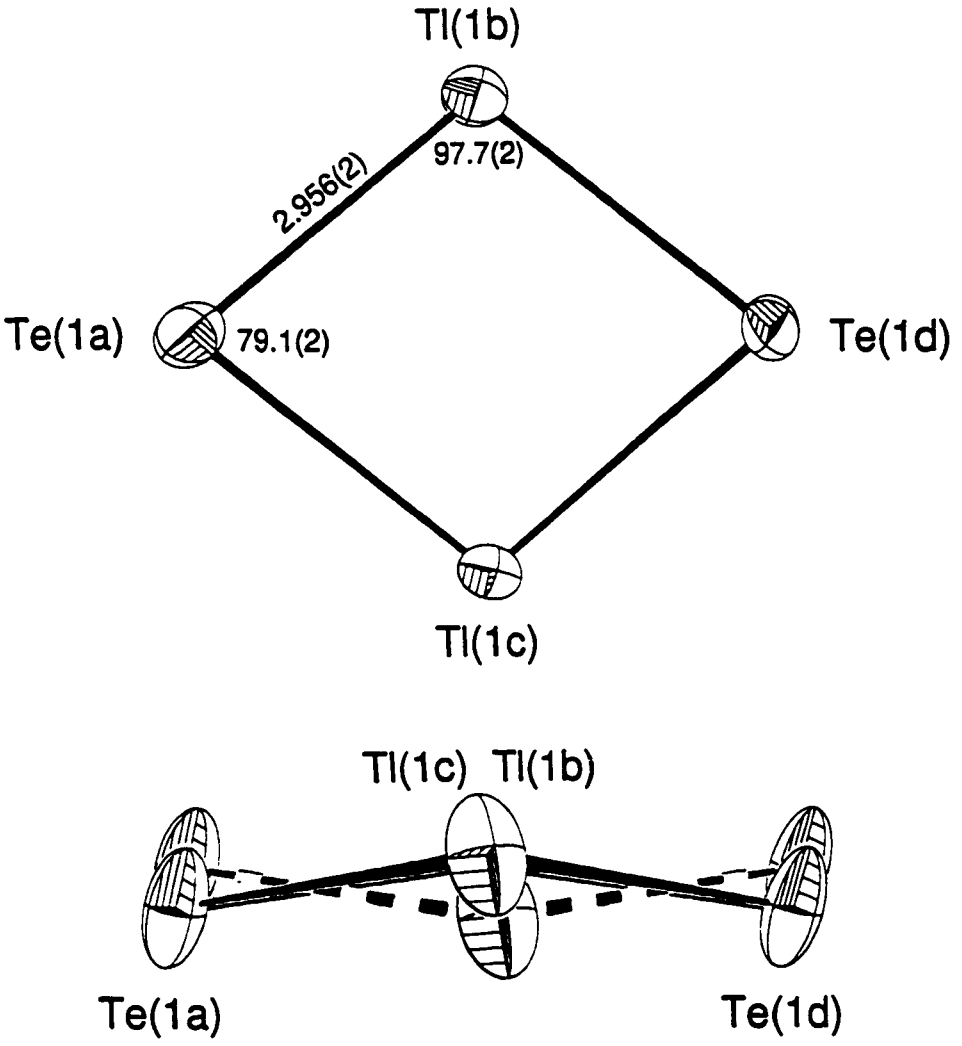

Figure 5.1. View of the $Tl_2Te_2^{2-}$ anion in the (2,2,2-crypt-K^+)$_2Tl_2Te_2^{2-}$ salt with thermal elllipsoids drawn at the 50% probability level. The positional disorder in the anion about a centre of symmetry in shown in the lower trace.

The Tl–Te distance in $Tl_2Te_2^{2-}$ [2.956(2) Å] is identical to the average Tl–Te bond distance [2.954(11) Å] observed in the previously characterized anion[44] and is much shorter than those observed in the alloy phases TlTe [3.398(5)–3.648(3) Å][167] and Tl_5Te_3 [3.142(9)–3.596(4) Å].[167,168] The transannular Tl···Tl distances in $Tl_2Te_2^{2-}$ [3.798(2) Å] and $Tl_2Se_2^{2-}$ [3.698(2) Å] are longer than in thallium metal (3.408 Å)[169] but are considerably shorter than those observed in the $(C_6H_5)_3P^+$ [4.047(1)–4.381(1) Å] and $(C_2H_5)N^+$ [4.381(1) Å] salts of the $Tl_2S_2(S_3)_2^{2-}$ anion,[170] which contains a planar Tl_2S_2-ring. The corresponding distance observed in the previously characterized (2,2,2-crypt-K^+)$_2Tl_2Te_2^{2-}$· en salt [3.600(3) Å] is significantly shorter than in the present structure and in $Tl_2Se_2^{2-}$ and is discussed below (see **Computational Results**). The Ch···Ch contacts observed in both anions [Se, 4.140(3) Å; Te, 4.552(2) Å] and in the previously characterized $Tl_2Te_2^{2-}$ anion [4.414(3) Å] are close to the sums of the Se and Te van der Waals radii [Se, 4.0 Å; Te, 4.4 Å].[124]

The average Tl–Ch–Tl and Ch–Tl–Ch bond angles in the $Tl_2Se_2^{2-}$ anion [83.34(1) and 96.21(7)°, respectively] are close to the 90° bond angles anticipated for a planar structure whereas those observed for $Tl_2Te_2^{2-}$ in the present study [(79.1(2) and 97.7(2)°] and in (2,2,2-crypt-K^+)$_2Tl_2Te_2^{2-}$·en [75.1(3) and 96.6(2)°] deviate from 90° to a greater extent. The angle trends observed in the $Tl_2Ch_2^{2-}$ anions, i.e., Se–Tl–Se < Te–Tl–Te and Tl–Se–Tl> Tl–Te–Tl, are in accord with the VSEPR rules[171] which predict that the Ch–Tl–Ch bond angles should decrease and the Tl–Ch–Tl bond angles should increase upon substitution with the more electronegative Se atom. Similar trends have been reported for the $M_2Ch_3^{2-}$ (M = Sn, Pb; Ch = S, Se, and/or Te) anion series.[82,171–174]

Structural Characterization of $Tl_2Te_2^{2-}$ by Solution NMR Spectroscopy.

The $Tl_2Te_2^{2-}$ anion has been previously characterized by ^{203}Tl and ^{205}Tl NMR spectroscopy at –40 °C in a saturated liquid NH_3 extract of KTlTe containing 2,2,2-crypt.[56] However, the spectra were exchange broadened ($\Delta\nu_{1/2}$ ~ 1000–3000 Hz) giving rise to poorly resolved $^2J(^{205}Tl–^{203}Tl)$ and $^1J(^{205}Tl–^{125}Te)$ couplings which could not be observed at temperatures above –40 °C. In the present work, the $Tl_2Te_2^{2-}$ anion was characterized by ^{203}Tl and ^{205}Tl NMR spectroscopy at 0 °C, resulting in well resolved spin–spin couplings. The ^{203}Tl and ^{205}Tl NMR spectra of the $Tl_2Te_2^{2-}$ anion in a saturated liquid NH_3 solution of KTlTe containing 2,2,2-crypt were also repeated at –70 °C, giving rise to $^2J(^{205}Tl–^{203}Tl)$ and $^1J(^{205}Tl–^{125}Te)$ values that are at variance with the previous values (see Table 5.4). Interestingly, no ^{125}Te resonances corresponding to the $Tl_2Te_2^{2-}$ anion could be observed in the present and previous studies.

The ^{203}Tl and ^{205}Tl NMR resonances corresponding to the known $TlTe_3^{3-}$ anion[56] were also observed in the en and liquid ammonia solutions with well resolved Tl–Ch couplings. The chemical shifts and spin–spin coupling constants for the $TlTe_3^{3-}$ and $Tl_2Te_2^{2-}$ anions as well as those for the $TlSe_3^{3-}$, $Tl_2Se_2^{2-}$, and Tl_2SeTe^{2-} anions[33,56] are listed in Table 5.4.

The experimental and simulated ^{205}Tl and ^{203}Tl NMR spectra of the $Tl_2Te_2^{2-}$ anion are depicted in Figure 5.2. Spectral simulations (Table 5.5) confirmed that the assigned satellite doublet spacings corresponded to $^1J(^{205}Tl–^{125}Te)$ and $J(^{205}Tl–^{203}Tl)$ couplings and are consistent with a solution structure for the $Tl_2Te_2^{2-}$ anions in which the thallium atoms and the chalcogen atoms are chemically equivalent.

Table 5.4. Chemical Shifts and Spin–Spin Coupling Constants for the $TlCh_3^{3-}$ and $Tl_2Ch_2^{2-}$ (Ch = Se and/or Te) Anions.

	chem. shift (ppm)		coupling const. J (Hz)		coupling const. K ($\times 10^{21}$ T^2J^{-1})		coupling const. K_{RC} ($\times 10^{21}$ T^2J^{-1})					
Anion [a]	$^{203,205}Tl$	^{77}Se	^{205}Tl–^{203}Tl	^{205}Tl–Ch [b,c]	Tl–Tl	Tl–Ch	Tl–Tl	Tl–Ch	solvent	T (°C)	Alloy	Ref.
$TlSe_3^{3-}$	2804			7211		53.67		15.19	NH_3	–20	KTlSe	33
	2829	140		7250		53.96		15.27	NH_3	–60	KTlSe	33
	2844	136		7239		53.87		15.25	NH_3	–70	KTlSe	33
$Tl^{77}Se_3^{3-}$	2841	137		7227 (7159)		53.79		15.22	NH_3	–70	$KTl^{77}Se$	33
$Tl_2Se_2^{2-}$	7681		3995	2228	9.761	15.52	1.060	4.692	NH_3	–40	KTlSe	33
	7642	384	3791	2210	9.263	16.38	1.006	4.654	NH_3	–60	KTlSe	33
	7595	372	3602	2261 (2254)	8.801	16.76	0.9560	4.744	NH_3	–70	KTlSe	33
$Tl_2Se_2^{2-}$	7689		4506	2265	11.01	16.79	1.190	4.752	en	0	$KTl(SeTe)_{0.5}$	33,56
	7598		3661	2258 (2265)	8.945	16.74	0.9672	4.737	NH_3	–70	$KTl(SeTe)_{0.5}$	33
$Tl_2{}^{77}Se_2^{2-}$	7596	371	3560	2253 (2229)	8.698	16.70	0.9405	4.727	NH_3	–70	$KTl^{77}Se$	33
Tl_2SeTe^{2-}	7910		< 2800		< 6.8		< 0.74		en	0	$KTl(SeTe)_{0.5}$	33,56
	7793		1945	2407 (Se)	4.752	17.84 (Se)	0.5138	5.050 (Se)	NH_3	–70	$KTl(SeTe)_{0.5}$	33
				3591 (Te)		16.02 (Te)		3.641				
$TlTe_3^{3-}$	453			16371		73.05		16.60	en	0	NaTlTe	this work
	426			16137 (13381)		72.00		16.36	NH_3	–70	KTlTe	this work
$Tl_2Te_2^{2-}$	8175		6337	4004	15.48	17.87	1.674	4.060	en	0	NaTlTe	this work
	8050		7591	3989	18.55	17.80	2.005	4.044	NH_3	–70	KTlTe	this work
	8153		6328	4200	15.46	18.74	1.672	4.258	en/ethylamine	–20	K_2Te/Tl_2Te	85
	8218		< 200	8006	< 0.50	35.72	< 0.050	8.115	NH_3	–40	KTlTe	56

[a] The $Tl_2{}^{77}Se_2^{2-}$ anion is isotopically enriched in ^{77}Se. [b] Ch denotes ^{77}Se or ^{125}Te. [c] Values in parentheses denote $^1J(^{203}Tl$–$^{77}Se)$.

Figure 5.2. NMR spectra of $Tl_2Te_2^{2-}$. (a) ^{205}Tl (115.444 MHz) and (b) ^{203}Tl (114.319 MHz) recorded at 0 °C in en solvent and simulated spectra (right-hand traces). The symbols used to label the peaks are defined in Table 5.5. and in the text.

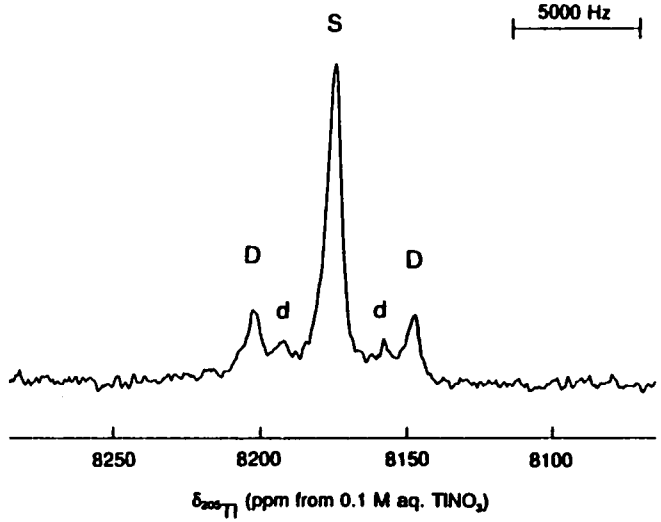
S
5000 Hz
D
d
d
D
8250
8200
8150
8100
δ_{205}Tl (ppm from 0.1 M aq. $TlNO_3$)

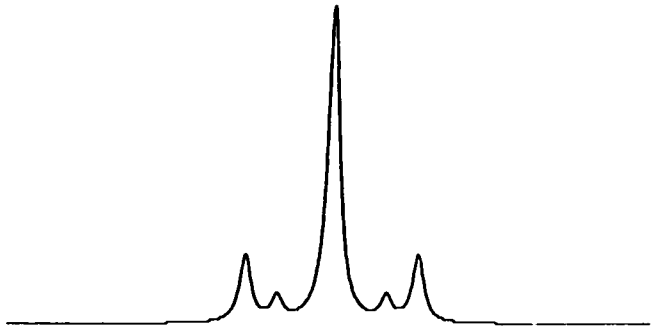

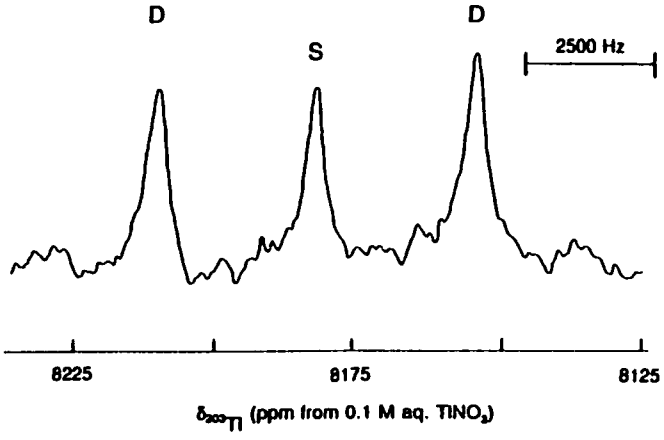
D
S
D
2500 Hz
8225
8175
8125
δ_{205}Tl (ppm from 0.1 M aq. $TlNO_3$)

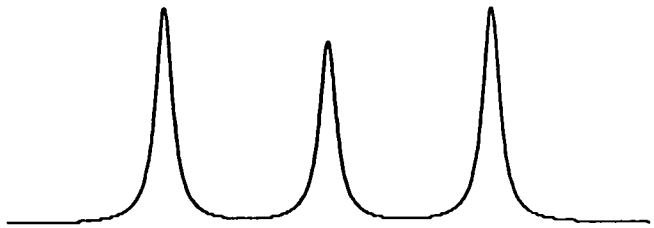

Table 5.5. Natural Abundance Isotopomers and Subspectra Used to Simulate the ^{205}Tl and ^{203}Tl NMR Spectra of $Tl_2Te_2^{2-}$.

isotopomer	relative intensity [a]		multiplicity of subspectrum [b]
	^{205}Tl	^{203}Tl	
$^{203(5)}Tl_2{}^0Te_2^{2-}$	0.8598	0.1505	S
$^{205}Tl^{203}Tl^0Te_2^{2-}$	0.3598	0.3598	D
$^{203(5)}Tl_2{}^0Te^{125}Te^{2-}$	0.1292[b]	0.0226[b]	d

[a] Natural abundances of the spin-½ nuclides used to calculate the isotopomer intensities were taken from ref. (74): ^{205}Tl, 70.5%; ^{203}Tl, 29.5%; ^{125}Te, 6.99%. The natural abundance of ^{123}Te (0.87%) is too low to contribute detectable isotopomer subspectra and is combined with the spinless tellurium atoms. [b] S denotes a singlet. D denotes a DOUBLET arising from $J(^{205}Tl–^{203}Tl)$ coupling, and d denotes a doublet arising from $^1J(^{205}Tl–^{125}Te)$ coupling.

The ^{205}Tl NMR spectrum of $Tl_2Te_2^{2-}$ consisted of an exchange-broadened singlet ($\Delta\nu_{1/2}$ ~1000 Hz) flanked by symmetric doublet satellites corresponding to $^1J(^{205}Tl-^{125}Te)$ and $J(^{205}Tl-^{203}Tl)$ couplings (Figure 5.2). The magnitude of the Tl–Tl coupling was confirmed by recording the ^{203}Tl NMR spectrum (Figure 5.2) in which the ^{205}Tl satellites were more intense than the central peak owing to the greater natural abundance of the ^{205}Tl nuclide (70.5%) when compared to that of ^{203}Tl (29.5%). The corresponding $^1J(^{203}Tl-^{125}Te)$ couplings could not be observed ($\Delta\nu_{1/2}$ ~1000 Hz).

Analysis of Spin–Spin Coupling Patterns. The Tl–Tl couplings observed in the $Tl_2Ch_2^{2-}$ (Ch = Se and/or Te) anions (Table 5.4) show a high degree of variability with environmental changes such as temperature, solvent, and nature of the counter cation, whereas the Tl–Ch coupling in all three anions are relatively insensitive to the environmental changes. For example, the Tl–Tl couplings observed for $Tl_2Se_2^{2-}$ in liquid NH_3 solvent decreased from 3995 to 3602 Hz (*ca.* 10%) when the temperature was decreased from –40 to –70 °C, but the Tl–Se couplings varied by only 50 Hz (*ca.* 2%). The variability in the Tl–Tl coupling constant for the $Tl_2Te_2^{2-}$ anion was significantly more pronounced (*ca.* 17%); however, the Tl–Te couplings varied only by *ca.* 5% under similar experimental conditions. This suggests that the $Tl_2Ch_2^{2-}$ anions are easily deformed about the fold angle and is discussed below (see **Computational Results**).

Chemical Shifts. The ^{203}Tl and ^{205}Tl chemical shifts of the $Tl_2Ch_2^{2-}$ (Ch = Se and/or Te) anions (Table 5.4) appeared in the Tl(1) region and contrast with those observed for the $TlCh_3^{3-}$ anions which appeared in the Tl(III) region. Similar ^{205}Tl chemical shifts have also

been reported for the trigonal bipyramidal $TlSnTe_3^{3-}$ (4196 ppm) and $TlPbTe_3^{3-}$ (3438 ppm) (Chapter 6) anions in which the thallium atoms are formally in the +I oxidation state. Based on the higher electronegativity of Se when compared to that of Te,[119] the shielding of the thallium NMR resonances in the $Tl_2Ch_2^{2-}$ anion series is anticipated to increase in the order $Tl_2Te_2^{2-} > Tl_2SeTe^{2-} > Tl_2Se_2^{2-}$. This trend has been noted for the $TlCh_3^{3-}$, $SnCh_3^{2-}$, $SnCh_4^{4-}$, $Pb_2Ch_3^{2-}$, $HgCh_2^{2-}$, and $CdCh_3^{2-}$ anion series[56] upon substitution with the more electronegative Se atom. Interestingly, the shielding trend observed for the $Tl_2Ch_2^{2-}$ anion series (Table 5.4) is the reverse of the order anticipated on the basis of electronegativity differences between Se and Te. A similar anomaly was also noted for the $Sn_4Se_{10}^{4-}$ anion (Chapter 4) in which the order, $\delta(^{77}Se_{terminal}) < \delta(^{77}Se_{bridging})$, anticipated on the basis of charge topology arguments[120] was reversed (Chapter 4). The anticipated order was observed for the related $Sn_2Se_6^{4-}$ and $Sn_2Te_6^{4-}$ anions (Chapter 3). It is also interesting to note that the thallium NMR resonances of the $Tl_2Ch_2^{2-}$ anions appeared within a small chemical shift range (600 ppm) as did the ^{113}Cd chemical shifts of $CdCh_2^{2-}$ (400 ppm),[56] but larger chemical shift ranges were observed for the $TlCh_3^{3-}$ (2400 ppm), $SnCh_3^{2-}$ (900 ppm), $SnCh_4^{4-}$ (1350 ppm), $Pb_2Ch_3^{2-}$ (1600 ppm), and $HgCh_2^{2-}$ (1400 ppm) anions.[56] However, in the absence of a knowledge of the ^{203}Tl and ^{205}Tl shielding tensors, the apparent anomalies in the shielding trends are presently not fully understood.

Raman Spectra of the $Tl_2Ch_2^{2-}$ (Ch = Se, Te) Anions.

The solid-state Raman spectra of the anions in $(2,2,2\text{-crypt-}K^+)_2Tl_2Se_2^{2-}$ and (2,2,2-

crypt-K^+)$_2$$Tl_2Te_2^{2-}$ are shown in Figure 5.3. The observed frequencies were assigned with the aid of LDFT and NLDFT calculations and their assignments are summarized in Table 5.6 along with their theoretical values (see **Computational Results**). The theoretical values of Tl_2ISeTe^{2-} are also listed in Table 5.6. Assignments for the 2,2,2-crypt-K^+ cation were made by comparison with values reported for the solid state Raman spectra of (2,2,2-crypt-K^+)I^- and require no further discussion.[175]

The vibrational modes of the $Tl_2Ch_2^{2-}$ anions were assigned under C_{2v} point symmetry of the butterfly structure where the Tl atoms lie in the $\sigma(xz)$-plane and the Ch atoms lie in the $\sigma(yz)$-plane and belong to the irreducible representations $3A_1 + A_2 + B_1 + B_2$. A total of 6 fundamental vibrational bands are expected, of which all modes are Raman active and five (A_1, B_1, B_2) are infrared active. Descriptions of the vibrational modes of the $Tl_2Ch_2^{2-}$ anions were derived from LDFT and NLDFT calculations and are depicted in Figure 5.4. The highest frequency mode, $\nu_1(A_1)$, corresponds to the symmetric breathing motion of the ring. The asymmetric combination of the Tl···Tl and Ch···Ch motions, $\nu_2(A_1)$, is at much lower frequency. The lowest totally symmetric mode, $\nu_3(A_1)$, is the inversion mode. The $\nu_4(A_2)$ mode corresponds to the simultaneous shortening (lengthening) of two non-adjacent Tl–Ch bonds and the lengthening (shortening) of the remaining two Tl–Ch bonds. The $\nu_5(B_1)$ mode corresponds to the displacement of both Tl atoms in the positive direction along the *x*-axis and the displacement of both Ch atoms in the negative *x*-direction parallel to the *x*-axis. For the $\nu_6(B_2)$ mode, the two Ch atoms are displaced in the positive direction along the *y*-axis and the Tl atoms are displaced in the negative *y*-direction parallel to the *y*-axis.

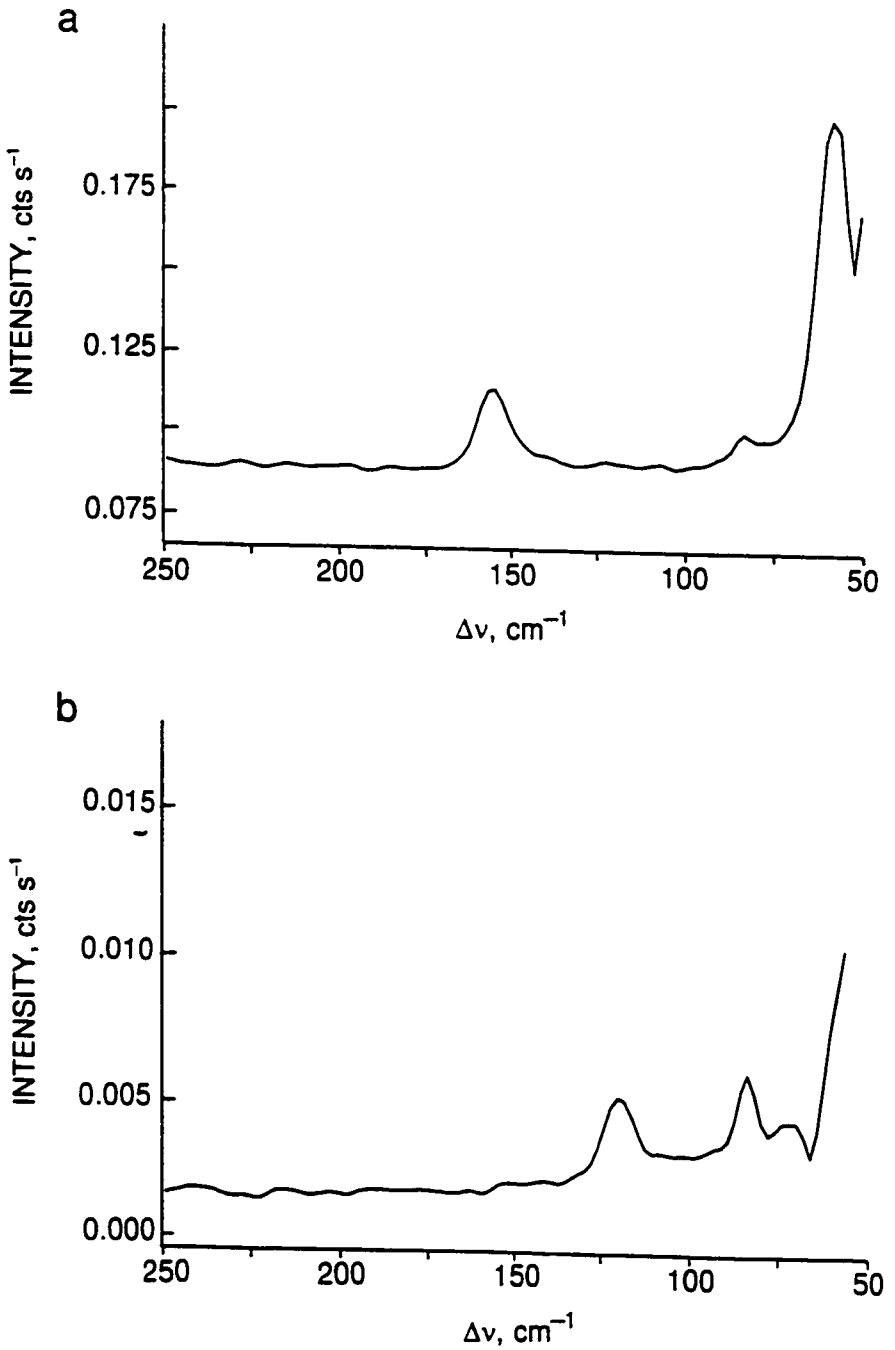

Figure 5.3. Raman spectra of (a) $Tl_2Se_2^{2-}$ and (b) $Tl_2Te_2^{2-}$ recorded in glass capillaries and at room temperature on powdered samples of the respective 2,2,2-crypt-K^+ salts by using the 1064-nm excitation of a Nd YAG laser.

Table 5.6. Experimental and Calculated Vibrational Frequencies (cm $^{-1}$), Assignments, and Mode Descriptions for the $Tl_2Ch_2^{2-}$ (Ch = Se and/or Te) Anions.[a,b]

exp.	LDFT		NLDFT		LDFT	
	PP/PP	PP/DZVP	PP/PP	PP/DZVP	ECP	Assignments
			$Tl_2Se_2^{2-}$ (C_{2v})			
155(24)	159(4)	163(3)	151(4)	156(3)	153(7)	$\nu_1(A_1)$
58(100)	72(0)	56(0)	72(0)	56(0)	62(0)	$\nu_2(A_1)$
	62(0)	38(5)	61(1)	43(5)	35(4)	$\nu_3(A_1)$
84(8)	94(0)	107(0)	84(0)	98(0)	91(0)	$\nu_4(A_2)$
139 sh	146(29)	150(26)	139(31)	144(25)	143(48)	$\nu_5(B_1)$
	145(24)	161(55)	140(24)	153(56)	143(27)	$\nu_6(B_2)$
			$Tl_2Te_2^{2-}$ (C_{2v})			
120(100)	123(3)	130(4)	118(3)	123(3)	119(2)	$\nu_1(A_1)$
73(20)	58(0)	47(0.5)	57(0)	45(0)	49(0)	$\nu_2(A_1)$
	51(0)	24(2)	49(0)	33(2)	26(2)	$\nu_3(A_1)$
84(85)	78(0)	90(0)	70(0)	81(0)	76(0)	$\nu_4(A_2)$
120(100)	116(20)	130(40)	110(22)	122(43)	116(35)	$\nu_5(B_1)$
	114(10)	118(13)	110(10)	113(13)	109(10)	$\nu_6(B_2)$

Table 5.6. Continued.[a]

Tl_2SeTe^{2-} (C_s)			
LDFT PP/PP	NLDFT PP/PP	LDFT ECP	Assignments
156(14)	151(4)	153(7)	$\nu_1(A_1)$
72(0)	72(0)	62(0)	$\nu_2(A_1)$
62(0)	61(1)	35(4)	$\nu_3(A_1)$
94(0)	84(0)	91(0)	$\nu_4(A_2)$
146(29)	139(31)	143(48)	$\nu_5(B_1)$
145(24)	140(24)	143(27)	$\nu_6(B_1)$

[a] The Raman spectra were recorded in glass capillaries on powdered samples at room temperature by using a 1064-nm excitation of a Nd YAG laser. Relative line intensities are given in parentheses. [b] The calculated relative line intensities, in km mol^{-1}, are given in parentheses.

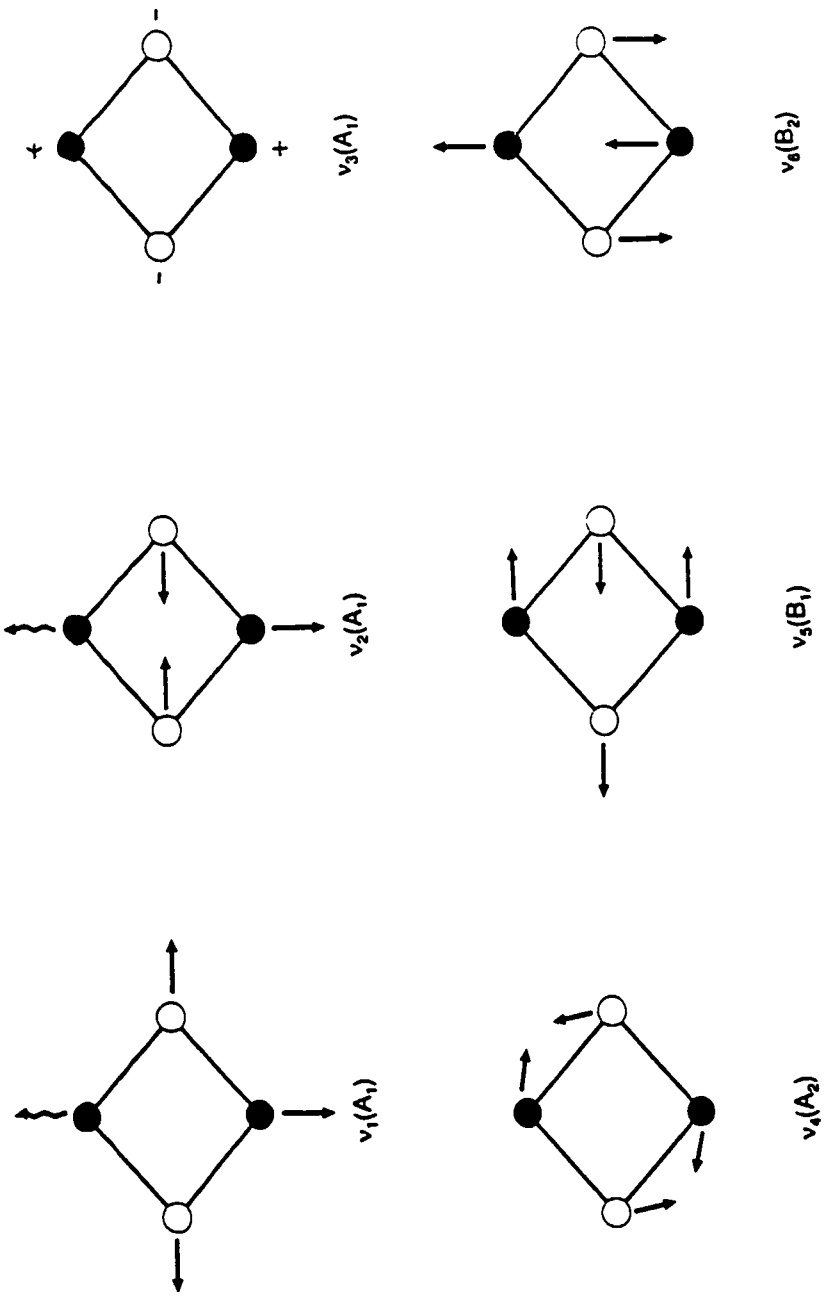

Figure 5.4. Vibrational modes of the $Tl_2Ch_2^{2-}$ (Ch = Se, Te) Anions.

It has not proven possible to observe all the Raman bands for $Tl_2Se_2^{2-}$ and $Tl_2Te_2^{2-}$. In general, the $Tl_2Te_2^{2-}$ anion modes are shifted to lower frequency relative to those of $Tl_2Se_2^{2-}$ by virtue of the reduced mass effect. For both anions, the assignments of the $\nu_1(A_1)$ vibrations are unambiguous and the $\nu_2(A_1)$, $\nu_3(A_1)$ and $\nu_5(B_1)$, $\nu_6(B_2)$ bands are expected to be near degenerate based on theoretical calculations. In the case of $Tl_2Se_2^{2-}$, the $\nu_5(B_1)$ and $\nu_6(B_2)$ bands overlap and are weak in comparison with $\nu_1(A_1)$ and are unambiguously assigned to the band at 139 cm^{-1} based on the calculated values. The $\nu_5(B_1)$ and $\nu_6(B_2)$ modes of $Tl_2Te_2^{2-}$ are also predicted to be similar in frequency to the more intense $\nu_1(A_1)$ band at 120 cm^{-1} and likely overlaps with this band. A band at 73 cm^{-1} in the Raman spectrum of $Tl_2Te_2^{2-}$ is tentatively assigned to the $\nu_2(A_1)$ and $\nu_3(A_1)$ modes of the anion and could likewise be assigned to a lattice mode because it is significantly higher in frequency than its calculated values and its counterparts in $Tl_2Se_2^{2-}$. The experimental $\nu_4(A_2)$ modes of both anions are similar and are in reasonable agreement with their calculated value.

Computational Results.

In order to better understand the structures, properties, and spectra of the $Tl_2Ch_2^{2-}$ (Ch = Se and/or Te) anions, density functional theory (DFT) calculations were performed. The calculations were used to assign the vibrational spectra of $Tl_2Se_2^{2-}$ and $Tl_2Te_2^{2-}$, to gain insight into the extent to which the anion environment influences the fold angle, and to better understand the nature of bonding and the relative magnitudes of the Tl–Ch and Tl–Tl NMR spin–spin couplings.

Geometries of, and Bonding in, the $In_2Ch_2^{2-}$ and $Tl_2Ch_2^{2-}$ (Ch = Se and/or Te) Anions. In order to understand the behaviour of the various basis set treatments used in this study, calculations for the presently unknown $In_2Se_2^{2-}$ and $In_2Te_2^{2-}$ anions, for which all-electron basis sets are available, are also included in this study (Table 5.7). The calculations for $In_2Te_2^{2-}$ show reasonable agreement between the geometric parameters calculated by using all-electron (VWN/DZVP) and all-pseudopotential (VWN/PP/PP) treatments with the latter calculation showing a slightly expanded structure. Agreement is not as good for the $In_2Se_2^{2-}$ anion with the interatomic distances being approximately 0.10 Å longer than the all-electron values. The structures calculated for the $Tl_2Te_2^{2-}$ anions by using an all-electron basis set for Se or Te and a pseudopotential on Tl (PP/DZVP) are not in good agreement with other calculations or with experiment, giving predicted Tl–Ch and Ch–Ch distances which are too long (Table 5.3). Consequently, the PP/PP results have been used, unless otherwise indicated, in the ensuing discussion of $Tl_2Ch_2^{2-}$.

The geometry derived for $Tl_2Se_2^{2-}$ is in good agreement with the experimental one at the LDFT and NLDFT levels when pseudopotentials are used for both Tl and Se (PP/PP). The Tl–Se distance is 0.03–0.04 Å too short (Table 5.3), whereas the Tl···Tl and Se···Se distances are too short by larger amounts (~0.15 Å). Similar calculations for Pb_9^{3-} and Pb_9^{4-} also underestimated the Pb···Pb distances.[29] As a consequence, the calculated Tl–Se–Tl bond angle is too small and the calculated Se–Tl–Se angle is too large by ~3° when compared to the experimental values. The calculated fold angle of 34° clearly shows that the optimum geometry is non-planar. However, the large fold angle also indicates that the structure is

Table 5.7. Calculated Vibrational Frequencies, Geometric Parameters, Charges, Mayer Valencies, and Bond Orders for the $In_2Ch_2^{2-}$ (Ch = Se or Te) Anions.

Frequencies (cm^{-1})				
$In_2Se_2^{2-}$		$In_2Te_2^{2-}$		
VWN/DZVP	VWN/PP/PP	VWN/DZVP	VWN/PP/PP	Assignments (C_{2v})
185(3)	167(2)	148(3)	135(2)	$\nu_1(A_1)$
88(0)	84(0)	61(0)	64(0)	$\nu_2(A_1)$
38(0)	38(0)	34(0)	43(0)	$\nu_3(A_1)$
136(0)	106(0)	110(0)	88(0)	$\nu_4(A_2)$
181(49)	159(29)	143(23)	127(13)	$\nu_5(B_1)$
178(28)	157(19)	144(26)	127(13)	$\nu_6(B_1)$

Geom. Param.	VWN/DZVP	VWN/PP/PP	VWN/DZVP	VWN/PP/PP
In···In (Å)	3.597	3.703	3.782	3.796
In–Ch (Å)	2.687	2.772	2.916	2.953
Ch···Ch (Å)	3.904	4.021	4.268	4.320
In–Ch–In (°)	84.0	83.8	80.9	80.0
Ch–In–Ch (°)	93.2	93.0	94.1	94.0
fold angle (°)[a]	24.4	25.9	32.2	34.5

Table 5.7. Continued.

Charges	VWN/DZVP	VWN/PP/PP	VWN/DZVP	VWN/PP/PP
In	–0.42	–0.43	–0.41	–0.45
Ch	–0.58	–0.57	–0.59	–0.55
Valencies				
In	2.30	2.29	2.18	2.30
Ch	1.97	2.20	1.96	2.26
Bond Orders				
In···In	0.38	0.20	0.25	0.17
In–X	0.96	1.05	0.97	1.07
X···X	0.04	0.11	0.02	0.12

[a] The fold angle in the $In_2Ch_2^{2-}$ anion structures is the dihedral angle between the two In_2Ch-planes.

clearly not tetrahedral. The LDFT/PP/PP and NDLFT/PP/PP values are in reasonable agreement with each other, with the NDLFT values being slightly larger than the LDFT values and showing slightly better agreement with the experimental values (Table 5.3). Calculations with an all-electron basis set for Se produced a structure with a Tl···Tl distance closer to the experimental distance, but the Tl–Se and Se···Se distances are too long.

The $Tl_2Se_2^{2-}$ anion charge is largely localized on the more electronegative Se atoms (–0.7 e) with the remainder on the Tl atoms (–0.3 e) (Table 5.8). The calculated Mayer valencies give values of 2 for Tl and Se, consistent with two Se atoms bonded to each Tl atom (Table 5.9). The mixed basis set results give larger separations for both anions. The Mayer bond order between the Tl and Se is just under 1 (0.95). There are weak interactions between the two Tl atoms (bond order, 0.14–0.15) and between the two Se atoms (bond order, 0.13–0.14). In order to show that these interactions are not exaggerated because of the predicted short Tl···Tl distance, bond orders were also calculated from the experimental geometry and resulted in values of 0.12 for Tl···Tl and 0.15 for Se···Se, confirming that the presence of these interactions is not due to the use of the shorter calculated Tl···Tl distance.

The calculated results for $Tl_2Te_2^{2-}$ follow the same trends as those of $Tl_2Se_2^{2-}$, and the differences between the calculated and experimental values for the present $Tl_2Te_2^{2-}$ structure are similar to those obtained for $Tl_2Se_2^{2-}$ (Table 5.3). The calculated Tl–Te distance at the VWN/PP/PP level is slightly shorter than the experimental value. The Tl–Te–Tl angle is predicted to be ~2° smaller than the experimental value and the Te–Tl–Te bond angle is predicted to be about ~5° larger. The fold angle is predicted to be larger in $Tl_2Te_2^{2-}$ (37.0°)

Table 5.8. Charges (e) in the $Tl_2Ch_2^{2}$ (Ch = Se and/or Te) Anions.[a]

	LDFT		NLDFT		LDFT
atom	PP/PP	PP/DZVP	PP/PP	PP/DZVP	ECP
		$Tl_2Se_2^{2-}$			
Tl	–0.29	–0.08	–0.26	–0.08	–0.11 (0.12)
Se	–0.71	–0.92	–0.74	–0.92	–0.89 (–1.12)
		$Tl_2Te_2^{2-}$			
Tl	–0.32	–0.11	–0.29	–0.11	0.00 (0.06)
Te	–0.68	–0.89	–0.71	–0.89	–1.00 (–1.06)

Tl_2SeTe^{2-}

atom	LDFT PP/PP	NLDFT PP/PP	LDFT ECP/DZVP
Tl	–0.30	–0.27	–0.06 (0.08)
Se	–0.69	–0.72	–0.85 (–1.10)
Te	–0.71	–0.74	–1.02 (–1.05)

[a] Natural Bond Orders populations are given in parentheses.

Table 5.9. Mayer Valencies and Mayer Bond Orders in the $Tl_2Ch_2^2$ (Ch = Se and/or Te) Anions.[a]

	LDFT		NLDFT	
	PP/PP	PP/DZVP	PP/PP	PP/DZVP
		$Tl_2Se_2^{2-}$		
Valencies				
Tl	2.04 (2.00)	1.72 (1.75)	2.00	1.71
Se	2.03 (2.01)	1.67 (1.69)	1.99	1.66
Bond Orders				
Tl···Tl	0.15 (0.12)	0.14 (0.12)	0.14	0.13
Tl–Se	0.95 (0.93)	0.79 (0.82)	0.93	0.88
Se···Se	0.14 (0.15)	0.09 (0.055)	0.33	0.08
		$Tl_2Te_2^{2-}$		
Valencies				
Tl	2.12 (2.07) [2.11]	1.79 (1.83) [1.86]	2.07	1.76
Te	2.13 (2.09) [2.11]	1.72 (1.76) [1.77]	2.08	1.70
Bond Orders				
Tl···Tl	0.15 (0.16) [0.15]	0.14 (0.13) [1.77]	2.08	1.70
Tl–Te	0.99 (0.96) [0.98]	0.82 (0.85) [0.87]	0.97	0.82
Te···Te	0.16 (0.18) [0.16]	0.07 (0.06) [0.04]	0.14	0.07

Table 5.9. Continued.[a]

	Tl_2SeTe^{2-}	
	LDFT PP/PP	NLDFT PP/PP
Valencies		
Tl	2.08	2.03
Se	2.06	2.02
Te	2.09	2.04
Bond Orders		
Tl···Tl	0.15	0.13
Tl–Se	0.96	0.94
Tl–Te	0.97	0.95
Te···Te	0.15	0.14

[a] Values in parenthesis refer to those calculated for the solid-state anion geometry in (2,2,2-crypt-K$^+$)$_2$Tl$_2$Te$_2^{2-}$ (present work) whereas those in square brackets refer to those in (2,2,2-crypt-K$^+$)$_2$Tl$_2$Te$_2^{2-}$·en.[44]

than in $Tl_2Se_2^{2-}$ (33.8°). Mayer valencies and bond orders for the $Tl_2Te_2^{2-}$ structures are similar to those predicted for $Tl_2Se_2^{2-}$ (Table 5.9), and use of the experimental geometry does not change the conclusion about the presence of weak Tl···Tl (bond order, 0.13–0.15) and Te···Te (bond order, 0.14–0.16) interactions. With the exception of the fold angle, the present experimental structure of the $Tl_2Te_2^{2-}$ is a better approximation of the gas-phase geometry than that previously determined in the crystal structure of $(2,2,2\text{-crypt-}K^+)_2Tl_2Te_2^{2-}\cdot en$[44] (see ***Vibrational Frequencies***). Comparison of the Tl···Tl and Te···Te distances reported for $(2,2,2\text{-crypt-}K^+)_2Tl_2Te_2^{2-}\cdot en$ with the calculated values shows that the experimental values are shorter than the calculated values by ~0.15 Å, and contrasts with the present structural determinations of $Tl_2Se_2^{2-}$ and $Tl_2Te_2^{2-}$ which give experimental Tl···Tl and Ch···Ch distances that are longer than the calculated values by the same amount.

Calculations were also performed on the Tl_2SeTe^{2-} anion (Tables 5.3, 5.8, 5.9) at the all PP and effective core potential (ECP) levels. The geometric parameters are as expected from the $Tl_2Se_2^{2-}$ and $Tl_2Te_2^{2-}$ anions. The fold angle is somewhat larger than that for the $Tl_2Se_2^{2-}$ anion and is more like that of $Tl_2Te_2^{2-}$. The ECP structure is flatter and has longer bond lengths. The electronic structure parameters and vibrational frequencies are as expected based on the above results.

The presence of weak interactions between the Tl atoms are validated by even larger In···In interactions calculated for $In_2Se_2^{2-}$ and $In_2Te_2^{2-}$ by using all-electron DZVP basis sets (Table 5.7) and indicate that the use of pseudopotentials is not biasing the predicted magnitudes of the Tl···Tl interactions. The Ch···Ch interactions calculated for $In_2Ch_2^{2-}$ are,

however, significantly weaker than those calculated for the $Tl_2Ch_2^{2-}$ anions.

The dependence of the calculated results on the form of the treatment of the core electrons was checked by using ECP calculations. The ECP results for the geometry of $Tl_2Se_2^{2-}$ do not differ significantly from the LDFT/PP/PP results, except that the predicted Tl–Se and Se···Se distances are slightly longer than the experimental ones. However, the fold angle is not changed significantly. The calculated frequencies at the ECP level are similar to the PP results except that the inversion frequency is lower at the ECP level by almost a factor of 2 (see ***Vibrational Frequencies***). The results for $Tl_2Te_2^{2-}$ at the ECP level are similar. As in the case of $Tl_2Se_2^{2-}$, the Tl–Te and Te···Te distances are longer at the ECP level when compared to the experimental values. The ECP calculation favors an even more planar structure than do the PP calculations and a larger Te–Tl–Te bond angle which is consistent with the crystal structure of $Tl_2Te_2^{2-}$ reported in this work.

The ECP results were also analyzed by using the Natural Bond Orbital (NBO) method of Weinhold and coworkers.[176] The NBO atomic populations (Table 5.10) show more ionicity when compared to the Mulliken charges. This is more pronounced for $Tl_2Se_2^{2-}$ than for $Tl_2Te_2^{2-}$. The NBO populations indicate that the Tl atoms carry slightly positive charges. The ECP results show larger charge differences than do the PP results with the largest differences found for $Tl_2Se_2^{2-}$.

The NBO analyses were used to further assess the bonding in the anions (Table 5.11). The analysis shows four two-centre Tl–Se bonds with populations of 1.96 e. The remaining bond population is in the σ^* orbital. The two-centre Tl–Se bond has 84% of the two electrons

Table 5.10. Natural Atomic Orbital Populations in the $Tl_2Ch_2^{2-}$ (Ch = Se and/or Te) Anions at the Effective Core Potential Level.

	Se	Te	Se/Te
Tl (*s*)	1.89	1.94	1.92
Tl (p_y)	0.47	0.33	0.34
Tl (p_x)	0.28	0.43	0.29
Tl (p_z)	0.26	0.24	0.45
Ch (*s*)	1.89	1.91	1.91 / 1.90
Ch (p_y)	1.68	1.64	1.73 / 1.62
Ch (p_x)	1.73	1.72	1.75 / 1.81
Ch (p_z)	1.78	1.78	1.71 / 1.71

Table 5.11. Natural Bond Order Analysis for the $Tl_2Ch_2^{2}$ (Ch = Se and/or Te) Anions.

orbital	orb. pop.	%*s*	%*p*	*s* (coeff.)	p_x (coeff.)	p_y (coeff.)	p_z (coeff.)
				$Tl_2Se_2^{2-}$ [b]			
Tl–Se	1.96 [Tl (16%)]	4.9	94.8	0.18 (–0.13)	–0.62	0.70 (0.06)	0.25
	[Se (84%)]	11.5	88.5	0.32	0.71	–0.56	-0.27
Tl l.p	2.00	93.3	7.7	0.97	–0.24	0.0	-0.08
Tl l.p.	0.20		99.6		–0.36		0.93
Se l.p.	1.98	77.4	22.6	0.88		0.47	
Se l.p.	1.82	2.1	97.8	0.15	0.15	–0.36	0.92
				$Tl_2Te_2^{2-}$ [c]			
Tl–Te	1.95 [Tl (17.9%)]	4.93	95.4	–0.16 (0.13)	–0.61	–0.70 (–0.05)	-0.30
	[Te (82.1%)]	9.5	90.5	0.31	0.71	0.59	0.24
Tl l.p.	2.00	94.3	5.7	0.97	–0.20		-0.08
Tl l.p.	0.22		100		–0.44		0.90
Te l.p.	1.98	79.6	20.4	0.89		0.45	
Te l.p.	1.81	1.5	98.5	0.15		–0.32	0.94

[a] The symbol, l.p., denotes lone pair. [b] Where Tl–Tl was chosen as the *x*-axis, Se–Se as the *y*-axis, and *z* is out of the plane. [c] Where Tl–Tl was chosen as the *y*-axis, Te–Te as the *x*-axis, and *z* is out of the plane.

on Se and 16% on Tl. The bonding is predominantly *p* in character with 95% *p*-character on Tl and 89% *p*-character on Se. For $Tl_2Te_2^{2-}$, the bonding pattern is the same with 82% of the bond localized on Te and 18% on Tl. The *p*-character on Te is 90% and that on Tl is 95%. The remaining valence electrons are found in lone pairs. There is essentially a doubly occupied lone pair of high *s*-orbital character on each thallium and chalcogen atom. This accounts for all except four of the valence electrons. These remaining electrons are predominantly in the Se lone pair which has 1.82 electrons and is predominantly an "out-of-plane" *p*-orbital, although there is some population in the *p*-orbital oriented towards the other Se atom. The atomic orbital populations given in Table 5.10 show that each *p*-orbital on the chalcogen atoms is deficient by about 0.25 e from being completely doubly occupied. The other 0.4 e is divided between the two Tl atoms and there is 0.20 e on each atom, mostly in the "out-of-plane" *p*-orbital with the rest in the *p*-orbital oriented along the Tl–Tl axis. The NBO analysis did not assign any of the orbitals to a weak Tl···Tl or Ch···Ch interaction, but to lone pairs. However, this is not inconsistent with the Mayer analysis which considers the total overlap of the orbitals between atoms. The NBO analysis "assigns" the lone pairs on the Tl atoms to *s*- and *p*-orbitals which can overlap given the short Tl···Tl distance, thus giving rise to the weak Mayer bond order between the Tl atoms. It is important to note that both analysis methods have some arbitrariness when weak interactions are present, but both show the possibility of a weak Tl···Tl interaction.

The eight highest-energy valence-MO's for $Tl_2Se_2^{2-}$ are shown in Figure 5.5 and are similar to those of $Tl_2Te_2^{2-}$. The HOMO (orbital a) is a lone pair ("in-plane" type) on the Se

Figure 5.5. Molecular orbitals for $Tl_2Se_2^{2-}$ contoured at 0.04 and at the LDFT level. The different shades denote the two different phases of the orbitals. Key: (a) HOMO; (b) NHOMO; (c) third; (d) fourth; (e) fifth; (f) sixth; (g) seventh; and (h) eighth highest occupied MO's.

a
b
c
d
e
f
g
h

mixed with a lone pair on Tl. The NHOMO (orbital b) is the antibonding combination of the "out-of-plane" lone pairs on the Se atoms. The next highest orbital (orbital c) shows a weak Se···Se interaction with most of the orbital describing lone pairs on Se and Tl. The next highest orbital (orbital d) shows a lone pair type interaction coupled with a bonding orbital between Tl and Se. The interactions between the two Tl–Se–Tl planes are antibonding. Orbital e is essentially the out-of-plane lone pair on the Se atoms and shows an interaction between the two chalcogens. Orbital f is another mixing of a *p*-orbital lone pair with the Tl–Se bonding orbital. Orbital g shows a Tl···Tl interaction arising mostly from the overlap of the valence *s*-orbitals on the Tl atoms. The most stable orbital, orbital h, is an antibonding combination of the valence *s*-orbitals on the Tl atoms with a small delocalization of the electron density on the Se atoms.

Three theoretical papers on the electronic structure of the $Tl_2Te_2^{2-}$ anion have been published[44,164,165] and used geometries constructed from the X-ray structure of $Tl_2Te_2^{2-}$ in $(2,2,2\text{-crypt-}K^+)_2Tl_2Te_2^{2-}\cdot$ en.[44] Corbett and Burns[44] used simple orbital arguments to rationalize the nonplanarity of the structure. Cave *et al.*[165] used extended Hückel theory and Hartree-Fock calculations with ECP's and a polarized triple zeta valence basis set to calculate the electronic structure of the $Tl_2Te_2^{2-}$ anion and of the tetrahedral-like $Pb_2Sb_2^{2-}$ and $Sn_2Bi_2^{2-}$ anions to determine when a structure is tetrahedral and when it is planar based on electronegativity differences and electron count. They found the butterfly structure of $Tl_2Te_2^{2-}$ to be 48 kcal mol^{-1} more stable than the planar structure. Axe and Marynick[164] used the spin-restricted scattered-wave Xα method to study the $Pb_2Sb_2^{2-}$, $Sn_2Bi_2^{2-}$, and $Tl_2Te_2^{2-}$ anions. The

six highest energy orbitals obtained for the energy minimized geometries of $Tl_2Se_2^{2-}$ and $Tl_2Te_2^{2-}$ in the present study are similar to those obtained by Axe and Marynick for $Tl_2Te_2^{2-}$ except for orbital c (their $7a_1$) which has an overall bonding interaction between the two Te (Se) atoms whereas they ascribe the interaction to donation of the Te atoms to the empty Tl orbitals. They suggest that the simplest description of $Tl_2Te_2^{2-}$ is two Te^{2-} anions bonded to two Tl^+ cations and that the difference between the Te···Te and Tl···Tl distances is in qualitative agreement with the larger absolute charges on the Te atoms which repel each other more than those on the two Tl atoms.

Vibrational Frequencies. The calculated vibrational frequencies are given in Table 6 and the modes for $Tl_2Se_2^{2-}$ and $Tl_2Te_2^{2-}$ are depicted in Figure 5.5 and are similar for Tl_2SeTe^{2-}, which must be assigned under C_s point symmetry. All of the modes are predicted to be very low in frequency with the highest frequency modes in the range 150–160 cm^{-1} and have been used to assign the experimental spectra (see **Raman Spectra of the $Tl_2Ch_2^{2-}$ (Ch = Se, Te) Anions**).

The inversion modes in all three anions are predicted to be very low; at the pseudopotential level, they are ~60 cm^{-1} for $Tl_2Se_2^{2-}$, ~50 cm^{-1} for $Tl_2Te_2^{2-}$ and ~90 cm^{-1} for Tl_2SeTe^{2-}. The low frequency values suggest that the potential energy surfaces for inversion of these butterfly-shaped anions are nearly flat and that these anions can be easily distorted along this mode by environmental effects such as crystal packing forces induced by anion···cation interactions or by solvent molecules of crystallization and can easily account for the differences between the fold angles observed for the two experimental structures of

$Tl_2Te_2^{2-}$ and those of the calculated structures. Although the calculated fold angle of 37° is in better agreement with the value of 39° observed in (2,2,2-crypt-K^+)$_2Tl_2Te_2^{2-}$· en, an even larger discrepancy exists between that of the experimental $Tl_2Se_2^{2-}$ structure (10°) and the calculated value (34°). This coordinate is represented by the lowest energy deformation mode (*vide supra*) and is the most easily deformed and least reliable experimental geometrical parameter for comparison with that of the isolated anion.

Spin–Spin Couplings. The relative magnitudes of the $J(^{203}Tl–^{205}Tl)$, $^1J(^{203,205}Tl–^{77}Se)$, and $^1J(^{205}Tl–^{125}Te)$ spin–spin coupling constants in the $Tl_2Ch_2^{2-}$ anions may be understood in terms of the calculated *s*-characters of the corresponding bonding interactions. The relativistically corrected $^1K(Tl–Ch)_{RC}$ and $K(Tl–Tl)_{RC}$ values are given in Table 5.4. The one-bond $K(Tl–Ch)_{RC}$ couplings (4.044×10^{21}–4.752×10^{21} T^2J^{-1}) are three to four times smaller in magnitude than those determined for the trigonal-planar $TlSe_3^{3-}$ (15.19×10^{21}–15.22×10^{21} T^2J^{-1}) and $TlTe_3^{3-}$ (16.36×10^{21}–16.60×10^{21} T^2J^{-1}) anions[56] where the hybridization on Tl is formally sp^2, giving a formal *s*-character of 33.3% for the Tl–Ch bonds. The smaller magnitudes of the $^1K(Tl–Ch)_{RC}$ couplings in $Tl_2Ch_2^{2-}$ are consistent with the %*s*-characters in the Tl–Ch bonds derived from NBO orbital population analysis. The *s*-characters for these bonds are 10.4% for $Tl_2Se_2^{2-}$ and 8.7% for $Tl_2Te_2^{2-}$, and when compared with the formal *s*-characters of their trigonal planar $TlCh_3^{3-}$ analogues are smaller by factors of 3.2 and 3.8, respectively.

The smaller Tl···Tl Mayer bond orders (0.14–0.15) are consistent with the smaller $K(Tl–Tl)_{RC}$ values when compared to the corresponding $^1K(Tl–Ch)_{RC}$ values (Table 5.4).

Although the NBO analyses do not explicitly assign any of the orbitals to Tl···Tl interactions in the $Tl_2Ch_2^{2-}$ anions, it is reasonable to expect this interaction to contain a significant *s*-character based on the high *s*-orbital character of the Tl lone pairs (Table 5.11), which are of proper symmetry to overlap. This overlap is represented by orbital g (Figure 5.4) and shows that the Tl···Tl interaction predominantly arises from overlap of the valence *s*-orbitals on the Tl atoms and may be the predominant contributor to the Tl–Tl coupling mechanism in the $Tl_2Ch_2^{2-}$ anions.

The Tl–Ch couplings in $Tl_2Ch_2^{2-}$ are relatively insensitive to temperature, solvent, and the nature of the counter cation; however, the Tl–Tl couplings in all three anions show a high degree of variation when one or all of these parameters are altered (Table 5.4). The variation of the Tl–Tl coupling is likely associated with the ease with which the fold angle can be deformed by environmental effects such as solvent coordination as indicated by the low frequencies of the inversion modes of the $Tl_2Ch_2^{2-}$ anions (Table 5.6). The deformability of the fold angle is expected to have little effect on the magnitudes of ^1J(Tl–Ch) and the Tl–Ch distances, since the Ch atoms are normal to the fold angle. Moreover, the ease of deformability of the fold angle is supported by the observation of two distinct fold angles and Tl···Tl distances for the $Tl_2Te_2^{2-}$ anion in (2,2,2-crypt-K^+)$_2Tl_2Te_2^{2-}\cdot$ en[44] and in (2,2,2-crypt-K^+)$_2Tl_2Te_2^{2-}$ (this work) and by the calculated optimized geometries of the $Tl_2Te_2^{2-}$ and $Tl_2Se_2^{2-}$ anions which give fold angles that differ significantly from those observed in the experimental structures.

Conclusion

The solution structure of the $Tl_2Te_2^{2-}$ anion has been studied by variable-temperature multi-NMR spectroscopy and confirmed by a detailed analysis of the first-order ^{205}Tl and ^{203}Tl subspectra arising from natural abundance isotopomer distributions. The X-ray crystal structure of the $Tl_2Te_2^{2-}$ anion has been determined in the absence of solvent in the crystal lattice. Density functional theory (DFT) calculations have confirmed that the butterfly geometries observed for the $Tl_2Se_2^{2-}$ and $Tl_2Te_2^{2-}$ anions in the solid-state are true minima in the gas phase but are highly deformable about the fold angle and is supported by the observed variation in the Tl–Tl coupling constants with solvent and temperature and by the observed and calculated low frequencies of the anion inversion modes. The present $Tl_2Te_2^{2-}$ anion structure was also shown by DFT calculations to be a better approximation of the gas-phase geometry than that reported in $(2,2,2\text{-crypt-K}^+)_2Tl_2Te_2^{2-}\cdot en$.[44] The magnitudes of $^1K(Tl–Cl)_{RC}$ and $K(Tl–Tl)_{RC}$ coupling constants were shown to correlate with the calculated %*s* characters determined for the corresponding bonds. Theory indicates that the Tl–Ch bonds are 2-centre-2-electron bonds of high *p*-character and that there is a significant concentration of *s*-electron density between the Tl atoms corresponding to bond orders of 0.14–0.15.

CHAPTER 6

MIXED HEAVY-METAL TRIGONAL BIPYRAMIDAL $TlMTe_3^{3-}$ (M = Sn, Pb) ANIONS

Introduction

The trigonal bipyramidal $M_2Ch_3^{2-}$ (M = Sn, Pb; Ch = S, Se, and/or Te) and $SnPbSe_3^{2-}$ anions[82,172-174] were previously synthesized and characterized by multi-NMR spectroscopy and the $M_2Ch_3^{2-}$ (Ch = Se, Te) anions by X-ray crystallography in (2,2,2-crypt-K^+)$_2M_2Ch_3^{2-}$. The $M_2Ch_3^{2-}$ anions possess trigonal bipyramidal structures with the equatorial chalcogen atoms bonded to the axial Group IV metals (Structure **II**). The small Ch–M–Ch (~90°) and

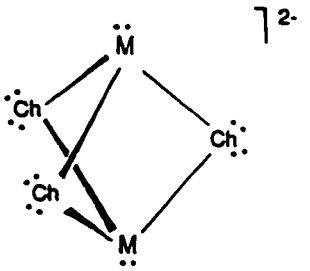

II

M–Ch–M (~70°) bond angles and the small magnitudes of the relativistically corrected reduced coupling constants, $^1K(M–Ch)_{RC}$, suggested substantial valence *p*-orbital involvement in the cage bonding and inert valence $5s^2$ and $6s^2$ electron lone pairs on M. These findings are consistent with a molecular bonding framework consisting of three valence *p*-orbitals on M lying along the three M–Ch bonds and two valence *p*-orbitals on

each chalcogen atom, one lying along the M–Ch bond and the other, a non-bonding orbital, lying in the equatorial plane (Structure **III**). However, the $K(M–M)_{RC}$ couplings observed for

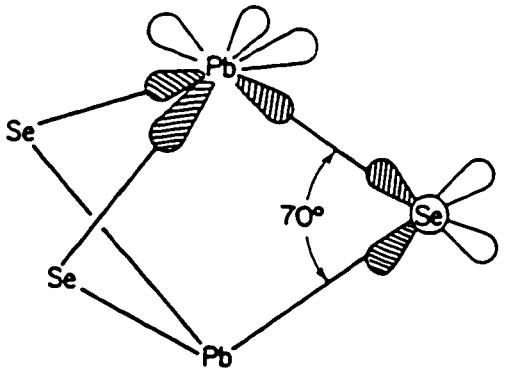

III

the $Sn_2Se_3^{2-}$ and $SnPbSe_3^{2-}$ anions were significantly larger than the $K(M–Ch)_{RC}$ couplings observed in the series of $M_2Ch_3^{2-}$ (M = Sn, Pb; Ch = S, Se, and/or Te) anions, and the M···M distances observed in the X-ray crystal structures were considerably shorter than the van der Waals radius of M.[124] The large couplings were rationalized on the basis of multiple coupling pathways and through-space interactions of the valence *s*-electrons on M, and the short M···M distances were rationalized on the basis of geometric constraints imposed by metal–chalcogen bonding.

In the present work, the $M_2Ch_3^{2-}$ series of trigonal bipyramidal anions has been extended to include the mixed-metal $TlMTe_3^{3-}$ anions which have been characterized by solution multi-NMR spectroscopy. The magnitudes of the relativistically corrected reduced Tl–M coupling constants have been used to evaluate the extent to which the weak M···M interactions of high *s*-character calculated by density functional theory at the local (LDFT) and nonlocal (NLDFT) levels contribute to the M–M coupling mechanism. The X-ray crystal

structure of the $TlPbTe_3^{3-}$ anion in (2,2,2-crypt-K^+)$_3TlPbTe_3^{3-}$·2en is also reported in the present Chapter.

Results and Discussion

Synthesis of the $TlMTe_3^{3-}$ (M = Sn, Pb) Anions.

The experimental approach involved the synthesis of the ternary $Tl_2M_2Te_3$ (M = Sn, Pb) alloys by fusion of the elements followed by reaction of the powdered alloys with K_2Te in en/ethylamine mixtures (Pb) or in en (Sn) in the presence of stoichiometric excesses of 2,2,2-crypt with respect to K^+. Crystals of (2,2,2-crypt-K^+)$_3TlPbTe_3^{3-}$·2en suitable for an X-ray diffraction study were formed upon addition of THF to the en/ethylamine solution studied by NMR spectroscopy.

X-ray Crystal Structure of (2,2,2-crypt-K^+)$_3TlPbTe_3^{3-}$·2en.

A summary of the crystal data and refinement results are given in Table 6.1. The final atomic coordinates and equivalent isotropic thermal parameters for the Tl/Pb, Te, and K atoms are summarized in Table 6.2. The most significant bond distances and angles in the $TlPbTe_3^{3-}$ anion are listed in Table 6.3. The structure of the 2,2,2-crypt-K^+ cations in the title compound is similar to that determined previously in K^+(2,2,2-crypt-K^+)$_3Pb_9^{4-}$,[29] with average K···O and K···N distances of 2.835(8) and 2.978(19) Å, respectively.

The title compound contains a trigonal bipyramidal anion of ~C_{3v} point symmetry (Figure 6.1) and is isostructural with previously characterized $M_2Ch_3^{2-}$ (M = Sn or Pb; Ch

Table 6.1. Summary of Crystal Data and Refinement Results for $(2.2.2\text{-crypt-K}^+)_3\text{-}TlPbTe_3^{3-}\cdot 2en$.

Formula	$C_{58}H_{124}N_{10}O_{18}K_3TlPbTe_3$
Space group (No.)	$P2_1/c$ (15)
a, Å	15.256(5)
b, Å	26.087(9)
c, Å	20.984(8)
α, deg	90.00
β, deg	93.03(3)
γ, deg	90.00
V, Å^{-3}	8339.6(51)
Z	4
mol. wt.	2161.33
ρ, g cm^{-3}	1.721
morphology	platelet
dimensions, cm	0.42 × 0.19 × 0.29
colour	deep red
refinement method	F^2
reflections used	5434
reflections suppressed ($F^2 < -2\sigma F^2$)	24
parameters refined	405
H-atom method	calculated
R_1 ($F^2 > 2\sigma F^2$)	0.0437
wR_2 (F^2)	0.0909
S ($F^2 > 2\sigma F^2$)	0.975
$\Delta\rho_{max}$, e Å^{-3}	0.498
$\Delta\rho_{min}$, e Å^{-3}	–0.875
w	$w_1 = 0.0309$
	$w_2 = 0.0000$

Table 6.2. Atomic Coordinates and Equivalent Isotropic Thermal Parameters ($Å^2$) for the Tl/Pb, Te, and K atoms in (2,2,2-crypt-K^+)$_3$TlPbTe$_3^{3-}$·2en.

	x	*y*	*z*	U_{eq}[a]
Tl(1)/Pb(1)	0.43926(3)	–0.06788(2)	–0.18632(3)	0.0796(2)
Te(1)	0.50000	0.02925(5)	–0.25000	0.0885(5)
Te(2)	0.62185(6)	–0.11714(3)	–0.18562(5)	0.0699(3)
K(1)	0.4473(2)	–0.27505(10)	0.08126(13)	0.0538(8)
K(2)	1.0000	–0.09925(14)	0.25000	0.0581(12)

[a] U_{eq} is defined as one-third of the trace of the orthogonalized U_{ij} tensor.

Table 6.3. Selected Bond Lengths (Å) and Bond Angles (deg) for (2,2,2-crypt-K^+)$_3$TlPbTe$_3^{3-}$·2en.[a]

Bond Lengths			
M–Te(1)	3.0324(14)	M···M	3.332(2)
M–Te(2)	3.0670(13)	Te(1)···Te(2)	4.427(2)
Bond Angles			
Te(1)–M–Te(2)	93.07(3)	M–Te(1)–M	66.65(4)
		M–Te(2)–M	65.66(3)

[a] The Tl–Te and Pb–Te bond distances in the crystal structure of (2,2,2-crypt-K^+)$_3$-TlPbTe$_3^{3-}$·2en are averaged owing to the symmetry equivalence of the Tl and Pb atoms; M is therefore used to denote the Tl and Pb atoms.

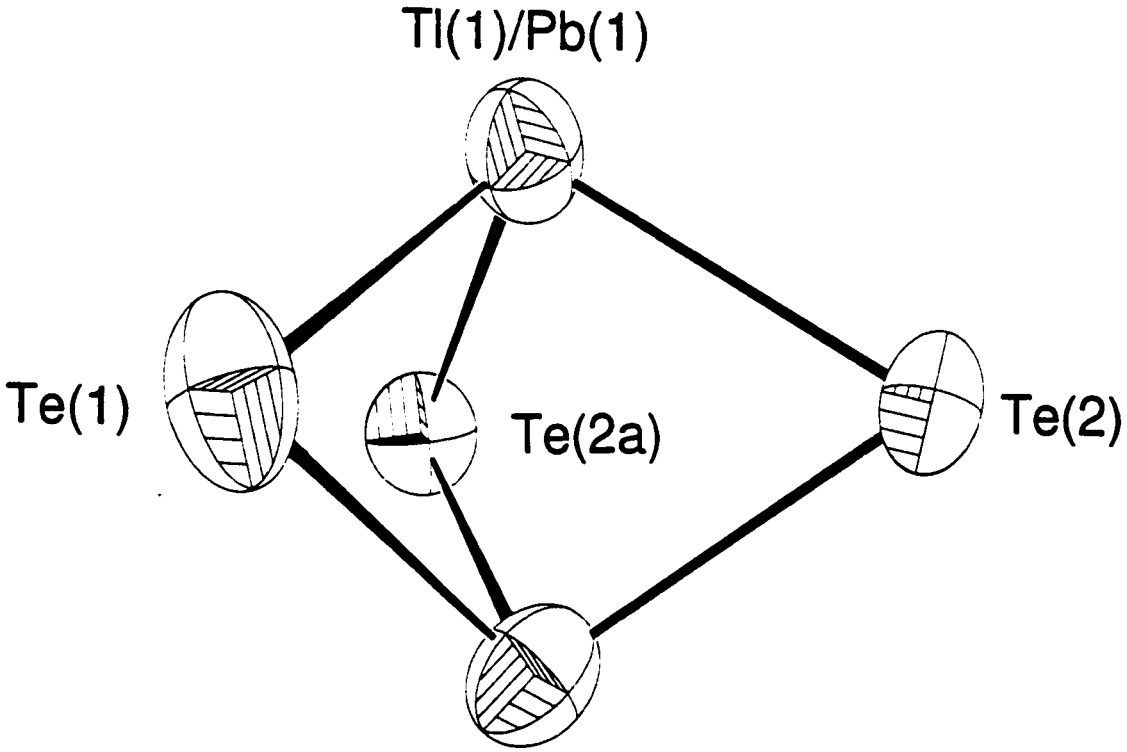

Figure 6.1. View of the $TlPbTe_3^{3-}$ anion in $(2,2,2\text{-crypt-}K^+)_3TlPbTe_3^{3-}\cdot 2en$ with displacement ellipsoids drawn at the 50% probability level.

= Se or Te) anion structures.[82,172-174] The anions in the present and in the previously reported structures possess short M···M distances, which is a general feature among structures containing trigonal bipyramidal X_2Y_3-units [(*t*-Bu)$_2$Si$_2$P$_3$(C$_6$H$_{11}$)$_3$, Si···Si = 2.518(3) Å;[177] ((Me$_3$Si)$_3$C)$_2$M$_2$Se$_3$, M···M = 2.515 Å (Si),[178] 2.672 Å (Ge);[179] Pn$_2$(W(CO)$_5$)$_3$, Pn···Pn = 2.279(4) Å (As),[180] 2.663(3) Å (Sb),[181] 2.818(3) Å (Bi)[182]] and $XX'Y_3$-units [SnMO$_3$(*t*-Bu)$_3$, Sn···M = 3.200(3) Å (In),[183] 3.306(3) Å (Tl);[184] (CO)$_5$MoSnTlO$_3$(*t*-Bu)$_3$, Sn···Tl = 3.298(1) Å;[183] ((CO)$_5$Mo)$_2$SnInO$_3$(*t*-Bu)$_3$, Sn···In = 3.078(1) Å[183]]. The Tl···Pb distance in $TlPbTe_3^{3-}$ [3.332(2) Å] is comparable to the M···M distances observed in the $Sn_2Ch_3^{2-}$ [Se, 3.090(3) Å; Te, 3.2760(6) Å] and in the $Pb_2Ch_3^{2-}$ [S, 3.1467(7) Å; Se, 3.2260(8) Å; Te, 3.249(2) Å] anion structures, and all the M···M distances are longer than the reported single-bond Sn–Sn[185] [Pb–Pb[186-187]] distances of 2.77–3.05 [2.84–2.97] Å. Although the M···M distances in the trigonal bipyramidal anion structures do not reflect single M–M bonds, significant M···M interactions corresponding to bond orders of 0.17–0.25 ($Sn_2Ch_3^{2-}$) and 0.13–0.28 ($Pb_2Ch_3^{2-}$) have been calculated for the anion structures by LDFT and NLDFT calculations (see **Computational Results**). The M···M interactions in $Sn_2Ch_3^{2-}$ and in $Pb_2Ch_3^{2-}$ were predicted to increase in the order Te > Se > S which is in qualitative agreement with the greater effective orbital overlap anticipated between M and the heavier chalcogen congeners. Interestingly, the reverse trend is observed in the X-ray crystal structures of $Sn_2Ch_3^{2-}$ and $Pb_2Ch_3^{2-}$ (*vide supra*) and most likely results from less accurately determined bond lengths and angles arising from the large anisotropies observed for the M and Ch atoms in the X-ray crystal structures. This anisotropy, as exemplified by the $Pb_2Te_3^{2-}$ anion structure (Figure

6.2a),[173] probably results from disorder and has only been partially resolved for $Sn_2Te_3^{2-}$ at −100 °C (Figure 6.2b).[82] In the present anion structure, one of the tellurium atoms, Te(1), possesses a slight anisotropy along the *x*-direction [U_{11}(Te(1)) = 0.1245(13) Å^2 when compared to U_{11}(Te(2)) = 0.0695(6) Å^2] and is indicated by the slightly more elongated shape of its thermal ellipsoid (Figure 6.1); however, the anisotropy is not as pronounced as those observed in the previously reported structures.

The M–Te distances in $TlPbTe_3^{3-}$ [3.0324(14)–3.0670(13) Å] are averages of Tl–Te and Pb–Te distances and arise from the symmetry equivalence of the Tl and Pb atoms. Comparable Pb–Te and Tl–Te distances have been observed in $Pb_2Te_3^{2-}$ [2.943(1) Å] and in $Tl_2Te_2^{2-}$ [2.954(2) Å; Chapter 5]. The Te–M–Te bond angle in $TlPbTe_3^{3-}$ [93.07(3)°] is close to the 90° bond angle anticipated for a predominantly *p*-bonded trigonal bipyramidal cage and is comparable to those observed in $Sn_2Ch_3^{2-}$ [Se, 87.9(1)–92.1(1)°; Te, 90.8(2)–90.9(1)°][82] and in $Pb_2Ch_3^{2-}$ [S, 86.16(9)–89.94(7)°;[33] Se, 87.13(3)–90.98(3)°;[172] Te, 91.8(2)[173,174]]. Similar bond angles have also been observed in the trigonal pyramidal $Pb(ChPh)_3^-$ anions [S, 90.32(4)– 96. 14(5)°; Se, 88.82(4)–96.57(4)°].[188] The M–Te–M bond angles in $TlPbTe_3^{3-}$ range from 65.66(3)–66.65(4)° and are similar to that observed in $Pb_2Te_3^{2-}$ [67.00(5)°]. The Ch···Ch distances observed in $TlPbTe_3^{3-}$ [4.427(2) Å] and in $Sn_2Ch_3^{2-}$ [Se, 3.741Å; Te, 4.103 Å] and $Pb_2Ch_3^{2-}$ [S, 3.605–3.731 Å; Se, 3.796–3.932 Å; Te, 4.25 Å] are near the sums of the corresponding van der Waals radii (S, 3.7 Å; Se, 4.0 Å; Te, 4.4 Å).[124]

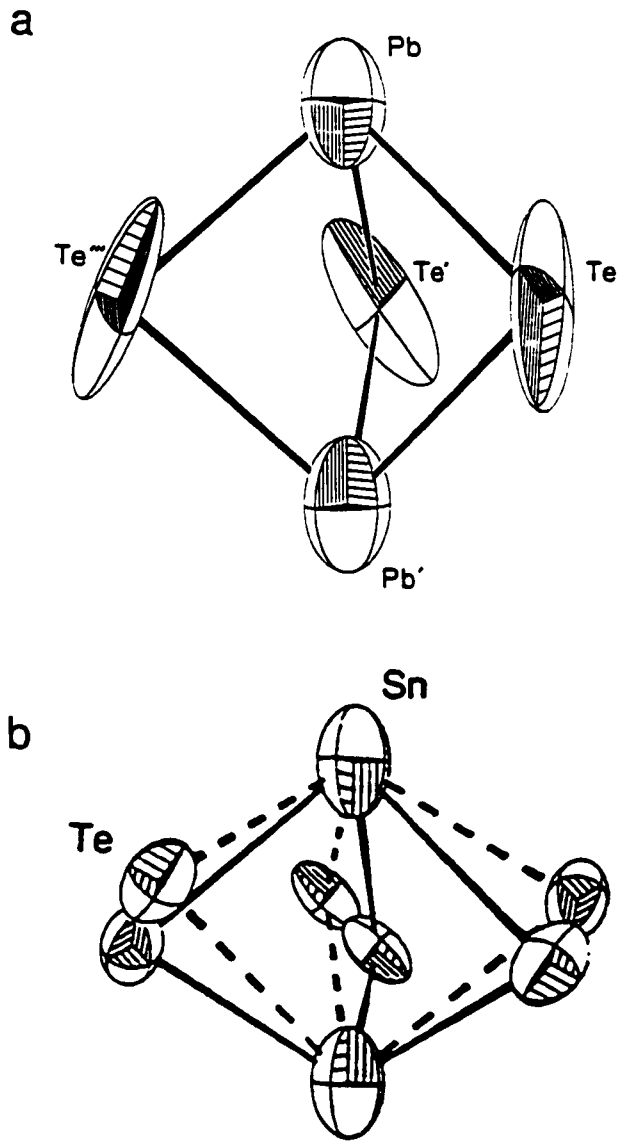

Figure 6.2. (a) View of the $Pb_2Te_3^{2-}$ anion in (2,2,2-crypt-K^+)$_2Pb_2Te_3$ [2-] [173] and (b) the $Sn_2Te_3^{2-}$ anion in (2,2,2-crypt-K^+)$_2Sn_2Te_3$ [2-] [82] depicting partial resolution of the disorder (the disorder in the two tin sites could not be resolved even at −100 °C). Displacement ellipsoids are drawn at the 50% probability level.

Structural Characterization of $TlMTe_3^{3-}$ (M = Sn, Pb) by NMR Spectroscopy.

The $TlMTe_3^{3-}$ anions were identified in solution by natural abundance ^{119}Sn, ^{205}Tl, ^{207}Pb, and ^{125}Te NMR spectroscopy. The experimental and simulated ^{119}Sn, ^{205}Tl, ^{207}Pb, and ^{125}Te NMR spectra are depicted in Figures 6.3–6.8. The chemical shifts and spin–spin coupling constants (scalar, J; reduced, K; and relativistically corrected reduced, K_{RC}) of the $TlMTe_3^{3-}$ anions as well as those of the some previously characterized $M_2Te_3^{2-}$ anions are listed in Table 6.4. The number of observed environments, the doublet and/or satellite doublet spacings corresponding to $J(^{207}Pb–^{203,205}Tl)$, $J(^{119}Sn–^{203,205}Tl)$, $^1J(^{207}Pb–^{125}Te)$, $^1J(^{205}Tl–^{125}Te)$, and $^1J(^{119}Sn–^{125}Te)$, and the I_S/I_C ratios are consistent with trigonal bipyramidal $TlMTe_3^{3-}$ structures having C_{3v} point symmetries and is supported by the trigonal bipyramidal geometry observed for the $TlPbTe_3^{3-}$ and $M_2Ch_3^{2-}$ (M = Sn or Pb; Ch = S, Se, or Te) anions in the solid state.

The ^{119}Sn, ^{205}Tl, and ^{125}Te NMR spectra of the deep red solution obtained by reacting $Tl_2Sn_2Te_3$ and K_2Te in a 1.0 : 1.4 molar ratio in en were recorded at 0 °C (Figures 6.3–6.5) and gave rise to two new signals as well as to several weak signals which were assigned to the previously characterized $SnTe_3^{2-}$ [$\delta(^{119}Sn)$ = –1160 ppm, $\delta(^{125}Te)$ = –410 ppm, $^1J(^{119}Sn–^{125}Te)$ = 4549 Hz],[56] HTe^- [$\delta(^{125}Te)$ = –1094 ppm, $^1J(^{125}Te–^1H)$ = 122 Hz],[71] and $Tl_2Te_2^{2-}$ [$\delta(^{205}Tl)$ = 8182 ppm, $^1J(^{205}Tl–^{125}Te)$ = 6348 Hz][56] anions. The new ^{119}Sn (129.8 ppm), ^{205}Tl (4196 ppm), and ^{125}Te (–887 ppm) resonances were assigned to the trigonal bipyramidal $TlSnTe_3^{3-}$ anion and are discussed below. The remaining spin–spin coupled resonances in the ^{119}Sn [–1216 ppm; $^1J(^{119}Sn–^{125}Te)$ = 4308 Hz] and ^{125}Te [–432 ppm;

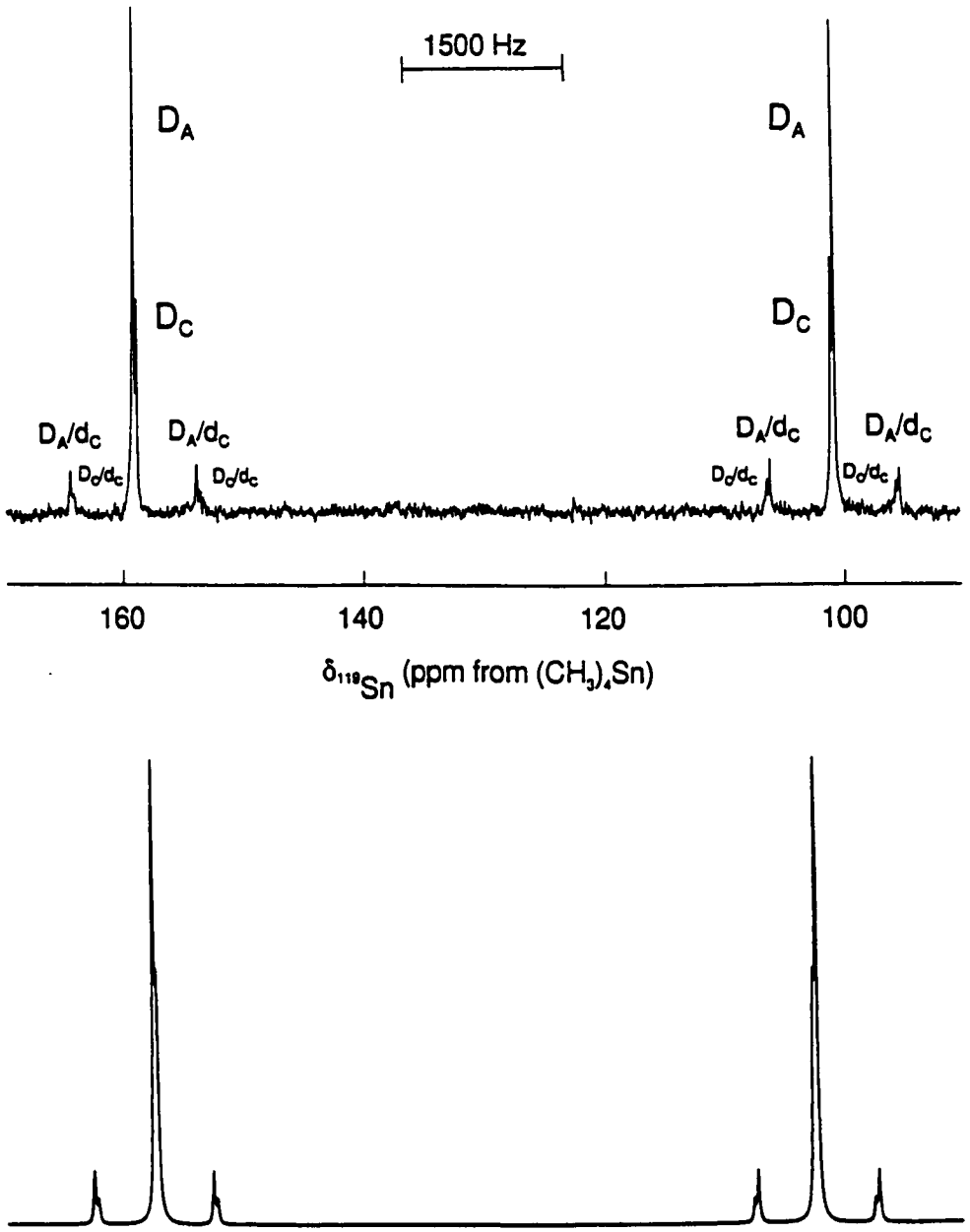

Figure 6.3. The observed (upper trace) and simulated (lower trace) ^{119}Sn NMR spectrum (111.922 MHz, 0 °C) of $TlSnTe_3^{3-}$. The symbols used to label the peaks are defined in Table 6.5 and in the text.

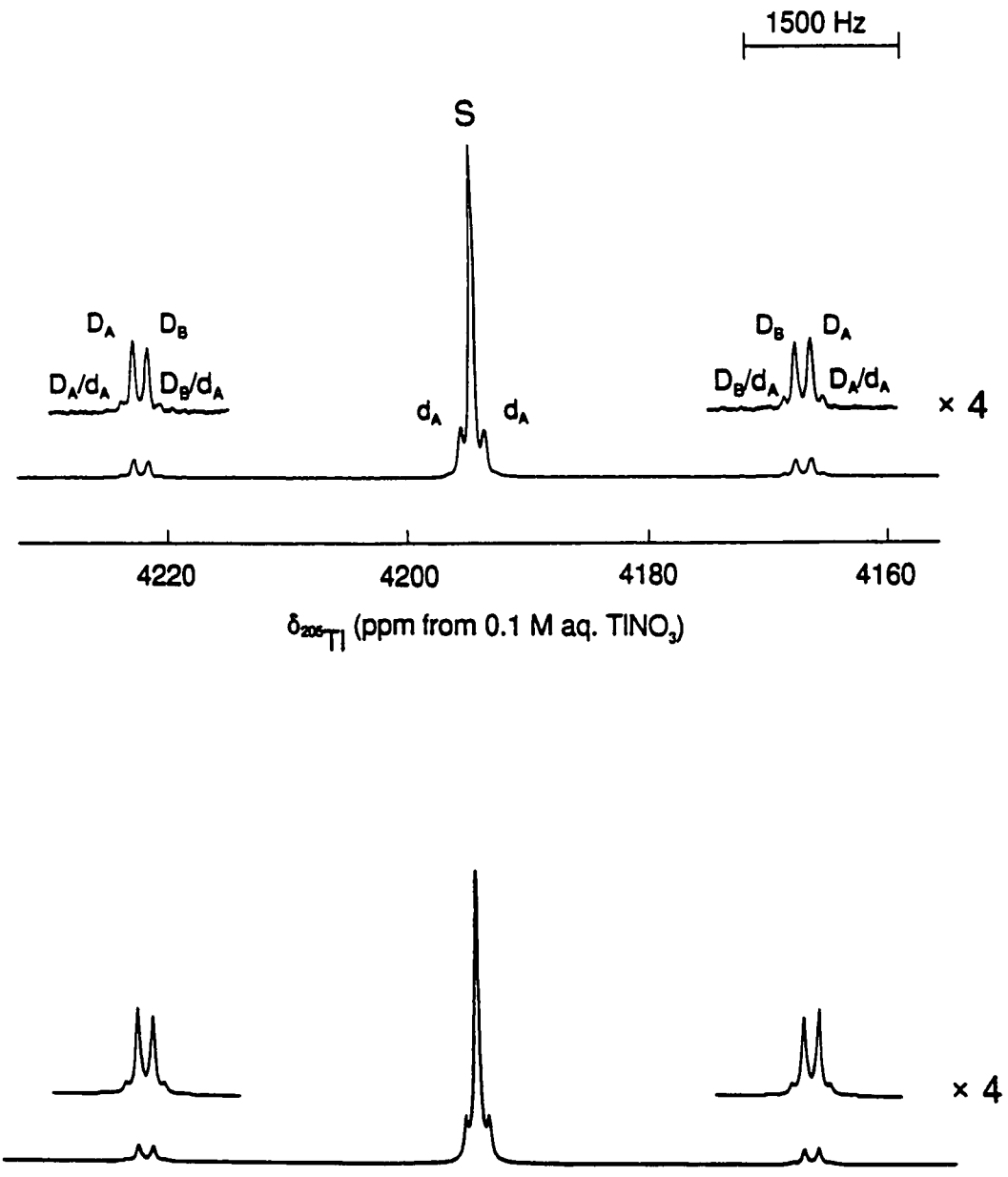

Figure 6.4. The observed (upper trace) and simulated (lower trace) ^{205}Tl NMR spectrum (115.444 MHz, 0 °C) of $TlSnTe_3^{3-}$. The symbols used to label the peaks are defined in Table 6.5 and in the text.

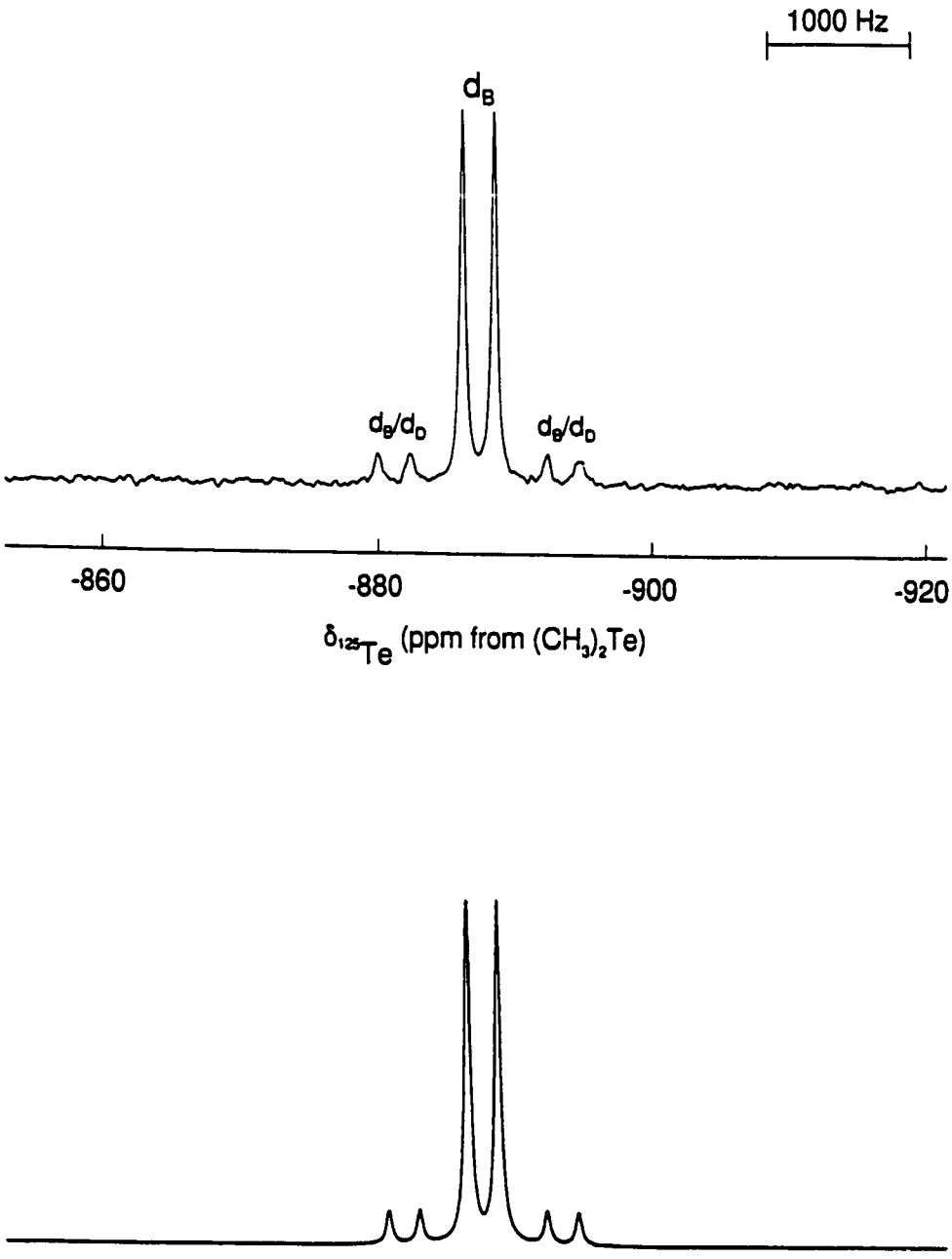

Figure 6.5. The observed (upper trace) and simulated (lower trace) ^{125}Te NMR spectrum (94.692 MHz, 0 °C) of $TlSnTe_3^{3-}$. The symbols used to label the peaks are defined in Table 6.5 and in the text.

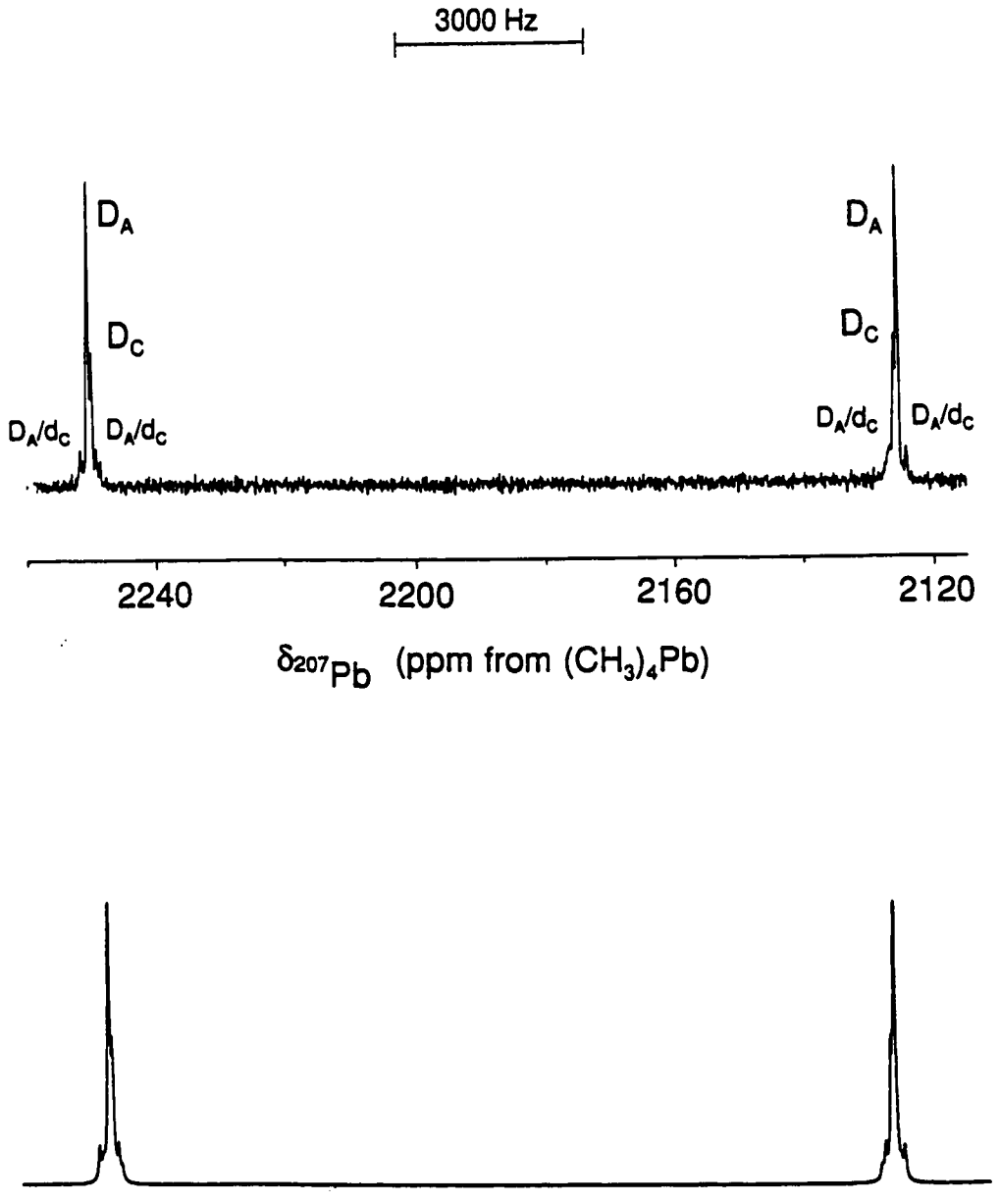

Figure 6.6. The observed (upper trace) and simulated (lower trace) ^{207}Pb NMR spectrum (104.631 MHz, –20 °C) of $TlPbTe_3^{3-}$. The symbols used to label the peaks are defined in Table 6.5 and in the text.

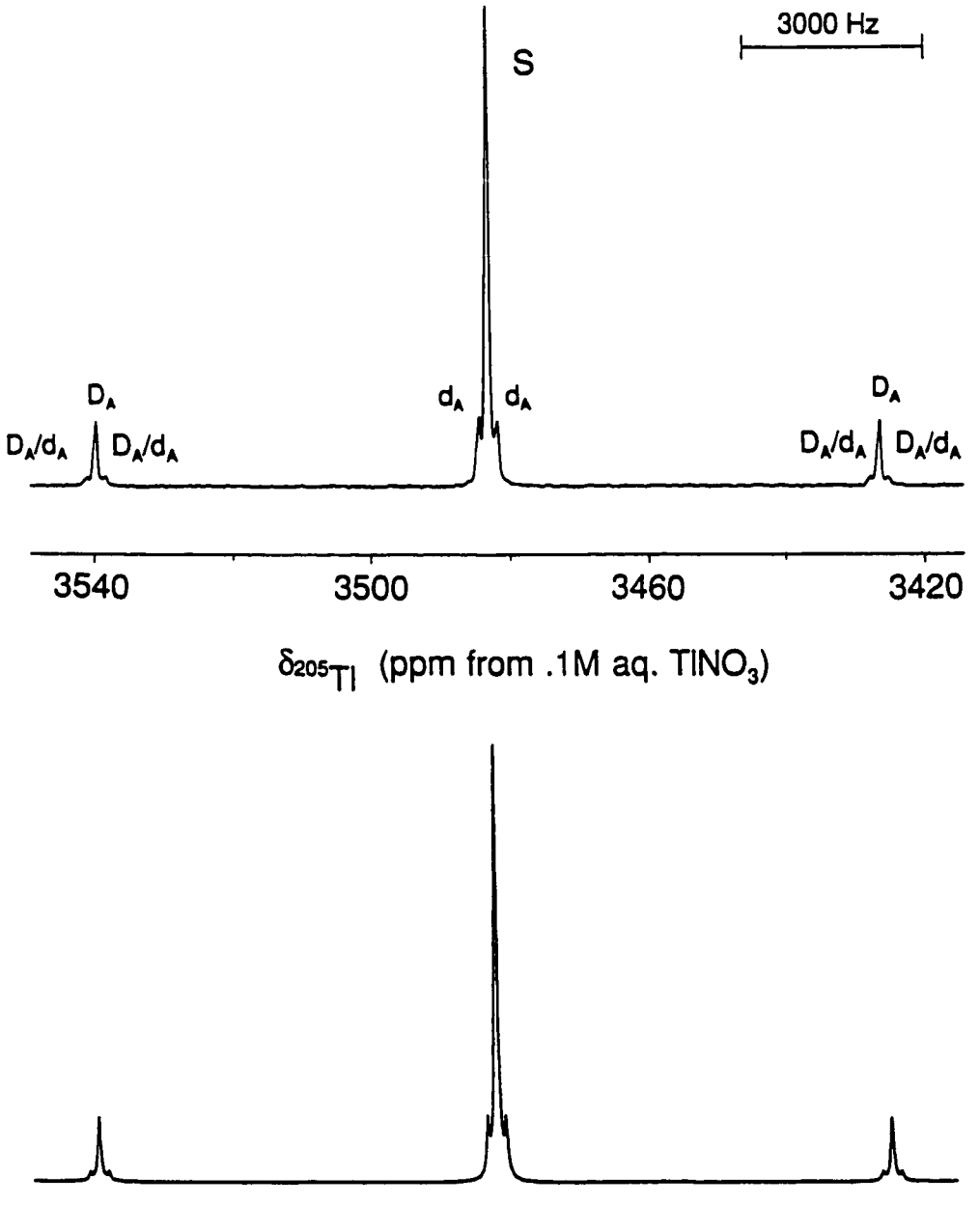

Figure 6.7. The observed (upper trace) and simulated (lower trace) ^{205}Tl NMR spectrum (115.444 MHz, –20 °C) of $TlPbTe_3^{3-}$. The symbols used to label the peaks are defined in Table 6.5 and in the text.

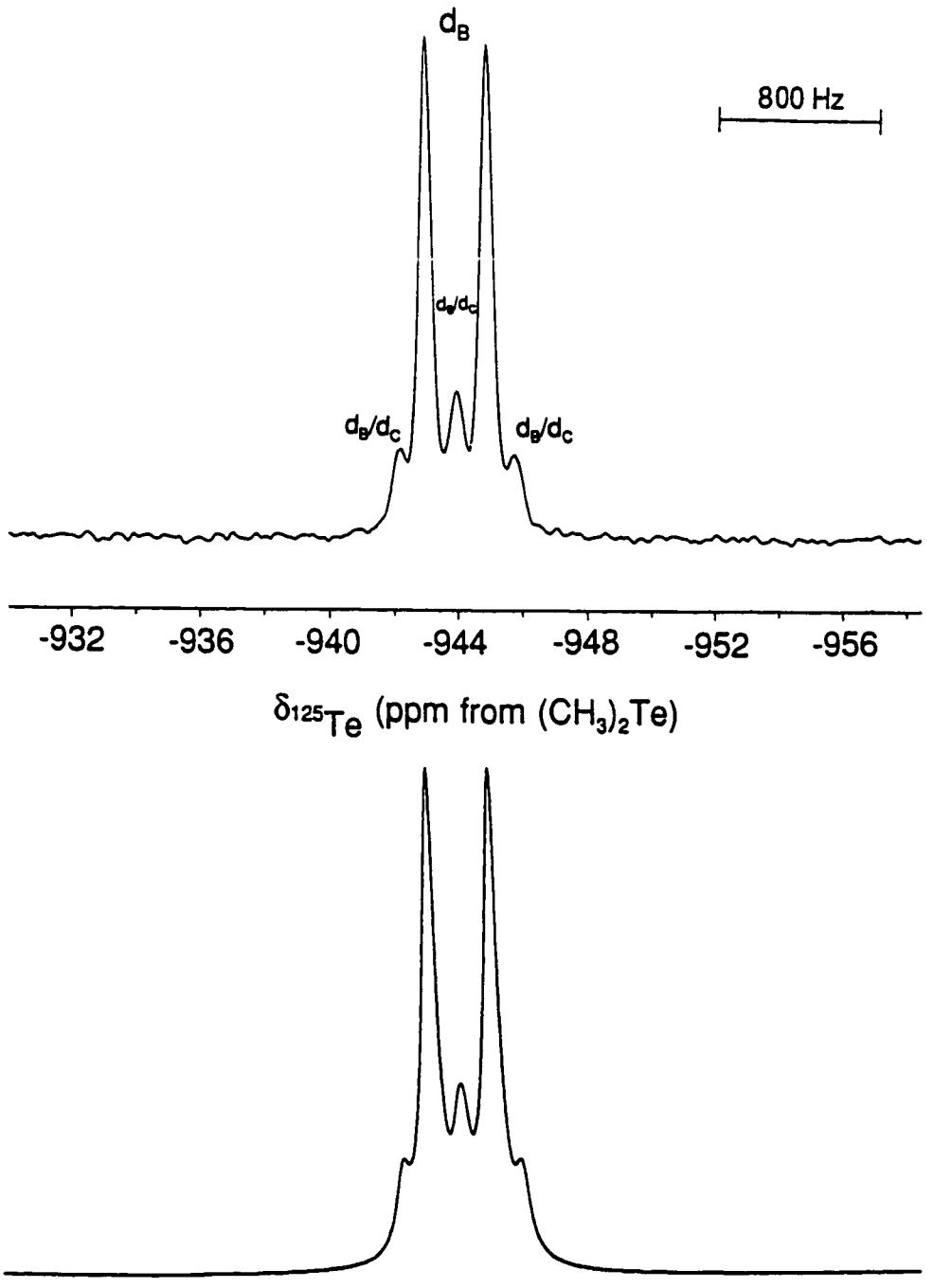

Figure 6.8. The observed (upper trace) and simulated (lower trace) ^{125}Te NMR spectrum (157.794 MHz, –20 °C) of $TlPbTe_3^{3-}$. The symbols used to label the peaks are defined in Table 6.5 and in the text.

Table 6.4. Chemical Shifts and Spin–Spin Coupling Constants for the $TlMTe_3^{3-}$,[a] $M_2Ch_3^{2-}$ (M = Sn or Pb; Ch = Se or Te),[b] and $SnPbSe_3^{2-}$ [c] Anions.

	chem. shift (ppm)				coupling const., J (Hz)		reduced coupling const, K and K_{RC} ($\times 10^{21}$ T^2J^{-1})			
anion	^{119}Sn	^{205}Tl	^{207}Pb	Ch	M–Ch	M–M	M–Ch	M–M	$(M\text{–}Ch)_{RC}$	$(M\text{–}M)_{RC}$
$TlSnTe_3^{3-}$	130	4196		–887	1180 (Sn)	6553 (^{119}Sn)	8.236 (Sn)	2.474	4.017 (Sn)	5.676
					221 (Tl)	6474 (^{117}Sn)	0.986 (Tl)		0.224 (Tl)	
$TlPbTe_3^{3-}$		3483	2188	–944	280 (Pb)	13086 (^{205}Tl)	3.485 (Pb)	8.832	0.786 (Pb)	9.377
						12962 (^{203}Tl)	1.370 (Tl)		0.311 (Tl)	
$Sn_2Se_3^{2-}$	421			12	397	1514	4.602	8.964	2.803	4.416
$Sn_2Te_3^{2-}$	59			–764	523		3.650		1.780	
$Pb_2Se_3^{2-}$			3302	–99	153		3.165		0.889	
$Pb_2Te_3^{2-}$			1727	–928	1074		1.611		3.636	
$SnPbSe_3^{2-}$	528		3439	–42	415 (Sn)	1514	4.813 (Sn)	1.209	2.922 (Sn)	2.763
					153 (Pb)		3.168 (Pb)		0.889 (Pb)	

[a] Present work. [b,c] Refs. (82) and (172).

$^1J(^{125}Te–Sn)$ = 4308 (^{119}Sn) and 4118 Hz (^{117}Sn)] NMR spectra remain unassigned. However, the magnitudes of the I_S/I_C ratios and the ^1J value, which is comparable to that determined for the Sn(IV) species $SnTe_3^{2-}$ (4549 Hz),[56] indicate that the species contains "Sn(IV)Te_3" units. Interestingly, only the $HOSnTe_3^{3-}$ anion was characterized by X-ray crystallography in the crystalline material obtained upon addition of THF to the deep red en solution (Chapter 3). The uncharacterized solution species has therefore been speculated to be $HOSnTe_3^{3-}$.

The ^{207}Pb, ^{205}Tl, and ^{125}Te NMR spectra of a deep red solution obtained by allowing $Tl_2Pb_2Te_3$ and K_2Te to react in a 1.0 : 1.6 molar ratio in en/ethylamine (1:1 v/v) in the presence of a molar excess of 2,2,2-crypt with respect to K^+ were recorded at –20 °C. The signal at –1094 ppm in the ^{125}Te NMR spectrum was assigned to HTe^-.[71] All remaining resonances in the ^{205}Tl, ^{207}Pb, and ^{125}Te NMR spectra were assigned to the trigonal bipyramidal $TlPbTe_3^{3-}$ anion and are discussed below. In addition to $TlPbTe_3^{3-}$, the known $TlTe_3^{3-}$ and $Pb_2Te_3^{2-}$ anions were also detected at 0 °C by ^{125}Te NMR spectroscopy in a red-brown solution obtained by reacting $Tl_2Pb_2Te_3$ and K_2Te in a 1.0 : 1.4 molar ratio in en and in the presence of a 50 mole% excess of 2,2,2-crypt. However, the resonances corresponding to the $TlPbTe_3^{3-}$ anion at 0 °C were exchange broadened ($\Delta\nu_{1/2}$ ~500–1000 Hz) and precluded accurate I_S/I_C and J-coupling determinations. Consequently, subsequent discussion of the NMR parameters for the $TlPbTe_3^{3-}$ anion refers to spectra obtained at –20 °C.

Analysis of Spin–Spin Coupling Patterns. The ^{119}Sn NMR spectrum of the $TlSnTe_3^{3-}$ anion was observed in the Sn(II) region (Figure 6.3) and consisted of an intense, sharp doublet arising from coupling to one thallium atom. The $J(^{119}Sn–^{205}Tl)$ = 6553 Hz and

$J(^{119}Sn–^{203}Tl)$ = 6474 components of the doublet could be resolved; the ratio, $J(^{119}Sn–^{205}Tl)/J(^{119}Sn–^{203}Tl)$ = 1.009, is in excellent agreement with the ratio $\gamma(^{205}Tl)/\gamma(^{203}Tl)$ = 1.010. The I_S/I_C value of the accompanying ^{125}Te satellites (calculated, 11.3%; theoretical, 11.3%) indicated that the tin environment was coupled to three chemically equivalent tellurium atoms. The ^{205}Tl NMR resonance of $TlSnTe_3^{3-}$ (Figure 6.4) was observed in the Tl(I) region and is a singlet flanked by three sets of symmetric doublet satellites arising from $^1J(^{205}Tl–^{125}Te)$, $J(^{205}Tl–^{119}Sn)$, and $J(^{205}Tl–^{117}Sn)$ couplings (Table 6.5). In addition, four weaker satellites were also observed in both the ^{119}Sn and ^{205}Tl NMR spectra of $TlSnTe_3^{3-}$ (D_B, D_A/d_C, D_B/d_A, and D_C/d_C in Figures 6.3 and 6.4) and their assignments are discussed below. The ^{125}Te NMR signal of the anion (Figure 6.5) comprised a doublet arising from unresolved $^1J(^{125}Te–^{203,205}Tl)$ coupling and accompanying unresolved doublet satellites corresponding to $^1J(^{125}Te–^{117,119}Sn)$.

The ^{207}Pb (Figure 6.6), ^{205}Tl (Figure 6.7), and ^{125}Te (Figure 6.8) NMR spectra of $TlPbTe_3^{3-}$ were similar to those of $TlSnTe_3^{3-}$. The ^{207}Pb NMR resonance consisted of a doublet resolved into $J(^{207}Pb–^{205}Tl)$ and $J(^{207}Pb–^{203}Tl)$ components and accompanying unresolved $^{123,125}Te$ satellite doublets. In the ^{205}Tl NMR spectrum of $TlPbTe_3^{3-}$, $^1J(^{205}Tl–^{123,125}Te)$ and $J(^{205}Tl–^{207}Pb)$ were observed as doublet satellites symmetrically flanked about an intense singlet. The counterparts to the four weaker satellites observed in the ^{119}Sn and in the ^{205}Tl NMR spectra of $TlSnTe_3^{3-}$ (*vide supra*) were observed only in the ^{207}Pb spectrum of $TlPbTe_3^{3-}$ (Figure 6.6) but not in the associated ^{205}Tl NMR spectrum (Figure 6.7) and are discussed below. The ^{125}Te NMR spectrum of $TlPbTe_3^{3-}$ (Figure 6.8) was a broad

doublet resulting from unresolved $^{1}J(^{125}Te–^{203,205}Tl)$ coupling and associated doublet satellites attributed to $^{1}J(^{125}Te–^{207}Pb)$.

The $^{*}M$ ($^{*}M = ^{119}Sn$ or ^{207}Pb), ^{205}Tl, and ^{125}Te NMR spectra of $TlMTe_3^{3-}$ (M = Sn, Pb) were simulated by using the natural abundances of the spin-½ nuclei ^{119}Sn, ^{203}Tl, ^{205}Tl, ^{207}Pb, and ^{125}Te;[74] the values of the observed coupling constants (Table 6.4); and the total line intensities and multiplicities of the most abundant isotopomers (Table 6.5) contributing significant first-order subspectra to the experimental ^{119}Sn, ^{205}Tl, ^{207}Pb, and ^{125}Te NMR spectra. The resulting simulations (Figures 6.3–6.8) are in excellent agreement with the experimental spectra and account for all the observed satellite peaks.

The $^{*}M$ ($^{*}M = ^{119}Sn$ or ^{207}Pb) NMR spectra of $TlMTe_3^{3-}$ consist of the superposition of four most abundant isotopomeric subspectra (Table 6.5). The most abundant subspectrum is a DOUBLET (D_A) arising from $J(^{*}M–^{205}Tl)$ coupling. The second most abundant isotopomer (Table 6.5) gives rise to a DOUBLET (D_C) resulting from $J(^{*}M–^{203}Tl)$. The third and fourth most abundant isotopomers give rise to DOUBLET-of-doublets (D_A/d_C and D_C/d_C) subspectra having different total line intensities owing to the different natural abundances of the ^{205}Tl (70.5%) and ^{203}Tl (29.5%) nuclides (Table 6.5). The $J(^{*}M–Tl)$ coupling gives rise to the DOUBLET (D_A or D_C in Table 6.5) in each subspectrum which is split into a satellite doublet (d_C) arising from $^{1}J(^{119}Sn–^{125}Te)$.

The ^{205}Tl NMR spectra of $TlMTe_3^{3-}$ consist of the superposition of six (Sn) and four (Pb) most abundant subspectra (Table 6.5). The two additional subspectra arise in the Sn analog because tin possess two spin-½ nuclides, ^{119}Sn and ^{117}Sn, whereas ^{207}Pb is the only

Table 6.5. Natural Abundance Isotopomers and Subspectra Used to Simulate the ^{119}Sn, ^{207}Pb, ^{205}Tl, and ^{125}Te NMR Spectra of the $TlMTe_3^-$ (M = Sn, Pb) Anions.

$^{205}Tl_m{}^{203}Tl_n{}^{*}M_o{}^{117}Sn_pM_{1-o-p}{}^{125}Te_qTe_{3-q}{}^{a}$					Total Intensity[b,c]			Multiplicity of Subspectrum[c,d]		
m	*n*	*o*	*p*	*q*	^{205}Tl	M	^{125}Te	^{205}Tl	M	^{125}Te
1	0	0	0	0	0.674 (0.623)			S S		
1	0	1	0	0	0.069 (0.182)	0.567 (0.567)		D_A (D_A)	D_A (D_A)	
1	0	0	1	0	0.061			D_B		
1	0	0	0	1	0.152 (0.140)		0.591 (0.546)	d_A (d_A)		d_B (d_B)
1	0	1	0	1	0.016 (0.041)[e]	0.128 (0.128)	0.061 (0.159)	D_A/d_A (D_A/d_A)	D_A/d_C (D_A/d_C)	d_B/d_D (d_B/d_C)
1	0	0	1	1	0.014[e]		0.054	D_B/d_A		d_B/d_D
0	1	1	0	0		0.237 (0.237)			D_C (D_C)	
0	1	1	0	1		0.054[e] (0.054)[e]	0.025 (0.067)[e]		D_C/d_C (D_C/d_C)	d_B/d_D (d_B/d_C)
0	1	0	0	1			0.247 (0.228)			d_B (d_B)
0	1	0	1	1			0.022[e]			d_B/d_D

Table 6.5. Continued.

[a] *M denotes ^{119}Sn or ^{207}Pb and M denotes spinless tin or lead nuclides. [b] Natural abundances of the spin-½ nuclides used to calculate isotopomer abundances were taken from ref. (74): ^{117}Sn, 7.61%; ^{119}Sn, 8.58%; ^{125}Te, 6.99%; ^{203}Tl, 29.5%; ^{205}Tl 70.5%; ^{207}Pb, 22.6 %. The natural abundances of ^{115}Sn (0.35%) and ^{123}Te (0.87%) are too low to contribute detectable isotopomer subspectra and are combined with the spinless tin and tellurium nuclides, respectively. [c] Total line intensities and subspectrum multiplicities for the $TlPbTe_3^{3-}$ anion, where appropriate, are given in parentheses. [d] S denotes a singlet; D_A, D_B, and D_C denote DOUBLETS arising from $J(^{205}Tl-{}^{*}M)$, $J(^{205}Tl-^{117}Sn)$, and $J(^{*}M-^{203}Tl)$, respectively; and d_A, d_B, d_C, and d_D denote doublets arising from $^{1}J(^{205}Tl-^{125}Te)$, unresolved $^{1}J(^{125}Te-^{203,205}Tl)$, $^{1}J(^{*}M-^{125}Te)$, and unresolved $^{1}J(^{125}Te-^{117,119}Sn)$ couplings, respectively. The symbols D/d generally denote DOUBLETS-of-doublets. [e] Isotopomers having multiplet line intensities below this value are too low to be observed and are not included in the summations of the simulated subspectra.

NMR active nuclide of lead. The most abundant DOUBLET subspectrum in the ^{205}Tl NMR spectrum of $TlSnTe_3^{3-}$ arises from Tl–Sn coupling and is split into its J(^{205}Tl–^{119}Sn) (D_A) and J(^{205}Tl–^{117}Sn) (D_B) components, and the less abundant DOUBLET-of-doublets subspectrum (Table 6.5) arising from Tl–Sn and Tl–Te couplings is also split into ^{119}Sn and ^{117}Sn components. This results in the observation of four additional satellites in the ^{205}Tl NMR spectrum of $TlSnTe_3^{3-}$ when compared to that of the Pb analogue.

The ^{125}Te NMR spectra of $TlMTe_3^{3-}$ should consist of the superposition of six (Sn) and four (Pb) most abundant isotopomers (Table 6.5). However, none of the individual components of the Te–Tl and Te–Sn couplings could be resolved owing to broad lines.

The spin–spin couplings observed between the axial metal atoms in $TlMTe_3^{3-}$ (M = Sn, Pb) are the first (Pb) and second (Sn) Tl–M couplings to be reported. A two-bond Tl–Sn coupling of 1293 Hz has been reported for the structurally related $SnTlO_3(t\text{-Bu})_3$.[183] In addition, J(^{119}Sn–^{203,205}Tl) values of 519–800 Hz have also been reported for the clusters $Sn_{8-x}Pb_xTl^{5-}$ (x = 0–4).[122] However, no Tl–Pb couplings were reported for these anions.

Chemical Shifts. The $TlPbTe_3^{3-}$ and $TlSnTe_3^{3-}$ anions can be viewed as being derived from $Pb_2Te_3^{2-}$ and $Sn_2Te_3^{2-}$ by replacement of a lead and tin atom, respectively, with a thallium atom. Based on electronegativity differences (χ_{Sn} = 1.96, χ_{Tl} = 2.04, and χ_{Pb} = 2.33), substitution should result in increased shielding of the tellurium resonances in both anions as well as the lead resonance in $TlPbTe_3^{3-}$, but deshielding of the tin resonance in $TlSnTe_3^{3-}$ relative to the ditin analogue. While the tellurium and tin resonances of the new anions are shifted to lower and higher frequencies, respectively, the lead resonance of $TlPbTe_3^{3-}$ is

shifted to a higher frequency when compared to that of $Pb_2Te_3^{2-}$ (Table 6.4). In contrast, substitution of a tin atom in $Sn_2Se_3^{2-}$ by the more electronegative lead atom resulted in the anticipated deshielding of the tin nucleus in the $SnPbSe_3^{2-}$ anion. This trend has also been noted for $Pb_2Ch_3^{2-}$ and for $TlCh_3^{3-}$, $SnCh_3^{2-}$, $SnCh_4^{4-}$, $HgCh_2^{2-}$ and $CdCh_2^{2-}$ (Ch = S, Se, and/or Te)[56] in which the shielding of the central atom decreased as the total electron-withdrawing ability of the attached ligand atoms increased. The larger high-frequency shift of the Pb resonance is qualitatively consistent with the larger dynamic chemical shift range predicted for ^{207}Pb when compared to those for ^{119}Sn and ^{125}Te by Ramsey's equation for nuclear shielding in which the paramagnetic term, σ^p, has a direct dependence on the radial term $\langle r^{-3} \rangle_{np}$ for the valence *p*-electrons (see Chapter 1). An extreme high-frequency shift has been noted by Pyykkö *et al.* as possibly being due to the "HAHA" effect (heavy-atom shift of the heavy atom) on the basis of relativistic extended Hückel calculations on PbH_3^-.[189,190] A similar effect is likely to be operative for the ^{207}Pb chemical shift of $TlPbTe_3^{3-}$. However, in the absence of a knowledge of the ^{207}Pb shielding tensors, the apparent anomalies in the ^{207}Pb shielding trends are presently not fully understood.

Computational Results

The results of the density functional theory calculations at the local (LDFT) and non-local (NLDFT) levels for the $M_2Ch_3^{2-}$ (M = Sn, Pb; Ch = S, Se, Te) anions series are summarized in Tables 6.6–6.11.

The geometries derived for the $Sn_2Ch_3^{2-}$ anion series are in good agreement with the

Table 6.6. Experimental and Calculated Geometric Parameters for the $Sn_2Ch_3^{2-}$ (Ch = S, Se, Te) Anions.

	expt.[a]	DZVP/ZVP		
		LDFT	NLDFT	ECP/DZP
$Sn_2S_3^{2-}$				
M···M (Å)	—	3.099	3.146	3.084
M–Ch (Å)	—	2.574	2.622	2.584
Ch···Ch (Å)	—	3.56	3.64	3.59
M–Ch–M (deg)	—	74.1	73.7	73.3
$Sn_2Se_3^{2-}$				
M···M (Å)	3.090(3)	3.167	3.221	3.167
M–Ch (Å)	2.654(5)	2.703	2.762	2.748
Ch···Ch (Å)	3.741	3.79	3.89	3.89
M–Ch–M (deg)	71.1(1)	71.7	71.4	70.4
$Sn_2Te_3^{2-}$				
M···M (Å)	3.270(6)	3.270	3.323	3.255
M–Ch (Å)	2.887(4)	2.926	2.989	2.987
Ch···Ch (Å)	4.103	4.20	4.30	4.34
M–Ch–M (deg)	68.7(1)	68.0	67.3	66.0

[a] Average Values.

Table 6.7. Experimental and Calculated Geometric Parameters for the $Pb_2Ch_3^{2-}$ (Ch = S, Se, Te) Anions.

	expt [a]	PP/DZVP		PP	
		LDFT	NLDFT	LDFT	ECP/DZP
$Pb_2S_3^{2-}$					
M···M (Å)	3.1467(7)	3.004	3.008	3.023	3.110
M–Ch (Å)	2.640(5)	2.660	2.685	2.633	2.616
Ch···Ch (Å)	3.67(2)	3.78	3.85	3.71	3.64
M–Ch–M (deg)	73.2(4)	68.4	68.2	70.1	72.9
$Pb_2Se_3^{2-}$					
M···M (Å)	3.184(3)	3.061	3.073	3.020	3.156
M–Ch (Å)	2.751(10)	2.792	2.820	2.719	2.775
Ch···Ch (Å)	3.88(2)	3.99	4.03	3.93	3.95
M–Ch–M (deg)	70.7(7)	66.6	66.2	67.5	69.3
$Pb_2Te_3^{2-}$					
M···M (Å)	3.249(2)	3.105	3.057	3.041	3.207
M–Ch (Å)	2.943(2)	2.980	2.622	2.921	3.003
Ch···Ch (Å)	4.25	4.41	4.36	4.32	4.40
M–Ch–M (deg)	67.01(6)	62.8	62.6	62.7	64.5

[a] Average Values.

Table 6.8. Charges (e) for the $M_2Ch_3^{2-}$ (M = Sn, Pb; Ch = S, Se, Te) Anions.

	DZVP/DZVP		
	LDFT	NLDFT	
$Sn_2S_3^{2-}$			
M	–0.30	–0.19	
Ch	–0.36	–0.54	
$Sn_2Se_3^{2-}$			
M	–0.18	–0.09	
Ch	–0.54	–0.72	
$Sn_2Te_3^{2-}$			
M	–0.14	–0.07	
Ch	–0.57	–0.62	
	PP/DZVP		PP/PP
	LDFT	NLDFT	LDFT
$Pb_2S_3^{2-}$			
M	0.23	0.26	0.02
Ch	–0.82	–0.84	–0.68
$Pb_2Se_3^{2-}$			
M	0.28	0.29	0.12
Ch	–0.85	–0.86	–0.74
$Pb_2Te_3^{2-}$			
M	0.27	0.13	0.08
Ch	–0.57	–0.62	–0.72

Table 6.9. Mayer Valencies and Mayer Bond Orders in the $M_2Ch_3^{2-}$ (M = Sn, Pb; Ch = S, Se, Te) Anions.

	$Sn_2Ch_3^{2-}$						$Pb_2Ch_3^{2-}$					
	LDFT						LDFT			NLDFT		
	all electron			pseudopotential								
	S	Se	Te	S	Se	Te	S	Se	Te	S	Se	Te
Valencies												
M	3.20	3.01	2.97	2.65	2.64	2.87	2.44	2.41	2.44	2.41	2.39	2.71
Ch	1.97	1.87	1.87	1.87	1.69	2.06	1.65	1.60	1.59	1.63	1.58	1.95
Bond Orders												
M···M	0.32	0.27	0.27	0.17	0.21	0.25	0.13	0.19	0.28	0.14	0.20	0.22
M–Ch	0.96	0.91	0.90	0.82	0.81	0.88	0.77	0.74	0.72	0.76	0.73	0.83
Ch···Ch	0.03	0.02	0.04	0.03	0.03	0.15	0.06	0.06	0.08	0.06	0.06	0.14

Table 6.10. Natural Bond Order Analysis in the $M_2Ch_3^{2-}$ (M = Sn, Pb; Ch = S, Se, Te) Anions at the ECP/DZP Level of Theory.

Orbital	Orb. Pop.		%*s*	%*p*	*s* (coeff.)	p_x (coeff.)	p_y (coeff.)	p_z (coeff.)
					$Sn_2S_3^{2-}$			
Sn–S	1.97	Sn [21.4%]	6.2	93.6	–0.25		–0.81, –0.07	0.52
		S [78.6%]	13.7	86.1	–0.37		0.60	–0.71
σ(Sn–S)*	0.09							
Sn lone pair	2.00		81.5	18.5	0.90			0.43
S lone pair	1.98		72.5	27.5	0.85		0.52	
S lone pair	1.86			100		1.00		
					$Sn_2Se_3^{2-}$			
Sn–Se	1.97	Sn [22.6%]	5.8	93.2	0.24		0.81, 0.07	0.52
		Se [77.4%]	10.1	89.7	0.32		–0.63	0.71
σ(Sn–Se)*	0.08							
Sn lone pair	2.00		82.8	17.2	0.91			0.41
Se lone pair	1.98		79.8	20.2	0.89		0.45	
Se lone pair	1.86			100		1.00		

Table 6.10. Continued

Orbital	Orb. Pop.		%s	%p	s (coeff.)	p_x (coeff.)	p_y (coeff.)	p_z (coeff.)
					$Sn_2Te_3^{2-}$			
Sn–Te	1.95	Sn [22.6%]	4.8	94.8	0.22		0.81	–0.53
		Te [77.4%]	8.2	91.6	0.29		–0.64	0.71
σ(Sn–Te)*	0.10							
Sn lone pair	1.99		85.7	14.3	0.91			0.38
Te lone pair	1.98		83.5	16.5	0.91		0.41	
Te lone pair	1.90			100		1.00		
					$Pb_2S_3^{2-}$			
Pb–S	1.97	Pb [21.9%]	4.6	95.3	–0.20, –0.09		–0.81, 0.08	0.54
		S [78.1%]	10.8	89.1	–0.33		0.63	–0.71
σ(Pb–S)*	0.09							
Pb lone pair	2.00		88.2	11.8	0.94			0.34
S lone pair	1.98		78.4	21.6	0.89		0.46	
S lone pair	1.86			100		1.00		

Table 6.10. Continued

Orbital	Orb. Pop.		%s	%p	s (coeff.)	p_x (coeff.)	p_y (coeff.)	p_z (coeff.)
					$Pb_2Se_3^{2-}$			
Pb–Se	1.97	Pb [22.4%]	4.6	95.2	0.19, –0.11		0.81	–0.54
		Se [77.6%]	8.0	91.8	0.28		–0.605	0.71
σ(Pb–Se)*	0.08							
Pb lone pair	2.00		89.3	10.7	0.94			0.33
Se lone pair	1.99		84.0	16.0	0.92		0.42	
Se lone pair	1.90			100		1.00		
					$Pb_2Te_3^{2-}$			
Pb–Te	1.95	Pb [24.8%]	3.9	95.9	0.17, –0.10		0.81	–0.54
		Te [75.2%]	7.4	92.4	0.27		–0.65	0.71
σ(Pb–Te)*	0.11							
Pb lone pair	1.99		91.2	8.8	0.96			0.29
Te lone pair	1.98		85.2	14.8	0.92		0.39	
Te lone pair	1.86			100		1.00		

Table 6.11. Natural Atomic Orbital Populations for the $M_2Ch_3^{2-}$ (M = Sn, Pb; Ch = S, Se, Te) Anions.

	S	Se	Te
$Sn_2Ch_3^{2-}$			
Sn (*s*)	1.73	1.76	1.81
Sn (p_x)	0.46	0.47	0.57
Sn (p_y)	0.46	0.47	0.57
Sn (p_z)	0.84	0.83	0.82
Ch (*s*)	1.87	1.88	1.88
Ch (p_x)	1.67	1.58	1.45
Ch (p_y)	1.73	1.90	1.90
Ch (p_z)	1.58	1.59	1.56
$Pb_2Ch_3^{2-}$			
Pb (*s*)	1.85	1.87	1.89
Pb (p_x)	0.48	0.47	0.55
Pb (p_y)	0.48	0.47	0.55
Pb (p_z)	0.75	0.72	0.69
Ch (*s*)	1.89	1.91	1.90
Ch (p_x)	1.64	1.56	1.46
Ch (p_y)	1.86	1.90	1.90
Ch (p_z)	1.56	1.61	1.60

experimental values at the LDFT level when all-electron basis sets are used for the Sn and the Ch atoms. The calculated Sn–Ch and Sn···Sn distances are 0.15–0.16 Å longer than the experimental values, but the M–Ch–M bond angles are in better agreement (Table 6.6). Agreement between the calculated and experimental values is not as good at the NLDFT level, which predicts longer Sn–Ch and Sn···Sn bond lengths. The geometries derived for the $Pb_2Ch_3^{2-}$ anion series at the ECP level are in reasonable agreement with the experimental values, with the Pb···Pb distances underestimated by 0.03–0.04 Å (Table 6.7). Similar calculations for the Pb_9^{3-} and Pb_9^{4-} anions also underestimated the Pb···Pb distances.[29] For both series of anions, the calculations reproduce the observed increase in the M···M distances with increasing size of the Ch atoms. Interestingly, this trend is not reproduced for the $Pb_2Ch_3^{2-}$ anion series at the LDFT level when pseudopotentials are used for the Pb and Ch atoms and contrasts with the results obtained for the $Tl_2Ch_2^{2-}$ anions (Chapter 5) where use of pseudopotentials provided the best agreement with the experimental values.

The bonding in the $Pb_2Ch_3^{2-}$ anion series is predicted to be significantly more ionic than in $Sn_2Ch_3^{2-}$ (Table 6.8). The calculated Mayer valencies for $Sn_2Ch_3^{2-}$ (Table 6.9) give values of 3 for Sn and 2 for the Ch atoms, consistent with three Ch atoms covalently bonded to each Sn atom. For the $Pb_2Ch_3^{2-}$ anion series, the calculated Mayer valencies give values of ~2.5 for Pb and ~1.6 for Ch and reflect the higher ionic component to the bonding. The calculated Pb–Ch Mayer bond orders (0.72–0.83) are significantly smaller than the Sn–Ch values (0.82–0.96) and also reflect more ionic Pb–Ch bonds. There are weak interactions between the M atoms in both anion series (bond order, 0.17–0.32 for Sn···Sn and 0.13–0.28

for Pb···Pb) and between the Ch atoms (bond order, 0.02–0.15 for $Sn_2Ch_3^{2-}$ and 0.06–0.15 for $Pb_2Ch_3^{2-}$). Interestingly, The M···M interactions in the $M_2Ch_3^{2-}$ anion series are predicted to increase in the order Te > Se > S despite the observed and calculated increase in the M···M distance with increasing Ch atom size. The calculated weak M···M interactions in $M_2Ch_3^{2-}$ are supported by the short bridgehead···bridgehead interactions observed in the structurally related $[(CH_3)_3Si)_3C]_2$-Si_2Se_3 (Si···Si, 2.515 Å)[178] molecule and in the Ge analog (Ge···Ge, 2.672 Å).[179] Unusually short transannular bridgehead···bridgehead contacts have been calculated for the 2,4,5-trioxa-subsituted bicyclo[1.1.1]propellanes (Si, 2.069 Å; Ge, 2.235 Å; Sn, 2.525 Å).[191] In contrast, the calculated structures of the MH_2-substituted Group IV bicyclo[1.1.1]propellanes, $M_2(MH_2)_3$ (M = Si, Ge, Sn), indicate the absence of M···M interactions[191] which was confirmed by the longer M···M distance [3.367(1) Å] observed in the crystal structure of 2,2,4,4,5,5-hexakis(2,6-diethylphenyl)pentastanna[1.1.1]propellane.[192]

The NBO analyses were used to further assess the bonding in the $M_2Ch_3^{2-}$ anion series (Table 6.10). The analysis shows two-centre M–Ch bonds with populations of 1.95–1.97. The remaining bond population is in the M–Ch σ^* orbital. The two-centre M–Ch bonds have ~80% of the two electrons on Ch and ~20% on M. The bonding is predominantly *p* in character with ~93–96% *p*-character on M and ~86–92% *p*-character on Ch (Table 6.10). The remaining valence electrons are found in lone pairs. There is essentially a doubly occupied lone pair of high *s*-orbital character on each metal atom (*ca.* 80–90%) and each chalcogen atom (*ca.* 70–85%) (Table 6.11). The *s*-orbital character of the Ch atom lone pair increases with increasing size of the atom. Each Ch atom also possesses a lone electron pair

of pure *p* character. As in the case of the $Tl_2Ch_2^{2-}$ anions (Chapter 5), the NBO analysis did not assign any orbital to weak Tl···Tl or Ch···Ch interactions, but to lone pairs. However, this is not inconsistent with the Mayer analysis which considers total overlap of orbitals between atoms. The NBO analysis "assigns" the lone pairs on the M atoms in $M_2Ch_3^{2-}$ to *s* orbitals, which are of proper symmetry for overlap, thus giving rise to weak Mayer bond orders between the M atoms and to the short M···M distances observed and calculated for the $M_2Ch_3^{2-}$anions.

The ten highest-energy valence-MO's for $Pb_2S_3^{2-}$ are shown in Figure 6.9 of which the seven highest are described below and are similar to those of $Pb_2Ch_3^{2-}$ (Ch = Se, Te) and $Sn_2Ch_3^{2-}$ (Ch = S, Se, Te). The HOMO (orbital a) is the antibonding combination of the "in-plane" lone pairs on the S atom. The NHOMO (orbital b) is the antibonding combination of the "out-of-plane" lone pairs on S with the lone pairs on Pb which are directed along the Pb···Pb axis. The next highest orbital (orbital c) is doubly degenerate and is the antibonding combination of the "in-plane" lone pairs on S. The fourth highest orbital (orbital d) is doubly degenerate and is the non-bonding combination of the "out-of-plane" lone pairs on S. The fifth highest molecular orbital (orbital e) is the Pb–S bonding orbital with significant delocalization on the S lone pairs. The sixth highest orbital (orbital f) shows weak S···S interactions with most of the orbital describing the in-plane interaction between the S atom lone pairs and the Pb atom lone pairs. The seventh orbital (orbital g) shows a Pb···Pb interaction arising mostly from the overlap of the valence *s* orbitals on the Pb atoms.

Coupling Constants. The small $^1K(M–Te)_{RC}$ values determined for $TlMTe_3^{3-}$ (M =

Figure 6.9. Molecular orbitals for $Pb_2S_3^{2-}$ contoured at 0.04 at the LDFT level. The different shades denote the two different phases of the orbitals. Key: (a) HOMO; (b) NHOMO; (c) third (doubly degenerate); (d) fourth (doubly degenerate); (e) fifth; (f) sixth; (g) seventh; (h) eighth; (i) ninth; and (j) tenth highest occupied MO's.

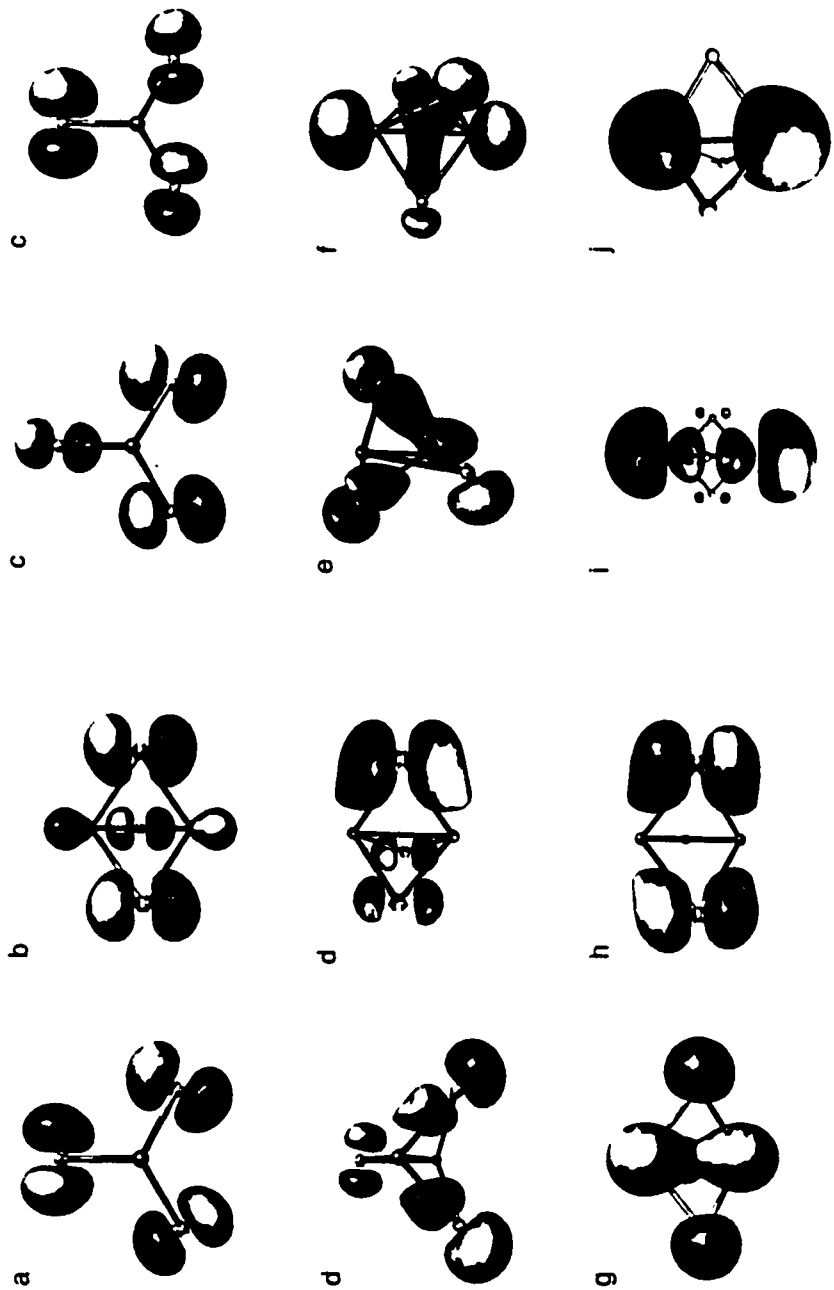
c
f
j
c
e
i
b
d
h
a
d
g

Sn, Pb) are comparable to those observed for $M_2Ch_3^{2-}$ (M = Sn, Pb; Ch = Se, Te) and $SnPbSe_3^{2-}$ (Table 6.4), suggesting that the *s*-character of the M–Ch bonds is greatly diminished and is consistent with LDFT and NLDFT calculations on $M_2Ch_3^{2-}$ (M = Sn, Pb; Ch = Se, S, and/or Te) which have indicated M–Ch bonds of low *s*-characters. In contrast, larger $^1K(Sn–Ch)_{RC}$ values ($\times 10^{21}$ T^2 J^{-1}) have been reported for anions in which the M–Ch bonds have higher *s*-characters, including for the sp^2-hybridized $SnCh_3^{2-}$ [Se, 14.45; Te, 14.91] and the sp^3-hybridized $SnCh_4^{4-}$ [Se, 10.31; Te, 10.06] anions;[56] the tetrahedral $Sn(SPh)_x(SePh)_y(TePh)_{4-x-y}$ molecule, where x = 0–3 and y = 0–4 [Se, 9.70–12.33; Te, 11.50–16.26];[193] the ditin $Sn_2Ch_6^{4-}$ [Se: monobridging (Se_{mb}) 6.26, terminal (Se_t) 14.13; Te: Te_{mb} 5.73, Te_t 13.64] and $Sn_2Ch_7^{4-}$ [Se: dibridging (Se_{db}) 8.00, Se_{mb} 9.33, Se_t 14.35; Te: Te_{db} 8.00, Te_{mb} 9.88, Te_t 13.87] anions (Chapter 3); and the adamantanoid $Sn_4Se_{10}^{4-}$ [Se_{mb} 10.79, Se_t 16.04] anions (Chapter 4). Large one-bond $K(Tl–Ch)_{RC}$ values have also been observed for the trigonal-planar $TlCh_3^{3-}$ anions (Chapter 5).

The $K(M–M)_{RC}$ couplings observed for the $TlMTe_3^{3-}$ (M = Sn, Pb), $SnPbSe_3^{2-}$, and $Sn_2Se_3^{2-}$ anions are considerably larger $^1K(M–Ch)_{RC}$ (Table 6.4) and contrast with the smaller $K(Tl–Tl)_{RC}$ values observed $Tl_2Ch_2^{2-}$ (Ch = Se and/or Te) when compared to $^1K(Tl–Ch)_{RC}$ (Chapter 5). For the $Tl_2Ch_2^{2-}$ anions, the relative magnitudes of $K(Tl–Tl)_{RC}$ and $^1K(Tl–Ch)_{RC}$ were shown to parallel with the calculated smaller Tl···Tl (0.14–0.15) and larger Tl–Ch (Se, 0.79–0.95; Te, 0.82–0.99) Mayer bond orders (Chapter 5). The relative magnitudes of $K(M–M)_{RC}$ and $^1K(M–Ch)_{RC}$ observed for the trigonal bipyramidal anions are inconsistent with the calculated smaller M···M bond orders (0.13–0.32) when compared to the larger

M–Ch values (0.72–0.96). Moreover, while the M···M bond orders calculated by theory for $M_2Ch_3^{2-}$ are comparable to those determined for $Tl_2Ch_2^{2-}$, the $K(M–M)_{RC}$ values observed for $M_2Ch_3^{2-}$ are *ca.* 2–5 times larger than those for $Tl_2Ch_2^{2-}$ and strongly suggest that the calculated weak M···M interactions of high *s*-orbital character (*vide supra*) do not contribute significantly to the M–M coupling mechanism in $M_2Ch_3^{2-}$. The apparent anomaly in $K(M–M)_{RC}$ can be rationalized on the basis of two significant structural differences between the butterfly-shaped $Tl_2Ch_2^{2-}$ and the trigonal bipyramidal $M_2Ch_3^{2-}$ anions: (1) The M–M couplings in $M_2Ch_3^{2-}$ may be transmitted through the three available M–Ch–M coupling pathways (Structure **II**) whereas only two coupling pathways are available in $Tl_2Ch_2^{2-}$ (Figure 5.1) and may also account for the larger $K(M–M)_{RC}$ and smaller $^1K(M–Ch)_{RC}$ observed in $M_2Ch_3^{2-}$. (2) The M–Ch–M bond angles are considerably larger in $Tl_2Ch_2^{2-}$ (~ 90°) than in $M_2Ch_3^{2-}$ (~ 55–70°). A correlation between bond angles and the magnitudes of two-bond couplings constants has been noted for organic molecules containing the H_2C and H_2C= fragments in which $|^2J(^1H–^1H)|$ was found to decrease with an increase in the H–C–H bond angles.[194] These findings have been confirmed by theoretical calculations.[194] The angular dependence of two-bond coupling constants has also been noted for $^2J(^{31}P–^{31}P)$,[195,196] $^2J(^{119}Sn–^{31}P)$,[195] and $^2J(^{195}Pt–^{119}Sn)$[197] couplings in numerous organometallic compounds and for $^2J(^{19}F–^{19}F)$ couplings in noble gas species which were found to be much larger in the $Ng_2F_3^+$ (Ng = Kr[198] or Xe[199]) cations where < F–Ng–F ~ 180° than in XeF_3^+,[200] XeF_5^+,[201,202] and $XeOF_3^+$,[203] where the F–Ng–F bond angles are ~ 90° and may also account for the differences in the relative magnitudes of $K(M–M)_{RC}$ observed in $M_2Ch_3^{2-}$ and in $Tl_2Ch_2^{2-}$.

Conclusion

The series of $M_2Ch_3^{2-}$ (M = Sn, Pb; Ch = S, Se, and/or Te) anions has been extended to include the mixed-metal $TlMTe_3^{3-}$ anions which have been characterized in solution by multi-NMR spectroscopy. A detailed analysis of the first-order ^{205}Tl, ^{207}Pb, ^{119}Sn, and ^{125}Te subspectra arising from natural abundance isotopomer distributions has confirmed that the trigonal bipyramidal geometry observed for the $M_2Ch_3^{2-}$ (M = Sn, Pb; Ch = Se, Te) and $TlPbTe_3^{3-}$ anions in the solid state is retained in solution. The small magnitudes of $^1K(M–Ch)_{RC}$ observed for the trigonal bipyramidal anions are consistent with predominantly *p*-bonded cages and is supported by local and nonlocal density functional theory calculations which have indicated M–Ch bonds of high *p*-character. Although theory has also indicated small M···M interactions in $M_2Ch_3^{2-}$ of high *s*-characters, the large $K(M–M)_{RC}$ couplings appear to arise predominantly from multiple coupling pathways and can be rationalized in terms of the small M–Ch–M bond angles observed in the X-ray crystal structures.

CHAPTER 7

THALLIUM SELENIDE POLYANIONS

Introduction

To date, relatively few polyselenide anions containing Tl^{I} or Tl^{III} have been characterized by X-ray crystallography and even fewer by multi-NMR spectroscopy. Thallium selenide anions characterized by X-ray crystallography include the $Tl_2Se_2^{2-}$,[33,166] $Tl_3Se_3(Se_4)_3^{3-}$,[203] $Tl_4Se_{16}^{4-}$,[204] $[Tl(Se_6)_2^{2-}]_\infty^2$,[205] and $Tl_5Se_5^{3-}$ [33] anions. Thallium selenide polyanions characterized by ^{203}Tl, ^{205}Tl, and ^{77}Se NMR spectroscopy include $TlSe_3^{3-}$ and $Tl_2Se_2^{2-}$,[33,56,166] and only the ^{77}Se NMR spectrum has been reported for $Tl_3Se_3(Se_4)_3^{3-}$.[203] A solution multi-NMR study of the en extracts of the alloy $NaTlSe_{0.5}Te_{1.5}$ containing a molar excess of 2,2,2-crypt led to the characterization of higher nuclearity thallium selenide anions as indicated by the observation of several multiplets in the Tl^{III} region of the ^{205}Tl NMR spectrum.[84] However, the poor signal-to-noise ratio in the ^{125}Te NMR spectrum and the inability to observe resonances in the Tl^{I} region precluded the characterization of these polyanions. Interestingly, the crystalline material isolated from these solutions was reported to be $(2,2,2\text{-crypt-}Na^+)_2Te_4^{2-}$.[40]

Recent ^{203}Tl, ^{205}Tl, and ^{77}Se NMR investigations in this laboratory have established the existence of the novel $Tl_4Se_5^{4-}$, $Tl_4Se_x^{4-}$, and $Tl_3Se_y^{m-}$ anions which were obtained by extraction of the alloy KTlSe in en and liquid NH_3 and in the presence of molar excess

amounts of 2,2,2-crypt.[33] Although the detailed structures of the latter two anions have not yet been determined, they were shown by a detailed analysis of the ^{203}Tl, ^{205}Tl, and ^{77}Se subspectra arising from natural abundance and isotopically-enriched (94.4% in ^{77}Se) isotopomer distributions to be tetra- and trinuclear with respect to thallium. Previous studies on classically-bonded tin chalcogenide anions have demonstrated that the nature of polyanions in solution can be influenced by the alloy composition.[56] It was therefore of interest to apply the same methodology to the study of classically-bonded thallium selenide polyanions.

The present Chapter reports the structural characterization by the X-ray crystallography and ^{203}Tl, ^{205}Tl, and ^{77}Se NMR spectroscopy of novel polynuclear thallium selenide anions which were obtained from extracts of the alloys NaTlSe and $NaTl_{0.5}Se$.

Results and Discussion

Synthetic Strategy.

The experimental approach involved the syntheses of the ternary alloys NaTlSe and $NaTl_{0.5}Se$ by fusion of the elements followed by extraction of the powdered alloys in en and en/THF (1:1 v/v) and in the presence of stoichiometric excess amounts of 2,2,2-crypt with respect to Na^+. The resulting solutions were characterized by NMR spectroscopy at 0 (en) and at –15 °C (en/THF). Low temperature (–70 °C) ^{203}Tl, ^{205}Tl, and ^{77}Se NMR spectra could not be recorded on liquid NH_3 extracts of the alloys NaTlSe and $NaTl_{0.5}Se$ amounts of 2,2,2-crypt in stoichiometric excess with respect to Na^+, as the samples gave rise to large amounts

of crystalline materials at temperatures below –20 °C. Consequently, all liquid NH_3 solutions were prepared in the absence of 2,2,2-crypt. Nuclear magnetic resonance spectroscopic investigations at –70 °C indicated that solutions prepared by extraction of the alloys NaTlSe and $NaTl_{0.5}Se$ contained the same polyanions. However, extracts of the latter alloy generally contained higher concentrations of the polyanions of interest (see Chapter 2) and gave rise to sharper and to better-resolved NMR spectra. Consequently, the ensuing discussion of the NMR parameters at –70 °C will refer to spectra recorded for the $NaTl_{0.5}Se$ alloy extracts.

All attempts to preparing suitable single crystals of (2,2,2-crypt-Na^+)$_4Tl_4Se_8^{4-}$·0.5en and (2,2,2-crypt-Na^+)$_x$(18-crown-6-Na^+)$_y$[$TlSe_{4/2}^-$]$_n^{1-}$·zTHF by the vapour phase diffusion of THF into en extracts of the alloys NaTlSe or $NaTl_{0.5}Se$ containing a molar excess or deficit of 2,2,2-crypt with respect to Na^+ failed to yield crystals after 8–12 months. Crystals suitable for an X-ray diffraction study were therefore prepared by the vapour phase diffusion of THF over a period of 8 months into en extracts of the alloy $NaTl_{0.5}Se$ containing an equimolar mixture of 18-crown-6 and 2,2,2-crypt, where the total amount of 2,2,2-crypt and 18-crown-6 was in stoichiometric excess of the available Na^+ ion.

X-ray Crystal Structures of (2,2,2-crypt-Na^+)$_4Tl_4Se_8^{4-}$·0.5en (1) and (2,2,2-crypt-Na^+)$_x$(18-crown-6-Na^+)$_y$[$TlSe_{4/2}^-$]$_n^{1-}$·zTHF (2).

A summary of the crystal data and refinement results is given in Table 7.1, where those corresponding to compound (2) are preliminary (see Chapter 2). The final and preliminary atomic coordinates and equivalent isotropic thermal parameters for compounds

Table 7.1. Summary of Crystal Data and Refinement Results for (2,2,2-crypt-Na^+)$_4Tl_4Se_8^{4-}$·0.5en (**1**) and (2,2,2-crypt-Na^+)$_x$(18-crown-6-Na^+)$_y[TlSe_{4/2}^-]^1_\infty$·$z$THF (**2**).[a]

	(**1**)	(**2**)
Formula	$C_{74}H_{152}N_{10}O_{24}Tl_4Se_8$	?
Space group (No.)	$P2_1/n$ (15)	$P2_1/n$ (15)
a, Å	14.768(3)	14.246(2)
b, Å	16.635(3)	14.360(3)
c, Å	21.254(4)	26.673(8)
α, deg	90.00	90.00
β, deg	94.17(3)	99.87(3)
γ, deg	90.00	90.00
V, Å^{-3}	5207.6(18)	5375.8(25)
Z	2	4 (?)
mol. wt.	3107.18	?
ρ, g cm^{-3}	1.982	< 1.92[b]
morphology	cube	platelet
dimensions, cm	0.05 × 0.05 × 0.05	0.10 × 0.15 × 0.22
colour	orange	orange
refinement method	F^2	F^2
refl. used	8169	8420
refl. suppressed ($F^2 < -2\sigma F^2$)	57	40
parameters refined	559	563
H-atom method	calculated	calculated
R_1 ($F^2 > 2\sigma F^2$)	0.0331	0.0458
wR_2 (F^2)	0.0446	0.1133
S ($F^2 > 2\sigma F^2$)	0.956	1.092
$\Delta\rho_{max}$, e Å^{-3}	1.137	2.710
$\Delta\rho_{min}$, e Å^{-3}	–0.628	–1.274
w	$w_1 = 0.0065$	$w_1 = 0.0415$
	$w_2 = 0.0000$	$w_2 = 74.3012$

[a] The results for (2,2,2-crypt-Na^+)$_x$(18-crown-6-Na^+)$_y[TlSe_{4/2}]^1_\infty$·zTHF (**2**) are preliminary.

[b] Determined by floatation in perfluorodecaline; see Chapter 2.

(1) and (2), respectively, are provided in Table 7.2. All important bond lengths and bond angles in the title compounds are listed in Table 7.3. For compound (1), the structure of the 2,2,2-crypt cation is similar to that determined in (2,2,2-crypt-Na^+)$_2Te_4^{2-}$,[40] with average Na···O and Na···N distances of 2.536(26) and 2.811(75) Å, respectively.

(2,2,2-crypt-Na^+)$_4Tl_4Se_8^{4-}$·0.5en (1). The crystal structure of compound (1) consists of crystallographically-well-behaved cations, anions, and solvent molecules. The most interesting aspect of the structure is the geometry of the $Tl_4Se_8^{4-}$ anion (~C_{2v} point symmetry) in which the thallium atoms are formally in the +III oxidation state, but are in two distinct chemical environments: two display trigonal planar coordination (Tl_P) and two are tetrahedrally coordinated (Tl_T) to selenium atoms (Figure 7.1a). The selenium atoms in the anion are in three different chemical environments: terminal Se_t atoms; Se_{mb} atoms bridging Tl_P and Tl_T atoms; and $Se_{mb'}$ atoms bridging Tl_T atoms (Figure 7.1a). Accordingly, four distinct Tl–Se bond distances are observed in the anion structure and increase in the order Tl_P–Se_t [2.4653(8) Å] < Tl_P–Se_{mb} [average, 2.593(2) Å] < Tl_T–$Se_{mb'}$ [2.6341(9) Å] < Tl_T–Se_{mb} [average, 2.669(6) Å]. This variation in the Tl–Se bond distances with the coordination about the thallium atoms is consistent with the total bond valence concept,[206] and the general trend, Tl–Se_t < Tl–Se_{mb}, is consistent with the expected higher relative bond order of the Tl–Se_t bonds. This trend has also been observed in $Sn_2Ch_6^{4-}$ (Chapter 3), $Sn_2Te_7^{4-}$, $Sn_4Ch_{10}^{4-}$, and $Sn_4Se_9^{4-}$ (Chapter 4) (Ch = Se or Te). Similar average Tl_T–Se distances have been reported for the $Tl_3Se_3(Se_4)_3^{3-}$ [2.64(3) Å],[203] $Tl_4Se_{16}^{4-}$ [2.66(3) Å],[204] $[Tl(Se_6)_2^{2-}]_\infty^\infty$ [2.639(2) Å],[205] and $Tl_5Se_5^{3-}$ [2.65(6) Å][33] anion structures. Interestingly, the structure of $Tl_5Se_5^{3-}$ contains mixed-

Table 7.2. Atomic Coordinates and Equivalent Isotropic Thermal Parameters (Å^2) for the Tl, Se, and Na atoms in (2,2,2-crypt-Na$^+$)$_4$Tl$_4$Se$_8^{4-}$·0.5en (**1**) and (2,2,2-crypt-Na$^+$)$_x$(18-crown-6-Na$^+$)$_y$[TlSe$_{4/2}^-$]$_\infty^1$·zTHF (**2**).

	x	y	z	U_{eq}[a]
		(1)		
Tl(1)	0.80002(2)	0.23531(2)	0.009235(13)	0.02462(7)
Tl(2)	0.93662(2)	0.41105(2)	0.007296(13)	0.02220(7)
Se(1)	0.70925(5)	0.11104(4)	–0.00155(4)	0.0359(2)
Se(2)	0.75824(5)	0.38680(4)	0.01228(4)	0.0321(2)
Se(3)	0.97622(4)	0.25501(4)	0.01501(3)	0.0260(2)
Na(1)	0.3516(2)	0.2629(2)	0.84090(12)	0.0262(6)
Na(2)	0.3866(2)	0.2980(2)	0.19094(12)	0.0266(6)
		(2)		
Tl(1)	0.49418(2)	0.77774(2)	0.254379(13)	0.02227(11)
Tl(2)	0.50616(3)	0.52758(2)	0.250831(13)	0.02249(11)
Se(1)	0.43133(7)	0.89695(5)	0.18032(3)	0.0269(2)
Se(2)	0.53812(7)	0.90967(6)	0.32534(3)	0.0291(2)
Se(3)	0.63092(7)	0.66016(6)	0.24038(4)	0.0273(2)
Se(4)	0.37317(7)	0.64479(6)	0.27153(3)	0.0292(2)
Na(1)	0.0317(3)	0.8757(3)	0.3067(2)	0.0388(10)
Na(2)	0.0710(3)	0.6768(3)	0.50377(14)	0.0380(10)

[a] U_{eq} is defined as one-third of the trace of the orthogonalized U_{ij} tensor.

Table 7.3. Selected Bond Distances (Å) and Bond Angles (deg) for (2,2,2-crypt-Na^+)$_4Tl_4Se_8^{4-}$·0.5en (**1**) and (2,2,2-crypt-Na^+)$_x$(18-crown-6-Na^+)$_y$[$TlSe_{4/2}^-$]$_\infty^1$-·zTHF (**2**).

Bond Lengths (Å)

(1)

Tl(1)–Se(1)	2.4653(8)	Tl(1)–Se(2)	2.5965(9)
Tl(1)–Se(3)	2.6167(9)	Tl(2)–Se(2)	2.6748(9)
Tl(2)–Se(3)	2.6632(9)	Tl(2)–Se(4)	2.6341(9)
Tl···Tl	3.5538(6)		

(2)

Tl(1)–Se(1)	2.6510(11)	Tl(1)–Se(2)	2.6753(11)
Tl(1)–Se(3)	2.6253(11)	Tl(1)–Se(4)	2.6639(11)
Tl(2)–Se(1A)	2.6690(11)	Tl(2)–Se(2A)	2.6368(11)
Tl(2)–Se(3)	2.6517(11)	Tl(2)–Se(4)	2.6620(11)
Tl···Tl	3.5985(9)		

Bond Angles (deg)

(1)

Se(1)–Tl(1)–Se(2)	133.44(3)	Se(1)–Tl(1)–Se(3)	129.90(3)
Se(3)–Tl(1)–Se(3)	96.58(2)	Se(4)–Tl(1)–Se(4A)	96.10(3)
Se(4)–Tl(1)–Se(3)	118.71(3)	Se(4)–Tl(1)–Se(3A)	117.75(2)
Se(4)–Tl(1)–Se(2)	116.50(3)	Se(4)–Tl(1)–Se(2A)	115.91(3)
Se(3)–Tl(1)–Se(2)	93.62(2)	Tl(1)–Se(2)–Tl(2)	84.77(2)
Tl(1)–Se(2)–Tl(3)	84.61(2)	Tl(2)–Se(2)–Tl(2A)	83.90(3)

(2)

Se(1)–Tl(1)–Se(3)	117.94(4)	Se(1)–Tl(1)–Se(4)	116.42(4)
Se(3)–Tl(1)–Se(4)	94.62(4)	Se(1)–Tl(1)–Se(2)	94.48(4)
Se(3)–Tl(1)–Se(2)	117.52(4)	Se(4)–Tl(1)–Se(2)	117.77(4)
Se(3)–Tl(2)–Se(4)	94.67(2)	Se(3)–Tl(2)–Se(1B)	115.24(4)
Se(4)–Tl(2)–Se(1B)	117.85(4)	Tl(2)–Se(3)–Tl(1)	85.44(3)
Tl(2)–Se(4)–Tl(1)	85.01(3)	Tl(1)–Se(1)–Tl(2A)	84.89(4)

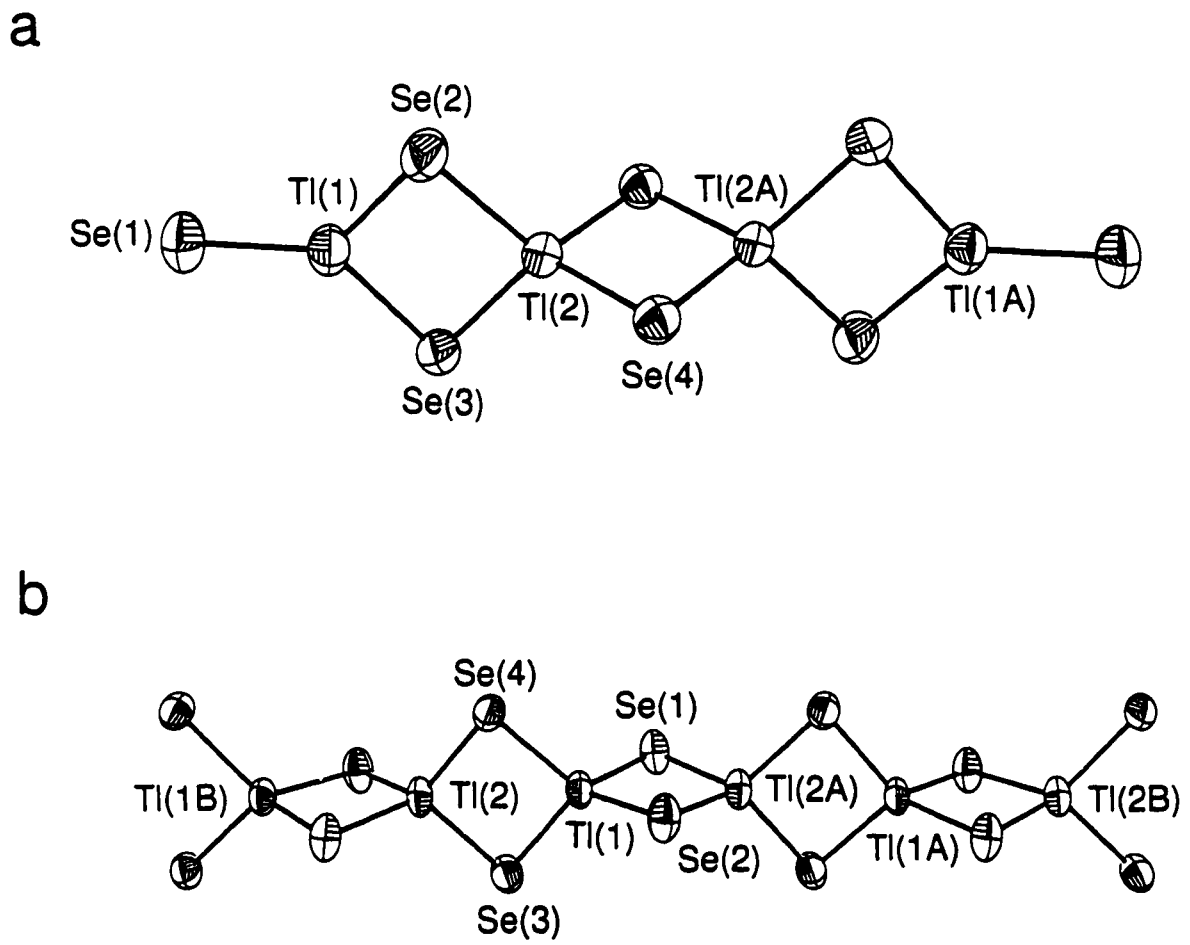

Figure 7.1. Views of (a) the $Tl_4Se_8^{4-}$ anion in (2,2,2-crypt-Na^+)$_4Tl_4Se_8^{4-}$·0.5en and (b) the $[TlSe_{4/2}^-]_\infty^1$ anion in (2,2,2-crypt-Na^+)$_x$(18-crown-6-Na^+)$_y[TlSe_{4/2}^-]_\infty^1$·$z$THF. Displacement ellipsoids are drawn at the 90% probability level.

valence Tl^{I} and Tl^{III} atoms where the former are in a trigonal-pyramidal environment similar to that observed in $TlPbTe_3^{3-}$ (Chapter 6). The Tl^{I}–Se distances in $Tl_5Se_5^{3-}$ are considerably longer than the Tl^{III}–Se distances and are consistent with the larger (1.570) and smaller (1.460) metallic radii of Tl^{I} and Tl^{III}, respectively.[124] None of the known thallium polyselenide structures contain thallium atoms in a trigonal planar environment. The present Tl_p–Se distances are therefore the first to be reported. The Tl^{III}···Tl^{III} distance in $Tl_4Se_8^{4-}$ is 3.5538(6) Å and is considerably shorter than the average Tl^{III}···Tl^{III} distances observed in $Tl_3Se_3(Se_4)_3^{3-}$ [3.76(9) Å] and in $Tl_4Se_{16}^{4-}$ [3.71(13) Å] and is consistent with the two coordination modes observed for the thallium atoms in the present anion structure (trigonal planar and tetrahedral) when compared to the single coordination environment (tetrahedral) observed in the known anion structures. The corresponding Tl^{III}···Tl^{III} bond distance was not reported for the $[Tl(Se_6)_2^{2-}]_\infty^2$ anion.

The average Se–Tl_T–Se bond angle in $Tl_4Se_8^{4-}$ [109.8(48)°] is close to the ideal tetrahedral angle of 109.5° and is similar to those observed in $Tl_3Se_3(Se_4)_3^{3-}$ [109.3(12)°], $Tl_4Se_{16}^{4-}$ [108.8(22)°], $[Tl(Se_6)_2^{2-}]_\infty^2$ [110.0(14)°], and $Tl_5Se_5^{3-}$ [108.1(63)°]. The average Se–Tl_p–Se bond angle is 119.9(12)° and is identical to the ideal D_{3h} bond angle of 120°. The average Tl–Se–Tl bond angle in the present anion structure is 84.4(27)° and is similar to that in $Tl_5Se_5^{3-}$ [85.8(44)°] but is considerably smaller than those in $Tl_3Se_3(Se_4)_3^{3-}$ [93.9(16)°] and in $Tl_4Se_{16}^{4-}$ [89.2(93)°]. Interestingly, the Tl–Se–Tl, Se–Tl–Se bond angles were not reported for the $[Tl(Se_6)_2^{2-}]_\infty^2$ anion.

(2,2,2-crypt-Na$^+$)$_x$(18-crown-6-Na$^+$)$_y$[TlSe$_{4/2}^-$]$_\infty^1$·zTHF (2). As mentioned in Chapter

2, the title compound is non-commensurate and contains severely disordered cations and solvent molecules. A preliminary refinement of the structure was attempted in the smaller crystal sub-lattice (Chapter 2) in which the geometry of the cations and solvent molecules could not be satisfactorily modeled, but that of the anion was accurately determined and is indicated by the small amplitudes of the Tl and Se anisotropic displacement ellipsoids at the 90% probability level (Figure 7.1b). The non-commensurate nature of the compound is clearly indicated by the packing diagram (Figure 7.2b) which shows overlapping anionic and cationic layers and contrasts with the packing diagram of the commensurate compound (2,2,2-crypt-Na^+)$_4Tl_4Se_8^{4-}$·0.5en (**1**) (Figure 7.2a), which consists of well-separated anionic and cationic layers. At present, attempts are being made to resolve the non-commensurate problem and to model the disorder in the cations and solvent molecules.

The most interesting aspect of the structure is the geometry of the $[TlSe_{4/2}^-]_\infty^1$ anion (Figure 7.1a) and has previously been observed in the alloy phase TlSe.[207] The anion geometry is comprised of edge-sharing distorted $TlSe_4$-tetrahedra forming an infinite one-dimensional chain running parallel to the *b*-axis of the unit cell and is isostructural with SiS_2,[208] $SiSe_2$,[208] and InP_2^{3-}.[209] The X-ray crystal structure of the isovalent $AlSe_2^-$ anion has also been reported in the compound $NaAlSe_2$,[210] but the anion geometry consists of corner-sharing adamantanoid Al_4Se_{10}-units forming $AlSe_2^-$ layers. The Tl^{III}–Se [average, 2.658(4) Å; range, 2.6358(11)–2.6753(11) Å] and Tl^{III}···Tl^{III} [3.5985(9) Å] distances in the title compound are considerably shorter and longer, respectively, than those reported for the anion in TlSe [2.670(2) and 3.486(1) Å, respectively] but are similar to the Tl_T–Se_{mb} and Tl···Tl

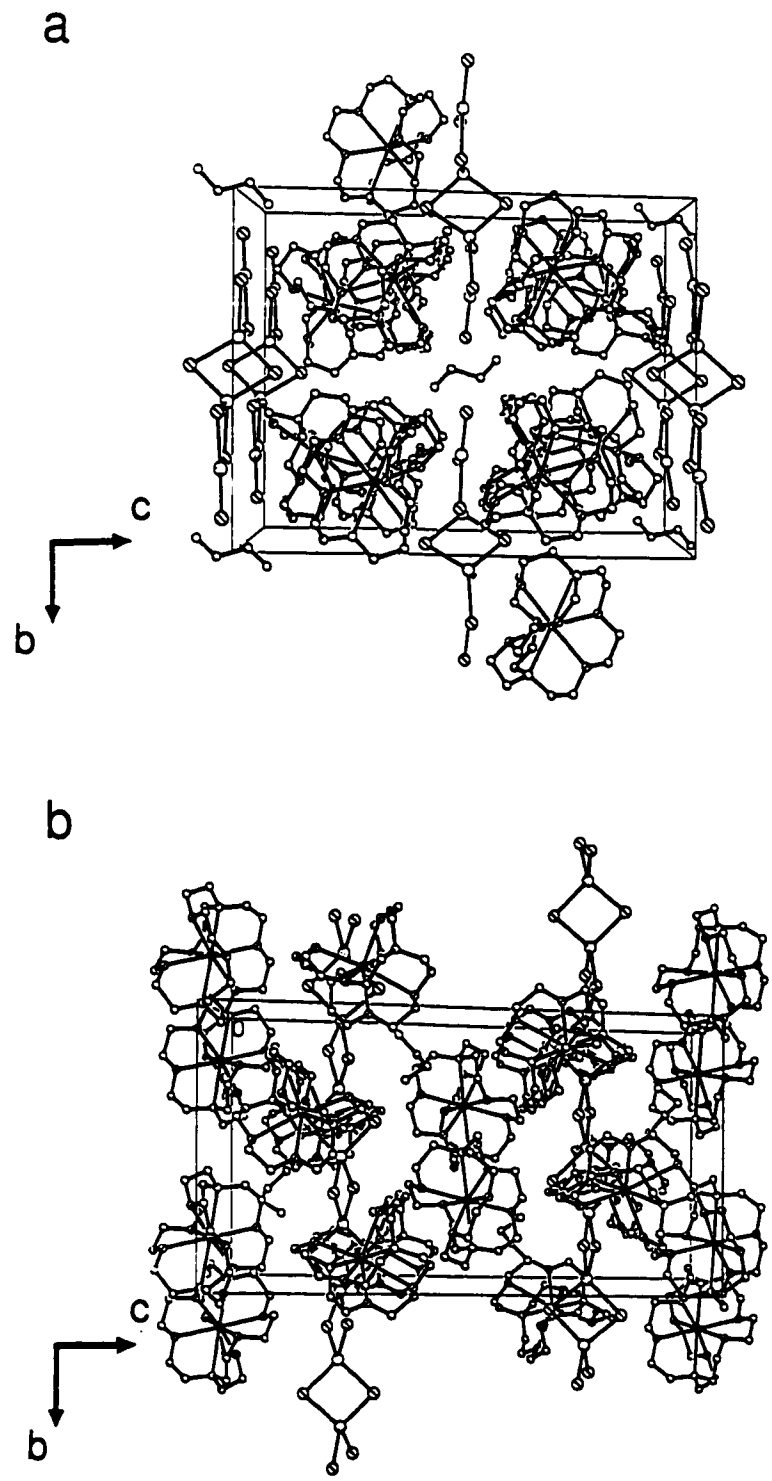

Figure 7.2. Unit cells of (a) commensurate (2,2,2-crypt-Na^+)$_4Tl_4Se_8^{4-}$·0.5en and (b) non-commensurate (2,2,2-crypt-Na^+)$_x$(18-crown-6-Na^+)$_y$[$TlSe_{4/2}^-$]$_\infty^1$·zTHF.

distances in $Tl_4Se_8^{4-}$ and in the previously-reported Tl/Se anion structures (*vide supra*). The average Se–Tl–Se [109.6(38)°] bond angle in the present anion structure is also similar to those in $Tl_4Se_8^{4-}$ and in the previously reported Tl/Se anion structures, whereas the Tl–Se–Tl bond angle [85.1(12)°] is similar only to those in $Tl_4Se_8^{4-}$ and in $Tl_5Se_5^{3-}$ (*vide supra*).

Structural Characterization by NMR Spectroscopy.

The $TlSe_3^{3-}$, $Tl_2Se_x^{n-}$, $Tl_3Se_y^{m-}$, and $Tl_3Se_z^{p-}$ anions were characterized in solution by direct observation of the spin-½ nuclides ^{203}Tl, ^{205}Tl, and ^{77}Se at their natural abundance levels.[74] The nuclearities of the thallium atoms in the polyanions were confirmed by the multiplet patterns arising from $J(^{205}Tl–^{203}Tl)$ couplings and, in the case of the $Tl_3Se_z^{p-}$ anion, by spectral simulation and is discussed below. No evidence was found for the $Tl_2Se_2^{2-}$, $Tl_4Se_5^{4-}$, and $Tl_4Se_x^{n-}$ anions which were detected by variable-temperature NMR spectroscopy in the en and liquid NH_3 extracts of the alloy KTlSe.[33,56,166] Interestingly, the $Tl_3Se_y^{m-}$ was also characterized by solution NMR spectroscopy in the KTlSe alloy extracts.[33] The chemical shifts and spin–spin coupling constants for the $TlSe_3^{3-}$, $Tl_2Se_x^{n-}$, $Tl_3Se_y^{m-}$, and $Tl_3Se_z^{p-}$ anions are listed in Table 7.4.

The 0 °C ^{203}Tl, ^{205}Tl, and ^{77}Se NMR spectra of the en extract of the alloy NaTlSe containing a molar excess of 2,2,2-crypt with respect to Na^+ consisted of five (Tl) and two (Se) resonances. A broad singlet ($\Delta\nu_{1/2}$ ~ 500 Hz) was observed in the Tl^{III} region of the $^{203,205}Tl$ NMR spectrum (2875 ppm) and was flanked by symmetric doublet satellites arising from $^1J(^{203,205}Tl–^{77}Se) = 7413$ and was assigned to the known trigonal-planar $TlSe_3^{3-}$ anion.[56]

Table 7.4. Chemical Shifts and Spin–Spin Coupling Constants for the $TlSe_3^{3-}$, $Tl_2Se_x^{n-}$, $Tl_3Se_y^{m-}$, and $Tl_3Se_z^{p-}$ anions.

	chemical shift (ppm)		coupling constant, J (Hz)			
anion	$^{203,205}Tl$	^{77}Se	^{205}Tl–^{203}Tl	$^{203,205}Tl$–^{77}Se	solvent	T (°C)
$TlSe_3^{3-}$	2875	127		7413	en	0
	2805	63		7897	NH_3	−70
$Tl_2Se_x^{n-}$	1895	210	455	3220	NH_3	−70
				5912		
				6282		
$Tl_3Se_y^{m-}$	5300 (Tl^{III})		3885[a]		en	0
	1824 (Tl^{I})		1391[b]			
	5276(Tl^{III})		4717[a]		NH_3	−70
	1811(Tl^{I})		921			
$Tl_3Se_z^{p-}$	1855		759			

[a] *Inter*environment coupling. [b] *Intra*environment coupling.

The associated ^{77}Se resonance was observed as a doublet (127 ppm) arising from unresolved $^{1}J(^{77}Se–^{205}Tl)$ and $^{1}J(^{77}Se–^{203}Tl)$ couplings. The remaining singlet in the ^{77}Se NMR spectrum (–432 ppm) was assigned to the known Se^{2-} anion, whereas those in the ^{203}Tl and ^{205}Tl NMR spectra did not correspond to known species. Two of the four new $^{203,205}Tl$ NMR resonances comprised a broad triplet ($\Delta\nu_{½}$ ~ 900 Hz) in the Tl^{I} region (Figure 7.3) and a broad doublet ($\Delta\nu_{½}$ ~ 500 Hz) in the Tl^{III} region (Figue 7.4) and were spin–spin coupled to each other as indicated by the identical magnitudes of the splitting in both NMR spectra, i.e., $J(^{205}Tl–^{203,205}Tl)$ = 3885 Hz. The multiplicity patterns are consistent with a solution species containing three thallium atoms in two chemically different environments: one in a Tl^{I} environment and two in Tl^{III} environments. Each component of the doublet resonance in the Tl^{III} region was also flanked by a pair of symmetric doublet satellites arising from $J(^{205}Tl–^{203}Tl)$ = 1391 Hz. This coupling arises from the magnetic non-equivalence of the ^{205}Tl and ^{203}Tl nuclides in the same chemical environment and was confirmed by recording the ^{203}Tl NMR spectrum in which the ^{205}Tl satellites are more intense than the central peak owing to the greater natural abundance of ^{205}Tl (70.5%) when compared to that of ^{203}Tl (29.5%).[74] Accordingly, the larger spin–spin coupling is assigned to *inter*environmental coupling arising from chemical and/or magnetic non-equivalence , whereas the smaller coupling is attributed to *intra*environmental coupling arising only from magnetic non-equivalence. Since no selenium satellites were observed, the selenium nuclearity cannot be inferred. The solution species can only be assigned the general formulation $Tl_3Se_y^{m-}$. The remaining two $^{203,205}Tl$ NMR resonances (Figures 7.3 and 7.4) remain unassigned.

Figure 7.3. The ^{205}Tl NMR spectrum (115.444 MHz, 0 °C) of the Tl^{I} environment of the $Tl_3Se_y^{m-}$ anion obtained by extraction of the alloy NaTlSe in en and in the presence of a stoichiometric excess of 2,2,2-crypt with respect to Na^+. The symbol (?) denotes an unassigned resonance.

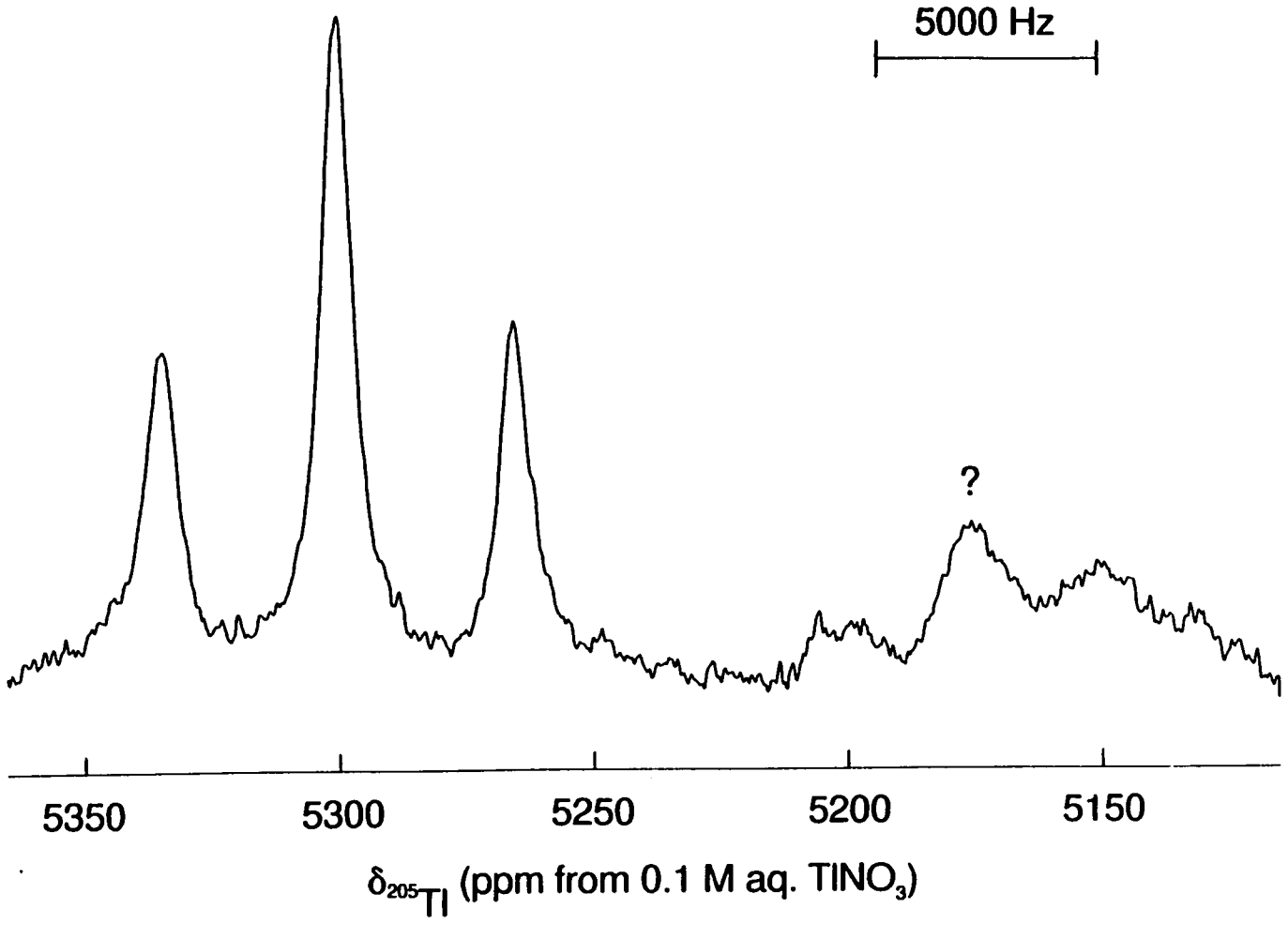
5000 Hz
?
5350
5300
5250
5200
5150
δ_{205}Tl (ppm from 0.1 M aq. $TlNO_3$)

Figure 7.4. (a) The ^{205}Tl NMR spectrum (115.444 MHz, 0 °C) and (b) the ^{203}Tl NMR spectrum (114.319 MHz, 0 °C) of the Tl^{III} environment of the $Tl_3Se_y^{m-}$ anion obtained by extraction of the alloy NaTlSe in en and in the presence of a stoichiometric excess of 2,2,2-crypt with respect to Na^+. Peaks labelled (†) and (‡) denote ^{203}Tl and ^{205}Tl satellites, respectively, and (?) denotes an unassigned resonance.

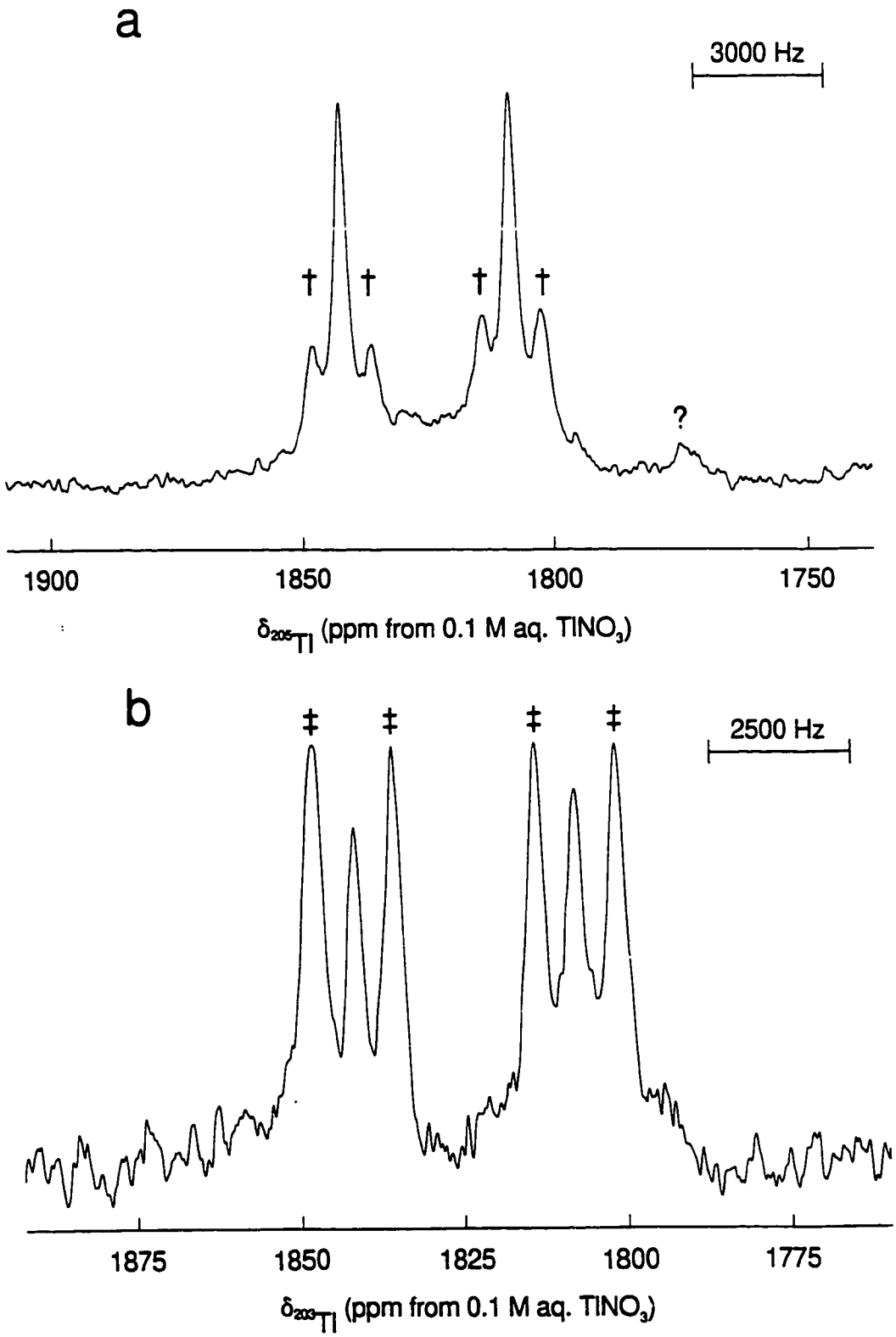
a
3000 Hz
†
†
†
†
?
1900
1850
1800
1750
δ_{205}Tl (ppm from 0.1 M aq. $TlNO_3$)
b
‡
‡
‡
‡
2500 Hz
1875
1850
1825
1800
1775
δ_{203}Tl (ppm from 0.1 M aq. $TlNO_3$)

The ^{203}Tl and ^{205}Tl NMR spectra of a solution obtained by extraction of the alloy NaTlSe in en/THF (1:1 v/v) containing a molar excess of 2,2,2-crypt with respect to Na^+ were recorded at –15 °C. The resonances corresponding to the $TlSe_3^{3-}$ and $Tl_3Se_y^{m-}$ anions were observed but had decreased in intensity, and the doublet resonance of the $Tl_3Se_y^{m-}$ anion was overlapping with an intense, broad ($\Delta\nu_{1/2}$ ~1500 Hz) signal (1872 ppm; Figure 7.5) which now corresponded to the major species in solution. Owing to the broad nature of the new resonance, no spin–spin couplings could be resolved. An attempt was also made to record the ^{77}Se NMR spectrum at –15 °C but resulted in probe ringing and precluded the observation of signals. The appearance of an additional intense resonance at –15 °C and the corresponding decrease in the intensity of the signals associated with the $TlSe_3^{3-}$ and $Tl_3Se_y^{m-}$ anions suggest a temperature-dependent condensation equilibrium involving the $TlSe_3^{3-}$, $Tl_3Se_y^{m-}$, and the new polyanions (see ***Condensation Equilibria***).

The line broadening observed in the ^{203}Tl and ^{205}Tl NMR spectra may be attributed to (a) relaxation due to chemical shielding anisotropy (CSA)[121] and/or (b) chemical exchange.[71] Line broadening arising from CSA has been reported for the ^{205}Tl NMR spectrum of $(CH_3)_2TlNO_3$ in D_2O solvent[211] and has also been observed in the ^{205}Tl NMR spectrum of the reference standard aqueous $TlNO_3$ and may contribute to some of the observed line broadening. Evidence for the second mechanism was obtained from the ^{205}Tl NMR spectrum of $Tl_2Se_2^{2-}$, which consisted of a broad signal at –20 °C but sharpened upon cooling to –70 °C, allowing the observation of the associated $^1J(^{203,205}Tl–^{77}Se)$ coupling[33,166] and is most likely the dominant line-broadening mechanism, particularly in solutions containing mixtures

Figure 7.5. (a) The ^{205}Tl NMR spectrum (115.444 MHz, –15 °C) and (b) the ^{203}Tl NMR spectrum (114.319 MHz, –15 °C) of the Tl^{III} environment of the $Tl_3Se_y^{m-}$ anion obtained by extraction of the alloy NaTlSe in en and in the presence of a stoichiometric excess of 2,2,2-crypt with respect to Na^+. Peaks labelled (†) and (‡) denote ^{203}Tl and ^{205}Tl satellites, respectively, and (*) corresponds to the $Tl_2Se_x^{n-}$ anion.

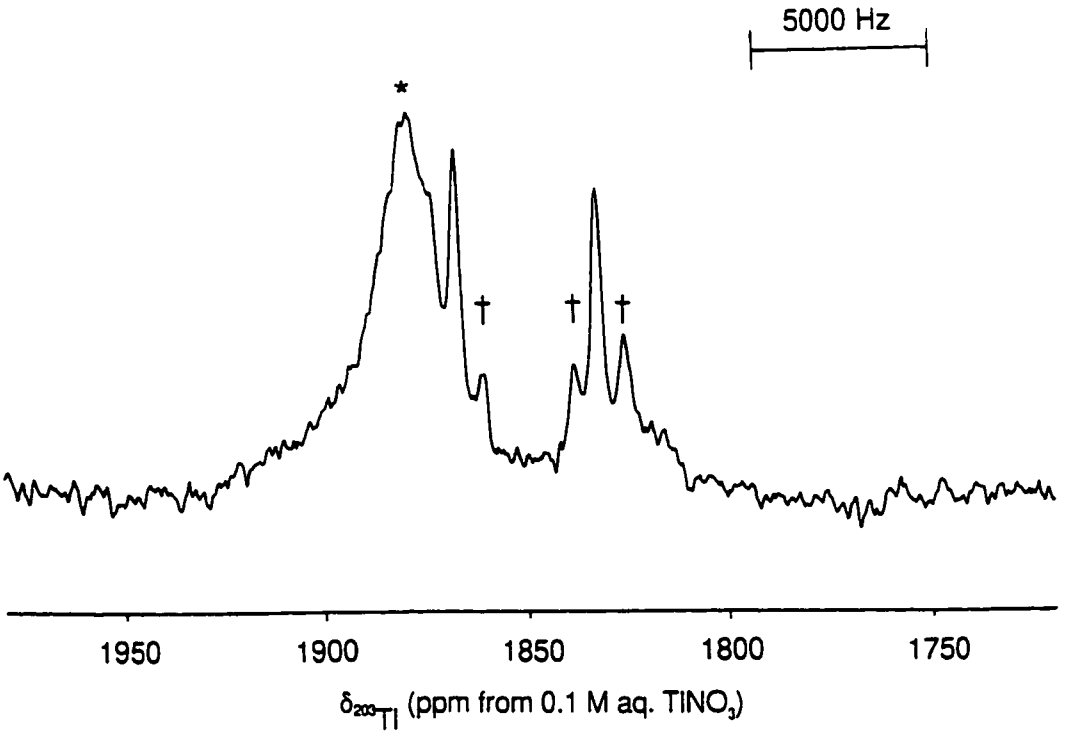
5000 Hz
*
†
†
†
1950
1900
1850
1800
1750
$\delta_{^{203}Tl}$ (ppm from 0.1 M aq. $TlNO_3$)

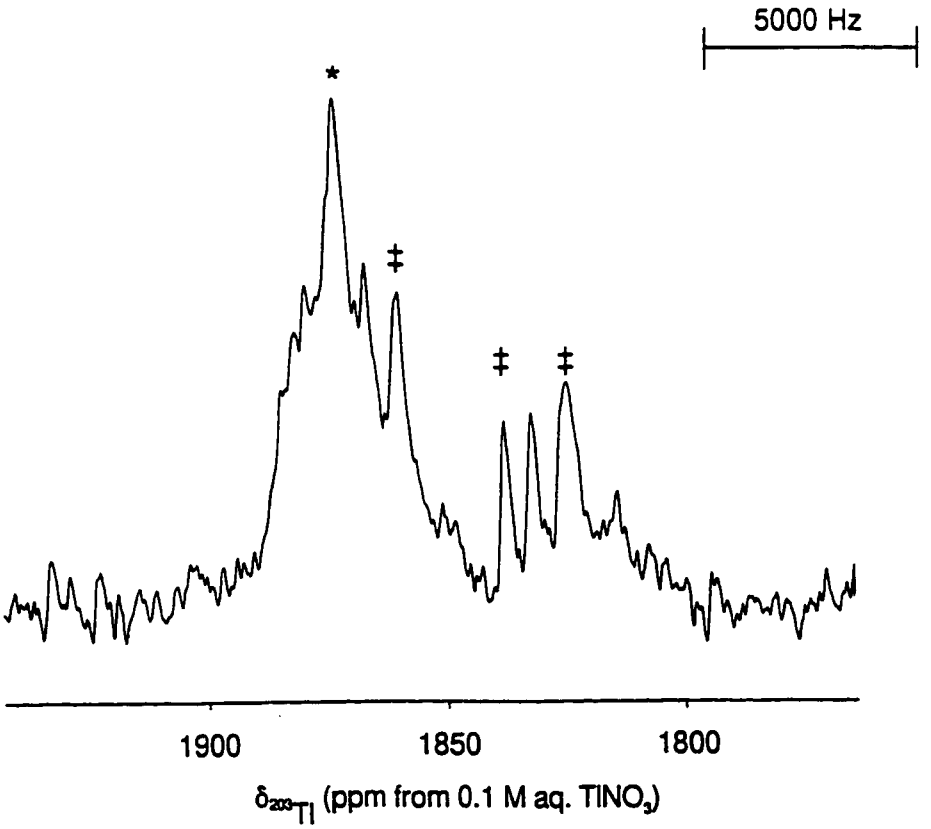
5000 Hz
*
‡
‡
‡
1900
1850
1800
$\delta_{^{203}Tl}$ (ppm from 0.1 M aq. $TlNO_3$)

of polyanions. It was therefore of interest to record the ^{203}Tl, ^{205}Tl, and ^{77}Se NMR spectra at lower temperatures.

A first attempt at recording the ^{205}Tl NMR spectrum of a liquid NH_3 extract of the alloy $NaTl_{0.5}Se$ containing a molar excess of 2,2,2-crypt failed, as the sample gave rise to large amounts of crystalline material at temperatures below –20 °C. Crystallization also occurred below –20 °C even when 2,2,2-crypt was used in a 90 mole% deficit with respect to Na^+. As noted in Chapter 1, the use of 2,2,2-crypt prevents strong ion-pair formation in solution which may give rise to additional line broadening by means of chemical exchange and has been reported for the ^{125}Te NMR spectrum of Te_3^{2-}.[71] Interestingly, Wilson and coworkers have reported the multi-NMR spectroscopic characterization of a variety of cluster anions of the main-group elements, including thallium, which were obtained upon extraction of binary alloys in en, but in the absence of 2,2,2-crypt.[122] Consequently, subsequent liquid NH_3 alloy extracts were prepared in the absence of 2,2,2-crypt.

The ^{203}Tl and ^{205}Tl NMR spectra of an intense orange-red liquid NH_3 extract of the alloy $NaTl_{0.5}Se$ were recorded at –30, –50, –60, and –76 °C. At the former three temperatures, the resonances were exchange-broadened ($\Delta\nu_{1/2}$ ~ 500–1000 Hz) and precluded accurate measurements of spin–spin couplings and I_S/I_C ratios. However, the temperature-dependent condensation equilibrium was confirmed by an increase in the intensity of the resonance of the new polyanion with decreasing temperature and by the decrease in the intensity of the signals associated with $TlSe_3^{3-}$ and $Tl_3Se_y^{m-}$. At –76 °C, the ^{203}Tl and ^{205}Tl NMR spectra were considerably sharper ($\Delta\nu_{1/2}$ ~ 100–250 Hz), allowing the determination

of some NMR parameters and is discussed below. The ^{77}Se NMR spectrum was also recorded at –76 °C and is described below.

Analysis of Spin–Spin Coupling Patterns at –76 °C. In addition to the weak resonances associated with the $TlSe_3^{3-}$ and $Tl_3Se_y^{m-}$ anions, the ^{203}Tl and ^{205}Tl NMR spectra (Figures 7.6–7.8) consisted of several signals which did not correspond to known species. The resonances in the $^{203,205}Tl$ NMR spectra at 1895 and 1855 ppm were assigned to the $Tl_2Se_x^{n-}$ and $Tl_3Se_z^{p-}$ anions, where that corresponding to the $Tl_2Se_x^{n-}$ anion is most likely the resonance detected at –15 °C, and are discussed in detail under subsequent sections. The remaining strong $^{203,205}Tl$ NMR resonances were observed at 5276 and 1811 ppm in the Tl^{I} and Tl^{III} regions, respectively, and overlapped with the resonances of the $Tl_3Se_y^{m-}$ anion (5275 and 1812 ppm) and could not be assigned as their counterparts in the Tl^{III} and Tl^{I} regions, respectively, were not observed, precluding a determination of the nuclearity of the thallium atoms in the polyanion. Interestingly, both the Tl^{I} resonance of $Tl_3Se_y^{m-}$ and the resonance overlapping with it were flanked by ^{77}Se satellites arising from $^{1}J(^{203,205}Tl–^{77}Se)$ = 597 and 451 Hz (Figure 7.8). However, peak overlap precluded I_S/I_C determinations and prevented the assignment of the ^{77}Se satellites to the appropriate Tl^{I} resonance. The remaining weak peaks in the ^{205}Tl NMR spectrum could not be assigned, and no additional structural information could be obtained for the $Tl_3Se_y^{m-}$anion.

The ^{77}Se NMR spectrum consisted of two strong features, a triplet and a doublet, and several weak signals (Figure 7.9). The triplet at 210 ppm ($^{1}J(^{77}Se–^{203,205}Tl)$ = 3248 Hz) was assigned to the $Tl_2Se_x^{n-}$ anion. The doublet at –104 ppm also arises from $^{1}J(^{77}Se–^{203,205}Tl)$ =

Figure 7.6. The ^{205}Tl NMR spectrum (115.444 MHz, –76 °C) of the solution obtained by extraction of the alloy $NaTl_{0.5}Se$ in liquid NH_3 in the absence of 2,2,2-crypt. (A) denotes the $Tl_2Se_x^{n-}$ anion and (a) and (a′) denote the associated ^{203}Tl and ^{77}Se satellites, respectively. (B) denotes the Tl^{III} environment of the $Tl_3Se_y^{m-}$ anion and (†) denotes the associated ^{203}Tl satellites. The symbol (‡) denotes the unassigned resonances overlapping with $Tl_3Se_y^{m-}$, and (*) denotes the five-line multiplet associated with the $Tl_3Se_z^{p-}$ anion. The remaining peaks are unassigned.

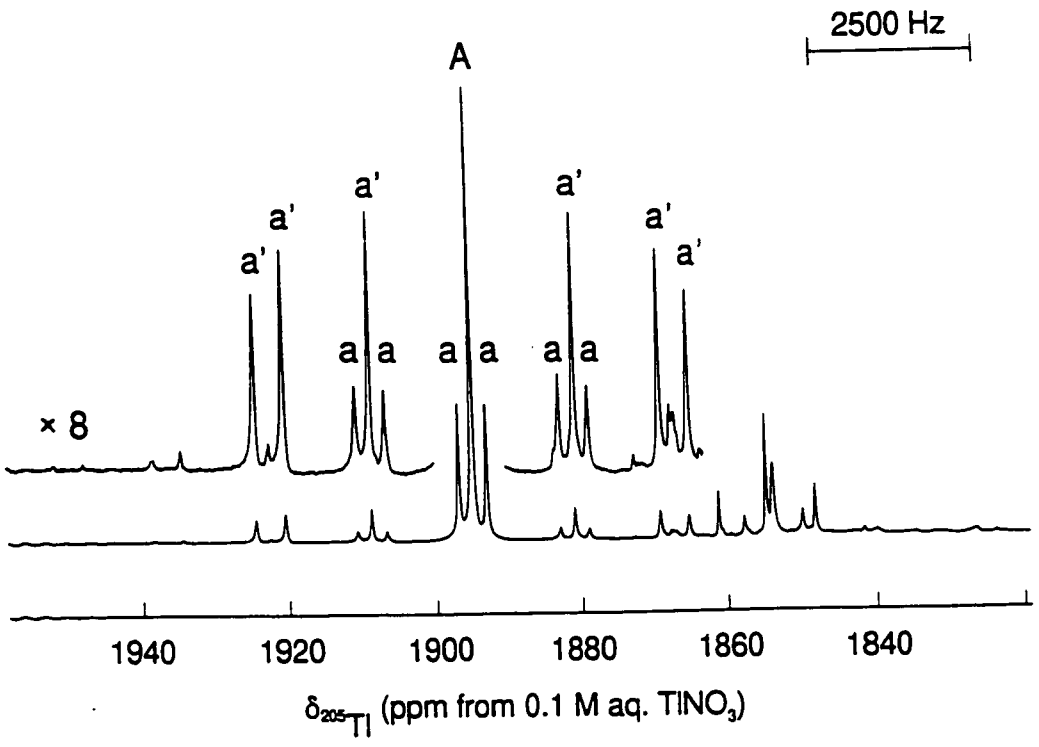
2500 Hz
A
a'
a
× 8
1940
1920
1900
1880
1860
1840
δ205Tl (ppm from 0.1 M aq. TlNO3)

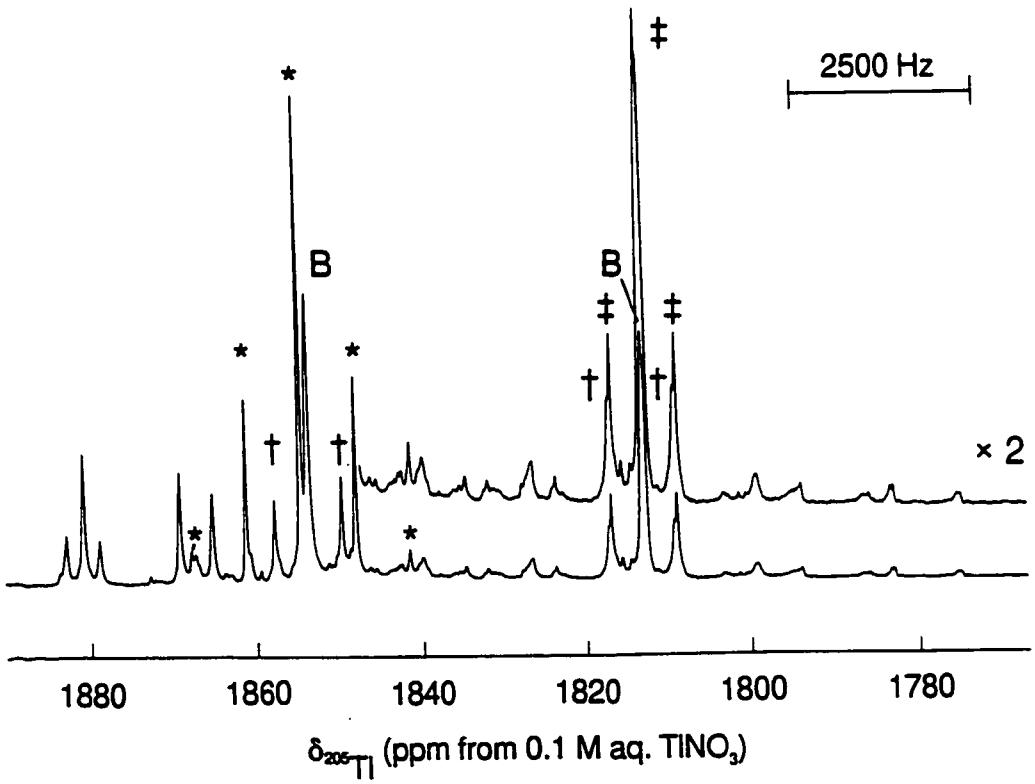
2500 Hz
B
*
†
‡
× 2
1880
1860
1840
1820
1800
1780
δ205Tl (ppm from 0.1 M aq. TlNO3)

Figure 7.7. The ^{203}Tl NMR spectrum (114.319 MHz, –76 °C) of the solution obtained by extraction of the alloy $NaTl_{0.5}Se$ in liquid NH_3 in the absence of 2,2,2-crypt. (A) denotes the $Tl_2Se_x^{n-}$ anion and (a) and (a′) denote the associated ^{205}Tl and ^{77}Se satellites, respectively. (B) denotes the Tl^{III} environment of the $Tl_3Se_y^{m-}$ anion and (†) denotes the associated ^{205}Tl satellites. The symbol (*) denotes the five-line multiplet associated with the $Tl_3Se_z^{p-}$ anion. The remaining peaks are unassigned.

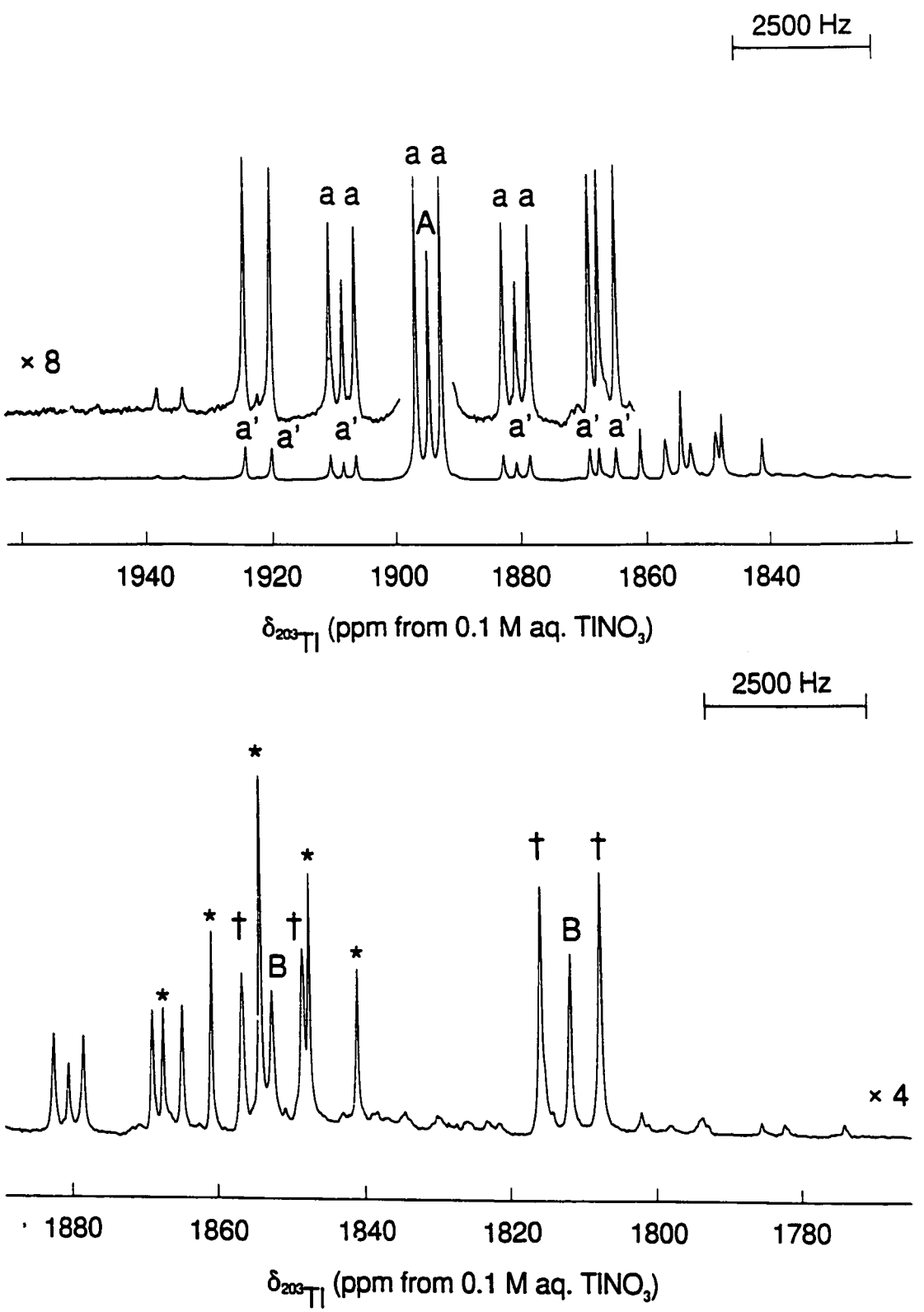
2500 Hz
a a
a a
A
a a
× 8
a'
a'
a'
a'
a'
a'
1940
1920
1900
1880
1860
1840
δ203Tl (ppm from 0.1 M aq. TlNO3)
2500 Hz
*
*
*
†
†
B
*
†
†
B
× 4
1880
1860
1840
1820
1800
1780
δ203Tl (ppm from 0.1 M aq. TlNO3)

Figure 7.8. The ^{205}Tl NMR spectrum (115.444 MHz, –76 °C) of the Tl^{I} environment of the $Tl_3Se_y^{m-}$ anion obtained by extraction of the alloy $NaTl_{0.5}Se$ in NH_3 in the absence of 2,2,2-crypt. Peaks labeled with (*) denote ^{77}Se satellites. The resolution-enhanced spectrum is shown in the lower trace and clearly indicates overlap of additional unassigned resonances denoted by (?).

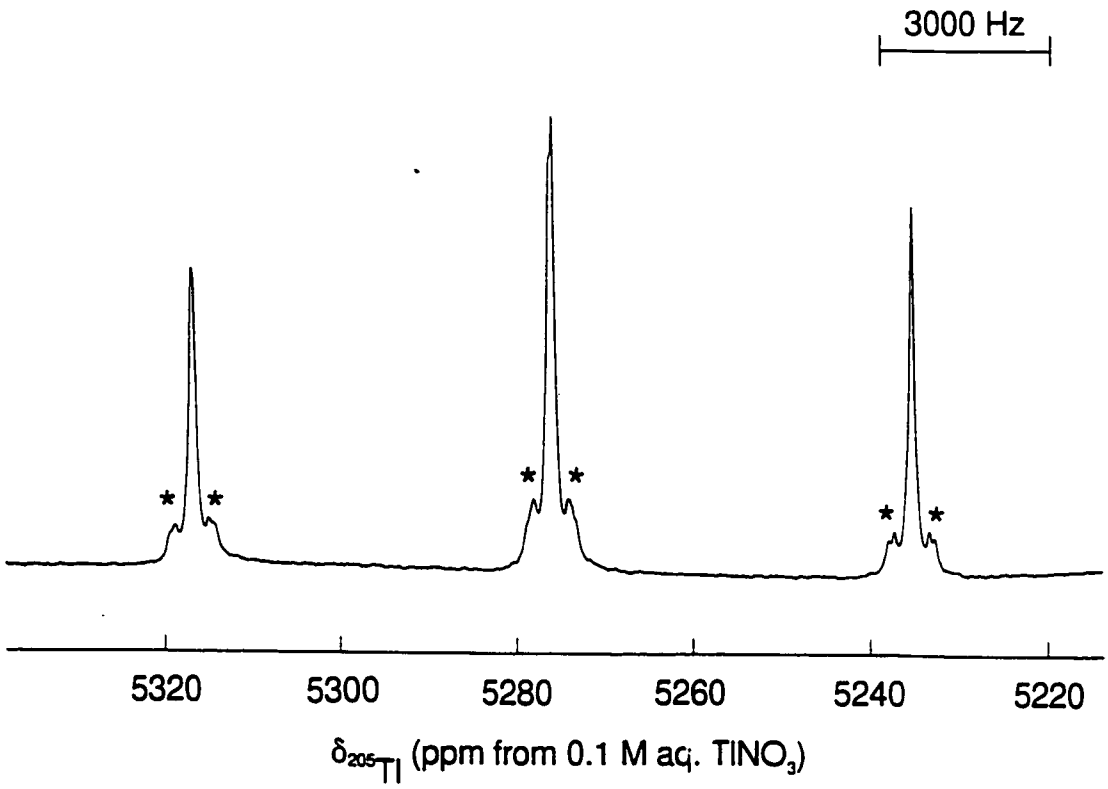
3000 Hz
*
*
*
*
*
*
5320
5300
5280
5260
5240
5220
δ_{205Tl} (ppm from 0.1 M aq. $TlNO_3$)

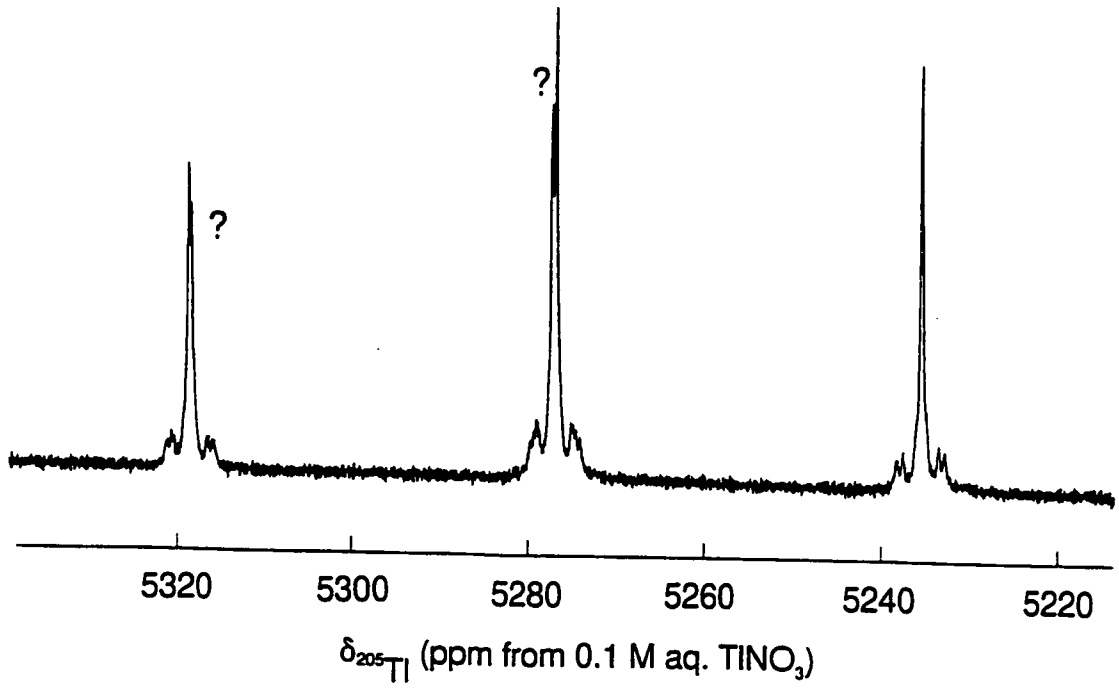
?
?
5320
5300
5280
5260
5240
5220
δ_{205Tl} (ppm from 0.1 M aq. $TlNO_3$)

Figure 7.9. The ^{77}Se NMR spectrum (95.383 MHz, –76 °C) of the solution obtained by extraction of the alloy $NaTl_{0.5}Se$ in liquid NH_3 in the absence of 2,2,2-crypt. (A) denotes the triplet associated with the $Tl_2Se_x^{n-}$ anion; (†) denotes the doublet resonance associated with $TlSe_3^{3-}$; and (‡) in the resolution-enhanced spectrum of the doublet resonance (shown in window) denotes ^{77}Se satellites. The remaining peaks are unassigned.

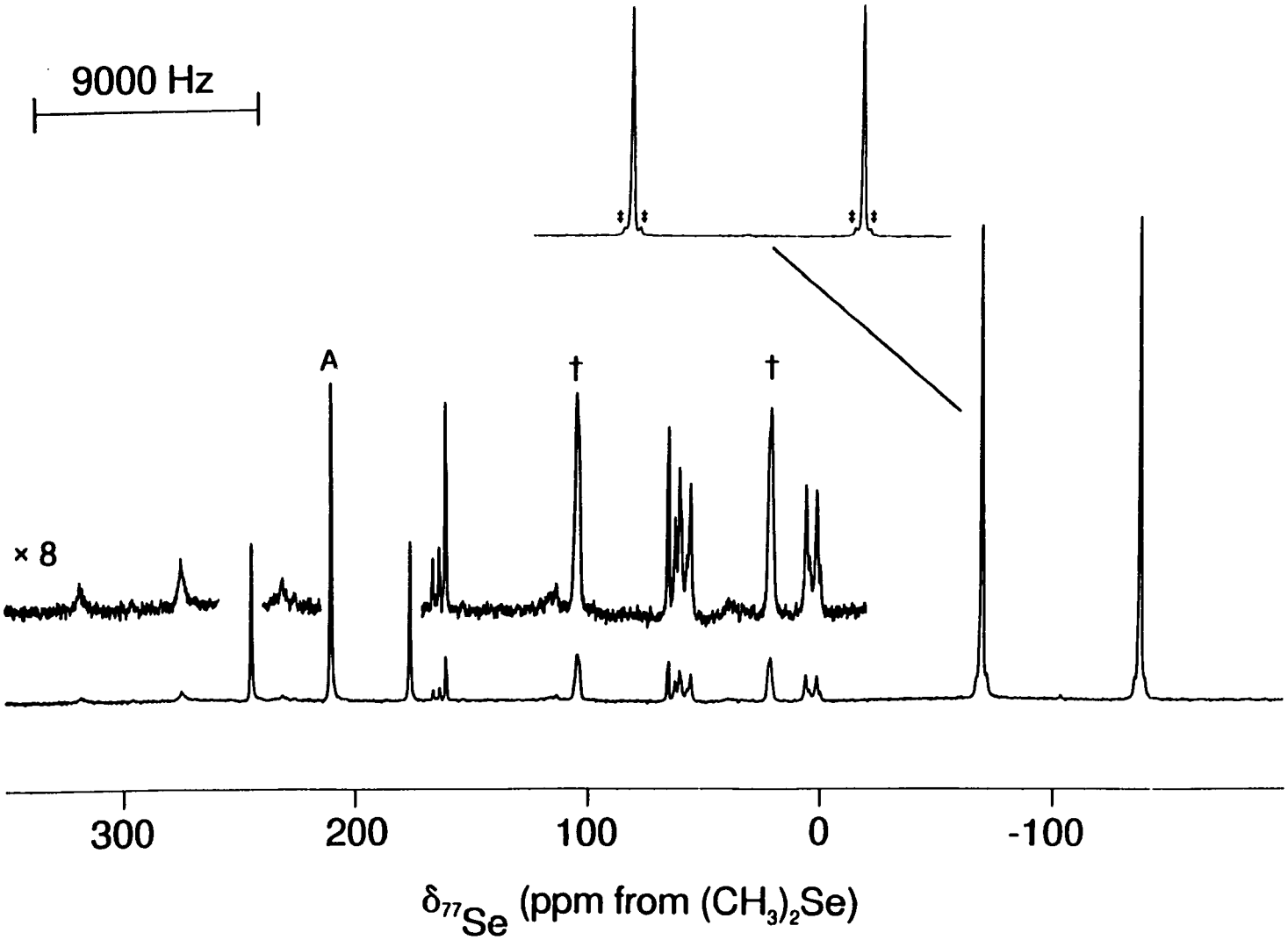
9000 Hz
A
†
†
× 8
300
200
100
0
-100
δ77Se (ppm from (CH3)2Se)

6419 Hz, but the coupling did not correspond to any determined from the ^{203,205}Tl NMR spectra. Interestingly, each component of the doublet was symmetrically flanked by a satellite doublet attributed to $^{1}J(^{77}Se–^{77}Se)$ and probably arises when one Se atom is spin-coupled to a ^{205}Tl nuclide and the other Se atom is spin-coupled to ^{203}Tl, rendering the two ^{77}Se nuclides magnetically non-equivalent, i.e., $^{205}Tl–^{77}Se–^{77}Se–^{203}Tl$. This suggests that the polyanion of interest contains a Tl–Se–Se–Tl bridge similar to the Sn–Ch–Ch–Sn bridge in the $Sn_2Ch_7^{4-}$ (Ch = Se, Te). A complete characterization of this anion is at present not possible. The weak doublet in the ^{77}Se NMR spectrum at 63 ppm was assigned to $TlSe_3^{3-}$; $^{1}J(^{77}Se–^{203,205}Tl)$ = 7897 Hz. The remaining resonances in the ^{77}Se NMR spectrum remain uncharacterized. It is important to note that the peak corresponding to Se^{2-} was not observed in the ^{77}Se NMR spectrum at –76 °C.

$Tl_2Se_x^{n-}$. The most intense signal in the ^{205}Tl NMR spectrum is a singlet in the Tl^{III} region (Figure 7.6) flanked by four sets of doublet satellites. The first doublet satellite arises from $J(^{205}Tl–^{203}Tl)$ = 455 Hz and was confirmed by recording the ^{203}Tl NMR spectrum (Figure 7.7) in which the ^{205}Tl satellites are more intense than the central peak owing to the greater natural abundance of ^{205}Tl (70.5%) when compared to that of ^{203}Tl (29.5%). The remaining satellites arise from $^{1}J(^{203,205}Tl–^{77}Se)$ = 3220, 5912, 6828 Hz as their relative intensities did not increase in the ^{203}Tl NMR spectrum; the corresponding I_S/I_C ratios are 2.0 : 1.3 : 1.0. Only the triplet resonance in the ^{77}Se NMR spectrum (Figure 7.9) could be assigned to the $Tl_2Se_x^{n-}$ anion based on $^{1}J(^{77}Se–^{203,205}Tl)$ = 3248 Hz. The $^{1}J(^{77}Se–^{203,205}Tl)$ = 6419 observed for the doublet resonance in the ^{77}Se NMR spectrum is at significant variance

with the values determined from the ^{205}Tl NMR spectrum and therefore cannot be associated with the $Tl_2Se_x^{n-}$ anion. The observed NMR multiplicity patterns and I_S/I_C ratios are consistent with a polyanion having the empirical formula $Tl_2Se_4^{2-}$ and containing two Tl^{III} atoms in one chemical environment and three distinct Se environments with 2, 1, and 1 atoms, respectively. One of the Se environments must be bridging two thallium atoms to account for the triplet pattern observed in the ^{77}Se NMR spectrum. However, no reasonable model can be proposed for the $Tl_2Se_4^{2-}$ which can account for all the observed multiplicity patterns. Interestingly, the empirical formula $Tl_2Se_4^{2-}$ corresponds to a molecular formula of $Tl_4Se_8^{4-}$, which could be the solution species of interest and is supported by the X-ray crystal structure of the $Tl_4Se_8^{4-}$ anion obtained from an analogous en extract of the alloy $NaTl_{0.5}Se$ (*vide supra*). The X-ray crystal structure of $Tl_4Se_8^{4-}$ ($\sim C_{2v}$ point symmetry) consists of three chemically unique Se environments with 4 (Se_{mb}), 2 ($Se_{mb'}$), and 2 (Se_t) atoms, respectively (see **X-ray Crystal Structures**), but two chemically different Tl^{III} atoms, Tl_P and Tl_T (Figure 7.1a). Consequently, the ^{205}Tl NMR spectrum of $Tl_4Se_8^{4-}$ should consist of two ^{205}Tl signals in a 1 : 1 ratio corresponding to the Tl_P and Tl_T environments of the anion, and each signal should be flanked by two sets of symmetric doublet satellites arising from $^1J(^{205}Tl_P-^{77}Se_t)$, $^1J(^{205}Tl_P-^{77}Se_{mb})$ and $^1J(^{205}Tl_T-^{77}Se_{mb})$, $^1J(^{205}Tl_T-^{77}Se_{mb'})$, respectively. The magnitudes of the couplings should increase in the order $^1J(^{205}Tl_P-^{77}Se_t) > {}^1J(^{205}Tl_P-^{77}Se_{mb}) > {}^1J(^{205}Tl_T-^{77}Se_{mb'}) > {}^1J(^{205}Tl_T-^{77}Se_{mb})$ on the basis of the sp^2-and the sp^3-hybridization of the Tl_P and Tl_T atoms, respectively, and on the basis of the relative magnitudes of the Tl–Se distances observed in the X-ray crystal structure of $Tl_4Se_8^{4-}$. The ^{77}Se NMR spectrum of $Tl_4Se_8^{4-}$ should consist of

a doublet and two triplets in a 2 : 4 : 2 ratio corresponding to the Se_t, Se_{mb}, $Se_{mb'}$ environments of the anion, respectively. As such patterns were not observed in the ^{205}Tl and ^{77}Se NMR spectrum, the solution species cannot be the $Tl_4Se_8^{4-}$ anion structure having a C_{2v} point symmetry.

An alternate geometry can be proposed for $Tl_4Se_8^{4-}$ (Structure IV) and contains one

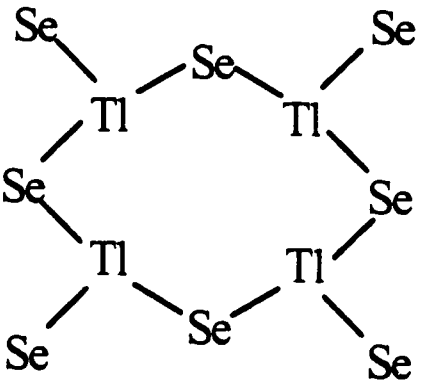

IV

Tl^{III} environment and two Se environments, Se_t and Se_{mb}. Accordingly, the ^{77}Se NMR spectrum should consist of a doublet arising from $^1J(^{77}Se_t-^{203,205}Tl)$ and a triplet arising from $^1J(^{77}Se_{mb}-^{203,205}Tl)$. However, a seven-line multiplet will be observed in the ^{203}Tl and ^{205}Tl NMR spectrum arising from the various natural abundance ^{203}Tl and ^{205}Tl isotopic distributions of the Tl_4 unit of the anion and will be identical to the multiplet pattern observed in the ^{205}Tl NMR spectrum of $(TlOC_2H_5)_4$.[212] For the time being, therefore, the solution species can only be assigned to the general formulation $Tl_2Se_x^{n-}$.

$Tl_2Se_x^{n-}$. An equally-spaced five-line multiplet was observed in the Tl^{III} region of the

^{205}Tl NMR spectrum (Figure 7.6) and arises from J(^{205}Tl–^{203}Tl) = 759 Hz. The multiplicity pattern was confirmed by recording the ^{203}Tl NMR spectrum (Figure 7.7) in which the intensities of the outer lines of the 5-line multiplet increase relative to the central peak and is consistent with the greater natural abundance of ^{205}Tl (70.5%) when compared to that of ^{203}Tl (29.5%). The nuclearity of the thallium atoms in the anion was confirmed by simulation of a Tl_3-unit containing chemically-equivalent Tl^{III} atoms at the natural abundance levels and by using the value of the observed Tl–Tl coupling constant and reproduced the observed multiplet pattern (Figure 7.10). The $Tl_3Se_z^{p-}$ anion therefore contains three chemically-equivalent Tl^{III} atoms and contrasts with the structure of the $Tl_3Se_y^{m-}$ anion which contains one Tl^{I} and two Tl^{III} atoms.

Condensation Equilibria. The systematic increase in the intensities of the ^{203,205}Tl NMR resonances of $Tl_2Se_x^{n-}$ and $Tl_3Se_z^{p-}$ with decreasing temperature, the decrease in the intensity of the resonances associated with the $TlSe_3^{3-}$ and $Tl_3Se_y^{m-}$ anions with decreasing temperature, and the disappearance of the signal corresponding to Se^{2-} in the ^{77}Se NMR spectrum at low temperatures suggest a complex temperature-dependent condensation equilibrium among the polyanions and is expressed by eq. (7.1) which is necessarily

$$TlSe_3^{3-} + Tl_3Se_y^{m-} + Se^{2-} \rightleftharpoons Tl_2Se_x^{n-} + Tl_3Se_z^{p-} \qquad (7.1)$$

unbalanced. This condensation equilibrium is similar to that observed among the $SnCh_3^{2-}$, $Sn_2Ch_6^{4-}$, $Sn_2Ch_7^{4-}$, and $Sn_4Ch_{10}^{4-}$ anions in basic media (Chapters 3 and 4). However, the condensation equilibrium among the tin anions was shown to be strongly influenced by the

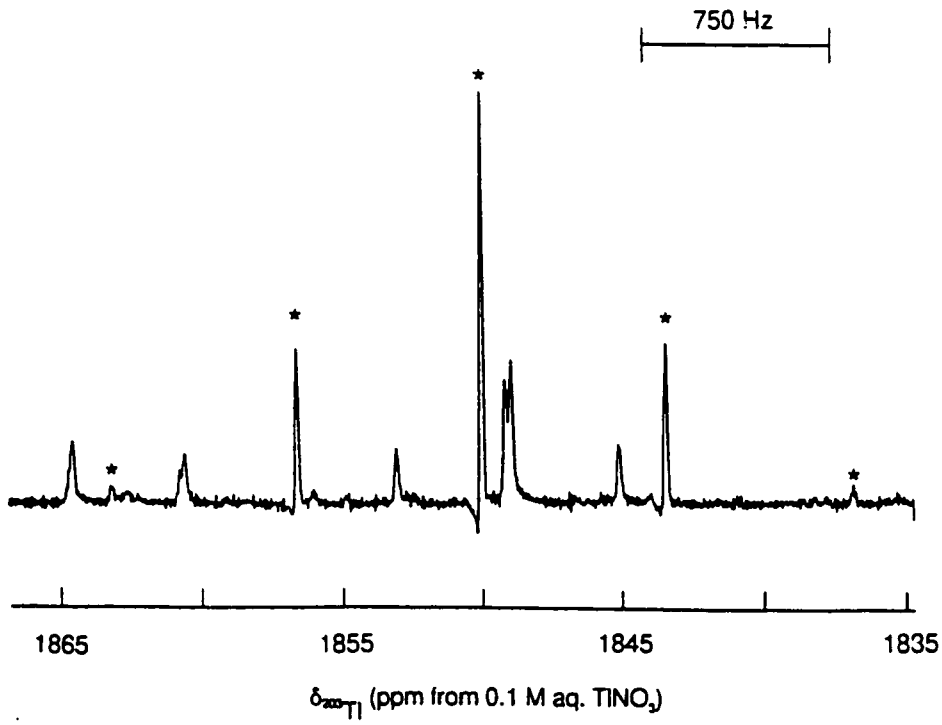

Figure 7.10. The resolution-enhanced ^{205}Tl NMR spectrum (115.444 MHz, –76 °C) of the $Tl_3Se_2^{P-}$ anion (upper trace; appropriate peaks are denoted with (*)) and the simulated spectrum (lower trace).

amount of 2,2,2-crypt, whereas the condensation mechanism among the thallium polyanions is temperature dependent and is speculated to be little influenced by the amount of 2,2,2-crypt. This is supported by the observation of resonances corresponding to the higher nuclearity anions at 0 and at −15 °C by ^{203,205}Tl NMR spectroscopy in solutions containing 2,2,2-crypt, with the intensities of the polynuclear anions generally increasing with a decrease in temperature. In the tin systems, the higher nuclearity anions were only observed at low temperatures by NMR spectroscopy when 2,2,2-crypt was used in deficit amounts with respect to the concentration of the alkali-metal cations present in solution.

Conclusion

The novel $Tl_4Se_8^{4-}$ anion has been isolated in the solid state as its 2,2,2-crypt-Na^+ salt and characterized by X-ray crystallography. Although the disorder in, and the non-commensurate nature of, the compound (2,2,2-crypt-Na^+)$_x$(18-crown-6-Na^+) $[_y^1[TlSe_{4/2}^-]]_z$·THF has not yet been resolved, the geometry of the $[_\infty^1[TlSe_{4/2}^-]]$ anion in the compound has been accurately determined and consists of an edge-sharing distorted $TlSe_4$-tetrahedra forming an infinite one-dimensional chain. The novel $Tl_2Se_x^{n-}$, $Tl_3Se_y^{m-}$, and $Tl_3Se_z^{p-}$ anions have been partially characterized by variable-temperature ^{203}Tl and ^{205}Tl and ^{77}Se NMR spectroscopy along with the known $TlSe_3^{3-}$ and Se^{2-} anions. The variable-temperature NMR spectroscopic study indicated that the anions are related by means of a temperature-dependent condensation equilibrium which is not dependent on the amount of 2,2,2-crypt in solution.

CHAPTER 8

SUMMARY AND DIRECTIONS FOR FUTURE RESEARCH

Summary

The present work is a significant extension of post-transition element polyanion chemistry and represents the first multi-NMR speciation study of two experimental parameters influencing the condensation processes of simple polychalcogenide anions in non-aqueous solvents. The two parameters are: (1) The deficit use of complexing agents such as 2,2,2-crypt and 18-crown-6 with respect to the amount of alkali-metal cations available in solution, as illustrated in the preparation of the $SnCh_3^{3-}$, $Sn_2Ch_6^{4-}$, $Sn_2Ch_7^{4-}$, and $Sn_4Ch_{10}^{4-}$ (Ch = Se, Te) anions in en and liquid NH_3 solvents. In the absence of complexing agents, the synthesis of oligomeric anions from simple monomers seems to be catalyzed by $A^+\cdots M^{n-}$ ion-pair formation (A = alkali-metal cation; M = monomeric anion). (2) Temperature, as demonstrated by the preparation of the $TlSe_3^{3-}$, $Tl_2Se_x^{n-}$, $Tl_3Se_y^{m-}$, and $Tl_3Se_z^{p-}$ anions in en and liquid NH_3 solvents at –76 °C. The condensation equilibria among the thallium polyselenide anions was noted to be little influenced by the amounts of complexing agents added to the solutions.

Density functional theory calculations at the local and nonlocal levels on the $Tl_2Ch_2^{2-}$ (Ch = Se and/or Te) and $M_2Ch_3^{2-}$ (M = Sn or Pb; Ch = S, Se, or Te) series of anions have indicated pure *p* bonded cages and significant M···M interactions arising from valence ns^2

lone pair-lone pair interactions. For the $Tl_2Ch_2^{2-}$ anions, the relative magnitudes of the calculated M–Ch and M···M bond orders were shown to parallel with the relative magnitudes of the relativistically corrected reduced M–Ch and M···M coupling constants deduced from solution multi-NMR spectroscopy. However, this is not the case for the $M_2Ch_3^{2-}$ anions as demonstrated by the magnitudes of the relativistically corrected Tl–M coupling constants observed for the $TlMTe_3^{3-}$ anions, which are *ca.* 2–5 times larger than the corresponding Tl–Te and M–Te couplings. The large M···M couplings in $M_2Ch_3^{2-}$ appear to arise from multiple coupling pathways and can be also be rationalized in terms of the small M–Ch–M bond angles observed in the X-ray crystal structures of the $M_2Ch_3^{2-}$ and $TlPbTe_3^{3-}$ anions.

The power of multi-NMR spectroscopy for the characterization of mixtures of polyanions in solution has been demonstrated. The X-ray crystal structures of a significant number of polyanions characterized by solution multi-NMR spectroscopy have been obtained. Anions which could not be obtained as their 2,2,2-crypt-A^+ salts (A = Na, K) were crystallized by using 18-crown-6 as the sequestering agent or by employing varying mixtures of 2,2,2-crypt and 18-crown-6. The direct correlation of bond distances with relativistically corrected reduced coupling constants deduced from NMR spectroscopy indicates that anion geometries may be retained in solution. The present work also demonstrates that Raman spectroscopy can be used as a corroborating structural tool. The Raman spectra of well-characterized polyanions such as $Sn_2Ch_6^{4-}$ and $Sn_4Ch_{10}^{4-}$ (Ch = Se, Te) may be used to infer the anion geometries of crystalline materials composed of structurally related (2,2,2-crypt-$A^+)_nM^{n-}$-type salts, particularly when crystals suitable for an X-ray structure determination

cannot be obtained. Density functional theory calculations at the local and nonlocal levels may be used to gain further insight into the bonding in post-transition element polyanions.

Directions for Future Research

Only crystals of the $Sn_2Ch_6^{4-}$ and $Sn_4Ch_{10}^{4-}$ (Ch = Se, Te) anions were obtained from en solutions containing mixtures of the $SnCh_3^{3-}$, $Sn_2Ch_6^{4-}$, $Sn_2Ch_7^{4-}$, and $Sn_4Ch_{10}^{4-}$ anions. An attempt should be made to obtain crystals of the $SnCh_3^{3-}$ and $Sn_2Ch_7^{4-}$ anions from the en solutions by using varying mixtures of 18-crown-6 and 2,2,2-crypt in a manner similar to that used to prepare crystals of the compounds (2,2,2-crypt-Na^+)$_4Tl_4Se_8^{4-}$·0.5en and (2,2,2-crypt-Na^+)$_x$(18-crown-6-Na^+)$_y$[$TlSe_{4/2}^-$]$_\infty^1$·zTHF (Chapter 7). This would be of considerable interest as it could lead to the optimization of the experimental parameters required to selectively crystallize an anion from solutions containing anion mixtures and may be employed to prepare crystals of the $Tl_2Se_x^{n-}$, $Tl_3Se_y^{m-}$, and $Tl_3Se_z^{p-}$ anions from en extracts of the alloys $NaTl_{0.5}Se$ and NaTlSe. The X-ray crystal structures of these anions may be then be used to interpret the ^{203}Tl, ^{205}Tl, and ^{77}Se NMR spectra of the liquid NH_3 and en extracts of the $NaTl_{0.5}Se$ and NaTlSe alloys and hence deduce the solution geometries of the polyanions.

The X-ray structures of the crystallographically uncharacterized $TlCh_3^{3-}$ (Ch = Se, Te) anions, which are known to coexist with $Tl_2Ch_2^{2-}$ in solution (Chapter 5 and refs. (33) and (156)), may also be prepared once the experimental parameters for selective crystallization are optimized.

The calculated structures of the hitherto unknown butterfly-shaped $In_2Ch_2^{2-}$ (Ch = Se, Te) anions are presented in this work. It would therefore be of interest to prepare these anions and to characterized them by X-ray crystallography and Raman spectroscopy. Multi-NMR spectroscopy may not be suitable for the characterization of the butterfly-shaped $In_2Ch_2^{2-}$ since both naturally occurring nuclides of indium, ^{113}In (4.28% natural abundance) and ^{115}In (95.72% natural abundance), are quadrupolar ($I = {}^9/_2$) with large width factors (45×10^{-59} and 55×10^{-59} m^4, respectively).

REFERENCES

1. Joannis, A. C. R. *Hebd. Seances Acad. Sci.* **1891**, *113*, 795.
2. Joannis, A. *Hebd. Seances Acad. Sci.* **1892**, *114*, 587.
3. Franklin, E. C.; Kraus, C. A. *Am. Chem. J.* **1900**, *24*, 83.
4. Kraus, C. A. *J. Am. Chem. Soc.* **1907**, *29*, 1557.
5. Smyth, F. J. *J. Am. Chem. Soc.* **1917**, *39*, 1299.
6. Peck, E. B. *J. Am. Chem. Soc.* **1918**, *40*, 335.
7. Chiu, C. Y.; Kraus, C. A. *J. Am. Chem. Soc.* **1922**, *44*, 1999.
8. Kraus, C. A. *J. Am. Chem. Soc.* **1922**, *44*, 1216.
9. Bergstrom, F. W. *J. Am. Chem. Soc.* **1926**, *48*, 146.
10. Bergstrom, F. W. *J. Phys. Chem.* **1926**, *30*, 12.
11. Zintl, E.; Goubeau, J.; Dullenkopf, W. *Z. Phys. Chem., Abt. A* **1931**, *154*, 1.
12. Zintl, E.; Kaiser, H. *Z. Anorg. Allg. Chem.* **1933**, *211*, 113.
13. Zintl, E.; Harder, A. *Z. Phys. Chem., Abt. A* **1931**, *154*, 47.
14. Zintl, E.; Dullenkopf, W. *Z. Phys. Chem., Abt. B*, **1932**, *16*, 183.
15. Laves, F. *Naturwissenchaften* **1941**, *29*, 240.
16. Kummer, D.; Diehl, L. *Angew. Chem., Int. Ed. Engl.* **1970**, *9*, 895.
17. Corbett, J. D.; Edwards, P. A. *J. Chem. Soc., Chem. Commun.* **1975**, p. 984.
18. Lehn, J. M.; Sauvage, J. P.; Dietrich, B. *J. Am. Chem. Soc.* **1970**, *92*, 2916.

19. Lehn, J. M.; Sauvage, J. P. *J. Chem. Soc., Chem. Commun.* **1971**, p. 440.

20. de Jong, F.; Reinhoudt, R. N. *Adv. Phy. Org. Chem.* **1980**, *17*, 279.

21. Abraham, M. H.; Ling, H. C. *J. Chem. Soc., Faraday Trans. I* **1984**, *80*, 3445.

22. Boss, R. D.; Popov, A. I. *Inorg. Chem.* **1986**, *25*, 1747.

23. Borrmann, H.; Pirani, A. M.; Schrobilgen, G. J. *Acta Crystallogr.* **1997**, *C53*, 1007.

24. Campbell, J.; Schrobilgen, G. J. *Inorg. Chem.* **1997**, *36*, 4078.

25. Edwards, P. A.; Corbett, J. D. *Inorg. Chem.* **1977**, *16*, 903.

26. Corbett, J. D.; Adolphson, D. G.; Merryman, D. J.; Edwards, P. A.; Armatis, F. J. *J. Am. Chem. Soc.* **1975**, *97*, 6267.

27. Corbett, J. D.; Edwards, P. A. *J. Am. Chem. Soc.* **1977**, *99*, 3313.

28. Edwards, P. A.; Corbett, J. D. *Inorg. Chem.* **1977**, *16*, 903.

29. Campbell, J.; Dixon, D. A.; Mercier, H. P. A.; Schrobilgen, G. J. *Inorg. Chem.* **1995**, *34*, 5798.

30. Burns, R. C.; Corbett, J. D. *J. Am. Chem. Soc.* **1982**, *104*, 2804.

31. Belin, C.; Mercier, H. *J. Chem. Soc., Chem. Commun.* **1987**, p. 190.

32. Mercier, H. P.; Angilella, V. E.; Belin, C. H. *New. J. Chem.* **1990**, *14*, 121.

33. Campbell, J. *Ph.D. Dissertation.* McMaster University, Hamilton, Ontario, 1997.

34. v. Schnering, H. G. *Angew. Chem., Int. Ed. Engl.* **1981**, *20*, 33.

35. (a) Corbett, J. D. *Chem. Rev.* **1985**, *85*, 383. (b) Burns, R. C.; Corbett, J. D.; Critchlow, S. C. In *Rings, Cluster, and Polymers of the Main Group Elements*;

Cowley, A. H., Ed.; American Chemical Society: Washington, DC, 1983; ACS Symp. Ser. No. 232, Chapter 6, pp. 95–110.

36. Wade, K. *Chem. Brit.* **1975**, *11*, 177.

37. Wade, K. *Avd. Inorg. Radiochem.* **1976**, *18*, 1.

38. Olah, G. A.; Wade, K.; Williams, R. E. *Electron Deficient Boron and Carbon Clusters*; John Wiley & Sons, Inc.: New York, NY, 1991; Chapter 1, pp. 1–9.

39. Müller, V.; Grebe, C.; Müller, U.; Dehnicke, K. *Z. Anorg. Allg. Chem.* **1993**, *619*, 416.

40. Devereux, L. A.; Schrobilgen, G. J.; Sawyer, J. F. *Acta Crystallogr.* **1985**, *C41*, 1730.

41. Huffmann, J. C.; Haushalter, R. C. *Z. Anorg. Allg. Chem.* **1984**, *518*, 203.

42. Fenske, D.; Baum, G.; Wolkers, H.; Schreiner, B.; Weller, F.; Dehnicke, K. *Z. Anorg. Allg. Chem.* **1993**, *619*, 489.

43. Borrmann, H.; Pirani, A. M.; Schrobilgen, G. J.; Willuhn, M. *Acta Crystallogr.* In preparation.

44. Burns, R. C.; Corbett, J. D. *J. Am. Chem. Soc.* **1981**, *103*, 2627.

45. Belin, C. H. E.; Charbonnel, M. M. *Inorg. Chem.* **1982**, *21*, 2504.

46. Sheldrick, W. S.; Schaaf, B. *Z. Naturforsch.* **1994**, *B49*, 655.

47. Critchlow, S. C.; Corbett, J. D. *Inorg. Chem.* **1984**, *23*, 770.

48. Krebs, B. *Angew. Chem., Int. Ed. Engl.* **1983**, *22*, 113.

49. Krebs, B.; Uhlen, H. *Z. Anorg. Allg. Chem.* **1987**, *459*, 35.

50. Krebs, B.; Hürter, H.-U. *Z. Anorg. Allg. Chem.* **1980**, *462*, 143.

51. Krebs, B.; Pohl, S.; Schiwy, W. *Z. Anorg. Allg. Chem.* **1972**, *393*, 241.

52. Schiwy, W.; Pohl, S.; Krebs, B. *Z. Anorg. Allg. Chem.* **1973**, *402*, 77.

53. Schiwy, W.; Blutau, C.; Gäthje, D.; Krebs, B. *Z. Anorg. Allg. Chem.* **1975**, *412*, 1.

54. Pohl, S. *Ph.D. Dissertation.* Christian-Albrecht Universität, Kiel, Germany, 1974.

55. Chou, J.-H.; Kanatzidis, M. G. *Inorg. Chem.* **1994**, *33*, 1001.

56. Burns, R. C.; Devereux, L. A.; Granger, P.; Schrobilgen, G. J. *Inorg. Chem.* **1985**, *24*, 2615.

57. Burns, R. C.; Corbett, J. D. *Inorg. Chem.* **1981**, *20*, 4433.

58. Krebs, B.; Hürter, H.-U. *Z. Anorg. Allg. Chem.* **1980**, *462*, 143.

59. Eisenmann, B.; Schäfer, H.; Schrod, H. *Z. Naturforsch.* **1983**, *B38*, 921.

60. Campbell, J.; Devereux, L. A.; Gerken, M.; Mercier, H. P. A.; Pirani, A. M.; Schrobilgen, G. J. *Inorg. Chem.* **1996**, *35*, 2945.

61. Krebs, B.; Uhlen, H. *Z. Anorg. Allg. Chem.* **1987**, *549*, 35.

62. Eisenmann, B.; Hansa, J. *Z. Kristallogr.* **1993**, *203*, 299.

63. Sheldrick, W. S.; Schaaf, B. *Z. Anorg. Allg. Chem.* **1994**, *620*, 1041.

64. Sheldrick, W. S.; Braunbeck, H. G. *Z. Naturforsch.* **1989**, *B44*, 851.

65. Sheldrick, W. S.; Braunbeck, H. G. *Z. Anorg. Allg. Chem.* **1993**, *619*, 1300.

66. Huffmann, J. C.; Haushalter, J. P.; Umarji, A. M.; Shenoy, G. K.; Haushalter, R. C. *Inorg. Chem.* **1984**, *23*, 2312.

67. Ansari, M. A.; Bollinger, J. C.; Ibers, J. A. *Inorg. Chem.* **1993**, *32*, 231.

68. Shreeve-Keyer, J. L.; Warren, C. J.; Dhingra, S. S.; Haushalter, R. C. *Polyhedron* **1997**, *16*, 1193.

69. Rudolph, R. W.; Wilson, W. L.; Parker, F.; Taylor, R. C.; Young, D. C. *J. Am. Chem. Soc.* **1978**, *100*, 4629.

70. Pons, B. S.; Santure, D. J.; Taylor, R. C.; Rudolph, R. W. *Electrochimica Acta* **1981**, *26*, 365.

71. Björgvinsson, M.; Schrobilgen, G. J. *Inorg. Chem.* **1991**, *30*, 2540.

72. *NMR and the Periodic Table*; Harris, R. K., Mann, B. E., Eds.; Academic Press: London, England, 1978.

73. Harris, R. K. *Nuclear Magnetic Resonance Spectroscopy: A Physicochemical View*; Longmann Scientific and Technical: Essex, England, 1986; Chapter 5, pp. 131–141.

74. Mason, J. In *Multinuclear NMR*; Mason, J., Ed.; Plennum Press: New York, NY, 1987; Appendix, pp. 626–627.

75. Ramsey, N. F. *Phys. Rev.* **1950**, *78*, 699.

76. Pople, J. A. *Mol. Phys.* **1964**, *7*, 301.

77. Webb, G. A. In *NMR of Newly Accessible Nuclei*; Laszlo, P., Ed.; Academic Press: New York, NY, 1983; Vol. 1, Chapter 4, pp. 79–101.

78. Jameson, C. J.; Mason, J. In *Multinuclear NMR*; Mason, J., Ed.; Plennum Press: New York, NY, 1987; Chapter 3. p. 61.

79. Sanders, J. C. P.; Schrobilgen, G. J. In *Multinuclear Magnetic Resonance in Liquids*

and Solids—Chemical Applications; Granger, P.; Harris, R. K., Eds.; Kluwer Academic Publishers: Dordrecht, 1990; NATO ASI Ser. C., Vol. 322; Chapter XI, pp. 157–186.

80. Pople, J. A.; Santry, D. P. *Mol. Phys.* **1964**, *8*, 1.

81. Pyykkö, P.; Wiesenfeld, L. *Mol. Phys.* **1981**, *43*, 557.

82. Björgvinsson, M.; Mercier, H. P. A.; Mitchell, K. M.; Schrobilgen, G. J.; Strohe, G. *Inorg. Chem.* **1993**, *32*, 6046.

83. Björgvinsson, M. *Ph. D. Dissertation.* McMaster University, Hamilton, Ontario, 1989.

84. Devereux, L. A. *M. Sc. Dissertation.* McMaster University, Hamilton, Ontario, 1985.

85. Czyborra, R. *B. Sc. Dissertation.* McMaster University, Hamilton, Ontario, 1990.

86. Dhingra, S. S.; Haushalter, R. C. *Polyhedron* **1994**, *13*, 2775.

87. Hägele, G.; Höffken, H.-W.; Mistry, F.; Spiske, R.; Weber, U.; Goudetsidis, S. *DSYMPC*, Release 0.940728E; Institut für Anorganische Chemie und Strukturchemie, Heinrich-Heine-Universität: Düsseldorf, Germany, 1994.

88. Sheldrick, G. M. *SHELXTL-Plus*, Release 5.03; Siemens Analytical X-ray Instruments, Inc.: Madison, WI, 1995.

89. The unit cell volume of a structure containing 2,2,2-crypt-K^- can provide a reliable count of the number of cations present in the unit cell and hence the charge on the anion(s) by assuming (a) an empirical volume of *ca.* 650 $Å^3$ for the 2,2,2-crypt-K^+ cation[44] and (b) that the crystal packing is dominated by the 2,2,2-crypt-K^+ cation.

90. Birchall, T.; Burns, R. C.; Devereux, L. A.; Schrobilgen, G. J. *Inorg. Chem.* **1985**, *24*, 890.

91. Krebs, B.; Wallstab, H.-J. *Inorg. Chim. Acta* **1981**, *54*, L123.

92. (a) Andzelm, J.; Wimmer, E.; Salahub, D. R. In *The Challenge of d and f Electrons: Theory and Computation*; Salahub, D. R.; Zerner, M. C., Eds.; ACS Symp. Ser. No. 394; American Chemical Society: Washington, DC, 1989; p. 228. (b) Andzelm, J. In *Density Functional Theory in Chemistry*; Labanowski, J.; Andzelm, J., Eds.; Srpinger-Verlag: New York, NY, 1991; p. 155. (c) Andzelm, J.; Wimmer, E. *J. Chem. Phys.* 1992, *96*, 1280.

93. Chen, H.; Kraskowski, M.; Fitzgerald, G. *J. Chem. Phys.* **1993**, *98*, 8710. (b) Troullier, N.; Martins, J. L. *Phys. Rev.* **1991**, *B43*, **1993**.

94. Godbout, N.; Salahub, D. R.; Andzelm, J.; Wimmer, E. *Can. J. Chem.* **1992**, *70*, 560.

95. Vosko, S. J.; Wilk, L.; Nusair, W. *Can. J. Phys.* **1980**, *58*, 1200.

96. (a) Becke, A. D. Phys. Rev. A 1988, 38, 3098. (b) Becke, A. D. In *The Challenge of d and f Electrons: Theory and Computation*; Salahub, D. R.; Zerner, M. C., Eds.; ACS Symp. Ser. No. 394; American Chemical Society: Washington, DC, 1989; p. 166. (c) Becke, A. D. *Int. J. Quantum. Chem. Symp.* **1989**, *23*, 599.

97. Perdew, J. P. *Phys. Rev. B* **1986**, *33*, 8822.

98. Stevens, W. J.; Krauss, M.; Basch, H.; Jasien, P. G. *Can. J. Chem.* **1992**, *70*, 216.

99. Huzinaga, S.; Andzelm, J.; Klobukowski, M.; Radzio-Andzelm, E.; Sakai, Y.; Tatewaki, H. *Gaussian Basis Sets for Molecular Calculations*; Physical Sciences

Data 16: Elsevier, Amsterdam, 1984.

100. Frisch, M. J.; Trucks, G. W.; Schlegel, H. B.; Gill, P. M. W.; Johnson, B. G. Robb, M. A.; Cheeseman, J. R.; Keith, T. A.; Peterson, G. A.; Montgomery, J. A.; Raghavachari, K.; Al-Laham, M. A.; Zakrzewksi, V. G.; Ortiz, J. V.; Foresman, J. B.; Cioslowksi, J.; Stefanov, B. B.; Nanayakkara, A.; Challacombe, M.; Peng, C. Y.; Ayala, P. Y.; Chen, W.; Wong, M. W.; Andres, J. L.; Replogle, E. S.; Gomperts, R.; Martin, R. L.; Fox, D. J.; Binkley, J. S.; Defrees, D. J.; Baker, J.; Stewart, J. J. P.; Head-Gordon, M.; Gonzales, C.; Pople, J. A. *Gaussian 94*; Gaussian, Inc.: Pittsburg, PA, 1995.

101. Komomicki, A.; Fitzgerald, G. *J. Phys. Chem.* **1993**, *98*, 1398 and references therein.

102. Mayer, I. *Chem. Phys. Lett.* **1983**, *97*, 270; *Theoretica Chim. Acta* **1985**, *67*, 315; *Int. J. Quantum Chem.* **1986**, *29*, 73.

103. Rudolph, R. W.; Wilson, W. L.; Taylor, R. C. *J. Am. Chem. Soc.* **1981**, *103*, 2480. The $\delta(^{125}Te)$ value reported for the $SnTe_4^{4-}$ anion in en solution in this reference is incorrect. Approximate ^{119}Sn and ^{125}Te chemical shifts were subsequently reported by Haushalter and coworkers,[66] and accurate values were later reported by Schrobilgen and coworkers.[56]

104. Klepp, K. O. *Z. Naturforsch.* **1991**, *B47*, 411.

105. For example, the $[SnSe_3^{2-}]_\infty$ anion in the Zintl phases Na_2SnSe_3-I (Eisenmann, B.; Hansa, J. *Z. Kristallogr.* **1993**, *203*, 297) and Na_2SnSe_3-II (Eisenmann, B.; Hansa, J. *Z. Kristallogr.* **1993**, *203*, 293).

106. Sheldrick, W. W.; Braunbeck, H.-G. *Z. Naturforsch.* **1992**, *B47*, 151.

107. Klepp, K. O. *Z. Naturforsch.* **1992**, *B47*, 197.

108. Eisenmann, B.; Hansa, J. *Z. Kristallogr.* **1993**, *203*, 297.

109. Eisenmann, B.; Hansa, J. *Z. Kristallogr.* **1993**, *203*, 303.

110. Dittmar, G. Z. Norg. Allg. Chem. **1978**, *453*, 68.

111. Sheldrick, W. S. *Z. Naturforsch.* **1988**, *B43*, 249.

112. Sheldrick, W. S.; Braunbeck, H.-G. *Z. Naturforsch.* **1990**, *B45*, 1643.

113. Campbell, J.; DiCiommo, D. P.; Mercier, H. P. A.; Pirani, A. M.; Schrobilgen, G. J.; Willuhn, M. *Inorg. Chem.* **1995**, *34*, 6265.

114. Park, C.-W.; Bell, M. A.; Ibers, J. A. *Inorg. Chem.* **1996**, *35*, 4555.

115. Gay, I. D.; Jones, C. H. W.; Sharma, R. D. *J. Magn. Reson.* **1989**, *84*, 501.

116. Brinkmann, C.; Eisenmann, B.; Schäfer, H. *Mater. Res. Bull.* **1985**, *20*, 299.

117. Huang, S.-P.; Dhingra, S.; Kanatzidis, M. G. *Polyhedron* **1990**, *9*, 1389.

118. Dean, P. A. W.; Srivastava, R. S. *Inorg. Chim. Acta* **1985**, *105*, 1.

119. Allen, L. C. *J. Am. Chem. Soc.* **1989**, *111*, 9003 and references therein.

120. Gimarc, B. M.; Ott, J. S. *J. Am. Chem. Soc.* **1986**, *108*, 4298.

121. Webb, G. A. In *NMR and the Periodic Table*; Harris, R. K.; Mann, B. E., Eds.; Academic Press: London, England, 1978; Chapter 3, p. 49.

122. Wilson, W. L.; Rudolph, R. W.; Lohr, L. L.; Taylor, R. C.; Pyykkö, P. *Inorg. Chem.* **1986**, *25*, 1535.

123. Park, C.-W.; Salm, R. J.; Ibers, J. A. *Angew. Chem., Int. Ed. Engl.* **1995**, *34*, 1879.

124. Pauling, L. *The Nature of the Chemical Bond, 3rd ed.*; Cornell University Press: Ithaca, NY, 1960; pp. 224, 257, 260, 514.

125. Greenwood, N. N.; Earnshaw, A. *Chemistry of the Elements*; Pergamon Press: Oxford, England, 1984; Chapter 6, pp. 174, 181.

126. Lu, Y.-J.; Ansari, M. A.; Ibers, J. A. *Inorg. Chem.* **1989**, *28*, 4049.

127. Krebs, B.; Müller, H. *Z. Anorg. Allg. Chem.* **1983**, *496*, 47.

128. Hampden-Smith, M. J.; Wark, T. A.; Rheingold, A.; Huffman, J. C. *Can. J. Chem.* **1991**, *69*, 121.

129. Gardner, D. R.; Fettinger, J. C.; Eichhorn, B. W. *Angew. Chem., Int. Ed. Engl.* **1994**, *33*, 1859.

130. Krebs, B.; Pohl, S.; Schiwy, W. *Angew. Chem., Int. Ed. Engl.* **1970**, *9*, 897. Twelve bands were reported for the Raman spectrum of $Na_4Sn_2S_6 \cdot 14H_20$: 391, 377, 341, 281, 190, 178, 151, 136, 118, 96, 59, and 44 cm^{-1} (relative intensities not given).

131. Balls, A.; Downs, A. J.; Greenwood, N. N.; Staughan, B. P. *Trans. Faraday Soc.* **1966**, *62*, 521.

132. Beattie, I. R.; Gilson, T.; Cocking, P. *J. Chem. Soc. A* **1967**, p. 702.

133. Beattie, I. R.; Gilson, T.; Cocking, P. *J. Chem. Soc. A* **1968**, p. 814.

134. Adams, D. M.; Chuchill, R. G. *J. Chem. Soc. A* **1970**, p. 697.

135. Pohl, S.; Schiwy, W.; Weinstock, N.; Krebs, B. *Z. Naturforsch.* **1973**, *B28*, 565.

136. Dean, P. A. W.; Manivannan, V. *Inorg. Chem.* **1990**, *29*, 2997.

137. Vittal, J. J.; Dean, P. A. W.; Payne, N. C. *Can. J. Chem.* **1992**, *70*, 792.

138. Dean, P. A. W.; Vittal, J. J.; Wu, Y. *Inorg. Chem.* **1994**, *33*, 2180.

139. Krebs, B.; Voelker, D.; Stiller, K. O. *Inorg. Chim. Acta.* **1992**, *65*, L101.

140. Ribes, M.; Olivier-Fourcade, J.; Philippot, E.; Maurin, M. *J. Solid State Chem.* **1973**, *8*, 195.

141. Pohl, S.; Krebs, B. *Z. Anorg. Allg. Chem.* **1976**, *424*, 265.

142. Eulenberger, G. *Acta Crystallogr.* **1976**, *B32*, 3059.

143. Eulenberger, G. *Z. Naturforsch.* **1981**, *B36*, 521.

144. Dörfelt, C.; Janeck, A.; Kobelt, D.; Paulus, E. F.; Scherer, H. *J. Organomet. Chem.* **1968**, *14*, P22.

145. Blecher, A.; Drager, M.; Mathiasch, B. *Z. Naturforsch.* **1981**, *B36*, 1361.

146. Mertzweiler, K.; Weisse, L. *Z. Naturforsch.* **1990**, *B45*, 971.

147. Mertzweiler, K.; Kraus, H. *Z. Naturforsch.* **1994**, *B49*, 621.

148. The addition of THF to an en extract of the alloy $NaSn_{0.43}Se$ (en:THF = 1:2 v/v) gave rise to a yellow-orange needles of $(Na^+)_4SnSe_4^{4-}\cdot 2en$. A data set was obtained for one of these crystals, but the structure could only be partially solved in the space group $P4_32_12$ because two en solvent molecules and a cation were highly disordered. The tetrahedral geometry of the anion could, however, be refined (Sn–Se, 2.52 Å).

149. Müller, A.; Cyvin, B. N.; Cyvin, S. J.; Pohl, S.; Krebs, B. *Spectrochimica Acta* **1976**,

A32, 67.

150. Philippot, E.; Ribes, M.; Maurin, M. *Rev. Chim. Miner.* **1971**, *8*, 99.

151. Wallis, B.; Wolf, G.-U.; Leibnitz, P. *Z. Anorg. Allg. Chem.* **1990**, *588*, 139.

152. Jost, K. H. *Acta Crystallogr.* **1964**, *17*, 1593.

153. Lüer, B.; Jansen, M. *Z. Kristallogr.* **1991**, *197*, 247.

154. Corbett, J. D. *Inorg. Chem.* **1968**, *7*, 198.

155. Critchlow, S. C.; Corbett, J. D. *Inorg. Chem.* **1984**, *23*, 770.

156. Cisar, A.; Corbett, J. D. *Inorg. Chem.* **1977**, *16*, 2484.

157. Martin, T. P. *Angew. Chem., Int. Ed. Engl.* **1986**, *25*, 197.

158. Marsh, R. E.; Shoemaker, D. P. *Acta Crystallogr.* **1953**, *6*, 197.

159. Hansen, D. A.; Smith, J. F. *Acta Crystallogr.* **1967**, *22*, 836.

160. Critchlow, S. C.; Corbett, J. D. *Inorg. Chem.* **1982**, *21*, 3286.

161. Critchlow, S. C.; Corbett, J. D. *Inorg. Chem.* **1985**, *24*, 979.

162. Simon, A.; Borrmann, H.; Craubner, H. *Phosphorus and Sulfur* **1987**, *30*, 507.

163. Donohue, J. *The Structure of the Elements*; John Wiley & Sons, Inc.: New York, NY, 1974; Chapter 8, pp. 302–310.

164. Marynick, D. S.; Axe, F. U. *Inorg. Chem.* **1988**, *27*, 1426.

165. Cave, R. J.; Davidson, E. R.; Sautet, P.; Canadell, E.; Eisenstein, O. *J. Am. Chem. Soc.* **1989**, *111*, 8105.

166. Borrmann, H.; Campbell, J.; Dixon, D. A.; Mercier, H. P. A.; Pirani, A. M.;

Schrobilgen, G. J. *Inorg. Chem.* **1997**, submitted.

167. Toure, A. A.; Kra, G.; Eholie, R.; Olivier-Fourcade, J.; Jumas, J.-C. *J. Solid State Chem.* **1990**, *87*, 229.

168. Schiwy, I.; Böttcher, P.; von Schnering, H. G. *Z. Kristallogr.* **1989**, *118*, 287.

169. Pearson, W. B. In *Handbook of Lattice Spacings and Structures of Metals*; Pergamon Press: Oxford, England, 1967; Bd. 2, S. 90.

170. Dhingra, S. S.; Kanatzidis, M. G. *Inorg. Chem.* **1993**, *32*, 2298.

171. Gillespie, R. J.; Hargittai, I. *The VSEPR Model of Molecular Geometry*; Simon & Schuster, Inc.: Boston, MA, 1991; Chapters 3 and 5.

172. Björgvinsson, M.; Sawyer, J. F.; Schrobilgen, G. J. *Inorg. Chem.* **1987**, *26*, 741.

173. Björgvinsson, M.; Sawyer, J. F.; Schrobilgen, G. J. *Inorg. Chem.* **1991**, *30*, 2231.

174. Park, C.-W.; Salm, R. J.; Ibers, J. A. *Can. J. Chem.* **1995**, *73*, 1148.

175. The Raman spectrum of microcrystalline (2,2,2-crypt-K^+)I^- displayed several very weak, broad bands in the 50–350 cm^{-1} region.[113] The most intense 2,2,2-crypt-K^+ band at 135 cm^{-1}, which probably overlaps with the $Tl_2Ch_2^{2-}$ bands (Chapter 5), was too weak to be observed in the Raman spectrum of $(enH^+)_2$(2,2,2-crypt-$K^+)_2Sn_2Se_6^{4-}$.[60]

176. (a) Reed, A. E.; Curtiss, L. A.; Weinhold, F. *Chem. Rev.* **1988**, *88*, 899. (b) Foster, J. P.; Weinhold, F. J. *J. Am. Chem. Soc.* **1980**, *102*, 7211. (c) Reed, A. E.; Weinhold, F. *J. Chem. Phys.* **1983** *78*, 4066. (d) Reed, A. E.; Weinstock, R. B.; Weinhold, F. *J. Chem. Phys.* **1985**, *83*, 735. (e) Reed, A. E.; Weinhold, F. *J. Chem. Phys.* **1985**, *83*,

1736.

177. Dreiss, M.; Gleiter, R.; Janoschek, R.; Pritzkow, H.; Reisgys, M. *Angew. Chem., Int. Ed. Engl.* **1994**, *33*, 1484.

178. Yoshida, H.; Takahara, Y.; Erata, T.; Ando, W. *J. Am. Chem. Soc.* **1992**, *114*, 1098.

179. Ando, W.; Watanabe, S.; Choi, N. *J. Chem. Soc., Chem. Commun.* **1995**, p. 1683.

180. Sigwarth, B.; Zsolnai, L.; Berke, H.; Huttner, G. *J. Organomet. Chem.* **1982**, *226*, C5.

181. Huttner, G.; Weber, U.; Sigwarth, B.; Scheidsteger, O. *Angew. Chem., Int. Ed. Engl.* **1982**, *21*, 411.

182. Huttner, G.; Weber, U.; Zsolnai, L. *Z. Naturforsch.* **1982**, *B37*, 707.

183. Veith, M.; Kunze, K. *Angew. Chem., Int. Ed. Engl.* **1991**, *30*, 95.

184. Veith, M.; Rösler, R. *Angew. Chem., Int. Ed. Engl.* **1982**, *21*, 858.

185. (a) von Preut, H.; Haput, H. J.; Huber, F. *Z. Anorg. Allg. Chem.* **1973**, *396*, 81. (b) Goldbert, D. E.; Harris, D. H.; Lappert, M. F.; Thomas, K. M. *J. Chem. Soc., Chem. Commun.* **1976**, p. 261. (c) Sita, L. R.; Kinoshita, I. *Organometallics* **1990**, *9*, 2865.

186. Preut, H.; Haput, H. J.; Huber, F. *Z. Anorg. Allg. Chem.* **1972**, *388*, 165.

187. Mellela, S. P.; Myrczek, J.; Bernal, I.; Geanangel, R. A. *J. Chem. Soc., Dalton Trans.* **1993**, p. 2891.

188. Dean, P. A. W.; Vittal, J. J.; Payne, N. C. *Inorg. Chem.* **1984**, *23*, 4232.

189. Pyykkö, P.; Görling, A.; Rösch, N. *Mol. Phys.* **1987**, *61*, 195.

190. Edlund, U.; Lejon, T.; Pyykkö, P.; Venkatachalam, T. K.; Buncel, E. *J. Am. Chem.*

Soc. **1987**, *109*, 5982.

191. Nagase, S. *Polyhedron* **1991**, *10*, 1299.

192. Sita, L. R.; Bickerstaff, R. D. *J. Am. Chem. Soc.* **1989**, *111*, 6454.

193. Arsenault, J. J. I.; Dean, P. A. W. *Can. J. Chem.* **1983**, *61*, 1516.

194. Maciel, G. E.; McIver, J. W., Jr.; Ostlund, M. S.; Pople, J. A. *J. Am. Chem. Soc.* **1970**, *92*, 4151 and references therein.

195. Cairns, M. A.; Dixon, K. R.; McFarland, J. J. *J. Chem. Soc., Dalton Trans.* **1975**, p. 1159.

196. Butler, G.; Eaborn, C.; Pidcock, A. *J. Organomet. Chem.* **1979**, *181*, 47.

197. Eaborn, C.; Pidcock, A.; Steele, B. R. *J. Chem. Soc., Dalton Trans.* **1979**, p. 767.

198. Gillespie, R. J.; Schrobilgen, G. J. *J. Chem. Soc., Chem. Commun.* **1974**, p. 90.

199. Gillespie, R. J.; Netzer, A.; Schrobilgen, G. J. *Inorg. Chem.* **1974**, *13*, 1455.

200. Gillespie, R. J.; Landa, B.; Schrobilgen, G. J. *J. Chem. Soc., Chem. Commun.* **1971**, p. 1543.

201. Gillespie, R. G.; Landa, B.; Schrobilgen, G. J. *J. Chem. Soc., Chem. Commun.* **1972**, p. 607.

202. Gillespie, R. J.; Schrobilgen, G. J. *Inorg. Chem.* **1974**, *13*, 765.

203. Dhingra, S. S.; Kanatzidis, M. G. *Inorg. Chem.* **1993**, *32*, 1350.

204. Dhingra, S.; Liu, F.; Kanatzidis, M. G. *Inorg. Chim. Acta* **1993**, *210*, 237.

205. Dhingra, S.; Kanatzidis, M. G. *Science* **1992**, *258*, 1769.

206. O'Keeffe, M. *Struct. Bonding* **1989**, *71*, 162.

207. Bradtmöller, S.; Kremer, R. K.; Böttcher, P. *Z. Anorg. Allg. Chem.* **1994**, *620*, 1073.

208. Peters, J.; Krebs, B. *Acta Crystallogr.* **1982**, *B38*, 1270.

209. Blase, W.; Cordier, G. *Z. Kristallogr.* **1991**, *195*, 109.

210. Eisenmann, B.; Hofmann, A. *Z. Kristallogr.* **1991**, *197*, 171.

211. Brady, F.; Matthews, R. W.; Forster, M. J.; Gillies, R. G. *Inorg. Nucl. Chem. Lett.* **1981**, *17*, 155.

212. Schneider, W. G.; Buckingham, A. D. *Disc. Faraday Soc.* **1962**, *34*, 147.

APPENDIX A

Table A1. The ^{205}Tl NMR Subspectra of Natural Abundance $TlTe_3^{3-}$.

Isotopomer[a]	Multiplicities and Binomial Intensities[b]	Statistical Factor (S)[c]	Probability (%, P)	Abundance (S × P)
5 5 5	1 : 3 : 3 : 1	1	$(0.0699)^3$	0.00034
5 5 0	1 : 2 : 1	3	$(0.0699)^2 \times (0.9214)$	0.01350
5 0 0	1 : 1	3	$(0.0699) \times (0.9214)^2$	0.17803
0 0 0	1	1	$(0.9214)^3$	0.7825

Multiplicity Patterns for the $TlTe_3^{3-}$ Subspectra:[d]

$\frac{0.00034}{8} \times 1$		$\frac{0.00034}{8} \times 3$		$\frac{0.00034}{8} \times 3$		$\frac{0.00034}{8} \times 1$	quartet subspectrum
	$\frac{0.01350}{4} \times 1$		$\frac{0.01350}{4} \times 2$		$\frac{0.01350}{4} \times 2$		triplet subspectrum
		$\frac{0.17803}{2} \times 1$		$\frac{0.17803}{2} \times 1$			doublet subspectrum
			0.07825				singlet subspectrum
0.00004	0.00338	0.08914	0.78900	0.08914	0.00338	0.00004	total intensity pattern
«0.01	0.004	0.113	1.00	0.113	0.004	«0.01	relative line intensities

Table A1. Continued.

[a] The symbol (5) denotes the spin-active ^{125}Te nuclide (6.99% natural abundance); (0) denotes the NMR inactive nuclides of tellurium (92.14% total natural abundance). For simplicity, the low abundant spin-½ nuclide, ^{123}Te (0.87% natural abundance), has not been included in the calculations. [b] The multiplicities and binomial intensities of an isotopomer can be obtained from the coefficients of the *a* and *b* terms in the binomial expansion of $(a + b)^n$, where *n* is the total number of spin-active (in this case ^{125}Te) nuclides in the isotopomer of interest. [c] The statistical factor of an isotopomer can be obtained from the individual terms of the binomial expansion of $(a + b)^n$ and is given by the general expression $n! / (a! \times b!)$ where *n* is the total number of nuclides in the isotopomer of interest and *a* and *b* are the total number of spin-active and spinless nuclides, respectively, in the isotopomer. [d] The contribution of an isotopomer to the individual components of a subspectrum is obtained by multiplying the abundance of the isotopomer with each coefficient of the binomial intensities and then dividing the resulting product by the sum of the coefficients. The subspectra are then appropriately superpositioned as indicated, summed, and normalized to give the relative line intensities in the observed NMR spectrum.